Electrochemical Characterization of Organic Polymers And Their Applications for Renewable Energy

by

Dukhan Kim

A dissertation submitted in partial fulfillment
of the requirements for the degree of
Doctor of Philosophy
(Macromolecular Science and Engineering)
in the University of Michigan
2022

Doctoral Committee:

Professor Anne J. McNeil, Chair
Professor Jinsang Kim
Professor Adam J. Matzger
Professor Charles C. L. McCrory

Dukhan Kim

dukhan@umich.edu

ORCID iD: 0000-0002-5190-2667

Dedication

To my family, who always cheer me up

Acknowledgements

First, I want to thank my advisor, Prof. Anne McNeil, for giving me an opportunity to work in her lab and providing great guidance to think about my research critically. She believed in and supported me finding my interest somewhere between chemistry and engineering, was patient with me, and listened to personal concerns. Not only did Prof. McNeil provide an invaluable perspective toward science, but I also learned how to organize and show my achievements, a precious treasure for my future life. I was lucky to meet her as my advisor and will never forget this period for the rest of my life.

Thank you to my committee, Prof. Jinsang Kim, Prof. Adam Matzger, and Prof. Charles McCrory for their guidance. I will never forget the moment that I knocked on Prof. Kim's door my first year at UM. I thank Prof. Kim for always encouraging me and listening to me when I've talked about my anxiety. I'm glad that I could end up on at least one project with Prof. Kim eventually. I also thank Prof. Matzger for helping me land on McNeil group in 2017. The Raman data that he helped me to collect was the first and probably the last one that I could receive from faculty level. I strive to imitate his energetic life and enthusiasm. When I first emailed Prof. McCrory about a group presentation in his 2017 class, I was mentally overwhelmed: it was my first U.S. talk in front of a large audience, and I worried about my language barrier. But Prof. McCrory highlighted my part and gave me long and sincere positive feedback personally. That helped me to have confidence in myself the past few years.

Nothing would happen without great collaborators. I would like to thank my collaborators, Dr. Emily Mueller, Dr. Daseul Yang for OPV work, Prof. Melanie Sanford, Dr. Thomas Vaid, Sanford subgroup for RFB work, and Dr. Danielle Fagnani for PVC work. It was a great pleasure sharing countless chemistry and science conversations which helped me become a better scientist. Also, I want to thank Prof. Dongil Lee, my Master's advisor, who opened the door of my research history and encouraged me to be a better researcher.

I truly thank my lab mates past and present who communicated with me, supported me, and made my days funnier. I had a concern for my language barrier as well as cultural difference when I first came in, but everyone that I've met in McNeil lab was nice, considerate, and patient. Also I want to thank friends from the Macro department for being wonderful, entertaining me, and giving me a chance to settle into the engineering community. Thanks to my friends in Korea, who gave me positive stimulation to live more enthusiastically.

Lastly, I would like to thank all my family. My parents and parents-in-law didn't have the obligation for supporting their 30-years-old kids, but they didn't hesitate to help us physically, economically, and emotionally. There are no words to describe their endless love and support. I hope they stay healthy so that I can give my love back to them for the rest of their lives. Thanks to my sister and brother-in-law who taught me when I was teenager, broke my limitations, and showed me a bigger world to dream.

A special thanks to Yena, my daughter, and JiYoun, my wife. They laughed, cried, and dreamed with me in my every moment and gave me the reason to live. The long journey since 2011 has been delightful because they were with me, and I swear that I will become a better father and husband for them. I love you.

Table of Contents

List of Figures

List of Tables

List of Charts

List of Schemes

List of Appendices

Abstract

Renewable energy technologies are clean resources of energy that have a much lower environmental impact than conventional energy technologies such as coal or petroleum. Renewable energy technologies can help to reduce energy imports and the use of fossil fuel which is the largest source of U.S. carbon dioxide emissions. Organic polymers have received significant interest as key materials for renewable energy. Conducting polymers with tunable electrical conductivities could serve as electrodes or active materials for various electronic devices. Semiconducting polymers with tunable band gaps are great candidates as the semiconducting layers of optoelectronic devices such as organic solar cells. Also, both conducting polymers and insulating polymers have been explored for energy storage devices such as active materials, separators, electrolytes, pseudocapacitors, and so on. In addition, conventional plastics are the most widely used materials due to their durability, longevity, impermeability, good strength to mass ratio compared to metals, wood, and glass. This thesis is situated at the intersection of analytical and electrochemistry of various ranges of polymers and their engineering application for sustainability.

Although the organic solar cell is a promising technology, it has a relatively short lifetime due to poor long-term stability, making it a challenge for commercialization. In chapter 2, we investigated a random sequence copolymer containing a conjugated poly(3-hexylthiophene) backbone and fullerene-functionalized side chains that serve as a general blend stabilizer for an organic solar cell device. We found that this copolymer could stabilize morphology for multiple

blends in thin films and the active layer of organic solar cell devices and enhance the thermal stability of the devices. Understanding and developing of copolymer compatibilizer should play an important role to improve device performance and stability.

A redox flow battery is a rising area in the secondary battery due to its advantages such as design flexibility, safety, and scalability. In chapter 3, we discussed the modified design of a nonaqueous redox flow battery containing a high effective concentration of redox-active materials in insoluble polymer beads. A bulk of charge can be stored on redox-active moieties covalently tethered to non-circulating, insoluble polymer beads. The charge is rapidly transferred between the electrodes and the beads through soluble redox-matched mediators. With the functionalized beads, the battery capacity increased without the need to make high solubility redox-active molecules.

In chapter 4, we develop an electrosynthetic approach to repurpose poly(vinyl chloride), which has a low recycling rate in most countries. The chlorine atoms from PVC are recovered under electroreductive conditions and then directly repurposed as a feedstock in a tandem electrooxidative chlorination reaction. Also, we discovered a redox mediator that facilitates the reductive dechlorination reaction. The proposed mechanism of the reduction process was informed by cyclic voltammetry and bulk electrolysis analyses. This approach has good potential that PVC waste that we made in our life as a chlorine source can be repurposed to produce value-added products.

Chapter 1: Introduction

1.1 Earth As a Pale Blue Dot

In 1990, the American astronomer Carl Edward Sagan said "Pale blue dot" when he realized that the Earth was a bright pixel six billion kilometers away when photographed from Voyager 1.[1] To date, Earth is still the only place that can hold life, and the pale blue dot emphasizes that there is nothing around to help us.

In the last few years, a series of climate crises has threatened the life of the earth. In February 2021, the state of Texas suffered its worst blackouts due to three heavy winter storms and cold weather.[2] In the 2019-2020 Australian bushfire season, which is known as the "black summer," bushfires destroyed homes and forests and killed more than one billion animals.[3] The World Meteorological Organization recognized a temperature of 38 °C (100.4 °F) in the Russian town of Verkhoyansk in June 2020 as a new Arctic temperature record.[4] Driving massive sea ice loss, average temperatures over Arctic Siberia had reached as high as 10 °C above normal for much of the previous summer.[5] Snow in the Sahara Desert, which sounds impossible, took place in early 2022 near the town of Ain Sefra in Algeria.[6]

As a consequence of human behavior (e.g., transportation), burning fossil fuels significantly affects greenhouse gas emissions and global climate change.[7] A significant reduction in greenhouse gas emissions during the COVID-19 pandemic shows the influence of human behaviors on greenhouse gas emissions. Due to limited movement and social and economic

activities in 2020, greenhouse gas emissions decreased by 7% compared to the previous year - the largest decline ever recorded.[8]

If the current status of greenhouse gas emissions is maintained, it is anticipated that the average global temperature will rise 5 °C.[9] Because climate change has resulted in life-threatening crises, researchers have focused on approaches to alleviate it. Researchers have shown that it is critical to suppress the average global temperature increase below 1.5 °C by 2100 and to reach net-zero CO_2 emissions by 2050.[10]

To respond to the urgency of these issues and raise awareness of climate change, leaders of countries and institutions around the world have established and implemented various policies related to the climate crisis and energy transition issues. For example, the Kyoto Protocol (1997)[11] and Paris Climate Accords (2015)[12] on climate change have reduced fossil fuels over several decades in response to rapid climate change. To support collaborative practices, in 2020 President Biden announced that the United States will return to the Paris Climate Accords and actively respond to climate change.[13]

On the economic side, leaders in the global market have significantly considered the costs of climate change and the economic benefits of energy transition.[14] Data have shown that the cost of renewable energy, such as solar and wind power, has secured price competitiveness compared to fossil fuels.[15] Many companies have begun to increase their investments in renewable energy and energy transition in their portfolios.[16] As this trend shows, there is a growing awareness that timely response to climate change can contribute to economic growth by playing a pivotal role in future industries.

For example, the electronic vehicle is one of the efforts of global companies to apply new forms of energy to actual products and services.[17] In the next couple of decades, electric vehicles

will become the mainstay of the automobile industry. Instead of an internal combustion engine, vehicles will have an electric motor. By improving alternative forms of energy, the use of fossil fuels will decline, and greenhouse gas emissions will begin to decline sharply. Removing internal combustion engine cars from the road will contribute positively to global climate change by significantly reducing CO_2 emissions.

Although the development of renewable energy and its application to new products and services were big stepping stones, we still have work to do to address the sustainability of this approach. To establish a system for dealing with renewable energy, such as solar, wind, bioenergy, and hydropower, it is essential to understand their characteristics and challenges to develop technology. Therefore, two closely related considerations will help address the issues of greenhouse gas emissions. In this thesis, we ask how we can *generate* energy; how we can *store* energy. Also, for achieving sustainability, we address another question of how we can *repurpose* plastic waste. To answer each question, we will discuss organic solar cells (chapter 2), the redox-flow battery (chapter 3), and polyvinyl chloride recycling (chapter 4).

1.2 How can we generate energy?

A solar cell, also called a photovoltaic cell, is an electrical device that converts the energy of light directly into electricity by way of the photovoltaic effect. When light with sufficient energy is absorbed, it causes excitation of an electron or other charge carrier to a higher-energy level. An electric potential is produced by the separation of charges, which are called free electron and free hole. When they reach to the location in the device where the charge transfer will lower the energy of the system, the separation step begins, resulting in the generation of electricity.

The solar cell market can be divided in several ways: product type, application, end-user, and geography. The product type that is currently dominating world technology in photovoltaics is crystalline silicon.[18] Not only does it have great efficiency (>20%) in commercial modules and excellent stability, but, in a growing number of regions, production cost is reducing. Organic solar cells are a third-generation, photovoltaic technology that uses organic materials to harvest energy

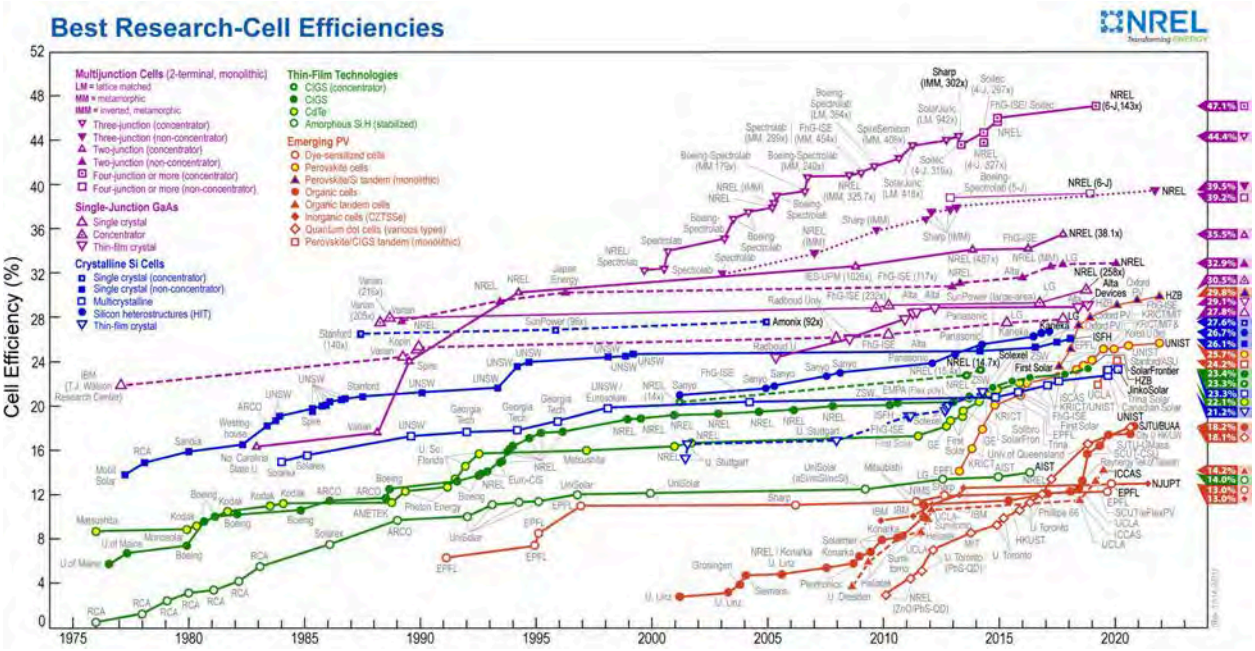

Figure 1.1. Best research-cell efficiencies reported by National Renewable Energy Laboratory (NREL).[19] (updated in December 2021)

from sunlight. Compared to silicon-based solar cells, unfortunately organic solar cells cannot compete for all the above factors at this point. (Figure 1.1)

Nevertheless, an organic solar cell is still an attractive technology because of its advantages, such as low weight, tunability, and inexpensive cost to fabricate.[20] Organic solar cells are flexible and customizable on the molecular level and have a potentially less adverse environmental impact. For example, an organic solar cell has advantages for integrated photovoltaics for buildings to be mounted on the roof or walls due to their flexibility, light weight, and construction of thin plastic foil. In addition, because the foils can be attached by double-sided sticky tape, repairs are simple after long-term use.[21] The market for building-integrated photovoltaics is small compared to the overall photovoltaic market (~5%).[22] Nevertheless, it could still become a promising, quickly growing market. The organic solar cell market size was valued at $62.56 million in 2019 and is projected to reach $142.30 million by 2027, growing at a compound annual growth rate (CAGR) of 12.5% between 2019 and 2027.[23]

Figure 1.2. Heliatek, German company, organic solar modules (top) on a wind turbine and (bottom) applied on the façade of an industrial building.[24]

The global, organic solar cell market is divided into small molecules and polymers. In 2021, the polymers segment was expected to dominate the market, because polymer solar cells have an additional potential to exhibit transparency, which suggests applications in windows, walls, flexible electronics, and others.[25] Because of improvements in conjugated polymer design over the last twenty-five years, the power conversion efficiencies (PCEs) for organic solar cells have risen from 3%[26] to recent, record-breaking values of >18% according to a National Renewable Energy Laboratory research team.[27]

Despite these promising advantages, a short device lifetime due to poor, long-term stability remains a challenge for commercialization.[28] Most organic solar cells consist of a blend of two materials: a conjugated polymer electron donor and a small molecule electron acceptor.[29] Initially, the physical blends of an electron donor and electron acceptor in the active layer are nano-scale domains and enable effective charge separation under light illumination.[30] However, with aging, they can phase-separate into larger, micron-scale domains in an enthalpically-driven process that results in a changed morphology over time. This transition reduces the efficiency of charge separation as well as PCEs.[31] A third component, such as a copolymer that is miscible with both the donor and acceptor can stabilize the active layer's blended morphology, but these additives are often tailored to match the specific donor/acceptor blend.[32]

In a previous study, the McNeil group evaluated how the sequence, composition, and blend concentration of copolymer additives affect morphological stability and device performances with conjugated poly(3-hexylthiophene) and fullerene-based acceptors.[33] As a result, a random copolymer with 20 mol% fullerene side-chain functionalization at 8 wt% in the blend showed the best performance for stabilizing a thin, film blend morphology and PCEs. Therefore, we

hypothesized that this type of copolymer could be miscible with other donor/acceptor systems and serve as a general compatibilizer.

In chapter 2, we demonstrate that the reported random sequence copolymer having fullerene side chains also serves as a general blend stabilizer for high-performing donors and acceptor molecule. We chose three different conjugated polymer/fullerene blends (PTB7, PTB7-Th, and PffBT4T-2OD with $PC_{71}BM$) for showing our strategy. In all cases, there were severe macroscale phase separation after annealing at high temperature without copolymer in thin films, while the phase separation was suppressed when the copolymer was mixed with donor/acceptor blends. Similarly, in the active layer of PffBT4T-2OD:$PC_{71}BM$ blends in fabricated devices, phase separation also reduced in copolymer-containing active layer after annealing. We attribute this thermal stability to the copolymer's ability to prevent fullerene aggregation.

However, devices with copolymer exhibited initial power conversion efficiency drop compared to devices without copolymer. We investigated factors for tracking this drop and observed lower absorption efficiency and lower electron current when the copolymer was added. With annealing, both devices with and without copolymer experienced performance losses in first 30 min annealing, but devices with copolymer showed relatively smaller losses as well as better thermal stability compared to control device. Overall, we suggest that the fullerene-functionalized poly(3-hexylthiophene) copolymer could be a general stabilizing additive to suppress macroscale phase separation in both conjugated polymer/fullerene thin films and photovoltaic devices, resulting good thermal stability of the devices.

1.3 How can we store the energy?

Solar and wind energy are environmentally friendly and are considered promising alternative energy resources for the future. However, inherent intermittency during the day and night limits the full utilization of these renewable resources.[34] Under this limitation, the battery market is growing explosively.[35] With the rapid growth of the electric vehicle market, the market for the battery that powers it is also receiving attention. There are several ways to classify batteries, but they can be divided into primary batteries, which are non-rechargeable, and secondary batteries, which are rechargeable. In the twentieth century, the lead-acid battery was a well-known secondary battery for grid-scale energy storage, because of its low capital cost and advanced technological support.[36] However, its disadvantages, such as limited cycling time, high maintenance cost, and contamination by lead encouraged other electrochemical approaches. The redox flow battery (RFB), which was first invented in 1974, exhibits advantages, such as design flexibility, safety, and scalability.[38]

A RFB is a type of electrochemical, energy-storage device in which chemical energy is provided by two chemical components (anolyte and catholyte) dissolved in liquids that are pumped through a system on separate sides of a membrane. (Scheme 1-1a)[40] RFBs have many advantages over other types. They achieve the complete separation of power and energy by using external

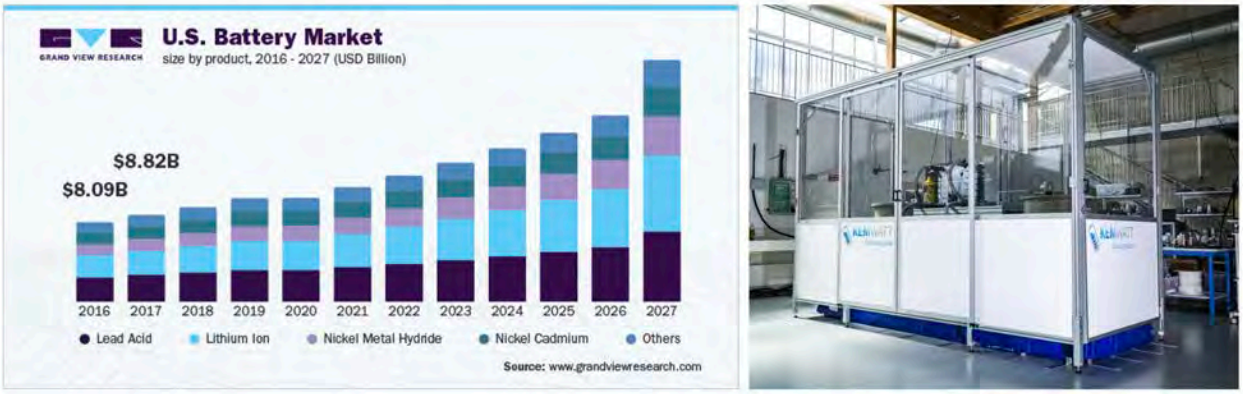

Figure 1.3. Battery market trend in U.S. (left) Organic RFB, Kemiwatt company (right).[39]

tanks, resulting in a flexible layout. RFBs are an economical choice in the range of kilowatts to megawatts because storage size and flow controls are easy to scale up by the installation of larger storage tanks to hold more electrolytes. In addition, RFBs have other advantages, such as a long life (more than twenty years), simple recharging by replacing the electrolyte liquid, no harmful emissions from charging-discharging, and so on.

The most common RFB is the vanadium RFB, which contains vanadium ions as charge carriers; it was initially studied by NASA.[41] Vanadium can exist in a solution in four different oxidation states to make a battery with a single electroactive molecule (different oxidation states of Vanadium) instead of two different molecules, anolyte and catholyte. The global redox flow battery market size was valued at $130.4 million in 2018 and is projected to reach $403.0 million by 2026, growing at a compound annual growth rate (CAGR) of 15.2% between 2019 and 2026.[42]

Nonaqueous RFBs contain organic electroactive molecules and supporting electrolytes in organic solvents, such as acetonitrile, dimethylformamide, and propylene carbonate. To take advantage of wide electrochemical windows of up to 5 V compared to ~1.5 V in an aqueous system, redox active molecules with high oxidation potentials and low reduction potentials can be used.[43] Redox-active molecules can be functionalized to create molecules with high solubilities (> 1 M),[44] thus enabling high energy density nonaqueous RFBs. However, at concentrations near 1 M, most redox active molecules become viscous, and ionic conductivity decreases, making them less suitable for use in RFBs.[45] An additional issue that must be addressed in RFBs is the crossover of the redox-active species between the anolyte and catholyte solutions. Once a redox-active species has crossed over to the opposite electrolyte solution, it is no longer electrochemically active, resulting in a loss in capacity for the RFB.[46]

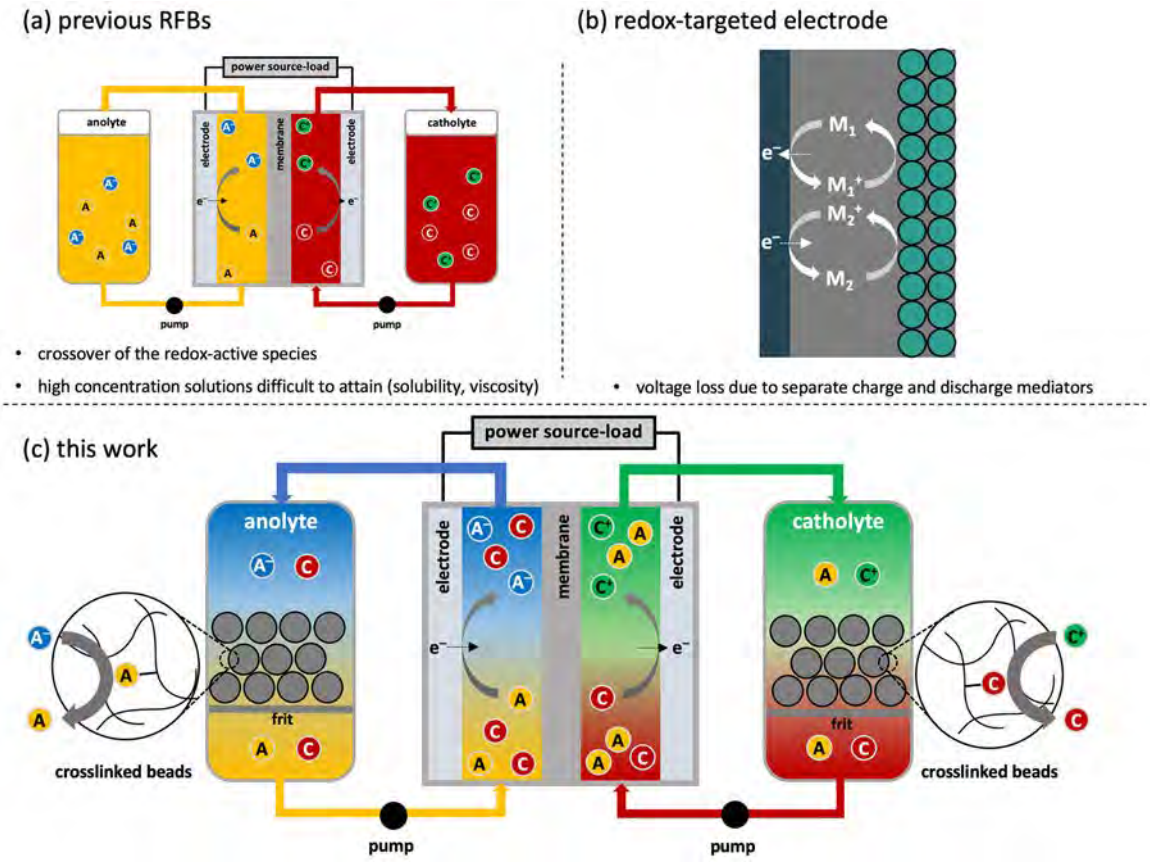

Scheme 1-1. Previous RFBs, A Redox-Targeted Electrode, and the Redox-Matched Flow Battery

An innovative concept, the redox-targeted electrode, was introduced by Wang, Grätzel and coworkers in 2006[47] and points the way to a system that could simultaneously address several of the issues discussed above. (Scheme 1-1b) Since the report, several more redox-targeted inorganic electrodes, or hybrid flow batteries with one redox-targeted electrode, have been reported,[48] as has a full redox-targeted flow battery[49] and an aqueous RFB with one redox-targeted organic polymer electrode[50].

In chapter 3, we introduce the non-aqueous redox-matched flow battery (RMFB), redox-active molecules are covalently tethered to crosslinked polystyrene polymer beads and these beads act as the charge storage material. (Scheme 1-1c) These beads are insoluble and non-circulating,

instead sit on the frit in the reservoir. The redox-active moieties are a ferrocene derivative for the catholyte beads and a viologen derivative for the anolyte beads. For each bead type, there are redox-matched soluble mediators with similar structures to the redox-active moieties on the beads. The mediators help charge transfer between the electrodes and the polymer beads. Due to similarity of structure, the redox potentials are nearly the same and this similarity enables a Nernstian equilibration between the soluble mediators and polymer-supported redox active species.

From this design strategy, we have several expected advantages. First, we use two redox-matched mediators for each polymer beads, so that there is no loss in voltaic efficiency due to multiple mediators with different redox potentials. Also, not only polymer-supported charge storage enables highly effective concentration of active material in the reservoirs without crossover of that material, but also low concentration of mediator solution gets rid of the need of high solubility material and high viscous solution.

An essential factor of this design is that redox exchange between the beads and solution-phase mediators occurs within several minutes, which is fast compared to the one-half cycle of the RMFB (< 60 min). We demonstrate that the charge transfer happens fast enough compared to the time scale. The crossover rates with various membrane options were monitored by microelectrode, which indicated fumasep ion-exchange membrane as best option for RMFB. The RMFB was first cycled with only the soluble mediators present and then with one and two redox equiv. of beads added to the anolyte and catholyte reservoirs. With one equiv of beads, the battery discharge capacity increased by 52%, and with two equiv. it increased by 112%, demonstrating the viability of the RMFB concept.

1.4 How can we repurpose plastic waste?

One important direction to achieve sustainability is dealing with plastic waste and developing methods to recycle them to save natural resources. Approximately 500 million tons of plastics are produced annually worldwide.[51] In 2020, we generated 900% more plastics than in 1980.[52] If we fail to reduce our usage, plastics in the oceans will outweigh fish pound for pound in 2050.[53] It is difficult to rapidly fix the increasing plastic consumption in various industries, including electronics, automotive, and others. The Covid-19 pandemic is driving an increase in the demand for various packaging products, including online purchases and personal protective equipment, such as gloves or masks.[54] Therefore, reducing the use of plastics but also recycling them have great advantages beyond saving energy and resources. They can reduce the amount of waste sent to landfills, prevent pollution by reducing the need to collect new raw materials, and conserve natural resources. The global recycled plastic market size was valued at USD 45.1 billion in 2019 and is expected to grow at a compound annual growth rate (CAGR) of 5.0% between 2020 and 2027.[55]

To date, plastics recycling has primarily involved mechanical recycling, which downgrades material quality and limits utility. Recycling rates (<10%) are unlikely to improve with mechanical recycling alone, leading to calls for innovations in chemical recycling.[56] Closed-loop recycling is a system in which the waste material of one process, such as the unwrapping of pallet stretch film, is used in the production of another, such as new can liners and pallet sheets. Closed-loop recycling starts with a collection of scrap plastic stretch film. Once collected plastic scraps are processed and turned into plastic pellets or resin. Closed-loop mechanical recycling reuses the resin and finally creates a new version of the same product.

Closed-loop chemical recycling, in which polymers are first depolymerized into their monomers and then repolymerized to generate a material with same function, has been realized for only hydrolyzable polymers, such as PET (polyethylene terephthalate).[57] However, in general, commercial plastics are not recycled in a circular closed-loop recycling due to lack of methods to selectively depolymerize polymers back to their original monomers.[58] These materials could be recycled in an open-loop process, wherein polymers are treated using various forms of treatment such as heat, chemical reactions, physical crushing to break down into smaller fragments. These fragments could be converted into new material different from their original purpose via other chemical processes. However, the leading open-loop process, anaerobic pyrolysis, is useful only for few hydrocarbon polymers because thermal degradation is unlikely to proceed naturally due to the high temperatures required.[59]

Poly(vinyl chloride) (PVC) is not recycled through any of these approaches and has the lowest recycling rate in most countries (0% in the United States),[59] even though it has a high-production-volume rate. A major problem in the recycling of PVC is the high chlorine content in raw PVC (around 56 % of the polymer weight) resulting uncontrolled hydrogen chloride (HCl) elimination and the high levels of hazardous plasticizers. Sadly, Ono and coworkers examined the biodegradation of PVC buried under soil for over 32 years and couldn't find any evidence of biodegradation.[60] Therefore, low recycling rates are concerning, because PVC poses a known health risk in the environment in the long term.[61]

In chapter 4, we discuss new recycling approaches for PVC waste. We develop an one-pot paired-electrolysis reaction to repurpose PVC waste and generate value-added chlorinated arene. Although HCl elimination from PVC is problematic in high-temperature recycling processes, HCl itself is a useful reagent in many chemical reactions. So, if we think about in different way, PVC

waste has an advantage to release HCl intentionally and can be used to produce chlorinated arene in a single-pot process. In the meantime, diethylhexyl phthalate (DEHP) which is the most common plasticizer used in PVC serves as a redox mediator and improves the synthetic yield. To characterize electrochemical behaviors of PVC and DEHP, we use cyclic voltammetry (CV) and measure redox reversibility of DEHP in the presence/absence of PVC. CV data also indicate the voltages at which redox events occur. Bulk electrolysis experiments in H-cell help understanding of mechanistic role of DEHP as redox mediator. We also demonstrate that a commercial PVC product can be used efficiently in these reactions, even in the presence of other plastics. This new open-loop recycling approach should inspire new strategies for PVC waste recycling to address sustainability.

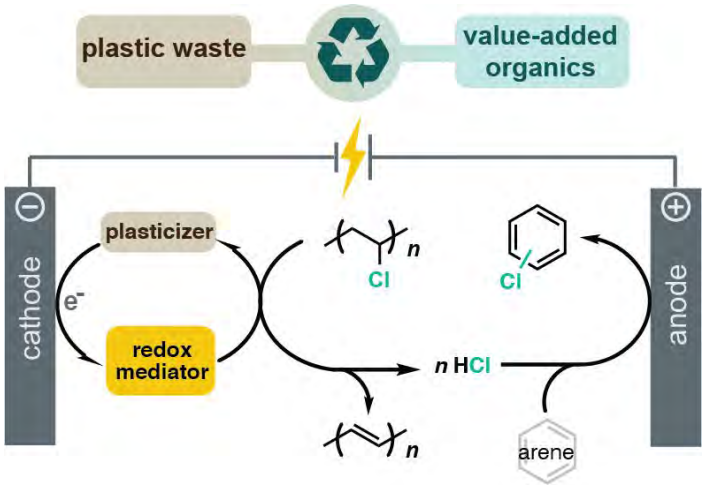

Scheme 1-2. General scheme of paired-electrolysis reaction for reductive dechlorination of PVC and oxidative chlorination of an arene

1.5 References

(1) Voyager 1's Pale Blue Dot. https://solarsystem.nasa.gov/resources/536/voyager-1s-pale-blue-dot/ (accessed Feb 15, 2022).

(2) Accounts, T. C. of P. Winter storm uri 2021. https://comptroller.texas.gov/economy/fiscal-notes/2021/oct/winter-storm-impact.php#:~:text=The%20storm%20contributed%20to%20at,%2480%20billion%20to%20%24130%20billion. (accessed Feb 15, 2022).

(3) 2020–21 Australian bushfire season. https://en.wikipedia.org/wiki/2020%E2%80%9321_Australian_bushfire_season (accessed Feb 15, 2022).

(4) WMO recognizes New Arctic Temperature Record of 38ºC. https://public.wmo.int/en/media/press-release/wmo-recognizes-new-arctic-temperature-record-of-38%E2%81%B0c (accessed Feb 15, 2022).

(5) Neuman, S. The Arctic has a new record high temperature, according to the U.N. https://www.npr.org/2021/12/14/1064042128/arctic-heat-record-siberia-climate-change (accessed Feb 15, 2022).

(6) In pictures: Snow falls in Algeria's Sahara Desert. https://www.bbc.com/news/world-africa-60045153 (accessed Feb 15, 2022).

(7) Burning of fossil fuels. https://ugc.berkeley.edu/background-content/burning-of-fossil-fuels/#:~:text=The%20effects%20of%20the%20burning,human%20and%20environmental%20health%20problems (accessed Feb 15, 2022).

(8) Rume, T.; Islam, S. D. U. Environmental effects of COVID-19 pandemic and potential strategies of sustainability. *Heliyon*, **2020**, *6,* e04965.

(9) Center for Science Education. Predictions of Future Global Climate. https://scied.ucar.edu/learning-zone/climate-change-impacts/predictions-future-global-climate (accessed March 15, 2022)

(10) IPCC press release summary for policymakers of IPCC ... https://www.ipcc.ch/site/assets/uploads/2018/11/pr_181008_P48_spm_en.pdf (accessed Feb 15, 2022).

(11) https://unfccc.int/process-and-meetings/the-kyoto-protocol/what-is-the-kyoto-protocol/kyoto-protocol-targets-for-the-first-commitment-period (accessed Feb 15, 2022).
(12) The Paris Agreement. https://www.un.org/en/climatechange/paris-agreement (accessed Feb 15, 2022).
(13) Fact sheet: President Biden Renews U.S. leadership on world stage at U.N. Climate Conference (COP26). https://www.whitehouse.gov/briefing-room/statements-releases/2021/11/01/fact-sheet-president-biden-renews-u-s-leadership-on-world-stage-at-u-n-climate-conference-cop26/ (accessed Feb 15, 2022).
(14) Natalie Marchant, W. This is how climate change could impact the global economy. https://www.weforum.org/agenda/2021/06/impact-climate-change-global-gdp/ (accessed Feb 15, 2022).
(15) United Nations. How renewable energy can be cost-competitive. https://www.un.org/en/chronicle/article/how-renewable-energy-can-be-cost-competitive (accessed March 15, 2022)
(16) Energy Transition Investment Trends 2022. https://about.bnef.com/energy-transition-investment/ (accessed Feb 15, 2022).
(17) Fessler, David C. The energy disruption triangle: three sectors that will change how we generate, use, and store energy. John Wiley & Sons, **2019**.
(18) Sopian, K.; S. L. Cheow; and S. H. Zaidi. An overview of crystalline silicon solar cell technology: Past, present, and future. *AIP Conference Proceedings.* **2017**, *1877*, 020004
(19) Best research-cell efficiency chart - nrel.gov. https://www.nrel.gov/pv/assets/pdfs/best-research-cell-efficiencies-rev211214.pdf (accessed Feb 15, 2022).
(20) Riede, M.; Spoltore, D.; Leo, K. Organic Solar Cells The Path to Commercial Success. Adv. Energy Mater. **2021**, *11*, 2002653.
Li, Y.; Xu, G.; Cui, C.; Li, Y. Flexible and Semitransparent Organic Solar Cells. Adv. Energy Mater. **2018**, *8*, 1701791.
Wang, Q.; Xie, Y.; Soltani-Kordshuli, F.; Eslamian, M. Progress in Emerging Solution-Processed Thin Film Solar Cells - Part I: Polymer Solar Cells. Renewable Sustainable Energy Rev. **2016**, *56*, 347−361.
Guo, J.; Min, J. A Cost Analysis of Fully Solution-Processed ITO-Free Organic Solar Modules. Adv. Energy Mater. **2019**, *9*, 180252

(21) Oesen, B.; Ullbrich, S.; Widmer, J.; Leo, K. Novel Thin-Film Photovoltaics—Status and Perspectives. In Green Photonics and Electronics **2017**, 263-287. Springer, Cham.

(22) Osseweijer, F. J.; Van Den Hurk, L. B.; Teunissen, E. J.; van Sark, W. G. A comparative review of building integrated photovoltaics ecosystems in selected European countries. *Renewable and Sustainable Energy Reviews,* **2018**, *90*, 1027-1040.

(23) Organic Solar Cells Market Size & Share: Industry Trends, 2021-2026. https://www.knowledge-sourcing.com/report/organic-solar-cells-market (accessed Feb 15, 2022).

(24) Heliasol - Heliatek GmbH. https://www.heliatek.com/en/products/heliasol/ (accessed Feb 15, 2022).

(25) Krebs, F. C. Fabrication and processing of polymer solar cells: A review of printing and coating techniques. *Solar energy materials and solar cells*, **2009**, *93*, 394-412.

(26) Wadsworth, A.; Hamid, Z.; Bidwell, M.; Ashraf, R. S.; Khan, J. I.; Anjum, D. H.; Cendra, C.; Yan, J.; Rezasoltani, E.; Guilbert, A. A. Y.; Azzouzi, M.; Gasparini, N.; Bannock, J. H.; Baran, D.; Wu, H.; de Mello, J. C.; Brabec, C. J.; Salleo, A.; Nelson, J.; Laquai, F.; McCulloch, I. Progress in Poly (3-Hexylthiophene) Organic Solar Cells and the Influence of Its Molecular Weight on Device Performance. *Adv. Energy Mater*. **2018**, *8*, 1801001.

(27) New design strategy pushes organic photovoltaics past 18% efficiency. https://www.nrel.gov/news/program/2021/new-design-strategy-increases-organic-pv-efficiency.html (accessed Feb 15, 2022).

(28) Turak, A. Device Stability in Organic Optoelectronics. Handbook of Organic Materials for Electronic and Photonic Devices, 2nd ed.; Elsevier, **2019**; pp 599−662.

(29) Lu, L.; Zheng, T.; Wu, Q.; Schneider, A. M.; Zhao, D.; Yu, L. Recent Advances in Bulk Heterojunction Polymer Solar Cells. *Chem. Rev*. **2015**, *115*, 12666−12731

(30) Treat, N. D.; Chabinyc, M. L. Phase Separation in Bulk Heterojunctions of Semiconducting Polymers and Fullerenes for Photovoltaics. *Annu. Rev. Phys. Chem.* **2014**, *65*, 59−81.

(31) Yu, G.; Gao, J.; Hummelen, J. C.; Wudl, F.; Heeger, A. J. Polymer Photovoltaic Cells: Enhanced Efficiencies via a Network of Internal Donor-Acceptor Heterojunctions. *Science* **1995**, *270*, 1789−1791.

Shaw, P. E.; Ruseckas, A.; Samuel, I. D. W. Exciton Diffusion Measurements in Poly(3-Hexylthiophene). *Adv. Mater*. **2008**, *20*, 3516−3520.

Hedley, G. J.; Ward, A. J.; Alekseev, A.; Howells, C. T.; Martins, E. R.; Serrano, L. A.; Cooke, G.; Ruseckas, A.; Samuel, I. D. W. Determining the Optimum Morphology in High-Performance Polymer-Fullerene Organic Photovoltaic Cells. *Nat. Commun*. **2013**, *4*, 2867.
Cardinaletti, I.; Kesters, J.; Bertho, S.; Conings, B.; Piersimoni, F.; D'Haen, J.; Lutsen, L.; Nesladek, M.; Van Mele, B.; Van Assche, G.; Vandewal, K.; Salleo, A.; Vanderzande, D.; Maes, W.; Manca, J. V. Toward Bulk Heterojunction Polymer Solar Cells with Thermally Stable Active Layer Morphology. *J. Photonics Energy* **2014**, *4*, 040997.
Savagatrup, S.; Printz, A. D.; O'Connor, T. F.; Zaretski, A. V.; Rodriquez, D.; Sawyer, E. J.; Rajan, K. M.; Acosta, R. I.; Root, S. E.; Lipomi, D. J. Mechanical Degradation and Stability of Organic Solar Cells: Molecular and Microstructural Determinants. *Energy Environ. Sci*. **2015**, *8*, 55−80.

(32) Bonasera, A.; Giuliano, G.; Arrabito, G.; Pignataro, B. Tackling Performance Challenges in Organic Photovoltaics: An Overview about Compatibilizers. *Molecules* **2020**, 25, 2200.
Cheng, P.; Zhan, X. Versatile Third Components for Efficient and Stable Organic Solar Cells. *Mater. Horiz.* **2015,** *2*, 462−485.

(33) Kong, C.; Song, B.; Mueller, E. A.; Kim, J.; McNeil, A. J. Random Copolymers Outperform Gradient and Block Copolymers in Stabilizing Organic Photovoltaics. *Adv. Funct. Mater*. **2019**, *29*, 1900467.

(34) Bird, L., Milligan, M., & Lew, D. (2013). *Integrating variable renewable energy: Challenges and solutions* (No. NREL/TP-6A20-60451). National Renewable Energy Lab.(NREL), Golden, CO (United States).

(35) Battery Market Size & Share: Industry Report, 2020-2027. https://www.grandviewresearch.com/industry-analysis/battery-market (accessed Feb 16, 2022).

(36) May, G. J., Davidson, A., & Monahov, B. Lead batteries for utility energy storage: A review. *Journal of energy storage*, **2018**, *15*, 145-157.

(37) Wu, X., Song, K., Zhang, X., Hu, N., Li, L., Li, W., ... & Zhang, H. Safety issues in lithium ion batteries: Materials and cell design. *Frontiers in Energy Research*, **2019**, *65*.

(38) Redox Flow Batteries (RFB). https://energystorage.org/why-energy-storage/technologies/redox-flow-

batteries/#:~:text=Redox%20flow%20batteries%20offer%20an,means%20for%20storing%20electrical%20energy (accessed Feb 15, 2022).

(39) Battery Market Size & Share: Industry Report, 2020-2027. https://www.grandviewresearch.com/industry-analysis/battery-market (accessed Feb 15, 2022). KEMIWATT: Your energy bank. https://kemiwatt.com/technology/ (accessed Feb 15, 2022).

(40) J. Noack, N. Roznyatovskaya, T. Herr, P. Fischer, *Angew. Chem. Int. Ed.* **2015**, 54, 9776–9809.

J. Winsberg, T. Hagemann, T. Janoschka, M. D. Hager, U. S. Schubert, *Angew. Chem. Int. Ed.* **2017**, 56, 686–711.

(41) Menictas, C.; Skyllas-Kazacos, M.; Lim, T. M. (Eds.). Advances in batteries for medium and large-scale energy storage: types and applications. **2014**, Elsevier.

(42) Redox flow battery market size, share: Industry Forecast - 2026. https://www.alliedmarketresearch.com/redox-flow-battery-market#:~:text=The%20global%20redox%20flow%20battery,energy%20and%20supply%20whenever%20needed (accessed Feb 15, 2022).

(43) M. Ue, K. Ida, S. Mori, *J. Electrochem. Soc.* **1994**, *141*, 2989.

R. M. Darling, K. G. Gallagher, J. A. Kowalski, S. Ha, F. R. Brushett, *Energy Environ. Sci.* **2014**, *7*, 3459–3477.

(44) S. G. Robinson, Y. Yan, K. H. Hendriks, M. S. Sanford, M. S. Sigman, *J. Am. Chem. Soc*. **2019**, *141*, 10171–10176

(45) J. Zhang, R. E. Corman, J. K. Schuh, R. H. Ewoldt, I. A. Shkrob, L. Zhang, *J. Phys. Chem. C* **2018**, *122*, 8159–8172.

(46) Y. K. Zeng, T. S. Zhao, L. An, X. L. Zhou, L. Wei, *J. Power Sources* **2015**, *300*, 438–443.

R. A. Potash, J. R. McKone, S. Conte, H. D. Abruña, *J. Electrochem. Soc.* **2016**, *163*, A338–A344.

W. Duan, R. S. Vemuri, J. D. Milshtein, S. Laramie, R. D. Dmello, J. Huang, L. Zhang, D. Hu, M. Vijayakumar, W. Wang, J. Liu, R. M. Darling, L. Thompson, K. Smith, J. S. Moore, F. R. Brushett, X. Wei, *J. Mater. Chem. A* **2016**, *4*, 5448–5456.

J. Moutet, J. M. Veleta, T. L. Gianetti, *ACS Appl. Energy Mater.* **2021**, *4*, 9–14.

K. H. Hendriks, S. G. Robinson, M. N. Braten, C. S. Sevov, B. A. Helms, M. S. Sigman, S. D. Minteer, M. S. Sanford, *ACS Cent. Sci.* **2018**, *4*, 189–196.

A. Shrestha, K. H. Hendriks, M. S. Sigman, S. D. Minteer, M. S. Sanford, *Chem. Eur. J.* **2020**, *26*, 5369–5373.

(47) Q. Wang, S. M. Zakeeruddin, D. Wang, I. Exnar, M. Grätzel, *Angew. Chem. Int. Ed.* **2006**, *45*, 8197–8200.

J. Ye, L. Xia, C. Wu, M. Ding, C. Jia, Q. Wang, *J. Phys. D: Appl. Phys.* **2019**, *52*, 443001.

(48) Q. Huang, H. Li, M. Grätzel, Q. Wang, *Phys. Chem. Chem. Phys.* **2013**, *15*, 1793–1797.

J. R. Jennings, Q. Huang, Q. Wang, *J. Phys. Chem. C* **2015**, *119*, 17522–17528.

E. Zanzola, C. R. Dennison, A. Battistel, P. Peljo, H. Vrubel, V. Amstutz, H. H. Girault, *Electrochim. Acta* **2017**, *235*, 664–671.

F. Pan, J. Yang, Q. Huang, X. Wang, H. Huang, Q. Wang, *Adv. Energy Mater.* **2014**, *4*, 1400567.

J. Yu, M. Salla, H. Zhang, Y. Ji, F. Zhang, M. Zhou, Q. Wang, *Energy Stor. Mater.* **2020**, *29*, 216–222.

Y. G. Zhu, Y. Du, C. Jia, M. Zhou, L. Fan, X. Wang, Q. Wang, *J. Am. Chem. Soc.* **2017**, *139*, 6286–6289.

C. Jia, F. Pan, Y. G. Zhu, Q. Huang, L. Lu, Q. Wang, *Sci. Adv.* **2015**, *1*, e1500886.

M. Zhou, Y. Chen, M. Salla, H. Zhang, X. Wang, S. R. Mothe, Q. Wang, *Angew. Chem. Int. Ed.* **2020**, *59*, 14286–14291.

(49) C. Jia, F. Pan, Y. G. Zhu, Q. Huang, L. Lu, Q. Wang, Sci. Adv. 2015, 1, e1500886

(50) M. Zhou, Y. Chen, M. Salla, H. Zhang, X. Wang, S. R. Mothe, Q. Wang, Angew. Chem. Int. Ed. 2020, 59, 14286–14291; Angew. Chem. 2020, 132, 14392–14397.

(51) The facts. https://plasticoceans.org/the-facts/ (accessed Feb 15, 2022).

(52) Plastic pollution accelerates climate change. https://blog.placetoplug.com/en/post/plastic-pollution-5da6dcbf52ff (accessed Feb 15, 2022).

(53) Harmony. Plastic recycling. https://harmony1.com/plastic-recycling/ (accessed Feb 15, 2022).

(54) Recycled plastic market size & share report, 2020-2027. https://www.grandviewresearch.com/industry-analysis/recycled-plastics-market(accessed Feb 15, 2022).

(55) Global Plastic Recycling Market to reach $47.3 billion by 2026. https://www.globenewswire.com/news-release/2021/10/22/2319279/0/en/Global-Plastic-Recycling-Market-to-Reach-47-3-Billion-by-2026.html (accessed Feb 15, 2022).

(56) R. Geyer, J. R. Jambeck, K. L. Law, Production, use, and fate of all plastics ever made. *Sci. Adv.* **2017***, 3*, e1700782

J. M. Garcia, M. L. Robertson, The future of plastics recycling. *Science* **2017***,* 358, 870–872

I. Vollmer, M. J. F. Jenks, M. C. P. Roelands, R. J. White, T. van Harmelen, P. de Wild, G. P. van der Laan, F. Meirer, J. T. F. Keurentjes, B. M. Weckhuysen, Beyond mechanical recycling: giving new life to plastic waste. *Angew. Chem. Int. Ed.* **2020**, *59*, 15402–15423

(57) G. W. Coates, Y. D. Y. L. Getzler, Chemical recycling to monomer for an ideal, circular polymer economy. *Nat. Rev. Mater.* **2020**, *5*, 501–516.

(58) Britt, P. F., Coates, G. W., Winey, K. I., Byers, J., Chen, E., Coughlin, B., Waymouth, R. **2019**. Report of the Basic Energy Sciences Roundtable on Chemical Upcycling of Polymers. USDOE Office of Science (SC)(United States).

(59) EPA, Advancing sustainable matrials management: 2018 Tables and figures. https://www.epa.gov/sites/default/files/2021-01/documents/2018_tables_and_figures_dec_2020_fnl_508.pdf (accessed August 31, 2021)

(60) Otake, Y., Kobayashi, T., Asabe, H., Murakami, N., & Ono, K. Biodegradation of low-density polyethylene, polystyrene, polyvinyl chloride, and urea formaldehyde resin buried under soil for over 32 years. Journal of Applied Polymer Science, **1995**, *56*, 1789-1796.

(61) Y.-T. Zhang, W. Wei, J. Sun, Q. Xu, B.-J. Ni, Treatment and resource recovery long-term effects of polyvinyl chloride microplastics on anaerobic granular sludge for recovering methane from wastewater. *Environ. Sci. Technol.* **2020,** *54*, 9662–9671

F. Ribeiro, E. D. Okoffo, J. W. O'Brien, S. Fraissinet-Tachet, S. O'Brien, M. J. Gallen, S. Samanipour, S. Leat Kaserzon, J. F. Mueller, T. S. Galloway, K. V. Thomas, Quantitative analysis of selected plastics in high commercial value Australian seafood by pyrolysis gas chromatography mass spectrometry. *Environ. Sci. Technol.* **2020**, *54*, 9408–9417

D. Lithner, A. Larsson, G. Dave, Environmental and health hazard ranking and assessment of plastic polymers based on chemical composition. *Sci. Total Environ.* **2011***, 409*, 3309

S. S. S. Rowdhwal, J. Chen. Toxic effects of di-2-ethylhexyl phthalate: An overview. *Biomed. Res. Int.* **2018**, 1750398

Chapter 2: Fullerene-Functionalized Poly(3-hexylthiophene) Additive Stabilizes Conjugated Polymer−Fullerene Blend Morphologies

This chapter has been published:
Kim, D.*, Mueller, E.A.*, Yang, D.S., Fagnani, D.E., Kim, J. and McNeil, A.J., Fullerene-Functionalized Poly(3-hexylthiophene) Additive Stabilizes Conjugated Polymer−Fullerene Blend Morphologies, *ACS Appl. Polym. Mater.* ***2021****, 10, 4861–4868*.

D. Kim and D. S. Yang made and analyzed devices, E. A. Mueller synthesized the copolymer, made and analyzed thin films, D. Kim and E. A. Mueller contributed to writing, D. E. Fagnani contributed intellectually.

2.1 Introduction

Over the last three decades, organic photovoltaics (OPVs) have emerged as a promising solar energy technology because they can be flexible, lightweight, and fabricated via inexpensive methods.[1–4] In a typical OPV device, the photoactive layer is an interpenetrating blend of an electron-donor and an electron-acceptor material, either of which can be small molecules or polymers.[5] To improve power conversion efficiencies (PCEs), researchers have tuned the chemical structures of the donor and acceptor materials to optimize their bandgaps. The most common donor/acceptor pair for OPVs has been poly(3-hexylthiophene) (P3HT) as the donor paired with phenyl-C_{61}-butyric acid methyl ester ($PC_{61}BM$) as the acceptor, which typically achieves PCEs of 3−5%.[6,7] In the past decade, researchers have shifted away from P3HT in favor of conjugated polymers with alternating electron-rich and electron-poor units along the backbone to improve visible light absorption and optimize the bandgap for charge transfer with a given acceptor.[8,9]

Over the last ten years, a variety of donor polymers have been designed that enable PCEs around 10%,[10,11] with some examples of record-breaking PCEs greater than 17% for tandem[12] and single-junction devices[13,14] in the last two years.

Despite improvements in device PCE, long-term stability remains a central challenge to OPV commercialization.[1,15] One factor impacting long-term stability is detrimental changes in the blend morphology over time. Initially, the physically blended donor and acceptor form a kinetically trapped morphology with nanoscale domains of each pure component and, depending on the donor/acceptor pair, an additional amorphous mixed phase.[16] This nanoscale morphology is important for effective charge separation because photogenerated excitons, which must migrate to domain interfaces to separate into holes and electrons, have diffusion lengths of less than 50 nm.[17−19] In an enthalpically driven process, the initial domains phase-separate into larger (e.g., micron-scale) domains with aging, which reduces the charge separation efficiency.[20,21] Phase separation is particularly problematic for blends that contain fullerenes, some of the most common acceptors, which diffuse throughout the active layer more easily than polymers.[22] Thus, measures to prevent active layer phase separation are necessary to maintain high PCE over time.

One method to stabilize device morphology is to add a compatibilizer as a third component into the active layer blend.[23,24] The compatibilizer localizes at the interface between immiscible phases, lowers the interfacial tension, and increases the interfacial adhesion.[25,26] Both small molecules[27−31] and polymers[32−42] have been used to stabilize domain sizes in active layer blends. In our previous work, we used a fullerene-functionalized P3HT copolymer to stabilize P3HT:$PC_{61}BM$ blend morphologies.[43]

We investigated how the copolymer sequence (e.g., random, gradient, and block), composition (e.g., 20, 35, and 50 mol % fullerene side-chains), and concentration in the blend (e.g., 2, 5, and 8 wt %) affected blend morphology over time. We found that a random copolymer with 20 mol % fullerene-functionalized side chains at 8 wt % in the blend was best at preventing micron-scale phase separation in annealed thin film blends and OPVs. In our work, and in other examples,[32,36,38,39,44] tailored compatibilizers were synthesized to match the specific donor and acceptor in the active layer of the OPV. Synthesizing custom compatibilizers is time-intensive and impractical for complex donor polymers. To circumvent this challenge, we hypothesized that our P3HT copolymer additive might be miscible with other conjugated polymers and serve as a general compatibilizer.

To test this hypothesis, we investigated how the fullerene-functionalized P3HT additive impacts morphology for three different blends of phenyl-C_{71}-butyric acid methyl ester ($PC_{71}BM$) with one of the following conjugated polymers (Chart 1): poly[[4,8-bis[(2-ethylhexyl)oxy]benzo[1,2-b:4,5-b']dithiophene-2,6-diyl][3-fluoro-2-[(2-ethylhexyl)carbonyl]-thieno[3,4-b]thiophene-diyl]] (PTB7),[45] poly[4,8-bis(5-(2-ethylhexyl)thiophen-2-yl)benzo[1,2-b;4,5-b′]dithiophene-2,6-diyl-alt-(4-(2-ethylhexyl)-3-fluorothieno[3,4-b]thiophene-)-2-carboxylate-2-6-diyl] (PTB7-Th),[46] and poly[(5,6-difluoro2,1,3-benzothiadiazol-4,7-diyl)-alt-(3,3‴-di(2-octyldodecyl)-2,2′;5′,2″;5″,2‴-quaterthiophen-5,5‴-diyl)] (PffBT4T2OD).[47] Each donor polymer was selected because it has a reported PCE ≥ 10% with $PC_{71}BM$. We found that the fullerene-functionalized P3HT copolymer suppresses micronscale phase separation for all three blends, likely by inhibiting $PC_{71}BM$ aggregation rather than via traditional blend compatibilization. Further studies showed that OPV devices fabricated with the PffBT4T-2OD:$PC_{71}BM$ blend showed the active layer morphology was stabilized when the copolymer was

added. We also investigated factors beyond morphology that could affect device performance. Overall, our results demonstrate that a fullerene-functionalized P3HT copolymer additive can stabilize different conjugated polymer thin film blends and prevent phase separation in the active layer of PffBT4T-2OD:$PC_{71}BM$ devices.

Chart 2-1. Chemical Structures of the Donor Polymers, the Acceptor, and the Additives Used in This Study[48−50]

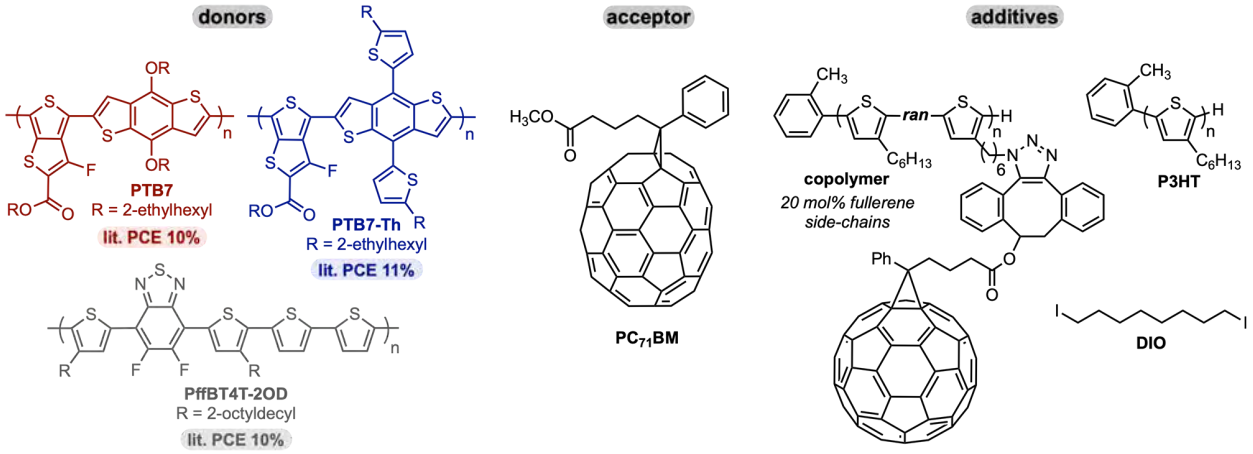

2.2 Results and Discussion

The copolymer additive was synthesized and characterized as reported in our previous studies to obtain 21 mol % side-chain functionalization, Mn = 21.0 kg/mol and Đ = 1.15 (Figures A1-11 to A1-16).[43] To probe the morphological stability of each system without any additives, we prepared and thermally annealed thin film blends of each donor (PTB7, PTB7-Th, or PffBT4T-2OD) with $PC_{71}BM$. The blend compositions for PTB7 or PTB7-Th:$PC_{71}BM$ (1.0:1.5)[48,49] and PffBT4T-2OD:$PC_{71}BM$ (1.0:1.2)[50] films were chosen based on previously reported optimized blend ratios for OPVs. The films were annealed under vacuum for 0−180 min at 200 °C to accelerate the aging process. Phase separation was quantified via optical microscopy, wherein the percent area that was filled with dark micron-scale $PC_{71}BM$ crystallites was determined using

ImageJ.[51] The PTB7 blends had significantly fewer aggregates (1.4 ± 0.8 area %) compared to the PTB7-Th (22 ± 3 area %) and PffBT4T-2OD (39.9 ± 0.9 area %) blends after 180 min of annealing (Figure 2-1, left). This smaller degree of phase separation may be due to the reduced crystallinity of PTB7 (Figure A1-42).[52,53] To understand how the copolymer additive affected these morphological changes, thin films were prepared with 8 wt % of the copolymer, annealed, and analyzed with the same method described above. In all cases, the aggregate area percent was reduced when the copolymer was added: 0.15 ± 0.02 area % (PTB7), 0.7 ± 0.1 area % (PTB7-Th), and 1.8 ± 0.2 area % (PffBT4T-2OD; Figure 2-1, right). In contrast, films with lower copolymer loading (4 wt %) exhibited more phase separation (Figure A1-18): 0.35 ± 0.03 area % (PTB7), 15 ± 1 area % (PTB7-Th), and 27.7 ± 0.1 area % (PffBT4T-2OD), consistent with our previous studies.[43] Because optical microscopy only probes phase separation on the micronscale, it is likely that nanoscale phase separation is still occurring. Indeed, in previous reports for similar systems (e.g., PTB7, PTB7-Th, with $PC_{71}BM$), nanoscale phase separation was observed prior to or concomitant with micron-scale phase separation.[54] As such, our results indicate that phase separation is occurring at a slower rate with the copolymer present. Overall, these results suggest that the copolymer could be a generalizable additive for stabilizing blends of multiple conjugated polymers with $PC_{71}BM$.

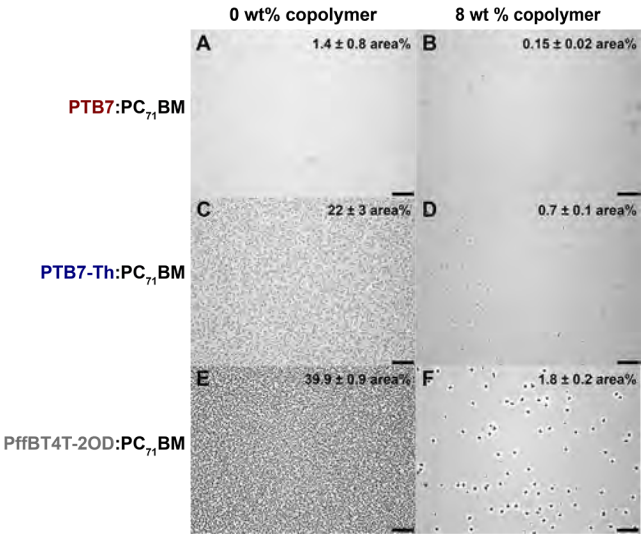

Figure 2.1. Optical microscope images of PTB7 (A and B), PTB7-Th (C and D), and PffBT4T-2OD (E and F) blended with $PC_{71}BM$ and 0 wt % (left) or 8 wt % (right) copolymer. All films were annealed under vacuum for 180 min at 200 °C. Scale bars represent 30 μm.

We then benchmarked the performance of our additive against diiodooctane (DIO), which is commonly used to optimize as-cast morphology by reducing domain sizes for PTB7[45,55] and PTB7-Th[56] while increasing domain sizes for PffBT4T-2OD[57] with $PC_{71}BM$. These optimal as-cast morphologies may still be far from thermodynamic equilibrium, resulting in phase separation over time.[54] Indeed, we found that blends with 3 vol % DIO, the volume ratio typically used in devices,[48–50] still underwent phase separation, albeit by reduced amounts compared to no additives (Figure 2-2A,B,C). By comparison, the thin films with copolymer gave the least amount of phase separation for all three donor polymers (Figure 2-2B). In addition, we analyzed thin films with 8 wt % P3HT to investigate whether adding a similar conjugated polymer without fullerene-functionalized side chains could stabilize the blend morphology, a strategy that has been successful for ternary OPVs.[58] Blends with P3HT (Figure 2-2D) exhibited similar amounts of phase separation to blends without any additives (Figure 2-2A), indicating that the fullerene-functionalized side chains on the copolymer are necessary to minimize micron-scale aggregates.

In all cases, the stability of blends with the copolymer or with the copolymer and DIO was greater than the others, demonstrating that the copolymer was the most effective additive for limiting micronscale phase separation in these blends.

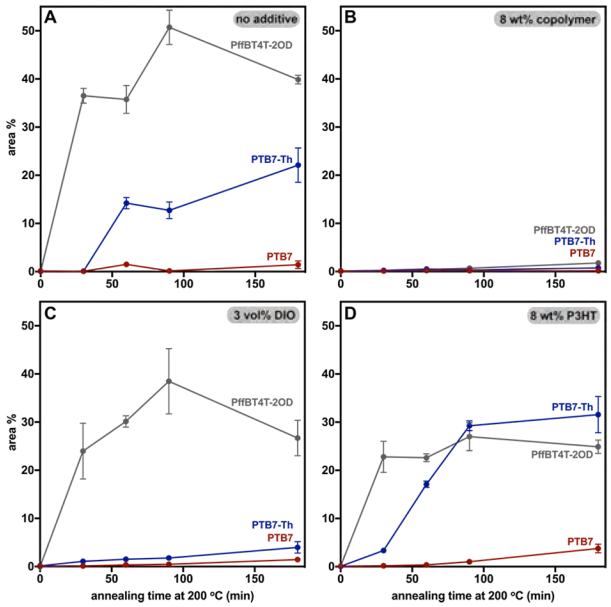

Figure 2.2. Area percent of $PC_{71}BM$ aggregates for thin film blends of PTB7 (red), PTB7-Th (blue), or PffBT4T-2OD (gray) with (A) no additive, (B) copolymer, (C) DIO, or (D) P3HT. All films were annealed at 200 °C under vacuum. Each data point represents the average from 3 images.

Because fewer micron-scale aggregates were observed in copolymer-containing films, we hypothesized that the copolymer was compatibilizing the blend morphology. More specifically, we hypothesized that the copolymer additive would localize at the interface between the donor and acceptor phases due to favorable miscibility with each one.[25] To test this hypothesis, we determined the surface free energies (γ) of each blend component to qualitatively assess their miscibility, where components with similar surface free energies would be more miscible with each other.[59–62]

Surface contact angles of water and glycerol were measured for neat thin films and used to calculate the surface free energy of each blend component (Table 2-1). Because both the solvents and the method used to calculate surface energy can affect the results,[63] we analyzed the relative differences in surface energy between each material that we studied. The three donor polymers studied had similar surface free energies of 21.9 mJ/m^2 (PTB7), 21.4 mJ/m^2 (PTB7-Th), and 19.2 mJ/m^2 (PffBT4T-2OD) and these surface energies were significantly lower than the surface energy of 28.0 mJ/m^2 for $PC_{71}BM$, consistent with previous reports.[60,64–66] Interestingly, the surface free energy of the copolymer (27.8 mJ/m^2) was nearly identical to that of $PC_{71}BM$, suggesting that the copolymer has enhanced miscibility with $PC_{71}BM$.[62] For comparison, the surface energy of P3HT was determined by the same method to be 20.8 mJ/m^2, which is more similar to that of the other donor polymers studied.

Table 2-1. Measured surface free energies (γ) and calculated wetting coefficients (ω_c), as well as calculated Flory-Huggins interaction parameters (χ)

material	γ_i^{total}(mJ/m^2)	copolymer ω_c[a]	$\chi_{i,copolymer}K$[b]
PTB7	21.9	–0.94	0.36
PTB7-Th	21.4	–0.94	0.50
PffBT4T-2OD	19.2	–0.96	0.87
$PC_{71}BM$	28.0	-	0.0036
copolymer	27.8	-	-
P3HT	20.7	-	-

[a] *for copolymer in donor:$PC_{71}BM$ blend*

[b] *K is a proportionality constant*[67,68]

To investigate whether the copolymer was localized at the interface between the donor and acceptor, the surface energies were used to calculate a wetting coefficient, ω_c, for an additive in a binary blend.[69] This unitless parameter is derived from the differences in interfacial surface energy for the additive with each component of the blend. When $\omega_c < -1$, the additive is localized in the $PC_{71}BM$ phase, when $-1 \leq \omega_c \leq 1$, the additive is localized at the interface between the phases in a blend, and when $\omega_c > 1$ the additive is localized in the donor phase. The wetting coefficient calculated for the copolymer additive in each blend was −0.94 (PTB7 and PTB7-Th) or −0.96 (PffBT4T-2OD), indicating that the copolymer may have had some degree of interface localization but likely is preferentially localized in the $PC_{71}BM$ phase (Table 2-1). For comparison, the wetting coefficients calculated for P3HT in the donor−acceptor blends were 1.37 (PTB7), 1.19 (PTB7-Th), and 0.63 (PffBT4T-2OD) demonstrating that without the fullerene-functionalized side chains, P3HT likely localizes in the donor phase or at the interface (Table A1-13). These results, combined with the optical microscopy studies, suggest that the copolymer is selectively inhibiting $PC_{71}BM$ aggregation to stabilize blend morphology. One possible mechanism for this stabilization is that the copolymer acts as nucleating agent for $PC_{71}BM$.[70] By introducing nucleation sites for $PC_{71}BM$, the copolymer would increase the rate of $PC_{71}BM$ nucleation relative to crystal growth and limit crystal size to the nanoscale.[71,72] If relevant, this process could be observed via differential scanning calorimetry (DSC) by an increase in $PC_{71}BM$ crystallization temperature.[65] However, $PC_{71}BM$ crystallization was not observed in DSC thermograms of PffBT4T-2OD:$PC_{71}BM$ blends with or without the copolymer, nor for blends of $PC_{71}BM$ with 8 wt % of the copolymer (Figures A1-40 and A1-41), suggesting that this mechanism is unlikely. Alternatively, the copolymer may be acting in a similar manner to polyfullerenes[73] or oligofullerenes[74,75] by preventing the small molecule $PC_{71}BM$ from diffusing and crystallizing to form aggregates. Indeed, annealing films of

just $PC_{71}BM$ (i.e., without the donor polymer) with 8 wt % copolymer additive or with 8 wt % P3HT for 180 min at 200 °C revealed micron-scale aggregates for the P3HT films alone (Figure A1-38). This result demonstrates that the copolymer likely has favorable interactions with the $PC_{71}BM$ that prevent $PC_{71}BM$ diffusion and aggregation in the thin films.

To further investigate the miscibility of the copolymer with each blend component, the Flory−Huggins interaction parameters (χ) were estimated.[63,76,77] This parameter is directly proportional to the enthalpy of mixing for amorphous liquids, with lower values indicating an increased thermodynamic preference for mixing.[78,79] These values can provide a qualitative comparison of the copolymer interactions with each component. Notably, the copolymer additive displays a very small Flory−Huggins interaction parameter with $PC_{71}BM$, indicating thermodynamically favorable mixing with $PC_{71}BM$ (Table 2-1). This result further supports that the conclusion that the copolymer additive is likely attenuating $PC_{71}BM$ aggregate formation during annealing.

To summarize, annealed thin films of several conjugated polymers blended with $PC_{71}BM$ exhibit less macroscale phase separation with 8 wt % of a fullerene-functionalized P3HT copolymer additive. From the surface contact angle analysis, we found that the copolymer additive may localize at the interface between donor polymer and $PC_{71}BM$ phases but more likely localizes with $PC_{71}BM$. Although we do not directly observe copolymer miscibility with $PC_{71}BM$, the lack of macroscale phase separation in annealed copolymer $PC_{71}BM$ thin films indicates that the copolymer likely stabilizes the blends by preventing $PC_{71}BM$ aggregation. Taken together, these results suggest that the copolymer could be a general additive for stabilizing donor-$PC_{71}BM$ blends.

To investigate the copolymer's impact on OPV device performance, we fabricated devices with and without the copolymer for the PffBT4T-2OD:$PC_{71}BM$ blend. This blend was chosen because it exhibited the most dramatic reduction in micron-scale aggregates when annealed with the copolymer in the thin film studies (Figures 2-1 and 2-2). An inverted device architecture (glass/ITO/ZnO/polymer blend/MoO_3/Ag, Figure A1-44) was used because it enables higher PCE than a conventional architecture.[80] The polymer blend was prepared by spincasting a PffBT4T-2OD:$PC_{71}BM$ solution with or without 8 wt% of the copolymer additive to achieve a final thickness of 215 ± 10 nm, where the weight ratio of polymer(s):$PC_{71}BM$ was 1.0:1.2.[81] Photovoltaic measurements were performed under simulated AM 1.5G conditions both before and after annealing. Each data point represents an average of six measurements obtained from three different devices fabricated on two different substrates. Devices with the copolymer exhibited an initial PCE of 6.0 ± 0.2% while devices without copolymer showed an initial PCE of 9.3 ± 0.2% (Table 2-2).

Table 2-2. The power conversion efficiency (PCE), fill factor (*FF*), open circuit voltage (V_{OC}), and short circuit current (J_{SC}) for PffBT4T-2OD:$PC_{71}BM$ devices with 0 wt% and 8 wt% copolymer

copolymer (wt%)	PCE (%)	FF	J_{SC} (mA/cm^2)	V_{OC} (V)
0	9.3 ± 0.2	0.7 ± 0.0	18.3 ± 0.3	0.7 ± 0.0
8	6.0 ± 0.2	0.6 ± 0.0	14.4 ± 0.7	0.7 ± 0.0

Before studying the thermal stability of devices with or without copolymer, we investigated the discrepancy in the initial PCE between the two types of blends. The open-circuit voltage (V_{OC}) was similar with or without the copolymer but the fill factor (FF) and the short circuit current (J_{SC}) both decreased with copolymer addition. Both of these parameters depend on the absorption

efficiency: therefore, the lower performance with the copolymer could be due to a reduction in absorption. Indeed, the UV spectrum for the blend containing copolymer exhibited lower overall absorption than the blend without the copolymer (Figures 2-3A (corrected for film thickness) and A2-50 (uncorrected)), presumably due to the lower molar absorptivity of the copolymer, the lower concentration of PffBT4T-2OD in the blend, and a slightly reduced film thickness with the copolymer (146 ± 2 nm) than without (156.4 ± 0.6 nm). The lower initial PCE with the copolymer additive is not likely due to changes in charge separation efficiency because the bandgap of the copolymer is intermediate between that of PffBT4T-2OD and $PC_{71}BM$ (Figure A1-43). Instead, the lower initial PCE with the copolymer additive could also be due to a reduction in charge mobility. To test this hypothesis, triboindentation was used to measure the electron current in the active layer (50 nm depth) for films with and without the copolymer (Figures 2-3B and A1-44). These studies revealed that the copolymer-containing active layer had lower electron current, suggesting that the copolymer impedes current when localized in or near the $PC_{71}BM$ phase. In addition to these factors, differences in the initial nanoscale morphology might also lead to differences in the initial PCE with or without the copolymer. However, energy-filtered transmission electron microscopy revealed qualitatively similar nanoscale morphologies for unannealed films with and without the copolymer (Figure A1-51). Taken together, these data suggest that a lower absorption efficiency along with reduced electron mobility, rather than changes in nanoscale morphology, led to the lower initial PCE with copolymer addition.

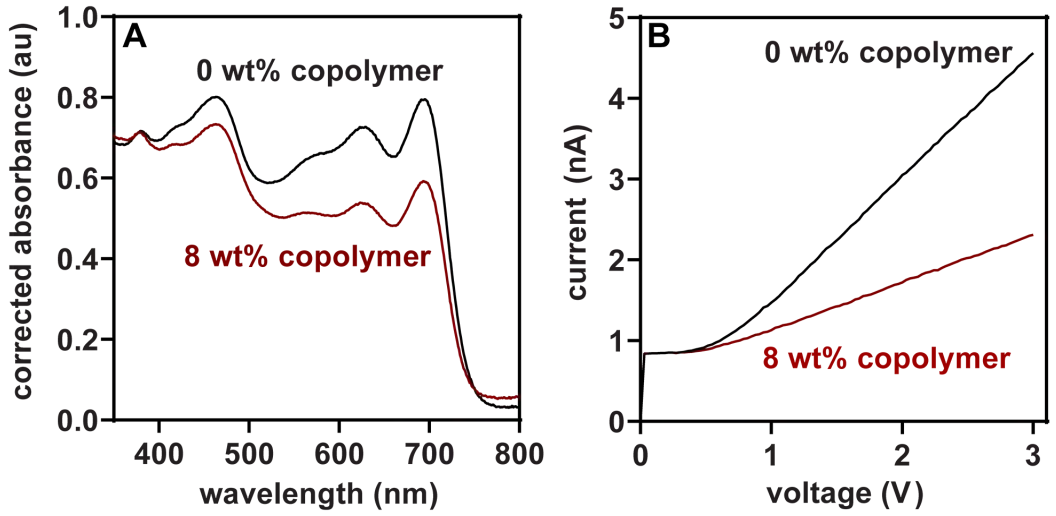

Figure 2.3. (A) UV-vis spectra of thin films with 0% (black) and 8 wt% (red) copolymer, adjusted to account for differences in film thickness. (The uncorrected spectra can be found in Figure A2-50.) (B) Plot of electron current versus voltage for devices with 0% (black) and 8 wt% (red) copolymer.

To evaluate device stability over time, thermal studies were performed by annealing the devices at 200 °C before MoO_3/Ag deposition. Based on our thin-film studies, we expected that the devices containing the copolymer additive would have better thermal stability over time than devices without the copolymer. However, both samples exhibited lower PCEs after annealing for 90 min at 200 °C. Optical microscope images revealed that both samples underwent significant macroscale phase separation during annealing (Figure A1-47). To attenuate this effect, we reduced the annealing temperature to 150 °C to better quantify the impact of the copolymer additive over time. After annealing for 30 min, the PCE for devices without copolymer dropped significantly (from 9.3 ± 0.2% to 2.6 ± 0.2%, Figure 2-4A). In contrast, the PCE for devices with the copolymer underwent a much smaller decrease (from 6.0 ± 0.2% to 2.9 ± 0.2%). After annealing at 180 min, the devices without copolymer fully degraded and were unmeasurable while devices with the copolymer maintained a PCE of 3.2 ± 0.4%.

The biggest difference in parameters between the two types of devices were in the V_{OC} changes over time; more specifically, the V_{OC} in the device without copolymer dropped steadily while copolymer-containing device showed minimal changes even at 180 min (Figure 2-4B). Additionally, optical microscopy images showed macroscale aggregates in the devices without copolymer (80 area %) while the copolymer-containing devices had no observable macroscale phase separation after annealing for 180 min (Figure 2-4D). These data suggest that the phase separation observed in devices without the copolymer likely facilitates charge recombination leading to a reduced V_{OC},[82,83] which is supported by the smaller shunt resistance of the annealed devices without the copolymer (Figure A1-46F and Table A1-15). In contrast, devices with the copolymer maintain their V_{OC} and shunt resistance during annealing.[84] Combined, these data suggest that the copolymer additive prevents macroscale phase separation resulting in better stability in V_{OC} of the OPV devices.

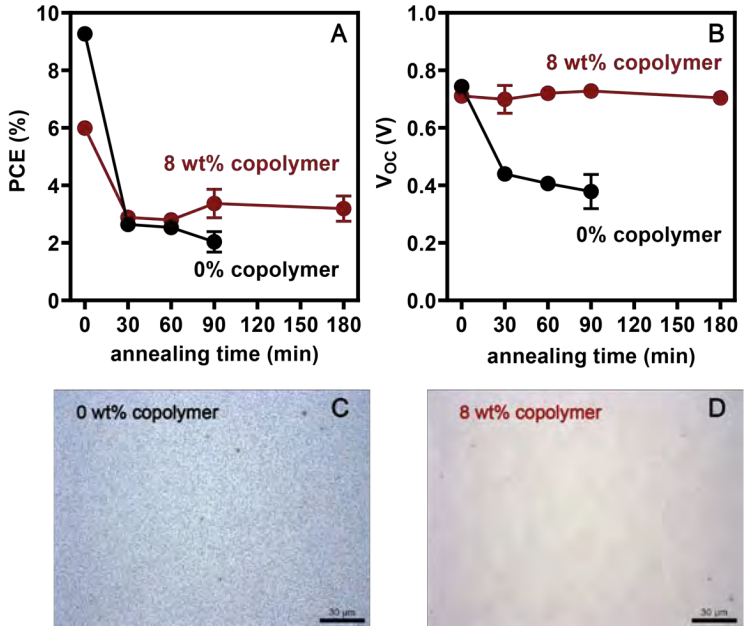

Figure 2.4. Plots of the (A) power conversion efficiency (PCE) and (B) open-circuit voltage (V_{OC}) for the PffBT4T-2OD:$PC_{71}BM$ OPV devices during annealing at 150 °C with 0 wt% (black) or 8 wt% (red) copolymer. Optical microscope images of unmasked portions of the PffBT4T-2OD:$PC_{71}BM$ OPV devices after 180 min of annealing at 150 °C with (C) 0 wt% or (D) 8 wt% copolymer. Scale bars represent 30 μm

2.3 Conclusion

In this work, we employ a fullerene-functionalized P3HT copolymer additive to stabilize the morphology for blends of three different donor polymers (PTB7, PTB7-Th, and PffBT4T-2OD) with $PC_{71}BM$. In all thin film blends, micron-scale aggregation was reduced when the copolymer was added, suggesting that the copolymer may be a general stabilizing additive. Based on surface energy analysis, the copolymer likely exhibits favorable miscibility with $PC_{71}BM$, rather than being interfacially active, and inhibits $PC_{71}BM$ aggregation upon thermal annealing. When the copolymer was added to PffBT4T-2OD:$PC_{71}BM$ devices, however, lower initial power conversion efficiencies were observed, due to reduced absorption and electron current. For annealed devices, the PCE decreased with increasing annealing time regardless of copolymer addition, although the relative PCE loss was smaller for devices with the copolymer. Furthermore, micron-scale aggregates only formed in devices without the copolymer after 180 min of annealing. Combined, these results suggest that the copolymer could be used as a general additive to stabilize the morphology of donor/acceptor blends and, when used, other factors besides morphology impact device performance.

2.4 References

(1) Riede, M.; Spoltore, D.; Leo, K. Organic Solar Cells-The Path to Commercial Success. *Adv. Energy Mater.* **2021**, *11*, 2002653.

(2) Li, Y.; Xu, G.; Cui, C.; Li, Y. Flexible and Semitransparent Organic Solar Cells. *Adv. Energy Mater.* **2018**, *8*, 1701791.

(3) Wang, Q.; Xie, Y.; Soltani-Kordshuli, F.; Eslamian, M. Progress in Emerging Solution-Processed Thin Film Solar Cells - Part I: Polymer Solar Cells. *Renewable Sustainable Energy Rev.* **2016**, *56*, 347−361.

(4) Guo, J.; Min, J. A Cost Analysis of Fully Solution-Processed ITO-Free Organic Solar Modules. *Adv. Energy Mater.* **2019**, *9*, 1802521.

(5) Lu, L.; Zheng, T.; Wu, Q.; Schneider, A. M.; Zhao, D.; Yu, L. Recent Advances in Bulk Heterojunction Polymer Solar Cells. *Chem. Rev.* **2015**, *115*, 12666−12731.

(6) Wadsworth, A.; Hamid, Z.; Bidwell, M.; Ashraf, R. S.; Khan, J. I.; Anjum, D. H.; Cendra, C.; Yan, J.; Rezasoltani, E.; Guilbert, A. A. Y.; Azzouzi, M.; Gasparini, N.; Bannock, J. H.; Baran, D.; Wu, H.; de Mello, J. C.; Brabec, C. J.; Salleo, A.; Nelson, J.; Laquai, F.; McCulloch, I. Progress in Poly (3-Hexylthiophene) Organic Solar Cells and the Influence of Its Molecular Weight on Device Performance. *Adv. Energy Mater.* **2018**, *8*, 1801001.

(7) Dang, M. T.; Hirsch, L.; Wantz, G. P3HT:PCBM, Best Seller in Polymer Photovoltaic Research. *Adv. Mater.* **2011**, *23*, 3597−3602.

(8) Holliday, S.; Li, Y.; Luscombe, C. K. Recent Advances in High Performance Donor-Acceptor Polymers for Organic Photovoltaics. *Prog. Polym. Sci.* **2017**, *70*, 34−51.

(9) Hou, J.; Park, M. H.; Zhang, S.; Yao, Y.; Chen, L. M.; Li, J. H.; Yang. Bandgap and Molecular Energy Level Control of Conjugated Polymer Photovoltaic Materials Based on Benzo[l,2-b:4,5-b′]-Dithiophene. *Macromolecules* **2008**, *41*, 6012−6018.

(10) National Renewable Energy Lab Best Research-Cell Efficiencies; https://www.nrel.gov/pv/assets/images/efficiency-chart.png (accessed: February 2021).

(11) Green, M.; Dunlop, E.; Hohl-Ebinger, J.; Yoshita, M.; Kopidakis, N.; Hao, X. Solar Cell Efficiency Tables (Version 57). *Prog. Photovoltaics* **2021**, *29*, 3−15.

(12) Meng, L.; Zhang, Y.; Wan, X.; Li, C.; Zhang, X.; Wang, Y.; Ke, X.; Xiao, Z.; Ding, L.; Xia, R.; Yip, H. L.; Cao, Y.; Chen, Y. Organic and Solution-Processed Tandem Solar Cells with 17.3% Efficiency. *Science* **2018**, *361*, 1094−1098.

(13) Cui, Y.; Yao, H.; Zhang, J.; Xian, K.; Zhang, T.; Hong, L.; Wang, Y.; Xu, Y.; Ma, K.; An, C.; He, C.; Wei, Z.; Gao, F.; Hou, J. Single-Junction Organic Photovoltaic Cells with Approaching 18% Efficiency. *Adv. Mater.* **2020**, *32*, 1908205.

(14) Liu, Q.; Jiang, Y.; Jin, K.; Qin, J.; Xu, J.; Li, W.; Xiong, J.; Liu, J.; Xiao, Z.; Sun, K.; Yang, S.; Zhang, X.; Ding, L. 18% Efficiency Organic Solar Cells. *Sci. Bull.* **2020**, *65*, 272−275.

(15) Turak, A. Device Stability in Organic Optoelectronics. Handbook of Organic Materials for Electronic and Photonic Devices, 2nd ed.; Elsevier, **2019**; pp 599−662.

(16) Treat, N. D.; Chabinyc, M. L. Phase Separation in Bulk Heterojunctions of Semiconducting Polymers and Fullerenes for Photovoltaics. *Annu. Rev. Phys. Chem.* **2014**, *65*, 59−81.

(17) Yu, G.; Gao, J.; Hummelen, J. C.; Wudl, F.; Heeger, A. J. Polymer Photovoltaic Cells: Enhanced Efficiencies via a Network of Internal Donor-Acceptor Heterojunctions. *Science* **1995**, *270*, 1789−1791.

(18) Shaw, P. E.; Ruseckas, A.; Samuel, I. D. W. Exciton Diffusion Measurements in Poly(3-Hexylthiophene). *Adv. Mater.* **2008**, *20*, 3516−3520

(19) Hedley, G. J.; Ward, A. J.; Alekseev, A.; Howells, C. T.; Martins, E. R.; Serrano, L. A.; Cooke, G.; Ruseckas, A.; Samuel, I. D. W. Determining the Optimum Morphology in High-Performance Polymer-Fullerene Organic Photovoltaic Cells. *Nat. Commun.* **2013**, *4*, 2867.

(20) Cardinaletti, I.; Kesters, J.; Bertho, S.; Conings, B.; Piersimoni, F.; D'Haen, J.; Lutsen, L.; Nesladek, M.; Van Mele, B.; Van Assche, G.; Vandewal, K.; Salleo, A.; Vanderzande, D.; Maes, W.; Manca, J. V. Toward Bulk Heterojunction Polymer Solar Cells with Thermally Stable Active Layer Morphology. *J. Photonics Energy* **2014**, *4*, 040997.

(21) Savagatrup, S.; Printz, A. D.; O'Connor, T. F.; Zaretski, A. V.; Rodriquez, D.; Sawyer, E. J.; Rajan, K. M.; Acosta, R. I.; Root, S. E.; Lipomi, D. J. Mechanical Degradation and Stability of Organic Solar Cells: Molecular and Microstructural Determinants. *Energy Environ. Sci.* **2015**, *8*, 55−80.

(22) Kronholm, D. F.; Hummelen, J. C. Fullerene-Based Acceptor Materials. Organic Photovoltaics; Wiley-VCH Verlag GmbH & Co. KGaA: Weinheim, Germany, **2009**; pp 153−178.

(23) Bonasera, A.; Giuliano, G.; Arrabito, G.; Pignataro, B. Tackling Performance Challenges in Organic Photovoltaics: An Overview about Compatibilizers. *Molecules* **2020**, *25*, 2200.

(24) Cheng, P.; Zhan, X. Versatile Third Components for Efficient and Stable Organic Solar Cells. *Mater. Horiz.* **2015**, *2*, 462−485.

(25) Di Lorenzo, M. L.; Frigione, M. Compatibilization Criteria and Procedures for Binary Blends: A Review. *J. Polym. Eng.* **1997**, *17*, 429−460.

(26) Koning, C.; Van Duin, M.; Pagnoulle, C.; Jerome, R. Strategies for Compatibilization of Polymer Blends. *Prog. Polym. Sci.* **1998**, *23*, 707−757.

(27) Wang, H.; Yang, L.; Lin, P.; Chueh, C.; Liu, X.; Qu, S.; Guang, S.; Yu, J.; Tang, W. A Simple Dithieno[3,2-b:2′,3′-d]PyrrolRhodanine Molecular Third Component Enables Over 16.7% Efficiency and Stable Organic Solar Cells. *Small* **2021**, *17*, 2007746 DOI: 10.1002/smll.202007746.

(28) Liu, L.; Zhang, H.; Xiao, B.; Liu, Y.; Xu, B.; Wang, C.; Wen, S.; Zhou, E.; Chen, G.; Im, C.; Tian, W. Effects of BTA2 as the Third Component on the Charge Carrier Generation and Recombination Behavior of PTB7: $PC_{71}BM$ Photovoltaic System. *Front. Chem. Sci. Eng.* **2021**, *15*, 127−137.

(29) Xu, B.; Sai-Anand, G.; Unni, G. E.; Jeong, H. M.; Kim, J. S.; Kim, S. W.; Kwon, J. B.; Bae, J. H.; Kang, S. W. Pyridine-Based Additive Optimized P3HT:$PC_{61}BM$ Nanomorphology for Improved Performance and Stability in Polymer Solar Cells. *Appl. Surf. Sci.* **2019**, *484*, 825−834.

(30) Xiao, M.; Zhang, K.; Jin, Y.; Yin, Q.; Zhong, W.; Huang, F.; Cao, Y. Low Temperature Processed High-Performance Thick Film Ternary Polymer Solar Cell with Enhanced Stability. *Nano Energy* **2018**, *48*, 53−62.

(31) Cheng, P.; Yan, C.; Lau, T.-K.; Mai, J.; Lu, X.; Zhan, X. Molecular Lock: A Versatile Key to Enhance Efficiency and Stability of Organic Solar Cells. *Adv. Mater.* **2016**, *28*, 5822−5829.

(32) Sivula, K.; Ball, Z. T.; Watanabe, N.; Fréchet, J. M. J. Amphiphilic Diblock Copolymer Compatibilizers and Their Effect on the Morphology and Performance of Polythiophene:Fullerene Solar Cells. *Adv. Mater.* **2006**, *18*, 206−210.

(33) Yang, C.; Lee, J. K.; Heeger, A. J.; Wudl, F. Well-Defined Donor-Acceptor Rod-Coil Diblock Copolymers Based on P3HT Containing C60: The Morphology and Role as a Surfactant in BulkHeterojunction Solar Cells. *J. Mater. Chem.* **2009**, *19*, 5416−5423.

(34) Lee, J. U.; Jung, J. W.; Emrick, T.; Russell, T. P.; Jo, W. H. Morphology Control of a Polythiophene-Fullerene Bulk Heterojunction for Enhancement of the High-Temperature Stability of Solar Cell Performance by a New Donor-Acceptor Diblock Copolymer. *Nanotechnology* **2010**, *21*, 105201.

(35) Kipp, D.; Verduzco, R.; Ganesan, V. Block Copolymer Compatibilizers for Ternary Blend Polymer Bulk Heterojunction Solar Cells-An Opportunity for Computation Aided Molecular Design. Molecular Systems Design and Engineering; Royal Society of Chemistry: **2016**; pp 353−369.

(36) Wang, M.; Sun, J.; Cai, X.; Huang, Y.; Li, F. Morphology Modulation of Organic Photovoltaics with Block Copolymer Additive Based on Rational Design Strategies. *Org. Electron.* **2021**, *88*, 106020.

(37) Li, Z.; Yan, L.; Shan, J.; Gu, H.; Lin, Y.; Wang, Y.; Tan, H.; Ma, C.-Q. Organic Amines as Targeting Stabilizer at the Polymer/Fullerene Interface for Polymer:$PC_{61}BM$ Solar Cells. *Energy Technol.* **2020**, *8*, 2000266.

(38) Su, Y.-A.; Maebayashi, N.; Fujita, H.; Lin, Y.-C.; Chen, C.-I.; Chen, W.-C.; Michinobu, T.; Chueh, C.-C.; Higashihara, T. Development of Block Copolymers with Poly(3-Hexylthiophene) Segments as Compatibilizers in Non-Fullerene Organic Solar Cells. *ACS Appl. Mater. Interfaces* **2020**, *12*, 12083−12092.

(39) Seibers, Z. D.; Collier, G. S.; Hopkins, B. W.; Boone, E. S.; Le, T. P.; Gomez, E. D.; Kilbey, S. M. Tuning Fullerene Miscibility with Porphyrin-Terminated P3HTs in Bulk Heterojunction Blends. *Soft Matter* **2020**, *16*, 9769−9779.

(40) Saito, M.; Tamai, Y.; Ichikawa, H.; Yoshida, H.; Yokoyama, D.; Ohkita, H.; Osaka, I. Significantly Sensitized Ternary Blend Polymer Solar Cells with a Very Small Content of the Narrow-Band Gap Third Component That Utilizes Optical Interference. *Macromolecules* **2020**, *53*, 10623−10635.

(41) Yang, T.; Ma, R.; Cheng, H.; Xiao, Y.; Luo, Z.; Chen, Y.; Luo, S.; Liu, T.; Lu, X.; Yan, H. A Compatible Polymer Acceptor Enables Efficient and Stable Organic Solar Cells as a Solid Additive. *J. Mater. Chem. A* **2020**, *8*, 17706−17712.

(42) Yang, D.; Cao, B.; Körstgens, V.; Saxena, N.; Li, N.; Bilko, C.; Grott, S.; Chen, W.; Jiang, X.; Heger, J. E.; Bernstorff, S.; MüllerBuschbaum, P. Tailoring Morphology Compatibility

and Device Stability by Adding PBDTTPD-COOH as Third Component to Fullerene-Based Polymer Solar Cells. *ACS Appl. Energy Mater.* **2020**, *3*, 2604−2613.

(43) Kong, C.; Song, B.; Mueller, E. A.; Kim, J.; McNeil, A. J. Random Copolymers Outperform Gradient and Block Copolymers in Stabilizing Organic Photovoltaics. *Adv. Funct. Mater.* **2019**, *29*, 1900467.

(44) Lutz, J. P.; Hannigan, M. D.; McNeil, A. J. Polymers Synthesized via Catalyst-Transfer Polymerization and Their Applications. *Coord. Chem. Rev.* **2018**, *376*, 225−247.

(45) Liang, Y.; Xu, Z.; Xia, J.; Tsai, S.-T.; Wu, Y.; Li, G.; Ray, C.; Yu, L. For the Bright Future-Bulk Heterojunction Polymer Solar Cells with Power Conversion Efficiency of 7.4%. *Adv. Mater.* **2010**, *22*, E135−E138

(46) Liao, S.-H.; Jhuo, H.-J.; Cheng, Y.-S.; Chen, S.-A. Fullerene Derivative-Doped Zinc Oxide Nanofilm as the Cathode of Inverted Polymer Solar Cells with Low-Bandgap Polymer (PTB7-Th) for High Performance. *Adv. Mater.* **2013**, *25*, 4766−4771.

(47) Liu, Y.; Zhao, J.; Li, Z.; Mu, C.; Ma, W.; Hu, H.; Jiang, K.; Lin, H.; Ade, H.; Yan, H. Aggregation and Morphology Control Enables Multiple Cases of High-Efficiency Polymer Solar Cells. *Nat. Commun.* **2014**, *5*, 5293.

(48) Ouyang, X.; Peng, R.; Ai, L.; Zhang, X.; Ge, Z. Efficient Polymer Solar Cells Employing a Non-Conjugated Small-Molecule Electrolyte. *Nat. Photonics* **2015**, *9*, 520−524.

(49) Huang, J.; Carpenter, J. H.; Li, C.-Z.; Yu, J.-S.; Ade, H.; Jen, A. K.-Y. Highly Efficient Organic Solar Cells with Improved Vertical Donor-Acceptor Compositional Gradient Via an Inverted Off-Center Spinning Method. *Adv. Mater.* **2016**, *28*, 967−974.

(50) Yan, Y.; Li, W.; Cai, F.; Cai, J.; Huang, Z.; Gurney, R. S.; Liu, D.; Lidzey, D. G.; Pearson, A. J.; Wang, T. Correlating Nanoscale Morphology with Device Performance in Conventional and Inverted PffBT4T-2OD: $PC_{71}BM$ Polymer Solar Cells. *ACS Appl. Energy Mater.* **2018**, *1*, 3505−3512.

(51) Campoy-Quiles, M.; Ferenczi, T.; Agostinelli, T.; Etchegoin, P. G.; Kim, Y.; Anthopoulos, T. D.; Stavrinou, P. N.; Bradley, D. D. C.; Nelson, J. Morphology Evolution via Self-Organization and Lateral and Vertical Diffusion in Polymer:Fullerene Solar Cell Blends. *Nat. Mater.* **2008**, *7*, 158−164.

(52) Hammond, M. R.; Kline, R. J.; Herzing, A. A.; Richter, L. J.; Germack, D. S.; Ro, H. W.; Soles, C. L.; Fischer, D. A.; Xu, T.; Yu, L.; Toney, M. F.; Delongchamp, D. M. Molecular

Order in High Efficiency Polymer/Fullerene Bulk Heterojunction Solar Cells. *ACS Nano* **2011**, *5*, 8248−8257.

(53) Collins, B. A.; Li, Z.; Tumbleston, J. R.; Gann, E.; McNeill, C. R.; Ade, H. Absolute Measurement of Domain Composition and Nanoscale Size Distribution Explains Performance in PTB7: $PC_{71}BM$ Solar Cells. *Adv. Energy Mater.* **2013**, *3*, 65−74.

(54) Dkhil, S. B.; Pfannmoller, M.; Saba, M. I.; Gaceur, M.; Heidari, H.; Videlot-Ackermann, C.; Margeat, O.; Guerrero, A.; Bisquert, J.; Garcia-Belmonte, G.; Mattoni, A.; Bals, S.; Ackermann, J. Toward High-Temperature Stability of PTB7-Based Bulk Heterojunction Solar Cells: Impact of Fullerene Size and Solvent Additive. *Adv. Energy Mater.* **2017**, *7*, 1601486.

(55) Lou, S. J.; Szarko, J. M.; Xu, T.; Yu, L.; Marks, T. J.; Chen, L. X. Effects of Additives on the Morphology of Solution Phase Aggregates Formed by Active Layer Components of High-Efficiency Organic Solar Cells. *J. Am. Chem. Soc.* **2011**, *133*, 20661−20663.

(56) Song, X.; Gasparini, N.; Baran, D. The Influence of Solvent Additive on Polymer Solar Cells Employing Fullerene and NonFullerene Acceptors. *Adv. Electron. Mater.* **2018**, *4*, 1700358.

(57) Zhang, Y.; Parnell, A. J.; Pontecchiani, F.; Cooper, J. F. K.; Thompson, R. L.; Jones, R. A. L.; King, S. M.; Lidzey, D. G.; Bernardo, G. Understanding and Controlling Morphology Evolution via DIO Plasticization in PffBT4T-2OD/ $PC_{71}BM$ Devices. *Sci. Rep.* **2017**, *7*, 44269.

(58) Landerer, D.; Mertens, A.; Freis, D.; Droll, R.; Leonhard, T.; Schulz, A. D.; Bahro, D.; Colsmann, A. Enhanced Thermal Stability of Organic Solar Cells Comprising Ternary D-D-A Bulk-Heterojunctions. *npj Flex. Electron.* **2017**, *1*, 11.

(59) Gao, M.; Liang, Z.; Geng, Y.; Ye, L. Significance of Thermodynamic Interaction Parameters in Guiding the Optimization of Polymer:Nonfullerene Solar Cells. *Chem. Commun.* **2020**, *56*, 12463−12478.

(60) Kim, J. S.; Lee, Y.; Lee, J. H.; Park, J. H.; Kim, J. K.; Cho, K. High-Efficiency Organic Solar Cells Based on End-Functional-GroupModified Poly(3-Hexylthiophene). *Adv. Mater.* **2010**, *22*, 1355−1360.

(61) Liu, Y.; Tang, D.; Zhang, K.; Huang, P.; Wang, Z.; Zhu, K.; Li, Z.; Yuan, L.; Fan, J.; Zhou, Y.; Song, B. Tuning Surface Energy of Conjugated Polymers via Fluorine Substitution of Side Alkyl Chains: Influence on Phase Separation of Thin Films and Performance of Polymer Solar Cells. *ACS Omega* **2017**, *2*, 2489−2498.

(62) Sun, Y.; Chien, S. C.; Yip, H. L.; Chen, K. S.; Zhang, Y.; Davies, J. A.; Chen, F. C.; Lin, B.; Jen, A. K. Y. Improved Thin Film Morphology and Bulk-Heterojunction Solar Cell Performance through Systematic Tuning of the Surface Energy of Conjugated Polymers. *J. Mater. Chem.* **2012**, *22*, 5587−5595.

(63) Shimizu, R. N.; Demarquette, N. R. Evaluation of Surface Energy of Solid Polymers Using Different Models. *J. Appl. Polym. Sci.* **2000**, *76*, 1831−1845.

(64) Ohori, Y.; Fujii, S.; Kataura, H.; Nishioka, Y. Improvement of Bulk Heterojunction Organic Solar Cells Based on PTB7:$PC_{61}BM$ with Small Amounts of P3HT. Jpn. *J. Appl. Phys.* **2015**, *54*, 04DK09.

(65) Wang, C.; Zhang, W.; Meng, X.; Bergqvist, J.; Liu, X.; Genene, Z.; Xu, X.; Yartsev, A.; Inganäs, O.; Ma, W.; Wang, E.; Fahlman, M. Ternary Organic Solar Cells with Minimum Voltage Losses. *Adv. Energy Mater.* **2017**, *7*, 1700390.

(66) Li, W.; Cai, J.; Cai, F.; Yan, Y.; Yi, H.; Gurney, R. S.; Liu, D.; Iraqi, A.; Wang, T. Achieving over 11% Power Conversion Efficiency in PffBT4T-2OD-Based Ternary Polymer Solar Cells with Enhanced Open-Circuit-Voltage and Suppressed Charge Recombination. *Nano Energy* **2018**, *44*, 155−163.

(67) Clark, M. D.; Jespersen, M. L.; Patel, R. J.; Leever, B. J. Predicting Vertical Phase Segregation in Polymer-Fullerene Bulk Heterojunction Solar Cells by Free Energy Analysis. *ACS Appl. Mater. Interfaces* **2013**, *5*, 4799−4807.

(68) Nilsson, S.; Bernasik, A.; Budkowski, A.; Moons, E. Morphology and Phase Segregation of Spin-Casted Films of Polyfluorene/PCBM Blends. *Macromolecules* **2007**, *40*, 8291−8301.

(69) Sumita, M.; Sakata, K.; Asai, S.; Miyasaka, K.; Nakagawa, H. Dispersion of Fillers and the Electrical Conductivity of Polymer Blends Filled with Carbon Black. *Polym. Bull.* **1991**, *25*, 265−271.

(70) Lindqvist, C.; Bergqvist, J.; Feng, C.-C.; Gustafsson, S.; Bäcke, O.; Treat, N. D.; Bounioux, C.; Henriksson, P.; Kroon, R.; Wang, E.; Sanz-Velasco, A.; Kristiansen, P. M.; Stingelin, N.; Olsson, E.; Inganäs, O.; Andersson, M. R.; Müller, C. Fullerene Nucleating Agents: A Route Towards Thermally Stable Photovoltaic Blends. *Adv. Energy Mater.* **2014**, *4*, 1301437.

(71) Lindqvist, C.; Sanz-Velasco, A.; Wang, E.; Bäcke, O.; Gustafsson, S.; Olsson, E.; Andersson, M. R.; Müller, C. Nucleation-Limited Fullerene Crystallisation in a Polymer-Fullerene Bulk-Heterojunction Blend. *J. Mater. Chem. A* **2013**, *1*, 7174−7180.

(72) Richards, J. J.; Rice, A. H.; Nelson, R. D.; Kim, F. S.; Jenekhe, S. A.; Luscombe, C. K.; Pozzo, D. C. Modification of PCBM Crystallization via Incorporation of C60 in Polymer/Fullerene Solar Cells. *Adv. Funct. Mater.* **2013**, *23*, 514−522.

(73) Dowland, S. A.; Salvador, M.; Perea, J. D.; Gasparini, N.; Langner, S.; Rajoelson, S.; Ramanitra, H. H.; Lindner, B. D.; Osvet, A.; Brabec, C. J.; Hiorns, R. C.; Egelhaaf, H. J. Suppression of Thermally Induced Fullerene Aggregation in Polyfullerene-Based Multiacceptor Organic Solar Cells. *ACS Appl. Mater. Interfaces* **2017**, *9*, 10971−10982.

(74) Ramanitra, H. H.; Dowland, S. A.; Bregadiolli, B. A.; Salvador, M.; Santos Silva, H.; Bégué, D.; Graeff, C. F. O.; Peisert, H.; Chassé, T.; Rajoelson, S.; Osvet, A.; Brabec, C. J.; Egelhaaf, H. J.; Morse, G. E.; Distler, A.; Hiorns, R. C. Increased Thermal Stabilization of Polymer Photovoltaic Cells with Oligomeric PCBM. *J. Mater. Chem. C* **2016**, *4*, 8121−8129.

(75) Wong, H. C.; Li, Z.; Tan, C. H.; Zhong, H.; Huang, Z.; Bronstein, H.; McCulloch, I.; Cabral, J. T.; Durrant, J. R. Morphological Stability and Performance of Polymer-Fullerene Solar Cells under Thermal Stress: The Impact of Photoinduced $PC_{60}BM$ Oligomerization. *ACS Nano* **2014**, *8*, 1297−1308.

(76) Li, Q.; Wang, L. M.; Liu, S.; Zhan, X.; Zhu, T.; Cao, Z.; Lai, H.; Zhao, J.; Cai, Y.; Xie, W.; Huang, F. Impact of Donor-Acceptor Interaction and Solvent Additive on the Vertical Composition Distribution of Bulk Heterojunction Polymer Solar Cells. *ACS Appl. Mater. Interfaces* **2019**, *11*, 45979−45990.

(77) Khlyabich, P. P.; Rudenko, A. E.; Thompson, B. C.; Loo, Y. L. Structural Origins for Tunable Open-Circuit Voltage in TernaryBlend Organic Solar Cells. *Adv. Funct. Mater.* **2015**, *25*, 5557−5563.

(78) Flory, P. J. Principles of Polymer Chemistry; Cornell University Press: Ithaca, NY, **1953**.

(79) Rubinstein, M.; Colby, R. H. Thermodynamics of Mixing. Polymer Physics; Oxford University Press: New York, NY, **2003**; pp 137−170.

(80) He, Z.; Zhong, C.; Su, S.; Xu, M.; Wu, H.; Cao, Y. Enhanced Power-conversion Efficiency in Polymer Solar Cells using an Inverted Device Structure. *Nat. Photonics* **2012**, *6*, 591−595.

(81) Wang, T.; Brédas, J.-L. Organic Photovoltaics: Understanding the Preaggregation of Polymer Donors in Solution and its Morphological Impact. *J. Am. Chem. Soc.* **2021**, *143*, 1822−1835.

(82) Kim, B.-G.; Jeong, E. J.; Park, H. J.; Bilby, D.; Guo, L. J.; Kim, J. Effect of Polymer Aggregation on the Open Circuit Voltage in Organic Photovoltaic Cells: Aggregation-induced

Conjugated Polymer Gel and its Application for Preventing Open Circuit Voltage Drop. *ACS Appl. Mater. Interfaces* **2011**, *3*, 674−680.

(83) Vandewal, K.; Tvingstedt, K.; Gadisa, A.; Inganäs, O.; Manca, J. V. On the Origin of the Open-Circuit Voltage of Polymer-Fullerene Solar Cells. *Nat. Mater.* **2009**, *8*, 904−909.

(84) Kim, M. S.; Kim, B. G.; Kim, J. The Effective Variables to Control the Fill Factor of Organic Photovoltaic Cells. *ACS Appl. Mater. Interfaces* **2009**, *1*, 1264−1629.

Chapter 3: A Nonaqueous Redox-Matched Flow Battery with Charge Storage in Insoluble Polymer Beads

Portions of this chapter have been submitted: DOI: 10.26434/chemrxiv-2021-mf70j
Kim, D.; Sanford, M. S.; Vaid, T. P.; McNeil. A. J., A Nonaqueous Redox-Matched Flow Battery with Charge Storage in Insoluble Polymer Beads

3.1 Introduction

In redox flow batteries (RFBs; Scheme 3-1a), redox-active materials are dissolved in two separate solutions, the anolyte and catholyte, which flow past two closely-spaced electrodes where the electrochemical reactions take place.[1,2] Because the anolyte and catholyte solutions are contained in external tanks, RFBs can be scaled easily and inexpensively to store large amounts of energy, which is advantageous for renewable energy obtained from intermittent wind and solar sources. One current focus in RFB research is on achieving high energy density, which is directly proportional to both the battery voltage (the difference in redox potential between the two redox-active materials) and the concentration of redox-active materials in solution. A high battery voltage is feasible in RFBs that use nonaqueous solvents such as acetonitrile, due to their wide electrochemical windows of up to 5 V or more[3,4] compared to ~1.5 V in aqueous systems. To take advantage of these wide electrochemical windows, redox-active organic molecules (ROMs) are used as the active materials because they can be synthetically tuned to exhibit high oxidation potentials[5–7] and low reduction potentials.[8–10] Additionally, ROMs can be functionalized to create molecules with solubilities of 1 M or greater,[11] enabling, in theory, high-energy-density organic,

nonaqueous RFBs. However, at concentrations near 1 M most ROM solutions become viscous and ionic conductivity decreases,[12] rendering them less suitable for use in RFBs.

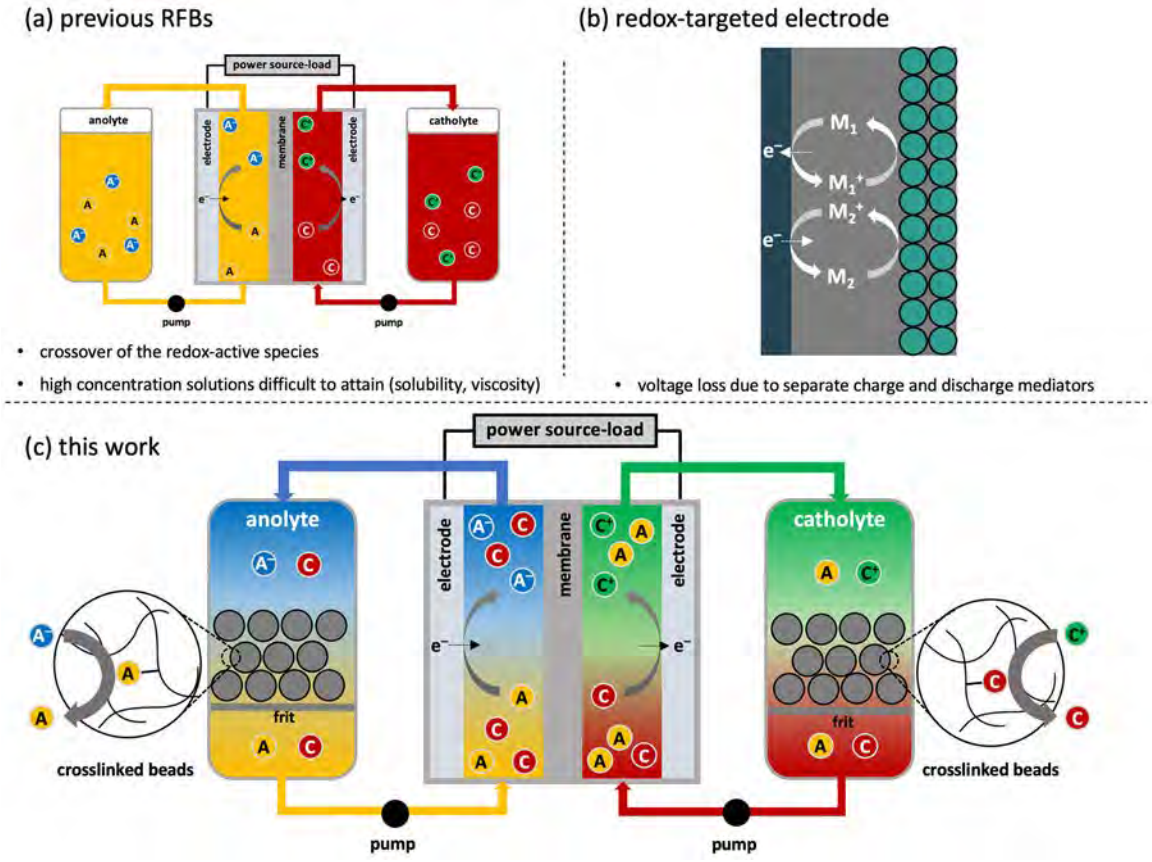

Scheme 3-1. Previous RFBs, A Redox-Targeted Electrode, and the Redox-Matched Flow Battery

Another issue that must be addressed in RFBs is crossover of the redox-active species between the anolyte and catholyte solutions. Once a redox-active species has crossed over to the opposite electrolyte solution, it is no longer electrochemically active, resulting in a loss in capacity for the RFB. One way that crossover has been addressed is by the creation of "symmetric" RFBs, which can be constructed in two different ways. In the first, the anolyte and catholyte solutions contain the same redox-active element, as in the vanadium RFB, which uses the $V^{2+/3+}$ couple in

the anolyte solution and the $V^{4+/5+}$ couple in the catholyte solution. As a consequence, the vanadium ions that cross over will simply enter into the other redox reaction in the next cycle. The other way to create a symmetric RFB is by using a 1:1 mixture of the positive and negative redox-active materials in both the anolyte and catholyte solutions, as is done in the iron-chromium aqueous RFB wherein the positive redox couple is $Fe^{2+/3+}$ and the negative redox couple is $Cr^{2+/3+}$.[13] In each solution only one ion participates in the battery charge and discharge while the other ion is a spectator. While this configuration mitigates the negative effects of crossover, half of the active material is not used and is thus not an efficient use of materials. Symmetric nonaqueous, organic RFBs have been made by using a ROM that can be both reversibly oxidized and reversibly reduced as both the positive and negative ROM[14–16] or by using a 1:1 mixture of two ROMs in both the anolyte and catholyte solutions,[9] as in the iron-chromium RFB. Alternatively, different positive and negative ROMs can be used to make an asymmetric RFB, but that requires the synthesis of oligomeric positive and negative ROMs and/or the use of specialized membranes minimize crossover.[17,18]

An innovative concept, the redox-targeted electrode, was introduced by Wang, Grätzel and coworkers in 2006[19,20] and points the way to a system that could simultaneously address several of the issues discussed above. In the redox-targeted electrode (Scheme 3-1b), an insoluble and poorly electrically conducting active material such as $LiFePO_4$ is not in direct electrical contact with the current collector. Instead, two soluble redox-active molecules are in a solution that bathes the $LiFePO_4$. One of the soluble mediators has a redox potential about 0.1 V positive of $LiFe^{II}PO_4/Fe^{III}PO_4$, and the other has a redox potential about 0.1 V negative of $LiFe^{II}PO_4/Fe^{III}PO_4$. The $LiFePO_4$ is charged by oxidation by the more positive mediator, which in turn is oxidized at the electrode. Discharge happens similarly through reduction by the more negative mediator. If the

$LiFePO_4$ were used as the positive active material in a flow battery, with the soluble molecular mediators circulating to the electrodes, and a similar setup were used for an insoluble negative active material, it would be possible to create a flow battery with high energy density, approaching that of a lithium-ion battery with the same active materials. One drawback of the system described by Wang and Grätzel is the use of two mediators for each electrode, which leads to a voltaic inefficiency, as charging happens through the higher potential mediator (for the positive electrode) and discharging through the lower potential mediator. In a full flow battery with four mediators (two for each electrode), each with a redox potential 0.1 V displaced from that of its electrode, there would be a 0.4 V difference between the charge and discharge voltage of the battery. Since that initial 2006 report, several more redox-targeted inorganic electrodes, or hybrid flow batteries with one redox-targeted electrode, have been reported,[21–26] as has a full redox-targeted flow battery[27] and an aqueous RFB with one redox-targeted organic polymer electrode.[28]

Inspired by the redox-targeting strategy described above, we introduce the concept of a redox-matched flow battery (RMFB). In the RMFB (Scheme 3-1c), redox-active molecules are covalently tethered to insoluble polymer beads and these beads act as the charge-storage material. In the RMFB reported herein, the redox-active moieties are a ferrocene derivative for the catholyte beads and a viologen derivative for the anolyte beads. For each bead type there is a matched soluble molecular mediator with a chemical structure similar to the redox-active moiety on the bead, such that the redox potentials are very nearly the same (hence the name "redox-matched" flow battery). In this way, the battery differs from the redox-targeting method described by Wang, Grätzel, and co-workers, where there are two mediators for each insoluble active material.[19,20] In our RMFB there is only one mediator for each insoluble redox-active material and charging/discharging is driven by the Nernstian potential difference due to the different ratio of oxidized/reduced species

in solution versus on the bead. There is a previous report of a redox-targeted $LiFePO_4$ electrode that is paired with a single soluble mediator that almost exactly matches the redox potential of the $LiFePO_4$, allowing an electrode with one Nernstian-driven mediator and the construction of a hybrid flow battery.[29] There is another report of a redox-targeted organic polymer electrode with only one mediator, cited above.[28] However, those "redox targeted" electrodes differ from our system in that one must find a suitable mediator with a redox potential well-matched to that of the solid active material, whereas in our "redox matched" system one can simply synthesize a mediator that is structurally analogous to the moiety on the bead and their redox potentials will be naturally matched.

As shown in Scheme 3-1, the soluble mediator circulates through the flow battery and is oxidized/reduced at the electrode, then flows past the polymer beads in the reservoir and undergoes redox exchange with the active moieties on the beads. Both the anolyte and catholyte solutions contain a 1:1 mixture of anolyte mediator (*A*) and catholyte mediator (*C*), which mitigates the negative effect of crossover of the mediators through the membrane. The soluble species that is in the "wrong" solution merely acts as a spectator and is not involved in the redox reactions at either the electrode or the beads. For example, a viologen in the catholyte solution would remain a dication as the ferrocene derivative is cycled between its neutral and +1 state. Only a small fraction of the viable active material is unused because the vast majority of charge is stored in the beads. With properly chosen polymer beads for functionalization, the effective concentration of active material can be 1 M or more. Yet the dissolved mediators can be at relatively low concentration, in the range of 25 mM or less. Consequently, the soluble species do not need to be engineered for high solubility, and the problems of high-concentration solutions, such as high viscosity, are avoided.

While this work was in progress, Sevov and Wong reported a redox-targeted electrode based on a crosslinked viologen polymer.[30] The monomer bis(4-vinyl-benzyl)viologen was polymerized to form heavily crosslinked, insoluble beads that were used as the charge-storage material. However, similar to the inorganic redox-targeted electrodes discussed above, two mediators were used to charge and discharge the crosslinked viologen charge-storage material. In addition, a flow battery was not demonstrated. Herein, we demonstrate an improved version of this redox-targeting approach wherein only a single redox-matched mediator is used (per electrode), so there is no loss in voltaic efficiency due to multiple mediators with different redox potentials. In addition, rather than requiring a new polymer to be synthesized for each new solid redox-active material, we utilize a synthetic platform that enables wide versatility in the redox-active moieties that can be attached to the polymer beads. Finally, we demonstrate a full RFB system (rather than one electrode) in a manner that should be generalizable to many different redox-active moieties.

3.2 Results and Discussion

We chose Merrifield resin, which consists of crosslinked polystyrene with chloromethyl functionalities, as our polymer support. Merrifield resin has been extensively used for solid-supported organic reactions, most notably peptide synthesis.[31] It is commercially available as beads in a variety of sizes, degrees of crosslinking, and degrees of chloromethyl functionalization. The chloromethyl groups offer a convenient handle for covalent attachment of organic moieties. We used beads containing 4.2 mmol of chlorine per gram (determined by elemental analysis (EA) of C, H, and Cl), which translates to a concentration of over 4 M in the dry, unfunctionalized beads. When the chlorine is substituted by the redox-active groups, the volume of the beads increases,

and the necessary swelling of the beads by solvent will further increase their volume, but 4 M is an encouragingly high initial effective concentration of active material.

For this initial demonstration of a RMFB, we chose derivatives of the very common and stable redox-active molecules viologen and ferrocene. The starting Merrifield resin beads (xPS-Cl) were functionalized with viologen groups and ferrocene groups by the one-step substitution reactions shown in Figure 3-1. Treatment of xPS-Cl with 1-methyl-4,4′-bipyridinium iodide in MeCN at reflux for 48 h yielded viologen-functionalized beads as the mixed chloride-iodide salt, [xPS-bpy-Me^{2+}][Cl^-][I^-]. Reaction completion was confirmed by disappearance of the C–Cl band in the Raman spectrum (at 665 cm^{-1}) and in the IR spectrum (at 672 cm^{-1}) (Figure A2-5 and A2-6 for spectra). Three rounds of ion exchange with NH_4PF_6 yielded the viologen-functionalized beads as the hexafluorophosphate salt, [xPS-bpy-Me^{2+}][PF_6^-]$_2$. Both the initial [xPS-bpy-Me^{2+}][Cl^-][I^-] beads and the ion-exchanged beads, [xPS-bpy-Me^{2+}][PF_6^-]$_2$, were examined by EA for C, H, N, Cl, and I, and the [xPS-bpy-Me^{2+}][PF_6^-]$_2$ beads were additionally analyzed for F content. There was no fractional conversion to [xPS-bpy-Me^{2+}][Cl^-][I^-] and fractional ion-exchange to [xPS-bpy-Me^{2+}][PF_6^-]$_2$ that was consistent with the EA data for both sets of beads. However, an assumption of 75% conversion in the initial functionalization reaction to create [xPS-bpy-Me^{2+}][Cl^-][I^-], followed by 95% ion exchange to give [xPS-bpy-Me^{2+}][PF_6^-]$_2$, gives a calculated EA that agrees reasonably well with the experimental EA mass % for N (3.80 calc, 3.44 exp), Cl (1.84 calc, 1.69 exp), and I (0.86 calc, 0.93 exp). Full details are provided in the appendix.

The ferrocene-functionalized beads were synthesized by the reaction of xPS-Cl with ferrocenecarboxylic acid and $^iPr_2NEt$ in DMF at 60°C for 24 h, yielding xPS-Fc. Raman spectroscopy of the ferrocene beads was not possible due to fluorescence of the ferrocene functionalities. Instead, reaction progress/completion was checked by IR spectroscopy (Figure A2-

5). The C–Cl band at 672 cm^{-1} disappeared after reaction, and a C=O band at 1714 cm^{-1} due to the ester linkage appeared. Elemental analysis for C, H, N, and Cl agreed most closely with conversion of 70% of the chloromethyl groups, and with 0.16 equiv of residual DMF per monomer unit (of any kind). Both bead types were soaked in electrolyte solution (CH_3CN, 0.50 M $[NBu_4][PF_6]$) and, as shown in Figure A2-9, CVs of those solutions showed that no electroactive species were leached from the beads.

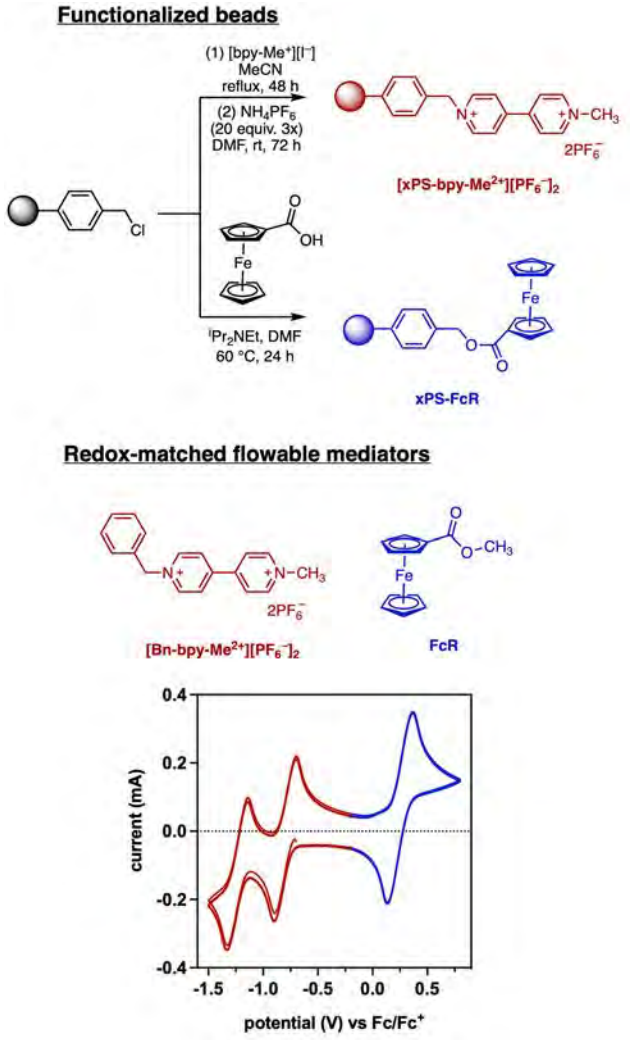

Figure 3.1. Syntheses of the two functionalized beads (top) and structures of the redox-matched mediators and a cyclic voltammogram of a mixed solution of 5 mM of each in CH_3CN with 0.50 M $[NBu_4][PF_6]$ at a glassy carbon electrode (bottom)

The soluble mediators, shown in Figure 3-1, were chosen to have structures analogous to the redox-active moieties on the polymer beads, such that their redox potentials would be very similar. Cyclic voltammetry (CH_3CN, 0.50 M $[NBu_4][PF_6]$) showed that the ferrocene mediator, FcR, has an $E_{1/2}$ = +0.255 V (vs ferrocene$^{+/0}$), while the viologen mediator [Bn-bpy-Me^{2+}][PF_6^-]$_2$ has $E_{1/2}$ = -0.785 V and -1.204 V (vs ferrocene$^{+/0}$). Only the first viologen reduction was used in the RMFB, affording a nominal voltage of 1.04 V.

For the soluble redox mediators to diffuse into the beads to undergo redox exchange, as depicted in Scheme 3-1, the beads must swell in the battery solvent/electrolyte system. Due to the high concentration of redox-active moieties in the beads, it is likely that self-exchange between tethered groups will facilitate electron transfer to the far interior of the beads so that it is not necessary for mediator to diffuse into the bead center. It is necessary, however, that the PF_6^- counterions move fully into and out of the beads to balance every charge transferred. To evaluate bead swelling we placed a known mass (~100 mg) of beads in a standard 5 mm NMR tube, added an excess of a solvent, and measured the change in height of the column of beads after 2 h. Our calibration of the NMR tubes indicated a volume of 130 μL per cm of height. The measured volume change was multiplied by a factor of 0.74 (the packing fraction of close-packed spheres) to account for the interstitial spaces between the beads. The swelling of both bead types, xPS-Fc and [xPS-bpy-Me^{2+}][PF_6^-]$_2$, was measured in CH_3CN, where it was 0.77 mL/g for the xPS-Fc and 0.96 mL/g for the [xPS-bpy-Me^{2+}][PF_6^-]$_2$. The bead swelling was also evaluated by optical microscope images of a statistical sample of dry and swollen beads, which yielded similar results (Figure A2-7 and Table A2-1). The swelling of both bead types represents a solvent content of the beads that should enable transport of molecular species into and out of the beads during redox exchange, while not excessively increasing the bead volumes such that the concentration of active species

becomes diluted (decreasing the energy density of the RMFB). The concentration of redox-active moieties in the CH_3CN-swollen beads is roughly 1.0 M in the viologen beads and 1.7 M in the ferrocene beads.

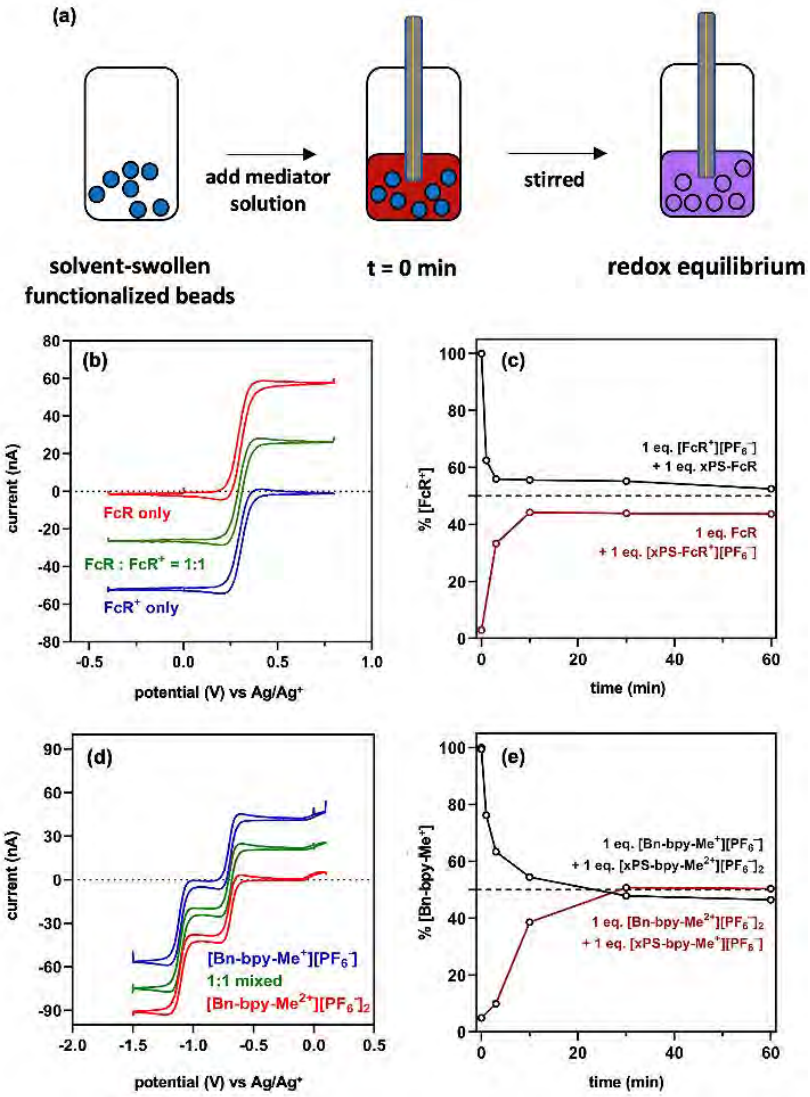

Figure 3.2. (a) Setup for monitoring redox exchange reactions over time using an ultramicroelectrode (Pt disk, 10 µm diameter). (b) Ultramicroelectrode CVs of 5.0 mM FcR, 5.0 mM FcR^+, and 2.5 mM each of FcR and FcR^+. (c) Change in solution-phase fraction of FcR^+ over time as FcR^+ interacts with xPS-Fc and FcR interacts with xPS-Fc^+. (d) Ultramicroelectrode CVs of 5.0 mM Bn-bpy-Me^{2+}, 5.0 mM Bn-bpy-Me^+, and 2.5 mM each of Bn-bpy-Me^{2+} and Bn-bpy-Me^+. (e) Change in solution-phase fraction of Bn-bpy-Me^+ over time as Bn-bpy-Me^+ interacts with xPS-bpy-Me^{2+} and Bn-bpy-Me^{2+} interacts with xPS-bpy-Me^+

For the functionalized polymer beads to serve as the charge-storage material in a RMFB, they must undergo electron exchange with the dissolved mediators on a timescale that is fast compared to one charge or discharge half-cycle of the battery. We therefore sought to determine the rate of these redox-exchange reactions before using them in a RFB, but to do so it was necessary to measure the individual concentrations of the same ROM in two different oxidation states (e.g., FcR and FcR^+) in a mixed solution—something that CV using a standard disk electrode does not do well. An ultramicroelectrode, on the other hand, yields CVs of the type shown in Figure 3-2b (FcR, FcR^+, and a 1:1 mixture of FcR and FcR^+) and Figure 3-2d (Bn-bpy-Me^{2+}, Bn-bpy-Me^+, and a 1:1 mixture of Bn-bpy-Me^{2+} and Bn-bpy-Me^+). The difference between the current at the oxidative plateau and the current at the reductive plateau in Figure 3-2b is proportional to the total concentration of FcR and FcR^+ present, with the absolute value of the anodic current proportional to the FcR concentration and the absolute value of the cathodic current proportional to the FcR^+ concentration.[32] The direct proportionality of the anodic and cathodic currents to the concentrations of FcR and FcR^+, respectively, holds only if FcR and FcR^+ have similar diffusion coefficients in the solvent/electrolyte system examined; the equivalence of the anodic and cathodic currents in the CV of a 1:1 solution of FcR and FcR^+ in Figure 3-2b confirms this to be the case. That is also true for Bn-bpy-Me^{2+} and Bn-bpy-Me^+, as indicated by the CVs in Figure 3-2d.

The rate of redox equilibration between the beads and dissolved mediators was determined by the procedure shown in Figure 3-2a. First, a measured quantity of beads was placed in a vial (in a nitrogen-filled glovebox) with a solution of 0.50 M $[NBu_4][PF_6]$ in CH_3CN to swell the beads. The excess liquid was decanted after 30 min. To the swollen beads was added a solution of an equivalent molar amount of its redox-matched mediator in the oxidation state opposite that of the redox moieties on the beads, and the change in redox state of the solution-phase species was

monitored. For example, for the xPS-Fc beads, a solution containing one equivalent of $[FcR^+][PF_6^-]$ (relative to the amount of redox-active Fc moieties on the beads) was added, such that at equilibrium there would be a 1:1 mixture of FcR and FcR^+ in solution (assuming that the solution-phase FcR and the bead-bound Fc moiety have the same redox potential). The suspension was gently stirred and the stirring paused to obtain CVs with the ultramicroelectrode. In separate experiments, the equilibrium was approached from the other direction; that is, the oxidized form of the ferrocene beads, $[xPS\text{-}Fc^+][PF_6^-]$, and the reduced form of the viologen beads, $[xPS\text{-}bpy\text{-}Me^+][PF_6^-]$, were prepared, and each was treated with their corresponding redox-matched mediator in the opposite oxidation state. In all four experiments the solutions came to equilibrium with an approximate 1:1 mixture of oxidized and reduced species in solution, as expected (Figure 3-2c and 3-2e). As shown in Figure 3-2c, the ferrocene systems came to equilibrium quickly, with the oxidation of xPS-Fc near equilibrium in 3 min and the reduction of $[xPS\text{-}Fc^+][PF_6^-]$ near equilibrium in 10 min. The viologen system was slower to equilibrate, reaching near-equilibrium in 10 min and full equilibrium in 30 min, in both the oxidative and reductive redox exchanges. Separate experiments in our flow battery reservoirs, not connected to the electrode cell but simply recirculating the electrolyte, showed a similarly fast redox exchange between the beads and solution-phase mediators (Figure A2-10). Overall, these results show that the beads should charge and discharge sufficiently quickly to function in a RMFB, where the charge or discharge times will be at least 60 min (corresponding to a 1C rate).

Initial attempts at full RMFBs used the nonselective mesoporous separators Celgard 2500 or Daramic 175 as the membrane. These membranes are often preferred over ion-exchange membranes because they are more stable in organic solvents and have lower resistance to ion transport. However, they allow relatively fast crossover of ROMs.[33] We expected that the use of

1:1 solutions of FcR and [Bn-bpy-Me^{2+}][PF_6^-]$_2$ in both the anolyte and catholyte solutions would mitigate the negative effects of that crossover. However, we observed poor capacity utilization of the beads in the RMFBs assembled with either Celgard or Daramic separators (Figure A2-15). We hypothesized that in those RMFBs the redox exchange between the mediators and the polymer beads is slow relative to the rate of crossover of redox-active material, resulting in incomplete utilization of the redox-active material in the beads. We therefore performed a separate investigation of crossover rates in our RFB system with these separators compared to a Fumasep FAP-375-PP anion-exchange membrane.

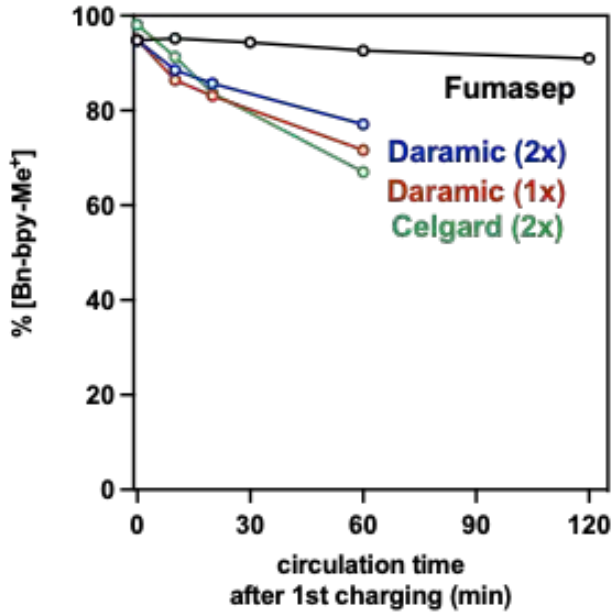

Figure 3.3. The change in concentration of [Bn-bpy-Me^+][PF_6^-] in the anolyte solution after the RFB (with no beads) has been charged and then circulation continued with no electrical charging or discharging, with a Fumasep anion-exchange membrane, Daramic mesoporous membrane (1 or 2 layers), or 2 layers of Celgard mesoporous membrane.

Solutions that were 15 mM in both [Bn-bpy-Me^{2+}][PF_6^-]$_2$ and FcR were placed on both sides of our RFB setup with no polymer beads present (see appendix for details, and Figure A2-8 for photographs of the RMFB setup). While circulating at 20 mL/min, the battery was charged to 1.40 V (0.36 V greater than the nominal battery voltage). Circulation was stopped and the concentrations of Bn-bpy-Me^{2+} and Bn-bpy-Me^{+} in the anolyte solution were determined by ultramicroelectrode CV, which indicated that the battery was 95% charged. Circulation was then continued with no potential applied, and the circulation stopped periodically to monitor the decay in Bn-bpy-Me^{+} concentration and increase in Bn-bpy-Me^{2+} concentration, as shown in Figure 3-3. That discharge can be due to either Bn-bpy-Me^{+} passing through the separator from the anolyte solution to the catholyte solution, or FcR^{+} passing from the catholyte solution to the anolyte solution and oxidizing Bn-bpy-Me^{+}. With a Daramic 175 separator, the charge of the anolyte solution dropped to 72% after 60 min. That discharge is fast enough that it may lead to incomplete charge/discharge of the polymer beads in a RMFB. A similar experiment was performed under identical conditions except for the use of a Fumasep FAP-375-PP anion-exchange membrane. In that case, as shown in Figure 3-3, the discharge due to crossover was significantly slower, with the viologen charge decreasing from 95% to 93% over 60 min and to 91% over 120 min. (This data is shown in Figures A2-11 to A2-14) We therefore used Fumasep FAP-375-PP membrane in the following RMFB experiments.

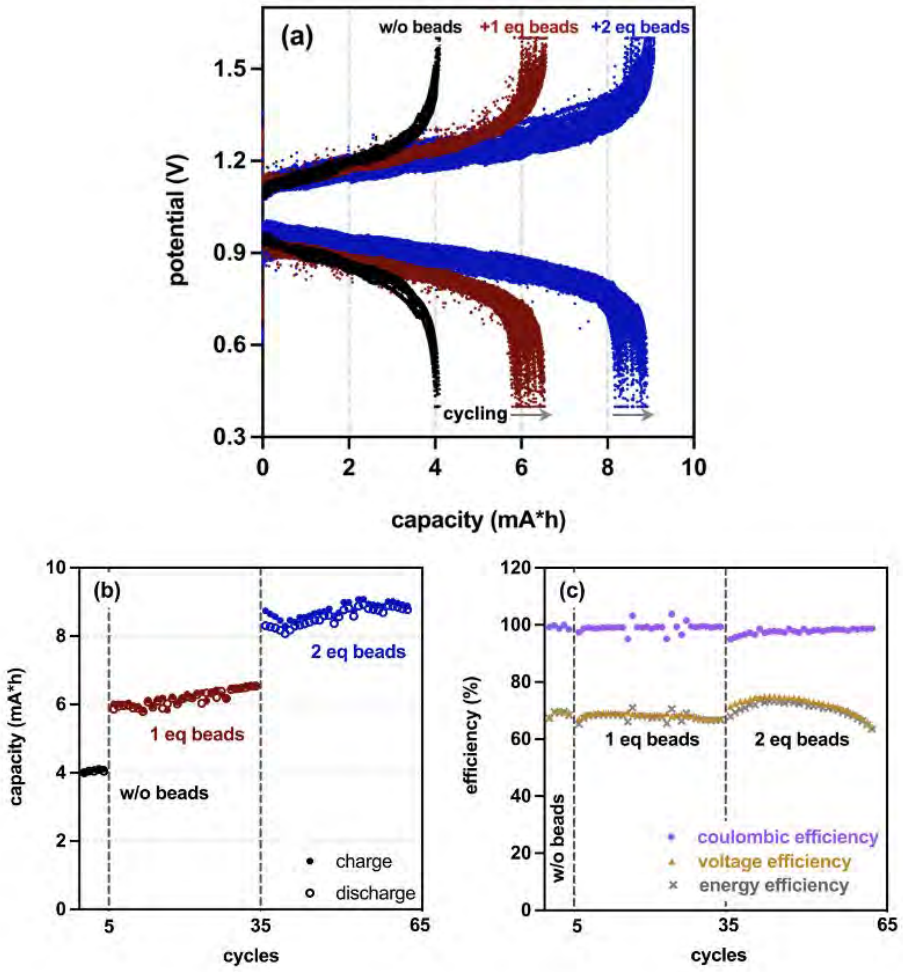

Figure 3.4. (a) Charge-discharge curves for the RMFB with no beads (black, 5 cycles), 1 equiv of beads (red, 30 cycles), and 2 equiv of beads (blue, 30 cycles), (b) capacity versus cycle number for each battery setup (capacity is increasing during cycling), and the (c) coulombic, voltaic, and energy efficiencies of each battery

A flow battery was set up with the initial conditions described above (12 mL of solution in each reservoir, CH_3CN, 0.50 M $[NBu_4][PF_6]$, 15 mM in both $[Bn\text{-}bpy\text{-}Me^{2+}][PF_6^-]_2$ and FcR) with no beads present. The RFB was charged and discharged galvanostatically at a current of 10 mA to cutoff voltages of 1.40 V (charge) and 0.50 V (discharge). The charge-discharge curves for 5 cycles are shown in Figure 3-4a. The theoretical capacity for this cell is 4.82 mAh, and 84% of that

capacity was attained with no beads present (see Figure 3-4b). Next the xPS-Fc beads were added to the catholyte reservoir and [xPS-bpy-Me^{2+}][PF_6^-]$_2$ beads were added to the anolyte reservoir. The quantity of beads added to each reservoir contained 0.180 mmol of redox-active moiety, such that the battery capacity would double if the full redox capacity of the beads was utilized. The RMFB was then cycled 30 times, and the charge-discharge curves are shown in Figure 3-4a while the capacities are shown in Figure 3-4b. After the addition of 1 equiv of beads, the average discharge capacity increased to 6.16 mAh, representing a 52% increase. When 2 equiv of beads were added, the average discharge capacity increased further to 8.56 mAh, representing a 112% increase over the battery without beads. Combined, these data demonstrate that charge can be efficiently stored on insoluble polymer beads and that charging can occur through solution-based mediators with matched redox potentials, highlighting the unique advantages of our generalizable RMFB system. Nevertheless, the net 4.51 mAh increase in capacity (for 2 equiv of beads) only corresponds to 47% of the theoretical 9.64 mAh capacity contained in those beads. Post-run CVs of the electrolyte solutions (Figure A2-16) show that both anolyte and catholyte solutions are essentially identical to those present before cycling, indicating that preferential crossover of the mediators, or their decomposition, is not an issue. Future studies will focus on identifying the inefficiencies (e.g., the interaction of current, flow rate, concentration of mediators, quantity of beads present, etc., and their effect on capacity utilization) with the long-term goal of further increasing these storage capacities.

3.3 Conclusion

The RMFB reported herein demonstrates an effective method for storing charge in a RFB on insoluble crosslinked polymer beads. Merrifield resin serves as a convenient substrate for the synthesis of ferrocene- and viologen-functionalized beads, and promises to be a versatile platform for the synthesis of polymer beads with other tethered redox-active moieties. These functionalized beads undergo redox exchange with their redox-matched soluble mediators on the relatively fast timescale of several minutes, which enables a Nernstian equilibration between beads and mediators in the reservoirs of a functioning RMFB. The RMFB architecture enables a high theoretical energy density without the requirement of high-concentration solutions, and without the possibility of crossover of the active material on the beads. While there is not yet complete utilization of the redox equivalents on the beads, studies are underway to modify the beads and/or flow battery operating parameters to capture the full capacity of the functionalized polymer beads.

3.4 References

(1) J. Noack, N. Roznyatovskaya, T. Herr, P. Fischer, *Angew. Chem. Int. Ed.* **2015**, *54*, 9776–9809.

(2) J. Winsberg, T. Hagemann, T. Janoschka, M. D. Hager, U. S. Schubert, *Angew. Chem. Int. Ed.* **2017**, *56*, 686–711.

(3) M. Ue, K. Ida, S. Mori, *J. Electrochem. Soc.* **1994**, *141*, 2989.

(4) R. M. Darling, K. G. Gallagher, J. A. Kowalski, S. Ha, F. R. Brushett, *Energy Environ. Sci.* **2014**, *7*, 3459–3477.

(5) Y. Yan, S. G. Robinson, M. S. Sigman, M. S. Sanford, *J. Am. Chem. Soc.* **2019**, *141*, 15301–15306.

(6) Y. Yan, T. P. Vaid, M. S. Sanford, *J. Am. Chem. Soc.* **2020**, *142*, 17564–17571.

(7) B. Silcox, J. Zhang, I. A. Shkrob, L. Thompson, L. Zhang, *J. Phys. Chem. C* **2019**, *123*, 16516–16524.

(8) X. Xing, Q. Liu, W. Xu, W. Liang, J. Liu, B. Wang, J. P. Lemmon, *ACS Appl. Energy Mater.* **2019**, *2*, 2364–2369.

(9) W. Duan, J. Huang, J. A. Kowalski, I. A. Shkrob, M. Vijayakumar, E. Walter, B. Pan, Z. Yang, J. D. Milshtein, B. Li, C. Liao, Z. Zhang, W. Wang, J. Liu, J. S. Moore, F. R. Brushett, L. Zhang, X. Wei, *ACS Energy Lett.* **2017**, *2*, 1156–1161.

(10) T. P. Vaid, M. S. Sanford, *Chem. Commun.* **2019**, *55*, 11037–11040.

(11) S. G. Robinson, Y. Yan, K. H. Hendriks, M. S. Sanford, M. S. Sigman, *J. Am. Chem. Soc.* **2019**, *141*, 10171–10176.

(12) J. Zhang, R. E. Corman, J. K. Schuh, R. H. Ewoldt, I. A. Shkrob, L. Zhang, *J. Phys. Chem. C* **2018**, *122*, 8159–8172.

(13) Y. K. Zeng, T. S. Zhao, L. An, X. L. Zhou, L. Wei, *J. Power Sources* **2015**, *300*, 438–443.

(14) R. A. Potash, J. R. McKone, S. Conte, H. D. Abruña, *J. Electrochem. Soc.* **2016**, *163*, A338–A344.

(15) W. Duan, R. S. Vemuri, J. D. Milshtein, S. Laramie, R. D. Dmello, J. Huang, L. Zhang, D. Hu, M. Vijayakumar, W. Wang, J. Liu, R. M. Darling, L. Thompson, K. Smith, J. S. Moore, F. R. Brushett, X. Wei, *J. Mater. Chem. A* **2016**, *4*, 5448–5456.

(16) J. Moutet, J. M. Veleta, T. L. Gianetti, *ACS Appl. Energy Mater.* **2021**, *4*, 9–14.

(17) K. H. Hendriks, S. G. Robinson, M. N. Braten, C. S. Sevov, B. A. Helms, M. S. Sigman, S. D. Minteer, M. S. Sanford, *ACS Cent. Sci.* **2018**, *4*, 189–196.

(18) A. Shrestha, K. H. Hendriks, M. S. Sigman, S. D. Minteer, M. S. Sanford, *Chem. Eur. J.* **2020**, *26*, 5369–5373.

(19) Q. Wang, S. M. Zakeeruddin, D. Wang, I. Exnar, M. Grätzel, Angew. *Chem. Int. Ed.* **2006**, *45*, 8197–8200.

(20) J. Ye, L. Xia, C. Wu, M. Ding, C. Jia, Q. Wang, *J. Phys. D: Appl. Phys.* **2019**, *52*, 443001.

(21) Q. Huang, H. Li, M. Grätzel, Q. Wang, *Phys. Chem. Chem. Phys.* **2013**, *15*, 1793–1797.

(22) J. R. Jennings, Q. Huang, Q. Wang, *J. Phys. Chem. C* **2015**, *119*, 17522–17528.

(23) E. Zanzola, C. R. Dennison, A. Battistel, P. Peljo, H. Vrubel, V. Amstutz, H. H. Girault, *Electrochim. Acta* **2017**, *235*, 664–671

(24) F. Pan, J. Yang, Q. Huang, X. Wang, H. Huang, Q. Wang, *Adv. Energy Mater.* **2014**, *4*, 1400567.

(25) J. Yu, M. Salla, H. Zhang, Y. Ji, F. Zhang, M. Zhou, Q. Wang, *Energy Stor. Mater.* **2020**, *29*, 216–222.

(26) Y. G. Zhu, Y. Du, C. Jia, M. Zhou, L. Fan, X. Wang, Q. Wang, *J. Am. Chem. Soc.* **2017**, *139*, 6286–6289.

(27) C. Jia, F. Pan, Y. G. Zhu, Q. Huang, L. Lu, Q. Wang, *Sci. Adv.* **2015**, *1*, e1500886.

(28) M. Zhou, Y. Chen, M. Salla, H. Zhang, X. Wang, S. R. Mothe, Q. Wang, *Angew. Chem. Int. Ed.* **2020**, *59*, 14286–14291.

(29) M. Zhou, Q. Huang, T. N. Pham Truong, J. Ghilane, Y. G. Zhu, C. Jia, R. Yan, L. Fan, H. Randriamahazaka, Q. Wang, *Chem* **2017**, *3*, 1036–1049.

(30) C. M. Wong, C. S. Sevov, *ACS Energy Lett.* **2021**, *6*, 1271–1279.

(31) A. R. Vaino, K. D. Janda, *J. Comb. Chem.* **2000**, *2*, 579–596.

(32) J. A. Kowalski, A. M. Fenton, B. J. Neyhouse, F. R. Brushett, *J. Electrochem. Soc.* **2020**, *167*, 160513.

(33) Z. Liang, N. H. Attanayake, K. V. Greco, B. J. Neyhouse, J. L. Barton, A. P. Kaur, W. L. Eubanks, F. R. Brushett, J. Landon, S. A. Odom, *ACS Appl. Energy Mater.* **2021**, *4*, 5443–5451.

Chapter 4: Open-Loop Recycling of Plasticized Poly(vinyl chloride) via Electro(de)chlorination

Portions of this chapter have been submitted:
Fagnani, D. E.; Kim, D.; Camarero, S. I.; Alfaro, J. F.; McNeil. A. J. Open-loop recycling of plasticized poly(vinyl chloride) via electro(de)chlorination

Fagnani, D. E. performed all of the electrosynthetic experiments, data analysis, created the figures, and wrote the original draft. Kim, D. performed all of the electroanalytical experiments, contributed to figure creation, data analysis, and editing the paper. The life cycle assessment was performed by Camarero, S. I.

4.1 Introduction

Achieving a circular economy for plastics will require recycling approaches that address each component of the complex waste stream.[1,2] To date, plastics recycling has predominantly involved mechanical recycling, which downgrades material quality and limits utility. Recycling rates (<10%)[3] are unlikely to improve with mechanical recycling alone, leading to calls for innovations in chemical recycling.[4,5] Closed-loop chemical recycling, in which polymers are first depolymerized (often to monomer) and then repolymerized to generate pristine material, has only been realized for hydrolyzable polymers such as poly(ethylene terephthalate) (PET). Whereas polymers with all-carbon backbones are not thermodynamically amenable to closed-loop methods.[6] These materials could be more practically recycled in an open-loop process, wherein polymers are broken down into smaller fragments that are feedstocks in other chemical processes. Nevertheless, the leading open-loop process, high-temperature anaerobic pyrolysis, is only useful for hydrocarbon polymers (e.g., polyethylene (PE), polypropylene (PP), and polystyrene (PS)). Meanwhile, poly(vinyl chloride) (PVC) is not recycled through any of these approaches and has

the lowest recycling rate in most countries (0% in the US) even though it has a high production rate.

These low recycling rates are concerning as PVC poses a known health risk in the environment.[8,9] In fact, PVC is ranked as the most hazardous polymer,[10] in part due to the plasticizing additives (e.g., phthalates),[11] which are carcinogenic and mutagenic, and the corrosive chlorine-containing byproducts formed upon degradation. Coincidentally, these additives and byproducts are also why PVC is difficult to recycle via mechanical approaches. Plasticizing additives are often 10–70% by mass, such that PVC must be separated from other plastics to avoid cross-contamination. Because complete separation is challenging, one of the most common PVC plasticizers ((2-ethylhexyl)phthalate, DEHP) has been found in other recycled plastics.[12] Even without additives, PVC is still not recycled by melt-processing or pyrolysis because hydrochloric acid (HCl) and other volatiles are rapidly eliminated upon heat treatment, which poses a safety hazard and corrodes equipment.[13] Although HCl elimination from PVC is problematic in high-temperature recycling processes, HCl itself is a useful reagent in many chemical reactions.[14] When reimagined from a synthetic point-of-view, PVC waste could instead be viewed as an easy-to-handle solid reagent that releases HCl on demand.

Herein, we describe an electrosynthetic approach that removes HCl from PVC and repurposes it. More specifically, we envisioned that chloride could be removed under electroreductive conditions and then directly used in a tandem electrooxidative chlorination reaction (Fig. 4-1a). Such paired-electrolysis reactions (strategic combinations of reduction and oxidation half-reactions) are often used to generate reactive halogen species (reductively at the cathode) and then halogenate a substrate (oxidatively at the anode).[15,16,17,18] We evaluated the

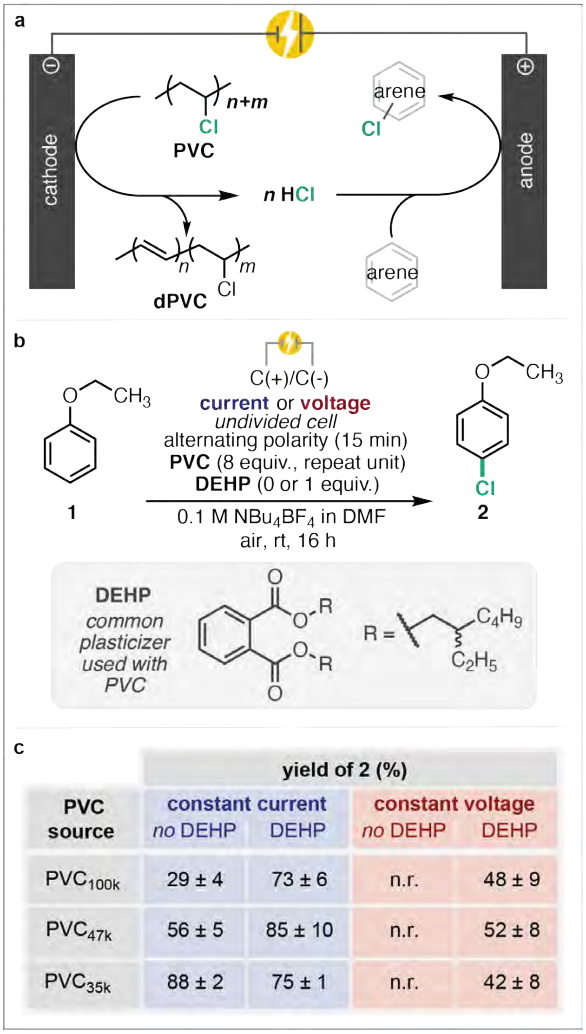

c

PVC source	yield of 2 (%) constant current *no* DEHP	constant current DEHP	constant voltage *no* DEHP	constant voltage DEHP
PVC_{100k}	29 ± 4	73 ± 6	n.r.	48 ± 9
PVC_{47k}	56 ± 5	85 ± 10	n.r.	52 ± 8
PVC_{35k}	88 ± 2	75 ± 1	n.r.	42 ± 8

Figure 4.1. Paired-electrolysis reaction, including (a) a general scheme for reductive dechlorination of PVC and oxidative chlorination of an arene, (b) the model reaction evaluated in this work, and (c) the effects of PVC molecular weight, presence of DEHP, and electrochemical conditions on the reaction yield. Yields are averages of two runs and measured by GC/MS (n.r. = no reaction).

proposed pair-electroysis herein and found that PVC can be used to produce value-added chlorinated organic products in a room temperature, air- and moisture-tolerant, single-pot process. We also show that the plasticizer DEHP[19] serves an advantageous role as a redox mediator, contrasting its adverse role in existent recycling technologies. The direct use of electrons is inexpensive, non-toxic, and has a small ecological footprint.[20,21,22] Moreover, a simplified life cycle assessment of only the materials and end of life stages revealed that the electrochlorination using PVC exhibited a 71% reduction in global warming potential (equiv. of CO_2 released per kg of chlorinated product) compared to the analogous process using HCl. Achieving circularity will require further optimization and include identifying uses for the dechlorinated polymer.

4.2 Results and Discussion

Reaction inspiration from the literature

The electroreduction of PVC was previously reported by a single group of scientists.[23,24,25] In their brief 1987 communication, Shapoval and coworkers noted solution-phase PVC degraded into polyene sequences (dechlorinated PVC, dPVC) by eliminating HCl upon exposure to negative voltage (–2.2 V versus saturated calomel electrode (SCE) on carbon electrodes.) The same reactivity occurred at a smaller potential with the plasticizer dioctyl phthalate present (–1.8 V versus SCE). This report demonstrates that PVC is susceptible to electroreductive dehydrochlorination and a common plastic additive may facilitate this reactivity, providing support for half of our envisioned paired-electrolysis reaction. A more recent report by Jiao and coworkers,[16] involving a paired-electrolysis reaction using dichloroethane as the chloride source, provided further support and inspiration for the enclosed work. Based on these precedents, we began evaluating the paired-electrolysis reaction using PVC as the chloride source.

Paired-electrolysis using PVC as a chloride source

The paired-electrolysis process was first tested in an undivided cell using ethoxybenzene (**1**) as the substrate (Fig. 4-1b). Dimethylformamide (DMF) was selected as the solvent because it has a wide electrochemical window and dissolves (or swells) all reaction components. Graphite was selected for both the cathode and anode because it is relatively inexpensive, and having identical electrodes enabled us to alternate the polarity to minimize polymer buildup on the electrodes. Tetrabutylammonium tetrafluoroborate (NBu_4BF_4) was chosen as the electrolyte so that the non-nucleophilic anion would not interfere with the dechlorination or chlorination reactions (compared to the halogen-containing electrolytes used by Shapoval and coworkers). The

reaction was screened using three different number-average molar masses (M_n) of PVC: PVC_{35k}, PVC_{47k}, and PVC_{100k}. Both PVC_{35k} and PVC_{47k} completely dissolved in DMF at room temperature, while PVC_{100k} partially dissolved and swelled. Reaction screening was first performed without the plasticizer DEHP. Under constant current electrolysis (galvanostatic conditions at 10 mA), the chlorination reaction proceeded to higher yields with the lower molar mass PVC (88% for PVC_{35k}), even though the total mass of polymer added was consistent in each case (Fig. 4-1c). This M_n dependence may be due to the increased diffusivity of smaller macromolecules compared to larger ones. Conformational differences may also play a role, wherein the larger macromolecules are more coiled and therefore have less accessible C–Cl bonds. In addition, reactions with the lower molar mass polymers will also have more individual chains (at the same mass loading), leading to more frequent collisions with the electrode. Nevertheless, with all PVC sources, build-up of black residue was observed on the electrodes after the reaction, suggesting that PVC was being reduced at the electrode surface.

Paired-electrolysis with plasticizer present

Next, the same chlorination reactions were performed with added DEHP to determine its impact. With DEHP, the reactions using PVC_{47k} and PVC_{100k} proceeded to higher yields (85% and 73%, respectively), while the already high yield using PVC_{35k} slightly decreased (to 75%). Little-to-no polymer residue was observed on the electrodes, suggesting that PVC was being indirectly reduced in solution rather than at the electrode surface. To further probe the effect of DEHP, the same reactions were performed under constant voltage (potentiostatic conditions at –1.3 V versus Ag/AgCl), which is the smallest voltage the reaction proceeded using an IKA ElectraSyn. Under these conditions, the chlorination reaction did not exhibit a dependance on the M_n when DEHP was

included (42–52% yield). Moreover, no reaction occurred at all without the DEHP (0% yield). The loss in reactivity without DEHP is important because it suggests that DEHP has an electrochemical effect on the paired-electrolysis reaction, possibly as a redox mediator. Under potentiostatic conditions, the substrate redox potentials must be matched to or smaller than the voltage set at the working electrode. The on/off switch in reactivity with and without DEHP indicates that PVC alone is unreactive at the set voltage. This requirement for DEHP differs under galvanostatic conditions, where the working potentials of the electrode automatically adjust to the potentials of the substrates in solution. In other words, without DEHP under galvanostatic conditions, the operating potential likely auto-adjusts to a larger voltage to reduce PVC directly. This effect of DEHP on the reduction potential of PVC was more closely evaluated in the subsequent mechanistic investigations.

PVC decreases reversibility of plasticizer reduction

To elucidate the mechanistic role of DEHP, several electroanalytical experiments were performed.[26] A cyclic voltammogram revealed that PVC alone does not show any redox activity within the solvent window. In contrast, DEHP undergoes two successive reductions ($E_{1/2}$ = –2.56 V and –2.74 V versus Ag/Ag^+) with a redox profile similar to one previously reported in acetonitrile (Fig. A3-12).[27] The first reduction is semi-reversible ($i_{pa}/i_{pc} < 1$) and the second reduction is essentially irreversible ($i_{pa}/i_{pc} = 0$), at a 100 mV/s scan rate. When PVC is added to the DEHP, the redox reversibility of DEHP decreases, suggesting electron transfer is occurring between the two species. The impact of PVC on the first reduction of DEHP was further analyzed following a protocol similar to the mediated electrochemical reduction of butyl halides.[28] More specifically, increasingly higher concentrations of PVC_{35k}, PVC_{47k}, or PVC_{100k} ([PVC] = 0–30

mM, repeat unit) were added to a solution of DEHP (1 mM) to vary the excess factor ([PVC]/[DEHP] = 0–30). Cyclic voltammetry of each solution was acquired (Fig. 4-2a). To reduce viscosity effects on the measurements, the overall concentration of PVC was kept low (see Table A3-15). The reversibility of the first DEHP reduction was plotted as a function of the excess factor, and this data was measured in triplicate over several different scan rates (25–500 mV/s) for each molar mass PVC (Figs A3-14,15,16). Representative data collected for PVC_{47k} is shown in Fig. 4-2b. The reversibility of the first DEHP reduction decreased with increasing concentration of PVC, suggesting that the singly reduced DEHP ($DEHP^{\bullet-}$) transfers an electron to PVC (Fig. 4-2c), resulting in a lower return oxidation current. This trend was magnified at slower scan rates, wherein the $DEHP^{\bullet-}$ has more time to encounter PVC, further decreasing the return oxidation current. Combined, these studies are consistent with the DEHP serving as a redox mediator in the PVC reduction.

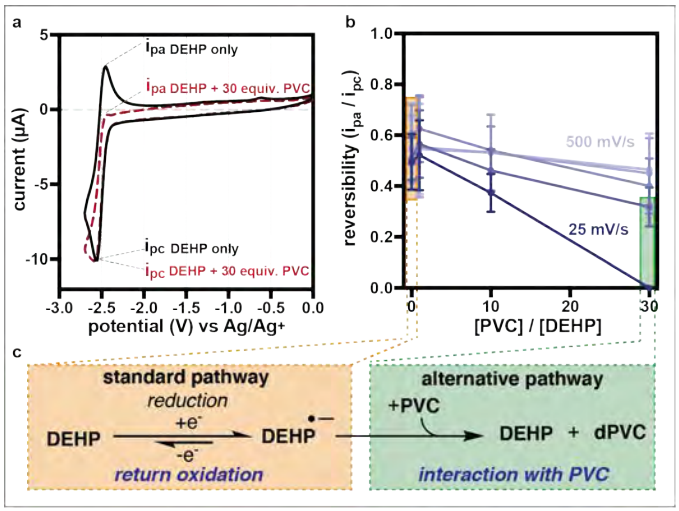

Figure 4.2. Representative cyclic voltammetry data. (a) CVs of the first reduction of DEHP and DEHP + 30 equiv. PVC47k collected at 100 mV/s, (b) redox reversibility as a function of excess factor ([PVC]/[DEHP]) measured in triplicate at several scan rates (25, 50, 100, 250, and 500 mV/s), and (c) scheme depicting the standard electrochemical pathway for the single reduction of DEHP and the alternative pathway when PVC is added.

Bulk electrolysis supports plasticizer-mediated PVC electroreduction

Further evaluation of DEHP's role as a redox mediator was obtained using a preparative-scale setup that mimicked the electrosynthesis conditions. More specifically, bulk electrolysis experiments of a divided cell containing DEHP and/or PVC at the cathode/working electrode and arene **1** at the anode/counter electrode were performed (Fig. 4-3a). These experiments were used to determine the voltage required to generate a set current (galvanostatic conditions, Fig. 4-3b) and vice versa (potentiostatic conditions, Fig. 4-3c). Under constant current conditions (–5 mA), DEHP alone (0.05 M) generated –2.6 V of overpotential until reaching its theoretical capacity (6.7 mA*h). GC/MS analysis after electrolysis showed that DEHP was partially degraded into 2-ethylhexanol and presumably other fragments that were not detectable, and that arene **1** remained unreacted at anode (Fig. A3-17). When PVC_{47k} (0.4 M, 8 equiv. repeat unit) was added to DEHP (0.05 M, 1 equiv.) and electrolyzed under the same current, a smaller overpotential (–2.5 V) was observed and the capacity was substantially increased (24 mA*h), indicating the mixed system generated more electrons than DEHP alone. Post-reaction analysis revealed less DEHP degradation than without PVC and quantitative conversion of arene **1** to chlorinated arene **2**. In contrast, bulk electrolysis on PVC alone required a much larger voltage (–3.5 V) to reach the same current. This voltage matches the solvent potential window, where solvent and/or electrolyte degradation may occur. Indeed, electrolyte degradation was observed by GC/MS analysis, which showed that tributylamine was formed at the cathode,[23] and arene **1** remained unreacted at the anode. The inability to chlorinate arene **1** with PVC alone in the bulk electrolysis setup differs from the galvanostatic synthetic trials, which proceeded with or without DEHP, albeit to different yields. It is possible that the exclusion of O_2 and H_2O in the bulk electrolysis setup, but not the synthetic trials, may have affected PVC degradation and arene chlorination. Bulk electrolysis

experiments were also performed under constant voltage to simulate potentiostatic electrosynthetic conditions (Fig. 4-3c). Each electrolysis was conducted for several min until a steady-state current was reached. When the cathode was set to –2.5 V, DEHP alone generated –3.8 mA of reduction current. Meanwhile, PVC alone produced a much smaller reduction current (–0.5 mA) at this voltage, indicating essentially no electrochemical activity. The largest reduction current (–5.5 mA) was generated when DEHP was mixed with PVC, indicating that more electrons are flowing through the system. This data again supports that PVC can only be reduced if DEHP is present when restricted to a voltage cutoff.

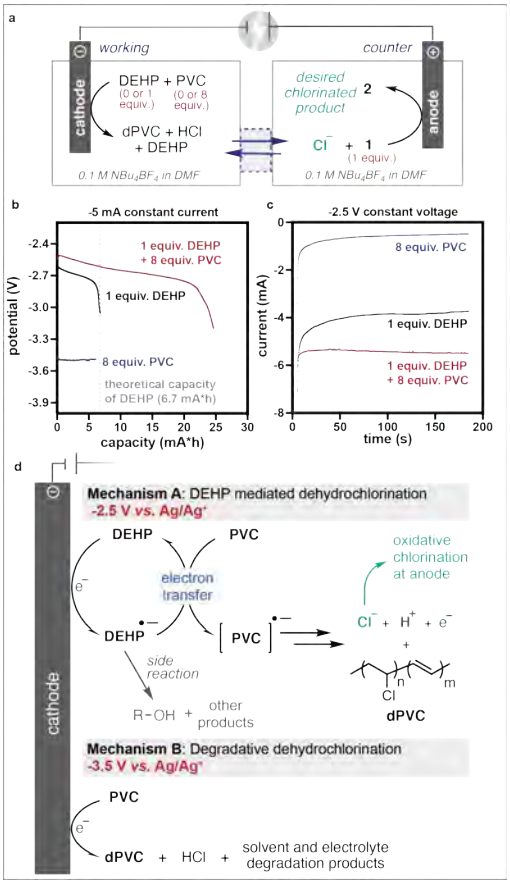

Figure 4.3. Bulk electrolysis data and proposed reductive dehydrochlorination mechanism. (a) Schematic of the bulk electrolysis setup and reactions occurring at each electrode, (b) voltage readout from constant current electrolysis, (c) current readout from constant voltage electrolysis, and (d) proposed mechanisms of the reductive dehydrochlorination reaction with and without DEHP.

Proposed mechanism

Taken together, the electrosynthesis and electroanalytical experiments suggest that two mechanisms are operable for PVC reduction (Fig. 4-3d). With DEHP, indirect reduction of PVC likely occurs, with DEHP serving as a redox mediator to shuffle electrons between the electrode and PVC. Without DEHP, PVC reduction requires a much larger voltage, and may be degraded by direct interaction at the electrode or from solvent/electrolyte degradation products that form at these extreme voltages.[23] It is important to note that electrolyte degradation was only observed under constant current conditions when DEHP was not included, in which mechanism B is the only option (Fig. A3-17).[29] In contrast, tributylamine was always observed in the reaction mixture when constant voltage was used, even with DEHP present, suggesting that both mechanisms are operating. Ultimately, the milder conditions offered by the galvanostatic DEHP-mediated pathway are preferred.

Upon reduction, chloride (Cl^-) is likely cleaved from PVC via a concerted electron transfer–bond breaking process, as is suggested for small molecule alkyl halides.[27] The resulting carbon-based radical on the polymer should be highly reactive, and may react with O_2 or H_2O, as has been observed previously,[30] or via another degradation pathway. The formation of both dPVC and the observed acidification of the reaction medium suggests that hydrogen is also released from the polymer upon reduction, likely as H^+(Fig. A3-18). Notably, the net release of HCl from PVC is a common reaction pathway with nucleophiles, heat, base, or acid.[31] In addition, control reactions wherein aqueous HCl is used in place of PVC during electrolysis proceed to high yields, further supporting the net release of HCl (Table A3-19). The released Cl^- ions ultimately chlorinate arene substrates at the anode. The mechanism for the electro-oxidative chlorination of arenes is still unresolved in the literature. Oxidation of Cl^- to either Cl_2 or hypochlorite (^-OCl) intermediates

have been proposed as the active chlorine species.[15,32,33,34,35] The fact that our process leads to higher yields when open to air rather than under N_2 supports a mechanism involving $^{-}$OCl. Control reactions wherein NaOCl was used as a chlorine source proceeded without applied potential, further supporting that $^{-}$OCl may be the active chlorine species (Table A3-19). Attempts to probe the involvement of radicals in this reaction were inconclusive; that is, radical trapping experiments with TEMPO inhibited the product formation in both PVC/DEHP and HCl control experiments (Table A3-19).

Substrate Scope

Chlorinated arenes can be found in pharmaceuticals, agrochemicals, disinfectants, dyes, electrical goods, and solvents.[36] To determine the scope of this method, we screened various aromatic and heteroaromatic substrates (Fig. 4-4). In an undivided cell, some substrates (e.g., anilides (**3**)) were consumed during electrolysis but did not yield any chlorinated products. In contrast, when HCl was used as the chlorine source, chlorinated anilide was formed. Combined, these studies suggest that some substrates may react directly with PVC and/or DEHP under the reductive conditions. To avoid this unintended reactivity, all subsequent reactions were performed in a divided cell. That is, the working and counter compartments were separated with an anion-exchange membrane, which minimizes crossover between the two sides. Compound classes that have been employed in other oxidative chlorination reactions were successfully employed herein using PVC as a chloride source.[15,17,33] These compounds include substituted benzenes, thiophenes, and several classes of N-heterocycles. Some compounds, including indole derivatives, generated lower yields because other oxidative reaction pathways (dimerization/oligomerization) competed with chlorination. Chlorinated pharmaceuticals **13** and **14** could be directly formed under these

conditions from their non-halogenated precursors. Though the yields need to be further optimized, the broad substrate scope and functional group tolerance is promising.

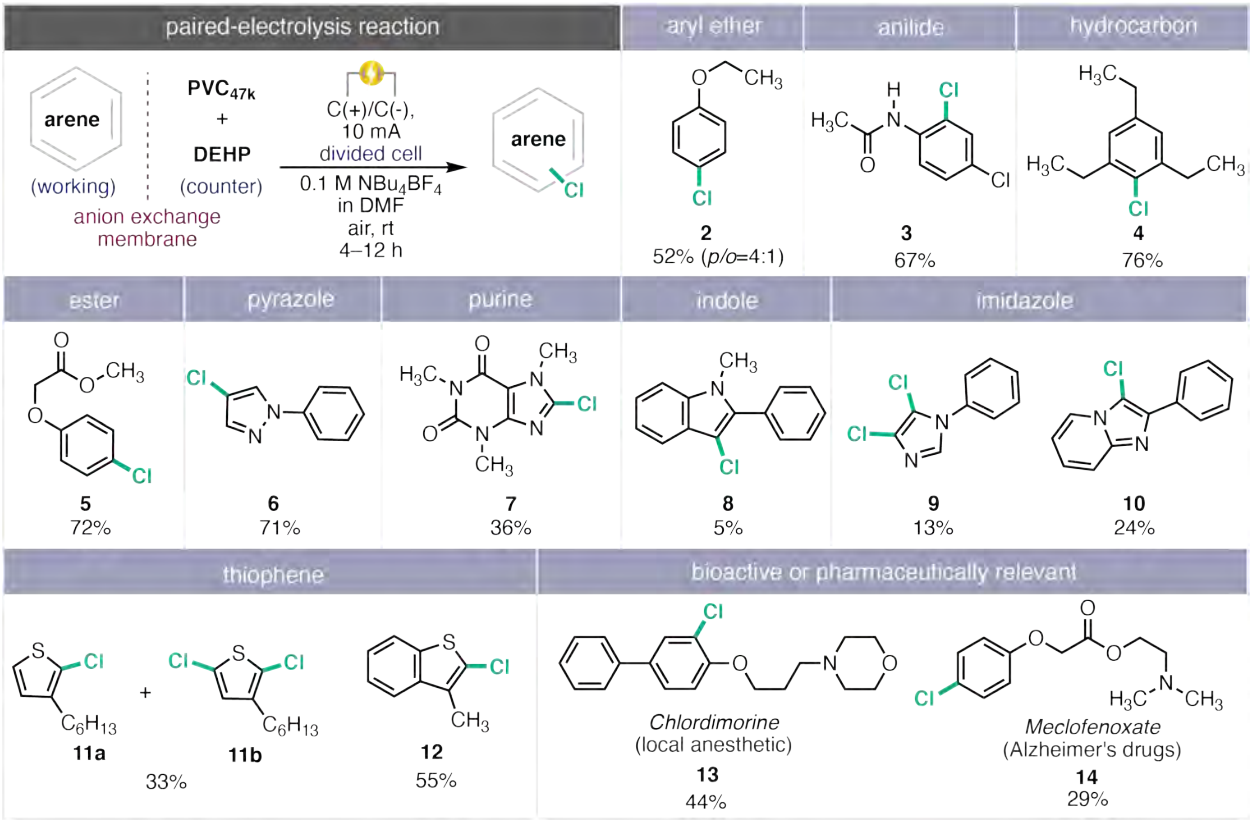

Figure 4.4. Schematic of divided-cell reaction setup and substrates investigated in this work, isolated yields are listed.

Commercial PVC tubing as chloride source

To determine whether this approach can be used with PVC waste, we employed PVC tubing (PVC_{tubing}) commonly used for liquid and gas transport in the research, medical, food, and beverage industries (Fig. 4-5a). The specific PVC_{tubing} used herein contained 32% by mass liquid additives, which was determined to be DEHP by ^{1}H and ^{13}C NMR analysis (Fig. A3-2,3,4). The solid material (PVC_{solid}) had a M_n of 83 kg/mol and was partially soluble in DMF. When the

galvanostatic trial reaction was performed using PVC_{solid} alone, a 32% yield of **2** was observed (Fig. 4-5b). This result is similar to the 29% yield observed with PVC_{100k} alone. When PVC_{tubing} was instead used, with the same total mass of polymer, the yield of **2** significantly increased to 63%. These results suggest that plasticized PVC waste can be used as is for the chloride source, without needing to add plasticizer. Although some manufactures are moving towards phthalate-free formulations,[37] this legacy additive is still prevalent in waste streams. Moreover, the dual-role of DEHP as plasticizer and redox mediator demonstrates that additives can serve one function during the lifetime of a plastic, and then be activated to serve a new function at the plastic's end-of-life. Moving forward, multi-purpose plastic additives can be imagined that facilitate end-of-life treatment of plastics, which could significantly improve the overall efficiency of plastics recycling.

Mixed plastic waste can be used

We also evaluated how well this reaction worked with other plastics present to simulate a mixed plastic waste stream (Fig. 4-5c). Excitingly, the overall yield of **2** was unchanged when the same mass of PET, PE, PP, and PS were added into the reaction mixture. Moreover, the plastic pieces made from PET, PE, and PP were insoluble in DMF and could be easily filtered out after the reaction was complete. These reactivity and solubility difference enables a facile separation PVC from other waste plastics.

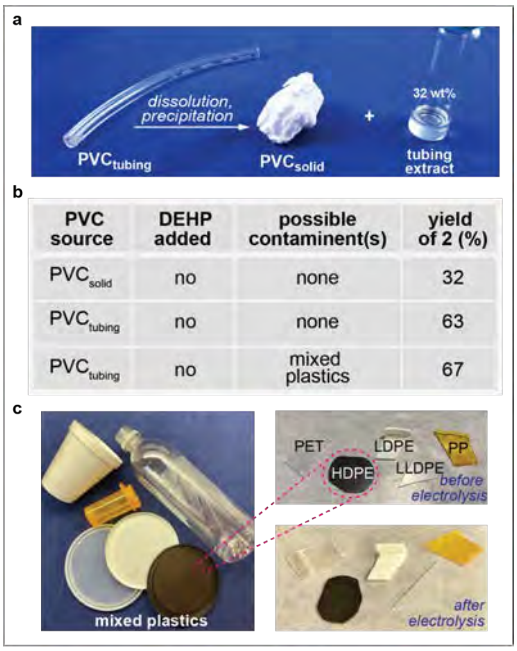

Figure 4.5. Evaluating real plastics in the paired-electrolysis reaction. (a) PVC tubing used to simulate PVC waste, (b) yields of galvanostatic trial reaction using arene 1 as the chlorination substrate, and (c) plastic items used to simulate a mixed plastics waste stream

Life cycle assessment

A preliminary comparative life cycle assessment (LCA) was conducted to estimate the potential environmental impacts of this approach.[38,39] More specifically, we sought an estimate of the decarbonization potential of the technology, which will help determine if this waste diversion strategy should be pursued further. Three different scenarios for the electrosynthetic production of **2** were compared. Scenario 1 uses HCl as the chloride source (3.2 equiv. Cl^- versus **2**). Scenario 2 uses PVC waste as the chloride source (8 equiv. Cl^- versus **2**) and the leftover dPVC is landfilled. Scenario 3 reflects a hypothetical, atom-economical situation in which PVC waste (1 equiv. Cl^- versus **2**) is used as the chloride source with a 100% dechlorination efficiency and the residual hydrocarbon content (dPVC) is pyrolyzed. (Note that in scenario 3, the hypothetically unused 7

equiv. of chloride is still landfilled.) For all three scenarios, the functional unit was defined as 1 kg of chlorinated arene **2**. The impact analysis was performed by tracking the greenhouse gas emissions using Global Warming Potential (GWP) metrics in kg CO_2 equiv. The relevant data was gathered from the literature and the Ecoinvent libraries in the LCA software, SimaPro v9.1.1. More details on the scope, system boundaries, assumptions, life cycle inventories, and life cycle impact assessment are presented in the appendix. It is important to note that this LCA only considered chloride source materials and end of life stages, under the assumption that the remaining stages and processes are constant for all scenarios.

With these caveats in mind, the LCA showed that using PVC waste as the chloride source (scenario 2) decreases the GWP by 71% compared to HCl (scenario 1) in the analyzed stages. This difference arises largely because HCl production has a GWP over 11 times higher than the supply chain of PVC waste. In scenario 3, in which PVC is fully dechlorinated and it is possible to pyrolyze the hydrocarbon content of the residual polymer, the CO_2 eq per kg of **2** decreases by 56% compared to HCl. The reason for the reduced impact (compared to scenario 2) is because mixed plastics pyrolysis has a higher GWP than landfilling due to it process energy requirements. Overall, these LCA results suggest that this electrochemical method is a promising approach for obtaining value from PVC waste. A more rigorous LCA will be performed in the future, alongside continued development of this process, including detailed characterization of all waste effluents. Future assessments with more environmental metrics could reveal benefits (e.g., in human toxicity or freshwater ecotoxicity) from transitioning from landfilling to chemical recycling of PVC waste.

4.3 Conclusion

Overall, this work demonstrates a proof-of-concept method for open-loop chemical recycling of PVC waste wherein the PVC is used as a reagent in a paired-electrolysis reaction to produce value-added organic products. These results also show that DEHP, which is currently used as a PVC plasticizer, functions as a redox mediator to improve the synthetic yields. Ultimately, the power of DEHP as a redox mediator is limited by the semi-reversibility of its reduction processes. The development of more stable redox mediators will enable a better understanding of the PVC reduction process and improve both mediator loading efficiencies and PVC dehydrochlorination percentages. Efforts along these lines are underway. Moreover, with further optimization, the partially or fully dehydrochlorinated PVC may also be valuable resource, potentially as a reactive polymer for hydrogenation (to polyethylene), crosslinking (elastomers), metathesis (depolymerization), or other functionalization reactions. The new functionality of DEHP uncovered in this work motivates a rethinking of plastic additives in the context of chemical recycling, wherein mediators are intentionally designed to facilitate recycling.

4.4 References

(1) L. T. Korley, T. H. Epps III, B. A. Helms B. A., A. J. Ryan, Toward polymer upcycling—adding value and tackling circularity. *Science,* **2021***, 373*, 66–69

(2) Ellen MacArthur Foundation. The new plastics economy: rethinking the future of plastics & catalyzing action. Ellen MacArthur Foundation, **2017**. https://www.ellenmacarthurfoundation.org/publications/the-new-plastics-economy-rethinking-the-future-of-plastics-catalysing-action (accessed on Aug 30, 2021).

(3) R. Geyer, J. R. Jambeck, K. L. Law, Production, use, and fate of all plastics ever made. *Sci. Adv.* **2017***, 3*, e1700782

(4) J. M. Garcia, M. L. Robertson, The future of plastics recycling. *Science,* **2017***, 358*, 870–872.

(5) I. Vollmer, M. J. F. Jenks, M. C. P. Roelands, R. J. White, T. van Harmelen, P. de Wild, G. P. van der Laan, F. Meirer, J. T. F. Keurentjes, B. M. Weckhuysen, Beyond mechanical recycling: giving new life to plastic waste. *Angew. Chem. Int. Ed.* **2020**, *59*, 15402–15423.

(6) G. W. Coates, Y. D. Y. L. Getzler, Chemical recycling to monomer for an ideal, circular polymer economy. *Nat. Rev. Mater.* **2020**, *5*, 501–516.

(7) EPA, Advancing sustainable matrials management: 2018 Tables and figures. https://www.epa.gov/sites/default/files/2021-01/documents/2018_tables_and_figures_dec_2020_fnl_508.pdf (accessed August 31, 2021)

(8) PVC has been detected in wastewater sludge. For ref, see: Y.-T. Zhang, W. Wei, J. Sun, Q. Xu, B.-J. Ni, Treatment and resource recovery long-term effects of polyvinyl chloride microplastics on anaerobic granular sludge for recovering methane from wastewater. *Environ. Sci. Technol.* **2020,** *54*, 9662–9671.

(9) PVC has been detected in aquatic life commonly consumed by humans. For ref, see: F. Ribeiro, E. D. Okoffo, J. W. O'Brien, S. Fraissinet-Tachet, S. O'Brien, M. J. Gallen, S. Samanipour, S. Leat Kaserzon, J. F. Mueller, T. S. Galloway, K. V. Thomas, Quantitative analysis of selected plastics in high commercial value Australian seafood by pyrolysis gas chromatography mass spectrometry. *Environ. Sci. Technol.* **2020**, *54*, 9408–9417.

(10) D. Lithner, A. Larsson, G. Dave, Environmental and health hazard ranking and assessment of plastic polymers based on chemical composition. *Sci. Total Environ.* **2011***,409*, 3309–3324.

(11) S. S. S. Rowdhwal, J. Chen. Toxic effects of di-2-ethylhexyl phthalate: An overview. *Biomed. Res. Int.* **2018**, 1750398.

(12) K. Pivenko, M. K. Eriksen, J. A. Martín-Fernández, E. Eriksson, T. F. Astrup, Recycling of plastic waste: Presence of phthalates in plastics from households and industry. *Waste management*, **2016**, *54*, 44–52.

(13) J. C. Worch, A. P. Dove, 100th Anniversary of Macromolecular science viewpoint: Toward catalytic chemical recycling of waste (and future) plastics. *ACS Macro Lett.* **2020***, 9*, 1494–1506.

(14) R. Lin, A. P. Amrute, J. Pérez-Ramírez, Halogen-mediated conversion of hydrocarbons to commodities. *Chem. Rev.* **2017***, 117*, 4182–4247.

(15) M. J. Llorente, B. H. Nguyen, C. P. Kubiak, K. D. Moeller, Paired electrolysis in the simultaneous production of synthetic intermediates and substrates *J. Am. Chem. Soc.* **2016***, 138*, 15110–15113.

(16) Y. Liang, F. Lin, Y. Adeli, R. Jin, N. Jiao, Efficient electrocatalysis for the preparation of (hetero)aryl chlorides and vinyl chloride with 1,2-dichloroethane. *Angew. Chem., Int. Ed.* **2019**, *58*, 4566– 4570.

(17) X. Dong, J. L. Roeckl, S. R. Waldvogel, B. Morandi, Merging shuttle reactions and paired electrolysis for reversible vicinal dihalogenations. *Science,* **2021***, 371*, 371, 507-514

(18) F. Liu, N. Wu, X. Cheng, Chlorination reaction of aromatic compounds and unsaturated carbon–carbon bonds with chlorine on demand. *Org. Lett.* **2021**, *23*, 3015–3020.

(19) J. N. Hahladakis, C. A. Velis, R. Weber, E. Iacovidou, P. Purnell, An overview of chemical additives present in plastics: Migration, release, fate and environmental impact during their use, disposal and recycling. *J. Hazard. Mater.* **2018***, 334*, 179–199.

(20) J. C. Siu, N. Fu, S. Lin, Catalyzing electrosynthesis: A homogeneous electrocatalytic approach to reaction discovery. *Acc. Chem. Res.* **2020**, *53*, 3, 547–560.

(21) S. Möhle, M. Zirbes, E. Rodrigo, T. Gieshoff, A. Wiebe, S. R. Waldvogel, Modern electrochemical aspects for the synthesis of value-added organic products. *Angew. Chem. Int. Ed.* **2018**, 57, 6018 –6041.

(22) A. Wiebe, T. Gieshoff, S. Möhle, E. Rodrigo, M. Zirbes, S. R. Waldvogel, Electrifying organic synethsis. *Angew. Chem. Int. Ed.* **2018**, *57*, 5594 –5619.

(23) G. S. Shapoval, A. P. Tomilov, A. A. Pud, K. V. Batsaolva, The electrochemical reductive degradation of PVC. *Polym. Sci.* **1987***, 29***,** 1564–1572.

(24) Y. V. Kontsur, G. S. Shapoval, A. A. Pud, Indirect electrochemical dehydrochlorination of polyvinylchloride. *J. Macromol. Sci. A,* **1995***, 32*, 687–693.

(25) Y. V. Kontsur, G. S. Shapoval, A. A.Pud, Electrochemical dehydrohalogenation of poly(vinylchloride) in pyridine. *Polym. Degrad. Stab.* **1998***, 60*, 515–516.

(26) R. Francke, D. R. Little, Redox catalysis in organic electrosynthesis: basic principles and recent developments. *Chem. Soc. Rev.* **2014***, 43*, 2492–2521.

(27) S. J. L. Lauw, J. H. Q. Lee, M. E. Tessensohn, W. Q. Leong, R. D. Webster, The electrochemical reduction of di-(2-ethylhexyl) phthalate (DEHP) in acetonitrile. *J. Electroanal. Chem.* **2017**, *794*, 103–111.

(28) C. P. Andrieux, I. Gallardo, J. M. Savaent, K.-B. Su. Dissociative electron transfer. Homogeneous and heterogeneous reductive cleavage of the carbon-halogen bond in simple aliphatic halides *J. Amer. Chem. Soc.* **1986***, 108***,** 638–647.

(29) C. E. Dahm, D. G. Peters,. Electrochemical reduction of tetraalkylammonium tetrafluoroborates at carbon cathodes in dimethylformamide. *J. Electroanal. Chem.* **1996***, 402*, 91–96.

(30) C. Decker, Oxidative degradation of poly(vinyl chloride). *J. Appl. Polym. Sci.* **1976***, 20*, 3321–3336.

(31) S. Moulay, Chemical modification of poly(vinyl chloride)—Still on the run. *Prog. Polym. Sci.* **2010***, 35*, 303–331.

(32) L. Appelbaum, D. Danovich, G. Lazanes, M. Michman, M. Oron, An electrochemical aromatic chlorination, comparison with electrophilic reaction. *J. Electroanal. Chem.* **2001***, 499*, 39–47.

(33) Z. Zhou, Y. Yuan, Y. Cao, J. Qiao, A. Yao, J. Zhao, W. Zuo, W. Chen, A. Lei, Synergy of anodic oxidation and cathodic reduction leads to electrochemical C—H halogenation. *Chin. J. Chem.* **2019***, 37*, 611–615.

(34) Yuan, Y.; Yao, A.; Zheng, Y.; Gao, M.; Zhou, Z.; Qiao, J.; Hu, J.; Ye, B.; Zhao, J.; Wen, H.; Lei, A. Electrochemical Oxidative Clean Halogenation Using HX/NaX with Hydrogen Evolution. *iScience* **2019**, *12*, 293– 303

(35) Y.-H. So, Selective chlorination of toluene by anodic oxidation. *J. Org. Chem.* **1985***, 50,* 5895–5896.

(36) U. Beck, E. Löser Chlorinated Benzene and Other Nucleus-Chlorinated Aromatic Hydrocarbons. In Ullmann's Encyclopedia of Industrial Chemistry, Wiley-VCH (2011).

(37) http://www.tygons3tubing.com (accessed August 26, 2021)

(38) ISO 14040:2006(en), Environmental management — Life cycle assessment — Principles and framework. https://www.iso.org/obp/ui/#iso:std:iso:14040:ed-2:v1:en.

(39) A simplified assessment was performed because this electrochemical process is still in the early development stage

Chapter 5: Conclusions and Future Directions

Renewable energy technologies are methods of capturing, storing, and using energy, that have less environmental impact than traditional energy technologies such as coal or petroleum. To establish a system for encouraging the use of renewable energy sources such as solar, wind, bioenergy, and hydropower, it is essential to understand their characteristics and challenges to developing their technologies.

In this thesis, we conducted three different studies and discussed 1) how a single copolymer containing a conjugated poly(3-hexylthiophene) backbone and fullerene-functionalized side-chains prevented phase separation in thin films and devices and enhanced thermal stability in photovoltaic devices; 2) how a non-aqueous, redox-matched, flow battery design achieved a high effective concentration of redox active materials in insoluble polymer beads; and 3) how we repurposed plasticized poly(vinyl chloride) via electro(de)chlorination.

In chapter 2, we investigated a random sequence copolymer for stabilizing the active layer morphology and enhancing thermal stability of organic photovoltaics. Due to the flexibility, light weight, inexpensive cost, and other advantages of organic photovoltaics, the market is growing rapidly.[1] However, device lifetime and thermal stability remain as challenges for commercialization. Previously McNeil group found that random sequence fullerene-functionalized poly(3-hexylthiophene) copolymer additives stabilized electron-donor/electron-

acceptor blends morphology. In this chapter, we used same random sequence copolymer for stabilizing morphology in the blends of three high-performing donor polymers (PTB7, PTB7-Th, and PffBT4T-2OD) with $PC_{71}BM$ to test the copolymer as a general blend additive. Optical microscopy data revealed that the copolymer-added thin film blends had suppressed micron-scale aggregation after annealing, suggesting that the copolymer may be a general stabilizer. Especially, out of the three donor polymers, PffBT4T-2OD showed the highest 40% area percent of $PC_{71}BM$ aggregation without copolymer. However, the area percent significantly dropped to 2% when the copolymer was added. Therefore, we fabricated the organic photovoltaics with the PffBT4T-2OD electron-donor to study the effect in the active layer. Though the phase separation was also suppressed in photovoltaic devices, we observed lower initial power conversion efficiencies (PCEs) were observed, due to reduced absorption and electron current with the copolymer. For annealed devices, the PCE decreased within 30 min annealing time in both with or without copolymer, although the PCE loss was smaller for devices with the copolymer. In addition, micron-scale aggregates only formed in devices without the copolymer after 180 min of annealing resulting failure to measure device performances while copolymer-containing devices survived until 180 min. Overall, these results suggest that the copolymer could be used as a general additive to stabilize the morphology of donor/acceptor blends.

Although, we found that enhanced stability from this strategy, future design strategies must address both device efficiency and thermal stability at the same time. We tested our copolymer for only one polymer donor – fullerene acceptor device, various types of donor-acceptor pairs could be explored in the future. For example, polymer donor-polymer acceptor[2], polymer donor-small

molecule acceptor[3], small molecule donor-polymer acceptor[4], and small molecule donor-small molecule acceptor[5] have been developed in recent years to improve device power conversion efficiency. We anticipate our strategy of using single copolymer containing donor and acceptor moiety in one molecule could play a role in stabilizing morphology in other pairs to improve device performance and thermal stability by matching polymer backbone of electron donor and copolymer.

In chapter 3, we discussed a redox matched flow battery (RMFB) by using insoluble polymer beads. After we generated an energy from sustainable source, we need to consider storing method due to inherent intermittency of renewable sources and mismatch of supply and demand during the day and night. A redox flow battery (RFB) is a type of secondary battery where chemical energy is provided by two redox-active materials dissolved in liquids which flowed through the system on separate sides of a membrane. Because the two redox-active materials, anolyte and catholyte, solutions are contained in external tanks, RFBs can be scaled easily and inexpensively to store large amounts of energy. Although redox flow battery is considered promising technology because of its design flexibility, safety, and scalability, it remains challenges that we need high concentration solution to attain large energy density and want to prevent crossover of the redox-active species.

In this chapter, we demonstrated a new type of nonaqueous RMFB by using a bulk of charge storage in a RFB on insoluble crosslinked polymer beads. Charge was stored in redox-active species which are covalently attached to the polymer beads and the beads sat on the frit in the reservoirs instead of circulating. We chose Merrifield resin as a polymer support for the

preparation of ferrocene and viologen functionalized beads, and two redox-matched mediators which have same structures of each polymer-supported redox active species as redox shuttles. From monitoring redox exchange reactions by using microelectrode, we demonstrated that there was fast enough charge transfer between polymer-supported redox-active moieties and each mediator to reach redox equilibrium. We investigated three different membranes as potential mebrane for RMFB, and Fumasep anion exchange membrane showed slowest crossover rate implying minimal loss of capacity from mediator solution. When 1 or 2 equiv. of functionalized beads were added into RMFB, the average discharge capacity increased 52% or 112%, respectively, which means the RMFB utilized a high energy density without the requirement of high-concentration solutions.

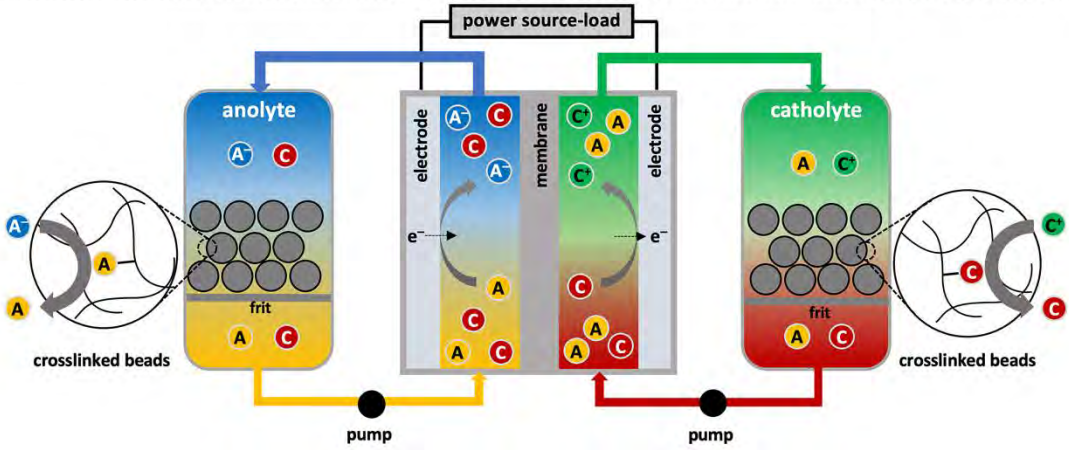

Scheme 5-1. Nonaqueous redox-matched flow battery

While there is not 100% complete utilization of the redox equivalents on the beads, studies are underway to modify the beads to investigate permeability, redox active species to achieve larger redox potential window, or flow battery operating parameters to achieve the higher capacity

utilization. First future idea is modifying the bead sizes. Current mesh size of Merrifield resin is 200-400 mesh which is having around 50 μm diameter. When the functionalized beads were added above 2 equiv., the stack of the beads started to prevent flowing of solution and clogged, resulting in difficulties for trying high equiv. (> 2 equiv.) RMFB system. We assume smaller mesh sizes bead (larger bead sizes over 100 μm) could achieve better permeability even with higher stack of the beads in the reservoir. Another idea is making nonaqueous RMFB with a larger potential difference between catholyte and anolyte. Two mediators from reported RMFB in chapter 3 have a redox potential difference of 1.04 V, which could be substantially improved by utilizing alternative anolytes and catholytes. One possibility for an alternative catholyte group is tris(dialkylamino)cyclopropenium. These moieties have good stability and more positive oxidation potential (0.8 V vs Fc/Fc^+) compared to ferrocene monomethylester (0.3 V vs Fc/Fc^+). Last idea is an aqueous RMFB. Aqueous redox-flow batteries have an advantage over nonaqueous systems because of nonflammable solvent (water). There may also be some cost advantages.[6] As such, we are interested in expanding this RMFB approach to include aqueous systems as well. To accomplish this goal, several types of hydrophilic cross-linked polymer beads with pendant groups amenable to functionalization have been reported.[7] These can serve as hydrophilic versions of the Merrifield resin, and when functionalized with redox-active moieties will serve as the stationary phase in an aqueous mediated redox-flow battery.

In chapter 4, we suggested new recycling approach for repurposing plasticized, polyvinyl chloride (PVC) via electro(de)chlorination. PVC is chlorine-containing polymer which is one of the most widely used such as pipes, profiles for windows, medical devices, and so on. At the end

of their life cycle, large amounts of plastic waste are produced, so there is environmental interest to recycle or repurpose this PVC waste. In this chapter, we demonstrated a new approach of open-loop chemical recycling of PVC waste by using paired-electrolysis with reductive dichlorination of PVC as well as oxidative chlorination of an arene to produce value-added chlorinated products. For enhancing electrodechlorination, we investigated (2-ethylhexyl)phthalate (DEHP) which is currently used as a PVC plasticizer as a redox mediator to improve the synthetic yields. DEHP poses health risk that it can increase the risk of cancer and birth defects by harming male reproductive system.[8] In cyclic voltammetry data, when PVC was added into DEHP solution, the returning oxidation current was significantly reduced in slow scan rate, indicating there was an electron transfer between two species supporting the role of DEHP as a redox mediator in the PVC reduction. Bulk electrolysis indicated that the combination of DEHP and PVC generated more electron than DEHP alone.

We covered only first semi-reversible reduction of DEHP in this chapter, future screening with more negative potential or investigating new functionality of DEHP (with more eletron-withdrawing or electron-donating group) could give us better understanding of the role of DEHP as a mediator in PVC reduction. We expect understanding the role of DEHP in PVC reduction as a redox mediator could help to improve PVC dehydrochlorination percentages as well as use polymer additives for intentional design to facilitate recycling. With further optimization, the partially or fully dehydrochlorinated PVC may also be valuable resource, potentially as a reactive polymer for hydrogenation, crosslinking, metathesis.

In overall, this chapter described our efforts to address sustainable development in plastic waste disposal. We expect that this work can become part of a new clean system and sustain improved quality of plastic waste management into the future.

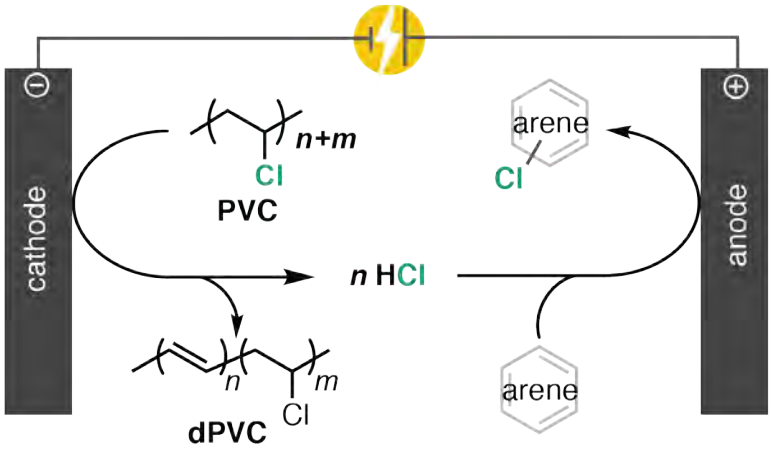

Scheme 5-2. General scheme of paired-electrolysis reaction for reductive dechlorination of PVC and oxidative chlorination of an arene.

References

(1) Riede, M.; Spoltore, D.; Leo, K. Organic Solar Cells-The Path to Commercial Success. *Adv. Energy Mater.* **2021**, *11*, 2002653

(2) Samson, S.; Rech, J.; Perdigon-Toro, L.; Peng, Z.; Shoaee, S.;, Ade, H.; You, W. Organic Solar Cells with Large Insensitivity to Donor Polymer Molar Mass across All Acceptor Classes. *ACS Applied Polymer Materials*, **2020**, *2*, 5300-5308.

Du, J.; Hu, K.; Zhang, J.; Meng, L.; Yue, J.; Angunawela, I.; Li, Y. Polymerized small molecular acceptor based all-polymer solar cells with an efficiency of 16.16% via tuning polymer blend morphology by molecular design. *Nature communications*, **2021**, *12*, 1-10.

(3) Jiang, K.; Wei, Q.; Lai, J. Y. L.; Peng, Z.; Kim, H. K.; Yuan, J.; Yan, H. Alkyl chain tuning of small molecule acceptors for efficient organic solar cells. *Joule*, **2019**, *3*, 3020-3033.

Eastham, N. D.; Dudnik, A. S.; Aldrich, T. J.; Manley, E. F.; Fauvell, T. J.; Hartnett, P. E.; Marks, T. J. Small molecule acceptor and polymer donor crystallinity and aggregation effects on microstructure templating: Understanding photovoltaic response in fullerene-free solar cells. *Chemistry of Materials*, **2017**, *29*, 4432-4444.

Samson, S.; Rech, J.; Perdigon-Toro, L.; Peng, Z.; Shoaee, S.; Ade, H.; You, W. Organic Solar Cells with Large Insensitivity to Donor Polymer Molar Mass across All Acceptor Classes. *ACS Applied Polymer Materials*, **2020**, *2*, 5300-5308.

(4) Miao, J.; Meng, B.; Ding, Z.; Liu, J.; Wang, L. Organic solar cells based on small molecule donors and polymer acceptors operating at 150° C. *Journal of Materials Chemistry A*, **2020**, *8*, 10983-10988.

Zhang, Z.; Miao, J.; Ding, Z.; Kan, B.; Lin, B.; Wan, X.; Wang, L. Efficient and thermally stable organic solar cells based on small molecule donor and polymer acceptor. *Nature communications*, **2019**, 10, 1-8.

(5) Oosterhout, S. D.; Savikhin, V.; Zhang, J.; Zhang, Y.; Burgers, M. A.; Marder, S. R.; Toney, M. F. Mixing behavior in small molecule: fullerene organic photovoltaics. *Chemistry of Materials*, **2017**, *29*, 3062-3069.

Zhou, R.; Jiang, Z.; Yang, C.; Yu, J.; Feng, J.; Adil, M. A.; Wei, Z. (2019). All-small-molecule organic solar cells with over 14% efficiency by optimizing hierarchical morphologies. *Nature communications*, **2019**, *10*, 1-9.

(6) Sánchez-Díez, E.; Ventosa, E.; Guarnieri, M.; Trovò, A.; Flox, C.; Marcilla, R.; Ferret, R. Redox flow batteries: Status and perspective towards sustainable stationary energy storage. *Journal of Power Sources*, **2021**, *481*, 228804.

(7) Loo, S. L.; Vásquez, L.; Athanassiou, A.; Fragouli, D. Polymeric Hydrogels—A Promising Platform in Enhancing Water Security for a Sustainable Future. *Advanced Materials Interfaces*, **2021**, *8*, 2100580.

Blöhbaum, J., Paulus, I., Pöppler, A. C., Tessmar, J., & Groll, J. Influence of charged groups on the cross-linking efficiency and release of guest molecules from thiol–ene cross-linked poly (2-oxazoline) hydrogels. *Journal of materials chemistry B*, **2019**, *7*, 1782-1794.

Parhi, R. Cross-linked hydrogel for pharmaceutical applications: a review. *Advanced pharmaceutical bulletin*, **2017**, *7*, 515-530.

(8) Meeker, J. D., Sathyanarayana, S., & Swan, S. H. Phthalates and other additives in plastics: human exposure and associated health outcomes. Philosophical transactions of the royal society B: biological sciences, **2009**, *364*, 2097-2113.

Appendices

Appendix 1: Supporting Information for Chapter 2

A1.1 Polymer and Fullerene Chemical Structures

Chart A1-1. Chemical structures of the donor polymers poly[[4,8-bis[(2-ethylhexyl)oxy]benzo[1,2-b:4,5-b0]dithiophene-2,6-diyl][3-fluoro-2-[(2-ethylhexyl)-carbonyl]-thieno-[3,4-b]thiophene-diyl]] (PTB7), poly[4,8-bis(5-(2-ethylhexyl)thiophen-2-yl)benzo[1,2-b;4,5-b′]dithiophene-2,6-diyl-alt-(4-(2-ethylhexyl)-3-fluorothieno[3,4-b]thiophene-)-2-carboxylate-2-6-diyl)] (PTB7-Th), and poly[(5,6-difluoro-2,1,3-benzothiadiazol-4,7-diyl)-alt-(3,3‴-di(2-octyldodecyl)-2,2′;5′,2″;5″,2‴-quaterthiophen-5,5‴-diyl)] (PffBT4T-2OD), the acceptor phenyl-C_{71}-butyric acid methyl ester ($PC_{71}BM$), and the copolymer, poly(3-hexylthiophene) (P3HT), and diiodooctane (DIO) additives used in this work

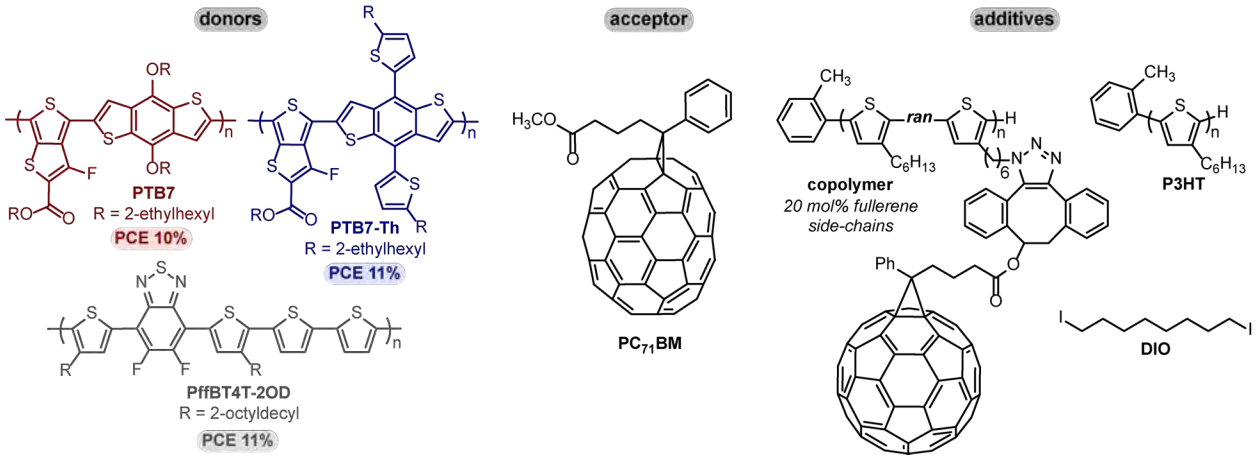

A1.2 Materials

Flash chromatography was performed on SiliCycle silica gel (40–63 μm). Thin-layer chromatography was performed on MACHEREY-NAGEL TLC plates (pre-coated with 0.20 mm silica gel 60 with fluorescent indicator UV254). Fused silica wafers were purchased from University Wafer and cut into square substrates (1.5 x 1.5 cm). Glass and indium tin oxide (ITO)/glass substrates (1.8 x 1.8 x 0.7 cm, ITO 15 Ω) were purchased from Luminescence Technology Corporation. Pure-C on copper TEM grids were purchased from Ted Pella Corporation.

$Ni(COD)_2$ was purchased from Strem Chemicals. Lithium diisopropylamide (LDA, 2.0 M in THF/n-heptane/ethylbenzene, 59/28/13 v/v) was purchased from Sigma Aldrich. 2,5-Dibromo-3-hexylthiophene (DB3HT) was purchased from ArkPharm and purified by dissolving in hexanes, stirring for 2 h with decolorizing carbon, filtering through a plug of silica gel, and concentrating in vacuo. N-bromosuccinimide (NBS) was purchased from Sigma Aldrich, recrystallized from water, and dried over P_2O_5. Isopropylmagnesium chloride (iPrMgCl, 2.0 M in THF, 25 mL), diiodooctane (DIO) (98%, containing Cu as a stabilizer), and PEDOT:PSS (3–4% suspension in H_2O) were purchased from Sigma Aldrich. Compounds **S1–S9**, **ran20$_{Br}$**, **ran20$_{N3}$**, and **copolymer** were prepared using modified literature procedures.[1] All monomer solutions for polymerizations were titrated with salicylaldehyde phenylhydrazone to obtain the active Grignard concentration.[2]

The polymers **PTB7** (lot # YY13230DC), **PTB7-Th** (lot # YY171760CH), and **PffBT4T-2OD** (lot # YY13086CB and YY1325OCB) were purchased from 1-Material – Organic Nano Electronic. [6,6]-phenyl-C_{61}-butyric acid methyl ester ($PC_{61}BM$, lot # RC160930) and [6,6]-phenyl-C_{71}-butyric acid methyl ester ($PC_{71}BM$, lot # TC200702) were purchased from Nano-C Inc. *N*-, Molybdenum(VI) oxide, (MoO_3, 99.97% trace metals basis), zinc acetate dihydrate ($Zn(OAc)_2Ÿ2H_2O$), and 2-methoxyethanol (2ME) were purchased from Sigma Aldrich. Silver pellets (Ag, 99.99% purity) were purchased from Kurt J. Lesker Company.

Tetrahydrofuran (THF) was dried and deoxygenated using an Innovative Technology (IT) solvent purification system composed of activated alumina, a copper catalyst, and molecular sieves. All water used was deionized. All other reagent grade materials and solvents were purchased from

Sigma Aldrich, Acros Organics, Alfa Aesar, or Fisher and used without further purification unless otherwise noted. The glovebox in which synthetic procedures were carried out was an MBraun LABmaster 130 with a N_2 atmosphere. The glovebox in which device fabrication was carried out was an ultra-high puritiy (<1ppm of H_2O and O_2) glovebox from LC Technology Solutions, INC.

A1.3 General Experimental

NMR Spectroscopy: Unless otherwise noted, ^{1}H, ^{13}C and ^{31}P NMR spectra were acquired at room temperature in deuterated solvents. For ^{1}H NMR spectra, a relaxation delay of 1 s was used for small molecules and 10 s was used for polymers. For ^{1}H and ^{13}C NMR spectra, the chemical shift data are reported in units of δ (ppm) relative to tetramethylsilane (TMS) and referenced to residual solvent. For ^{31}P spectra, the chemical shift data are reported in units of δ (ppm) relative to 85% H_3PO_4 in H_2O. Multiplicities are reported as follows: singlet (s), doublet (d), doublet of doublets (dd), triplet (t), quartet (q), multiplet (m), broad signal (br).

High Resolution Mass Spectrometry (HRMS): High-resolution mass spectrometry data were obtained on a Micromass AutoSpec Ultima Magnetic Sector mass spectrometer.

Fourier-Transform Infrared (FTIR) Spectroscopy: FTIR spectroscopy data were obtained on a Thermo-Nicolet IS-50 using the attenuated total reflectance (ATR) accessory on neat samples.

Gas Chromatography: Gas chromatography was carried out using a Shimadzu GC 2010 containing a Restek RXI-5MS (crossbound 5% diphenyl–95% dimethyl polysiloxane; 15 m, 0.25 mm ID, 0.25 μm df) column.

Size-Exclusion Chromatography (SEC): For SEC analysis, all polymers were dried under vacuum overnight, dissolved (~0.5 mg polymer/mL) in THF spiked with trace toluene (<1 vol%) with mild heating if necessary, and filtered through a 0.2 μm PTFE filter.

SEC was performed with THF as the eluent at 40 °C and at a flow rate of 1.0 mL/min on two different instruments. The data presented correspond to the absorbance at 254 nm with the maximum intensity normalized to 1.

SEC #1: Malvern Viscotek GPCMax VE2001 equipped with two Viscotek LT-5000L 8 mm (ID) × 300 mm (L) columns, and Viscotek TDA 305 and Viscotek PDA detectors. Apparent molar masses were calculated using 9 polystyrene standards from 377,400 g/mol to 580 g/mol.

SEC #2: Shimadzu GPC/SEC equipped with two Styragel HT 7.8 mm (ID) x 300 mm (L) columns and a PSS Gram column 8 mm (ID) x 300 mm (L), and a RI (refractive index) detector and an UV diode array detector. Apparent molar masses were calculated using polystyrene standards from 1,000,000 g/mol to 92 g/mol.

SEC #3: Same instrument as #2 (Shimadzu GPC/SEC) equipped with different columns (three Phenomenex Phenogel™ 10 µm Linear (2), LC Column 300 x 7.8 mm). Apparent molar masses were calculated using polystyrene standards from 1,000,000 g/mol to 92 g/mol.

Differential Scanning Calorimetry (DSC): DSC was performed under N_2 on a TA Instruments DSC Q2000 equipped with a TA RCS cooling accessory. Neat solid samples (~4–5 mg) were placed in aluminum Tzero Low-Mass Hermetic pans and sealed with Tzero Hermetic lids using a TA Instruments crimper. Blend samples were drop cast from a 19.8 mg/mL solution in *ortho*-dichlorobenzene/chlorobenzene (*o*-DCB/CB 50/50, v/v) into aluminum Tzero Hermetic pans, dried *in vacuo* overnight and sealed with Tzero Hermetic lids using a TA Instruments crimper. Samples were cycled between 0 °C and 350 °C at a ramp rate of 10 °C/min with 5 min isotherms at the minimum/maximum temperatures.

Substrate Cleaning: Substrates for films and devices were cleaned via scrubbing with undiluted Hellmanex III Detergent then rinsing with DI water. The substrates were then sonicated for 15 min in each of the following solvents: DI water, acetone, and iPrOH. Clean substrates were then dried in an oven at 140 °C for 16 h and stored in a clean petri dish wrapped in aluminum foil.

Optical Microscopy: Thin film samples were examined using a Leica DMCB optical microscope with a 40x objective lens. Images were recorded with an attached QICAM Fast 1394 digital video camera and analyzed with ImageJ.

Image Analysis with ImageJ: Images were saved as .tiff files to open in the ImageJ software. Once loaded in the software, images were converted to black and white by clicking “Image” and selecting “Color,” then “Split Channels” from the dropdown menu. Three images were generated and the “(blue)” (PTB7, PTB7-Th) or “(green)” (PffBT4T-2OD) channel image was selected for

further analysis. The image background was subtracted by clicking “Process” then “Subtract Background” from the dropdown menu which opened a new window. In the new window, default rolling ball radius (50 pixels) was used and “light background” was checked to ensure even background subtraction. In the “Image” tab, “Adjust” then “Threshold” were selected, opening a new window showing the minimum and maximum threshold limits for detecting particles (dark domains), now depicted in red on the image. Selecting “Apply” defined the particle sizes/areas and displayed them in black on the image. To calculate the black particle percent area, “Analyze” then “Analyze Particles” was selected. In the resulting window, the size was set to “0.0001-infinity” then “display results,” “Summary,” “Include Holes” and “Clear Results” were checked and “OK” was selected. The tabulated data points and results summary (with % area of particles relative to whole image), each appeared in separate windows.

Surface Contact Angle Goniometry: The surface contact angles were measured for water and glycerol and calculated with CAM 100 KSV Instrumental Ltd software. The surface contact angles were calculated by averaging angles from 10 frames for each droplet, three droplets per film, and at least three films. The surface energies were calculated using the Wu Harmonic Mean method.[3,4]

Variable-angle Spectroscopic Ellipsometry: Thin film thicknesses were determined by variable-angle spectroscopic ellipsometry of films on silicon wafers. Near-infrared (1100 nm–1600 nm) spectroscopic data were recorded by J.A. Woollam M-2000 ellipsometer followed by thickness measurement by Cauchy-model fitting.[5]

Ultraviolet-visible (UV-vis) Spectroscopy: UV-vis spectra of thin films were acquired using a Thermo Scientific Evolution 220 UV-vis spectrophotometer.

Bulk Heterojunction Solar Cell Device Fabrication and Measurement: Solar cell devices have the following inverted structure: glass/ITO/ZnO(40 nm)/blend/MoO_3(20 nm)/Ag(100 nm). The indium tin oxide (ITO) substrates were cleaned as described, then exposed to 245 nm ultraviolet light under oxygen flow for 15 min. 0.5 M ZnO sol–gel solution was prepared by dissolving (2.195 g, 0.01 mol) of zinc acetate dihydrate ($Zn(OAc)_2$*$2H_2O$) in 20 mL of 2-methoxyethanol (2ME). A

(0.611 g, 0.01 mol) of monoethanolamine was added into the stock solution as a stabilizer and the mixture was stirred at 60 °C for 4 h. The solution was then cooled to rt and aged for > 24 h. An aliquot of the ZnO solution (80 μL) was spin-cast on ITO-coated glass substrates at 3000 rpm for 60 s, followed by thermal annealing in air at 150 °C for 20 min. Polymer solutions were prepared as described for optical microscopy and stirred at 60 °C for 12 h before spin-casting under N_2. An aliquot of the hot polymer solution (100 μL) was spin-cast at 800 rpm for 180 s, generating thin films (215 ± 10 nm) as measured with spectroscopic ellipsometry. After spin-casting the polymers, the films were either directly transferred or thermally annealed (for 10, 30, 60, 90, 180 min) then transferred to an Angstrom Engineering AMOD thermal evaporation chamber containing MoO_3 and Ag pellets. Molybdenum masks with 1 mm radius circular openings were placed on the sample to form devices with a total area of 3.14 mm^2. MoO_3 and Ag were evaporated sequentially onto the film at a rate of 1 Å/s under the base pressure of 3×10^{-7} torr.

J-V characteristics of the devices were recorded by a HP 4156a semiconductor parameter analyzer. The transparent glass/ITO side was illuminated with simulated AM 1.5G at 1 sun intensity (100 mW/cm^2). The intensity of the solar simulator was calibrated by the National Renewable Energy Laboratory (NREL)-traceable Si reference cell. The reverse bias saturation current (J_o) was obtained from the *J-V* curve at -1 bias voltage in the dark. The series resistance (R_s) of each device was extracted from the inverse slope of the *J-V* curve at the open circuit voltage (V_{OC}).

Energy-filtered Transmission Electron Microscopy (EF-TEM): Energy-filtered transmission electron microscopy (EF-TEM) was carried out on a JEOL 3100R05 Double Cs Corrected TEM/STEM operating at 300 kV, which was equipped with a Gatan Quantum 969 Imaging Filter (GIF) with a K2 direct electron detector. A pair of low-loss EF-TEM images were acquired for 5 s using a 5 eV wide energy selecting slit centered at 19 and 29 eV. Maximum contrast was then produced by dividing the lower energy loss image by that of the higher loss image. Bright regions in these images correspond to polymer-rich regions, while the darker regions correspond to fullerene-rich domains.[6] Elastic TEM images were acquired for 2 s using a 10 eV wide energy selecting slit centered at 0 eV.

Nano-Indented Electrical Contact Resistance (ECR): Hysitron TI 950 Triboindenter was used for point measurement of conductivity during indentation of the film. The electron current of the spin-cast active layer (PffBT4T-2OD:$PC_{71}BM$ or PffBT4T-2OD:copolymer:$PC_{71}BM$) on ITO/ZnO was obtained with a nanoECR (Electrical Contact Resistance) transducer at 50 nm thickness. A Berkovich conductive ceramic probe was used for the indentation. A silver paste was used to secure the sample on the ECR stage with copper as the top surface for better conductivity. The stage is electrically connected to the system for current measurement.

Thin film preparation for triboindentation

Blends with DIO. Thin films were prepared as described (S5) for solar cell fabrication except without the Ag and MoO_3 layers.

Blends with copolymer and DIO. Thin films were prepared as described above (S5) for solar cell fabrication except without the Ag and MoO_3 layers.

A1.4 Small Molecule Syntheses

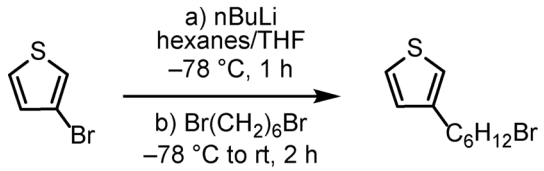

S1

3-(6-bromohexyl)thiophene (S1). An oven-dried Schlenk flask equipped with a stir bar and septum was cooled under vacuum and refilled with N_2 (3x total). To this flask was added 3-bromothiophene (1.00 mL, 10.7 mmol, 1.00 equiv) and dry hexanes (6.62 mL). This solution was cooled to -78 °C and a 2.5 M solution of *n*BuLi (4.90 mL, 12.3 mmol, 1.15 equiv) was added dropwise over 5 min. The solution was stirred for 10 min before adding dry THF (7.95 mL) dropwise. The resulting solution was stirred for 1 h before adding 1,6-dibromohexane (4.90 mL, 32.1 mmol, 3.00 equiv), warming to rt, and stirring for 2 h. The solution was quenched with sat. $NaHCO_3$ (10 mL), and the aqueous layer was extracted with Et_2O (2 x 5 mL). The organic layers were combined and washed with H_2O (1 x 15 mL) and brine (1 x 15 mL), dried over $MgSO_4$, filtered, and concentrated in vacuo to yield an orange oil. The excess 1,6-dibromohexane was removed by distillation. The remaining orange oil was purified by silica gel column chromatography (100% hexanes) to yield a colorless oil, which was heated to 55 °C in vacuo for 10 h to remove excess 1,6-dibromohexane (379 mg, 14%). HRMS (EI): Calcd. for $[M]^+$ 246.0078; found 246.0068.

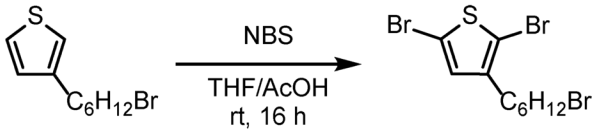

S1 **S2**

2,5-dibromo-3-(6-bromohexyl)thiophene (S2). To a 20 mL vial equipped with a septum were added **S1** (275 mg, 1.11 mmol, 1.00 equiv) and THF (2.78 mL). The resulting solution was sparged with N_2 for 10 min. To this vial was added AcOH (2.78 mL) and recrystallized NBS (494 mg, 2.78 mmol, 2.50 equiv). The solution was stirred in the dark under N_2 at rt for 16 h. The reaction solution was quenched using saturated aq. $NaHCO_3$ (5 mL) and extracted with Et_2O (3 x 5 mL). The combined organic layers were washed with water (15 mL) and brine (15 mL), dried over $MgSO_4$, filtered, and concentrated in vacuo. The resulting orange oil was purified by silica gel column

chromatography (100% hexanes) to obtain a colorless oil (158 mg, 35%). HRMS (EI): Calcd. for $C_{10}H_{13}Br_3S$ $[M]^+$ 401.8288; found, 401.8278.

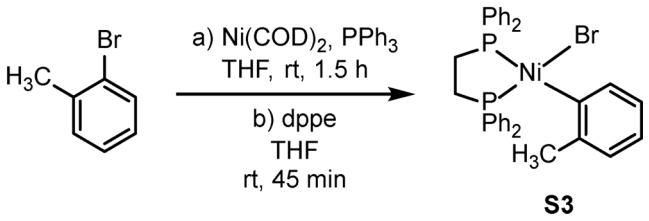

S3

(*o*-tolyl)(1,2-bis(diphenylphosphino)ethane)nickel bromide (S3). In a glovebox, to a 20 mL vial equipped with a stir bar was added $Ni(COD)_2$ (77.3 mg, 0.281 mmol, 1.00 equiv), PPh_3 (151 mg, 0.574 mmol, 2.04 equiv), and dry THF (1.4 mL). The resulting mixture was stirred for 5 min before 2-bromotoluene (36.7 µL, 0.309 mmol, 1.10 equiv) was added. The solution was stirred for 90 min at rt, yielding an opaque orange suspension. Then dppe (114 mg, 0.286 mmol, 1.02 equiv) was added and the mixture was stirred for 45 min at rt. Hexanes (15 mL) were added as the top layer and the mixture was cooled to –35 °C for 24 h. The resulting yellow-orange solid was isolated via filtration inside the glovebox, washed with hexanes (3 x 5 mL), and recrystallized from DCM/hexanes at –35 °C to yield a yellow crystalline solid (88 mg, 51%). HRMS (EI): Calcd. for $[M]^+$ 626.0438; found 626.0422.

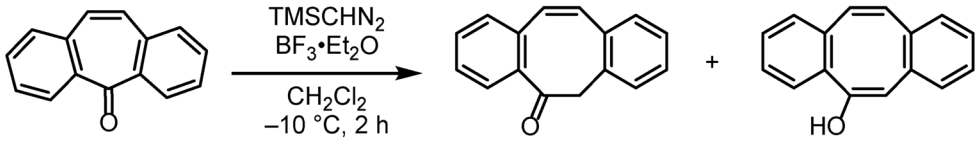

S4 **S4'**

6*H*-Dibenzo[a,e]cyclooctatrien-5-one (S4). In a N_2 flushed 100 mL round-bottom flask was added dibenzosuberenone (3.10 g, 15.0 mmol, 1.00 equiv) and $BF_3 \cdot OEt_2$ (2.80 mL, 22.7 mmol, 1.50 equiv), and DCM (30 mL). The solution was cooled to –10 °C. A 0.75 M solution of trimethylsilyl diazomethane in DCM (32.0 mL, 24.0 mmol, 1.60 equiv) was added to the solution dropwise over 1 h and then stirred at –10 °C for an additional 2 h. Then AcOH (0.2 mL) was added to quench the reaction solution. The mixture was poured into ice water (150 mL). The aqueous layer was extracted with DCM (3 x 100 mL) and the combined organic layers were washed with brine (100 mL), dried over $MgSO_4$, and filtered. The filtrate was concentrated in vacuo and the crude product was purified by silica gel column chromatography (10–70% DCM in hexanes) to give dibenzocyclooctenone (**S4**) as a white solid (1.13 g, 34%) and dibenzocyclooctadienol (**S4'**)

as a viscous transparent liquid (2.10 g, 63%). HRMS (EI): Calcd. For $C_{16}H_{12}O$ $[M]^+$ 220.0888; found, 220.0884.

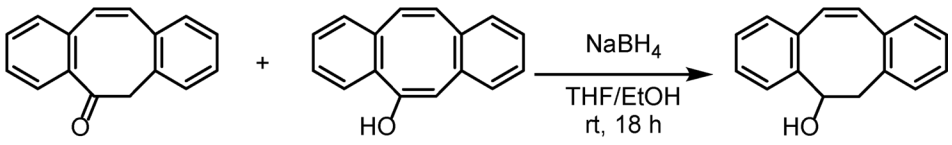

S4 **S4'** **S5**

5,6-Dihydro-dibenzo[a,e]cycloocten-5-ol (S5). Sodium borohydride (0.388 g, 10.3 mmol, 2.00 equiv) was slowly added to a stirred solution of **S4**/**S4'** (1.13 g, 5.13 mmol, 1.00 equiv) in THF/EtOH (1/1, v/v, 60 mL). The solution was stirred at rt for 18 h, then quenched by slow addition of AcOH (0.5 mL). The mixture was concentrated in vacuo, and the yellow residue was dissolved in DCM (50 mL) and washed with brine (50 mL). The aqueous layer was extracted with DCM (4 x 50 mL). The combined organic layers were dried over $MgSO_4$, treated with decolorizing carbon, filtered and concentrated in vacuo to give a white solid (723 mg, 63%). HRMS (EI): Calcd. For $C_{16}H_{14}O$ $[M]^+$ 222.1045; found, 222.1046.

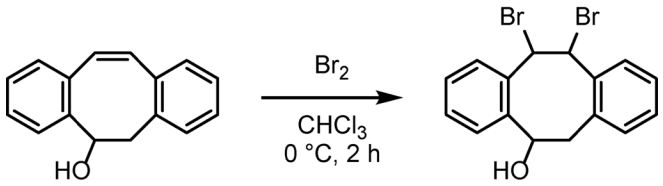

S5 **S6**

11,12-Dibromo-5,6,11,12-tetrahydro-dibenzo[a,e]cycloocten-5-ol (S6). Into a N_2-filled round-bottom flask was added **S5** (0.642 g, 2.89 mmol, 1.00 equiv) and $CHCl_3$ (15 mL) and the resulting solution was cooled to 0 °C using an ice-water bath. A solution of Br_2 (0.150 mL, 2.93 mmol, 1.01 equiv) in $CHCl_3$ (5 mL) was added dropwise over 3 min. After stirring for 2 h, the resulting solution was quenched with saturated aq. $Na_2S_2O_3$ (20 mL), and washed with H_2O (20 mL) and brine (20 mL). The organic layer was dried over $MgSO_4$, filtered, and concentrated in vacuo, affording a yellow oil. The crude product was purified by silica gel column chromatography (5–70% DCM in hexanes) to obtain a viscous, colorless oil (480 mg, 44%). HRMS (EI): Calcd for $C_{16}H_{13}BrO$ $[M–HBr]^+$ 300.0150; found, 300.0156

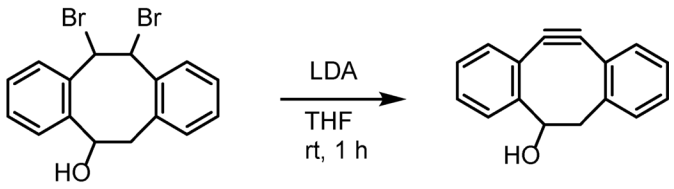

S6 **S7**

5,6-Dihydro-11,12-didehydro-dibenzo[a,e]cycloocten-5-ol (S7). To an oven-dried 10 mL Schlenk flask under N_2 that was equipped with a stir bar and septum was added a solution of **S6** (304 mg, 0.796 mmol, 1.00 equiv) dissolved in dry DCM (0.5 mL). The DCM was removed in vacuo and dry THF (7.96 mL) was added. The solution was cooled to 0 °C and a 1.75 M solution of LDA in THF/heptane/ethylbenzene (59/28/13, v/v) (1.82 mL, 3.18 mmol, 4.00 equiv) was added dropwise. The resulting solution was stirred for 5 min at 0 °C, then warmed to rt and stirred for 1 h. The reaction solution was slowly quenched with H_2O (1.50 mL) and the solvent was removed in vacuo. The resulting brown oil was purified by silica gel chromatography (25–100% DCM in hexanes) to yield a white solid (158 mg, 90%). HRMS (CI): Calcd. For $[M+H]^+$ 221.0961; found 221.0958

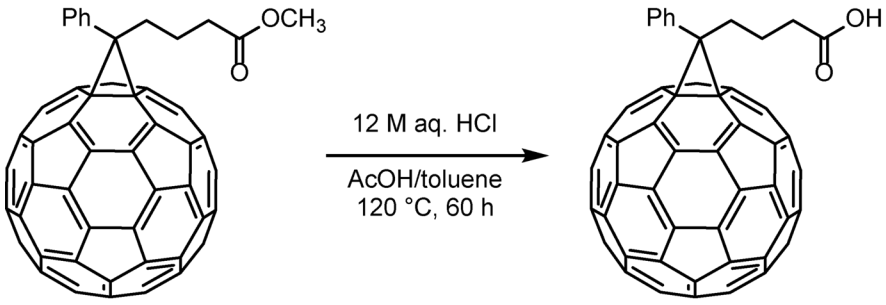

$PC_{61}BM$ **S8**

phenyl-C_{61}-butyric acid (S8). Phenyl-C_{61}-butyric acid methyl ester (PCBM) (550 mg, 0.604 mmol, 1.00 equiv) was dissolved in toluene (80 mL) and AcOH (40 mL) in a 350 mL bomb flask. Then aq. HCl (12 M, 20 mL) was added. The flask was sealed and heated to 120 °C for 60 h with vigorous stirring. The mixture was then cooled to rt. The now heterogeneous organic layer was separated from the aqueous layer and filtered. The resulting brown solid was washed sequentially with MeOH, acetone, toluene, and Et_2O (30 mL each), to afford a brown powder (541 mg, quant). The product was carried to the next step without further purification. HRMS (ESI-): Calcd. For $C_{71}H_{11}O_2$ $[M–H]^-$ 895.0765; found, 895.0750.

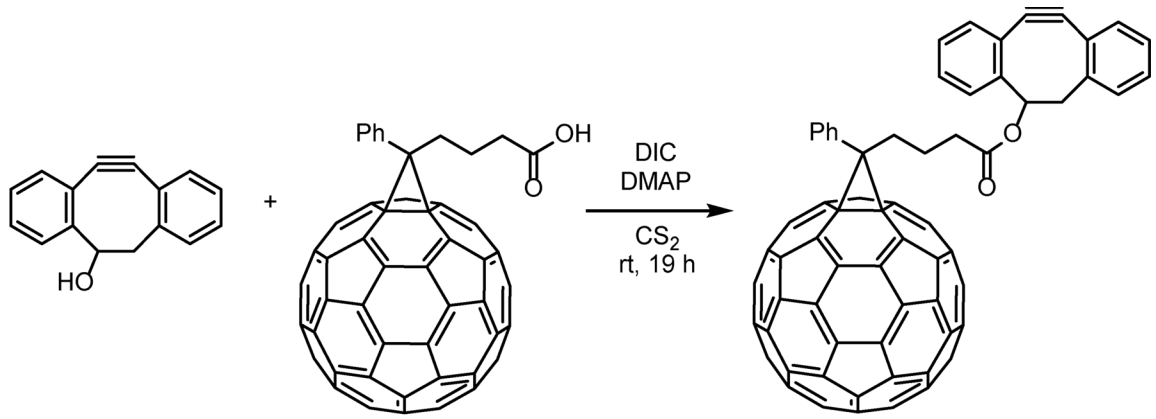

S7 **S8** **S9**

PCB-DIBO (S9). To a flame dried 50 mL round-bottom flask equipped with a stir bar was added **S8** (314 mg, 0.350 mmol, 1.00 equiv) and DMAP (53.6 mg, 0.438 mmol, 1.25 equiv). To this flask was then added CS_2 (24 mL), DIC (82.4 μL, 0.526 mmol, 1.50 equiv), and a 0.015 M solution of **S7** in CS_2 (36 mL, 0.526 mmol, 1.50 equiv). The solution was stirred for 19 h at rt. The reaction solution was quenched with water (5 mL) and extracted with DCM (3 x 10 mL). The organic layers were washed with water (20 mL) and brine (20 mL), dried over $MgSO_4$, filtered, and concentrated in vacuo. The resulting solid was purified by silica gel chromatography (10-40% DCM in hexanes) to yield a brown solid (184 mg, 48%). MALDI-TOF-MS: Calcd. For $C_{87}H_{22}O_2$ [M] = 1099.162; found,1097.508.

A1.5 Polymerization and Post-polymerization Modifications

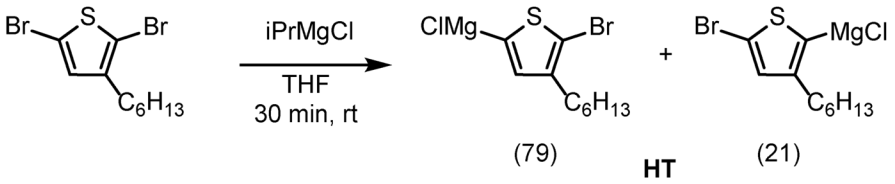

HT monomer activation. In a N_2-filled glovebox, 2,5-dibromo-3-hexylthiophene (193 mg, 0.593 mmol, 1.00 equiv) was dissolved in THF (5 mL) in an 8 mL vial equipped with a stir bar. To this vial was added a 2.10 M solution of iPrMgCl in THF (250 µL, 0.525 mmol, 0.890 equiv) and the resulting solution was stirred for 30 min at rt. An aliquot (0.1 mL) was quenched with 12 M aq. HCl (0.1 mL), extracted with $CHCl_3$ (2 x 1 mL), dried over $MgSO_4$, filtered, and analyzed by GC, showing a mixture of **HT** regioisomers in a 79:21 ratio and active Grignard concentration of 0.080 M.

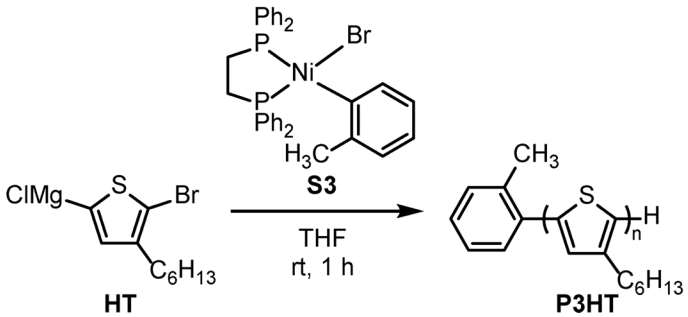

P3HT. In a N_2-filled glovebox, to a 50 mL Schlenk flask equipped with a stir bar and septum was added a 0.080 M solution of **HT** in THF (5.00 mL, 0.400 mmol, 180 equiv), and additional THF (25 mL). Outside of the glovebox under N_2, the solution was cooled to 0 °C and to the flask was added a 0.85 mM solution of **S3** in THF (2.82 mL, 2.2 µmol, 1.0 equiv) via syringe pump at 0.26 mL/min. Once catalyst addition was complete, the resulting solution was stirred for 70 min at 0 °C. The polymerization was quenched with 12 M aq. HCl (20 mL) while stirring, then precipitated into MeOH (100 mL) and the solids were collected on filter paper. Sequential Soxhlet extraction of the solids with acetone, MeOH, hexane, and $CHCl_3$ afforded a purple solid (47 mg, 70%). $M_{n,SEC}$ = 28.1 kg/mol, $M_{n,NMR}$ = 26.7, Đ = 1.23, regioregularity = 99%. The M_n obtained by SEC is an overestimation, in reasonable agreement with a previous report.[7]

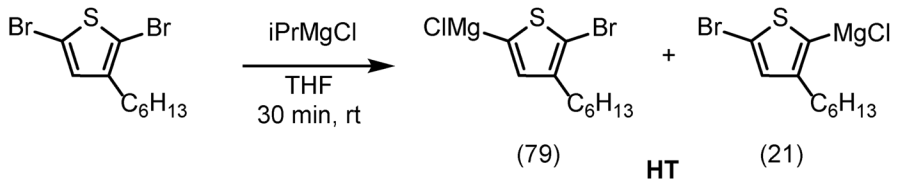

HT monomer activation. In a N_2-filled glovebox, 2,5-dibromo-3-hexylthiophene (234 mg, 0.719 mmol, 1.00 equiv) was dissolved in THF (6.89 mL) in a 20 mL vial equipped with a stir bar. To this vial was added a 1.93 M solution of iPrMgCl in THF (298 µL, 0.575 mmol, 0.800 equiv) and the resulting solution was stirred for 30 min at rt after which the active Grignard concentration was 0.089 M. An aliquot (0.1 mL) of this solution was quenched with 12 M aq. HCl (0.1 mL), extracted with $CHCl_3$ (2 x 1 mL), dried over $MgSO_4$, filtered, and analyzed by GC, showing a mixture of **HT** regioisomers in a 79:21 ratio and 92% monomer activation.

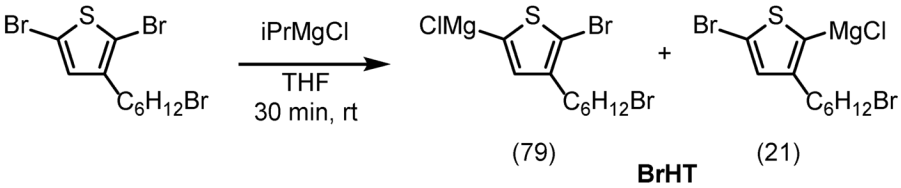

BrHT monomer activation. In a N_2-filled glovebox, 2,5-dibromo-3-(6-bromohexyl)thiophene (148 mg, 0.365 mmol, 1.00 equiv) was dissolved in THF (3.53 mL) in an 8 mL vial equipped with a stir bar. To this vial was added a 1.93 M solution of iPrMgCl in THF (160 µL, 0.309 mmol, 0.850 equiv) and the resulting solution was stirred for 30 min at rt after which the Grignard concentration was 0.091 M. An aliquot (0.1 mL) was quenched with 12 M aq. HCl (0.1 mL), extracted with $CHCl_3$ (2 x 1 mL), dried over $MgSO_4$, filtered, and analyzed by GC, showing a mixture of BrHT regioisomers in a 79:21 ratio and 97% monomer activation.

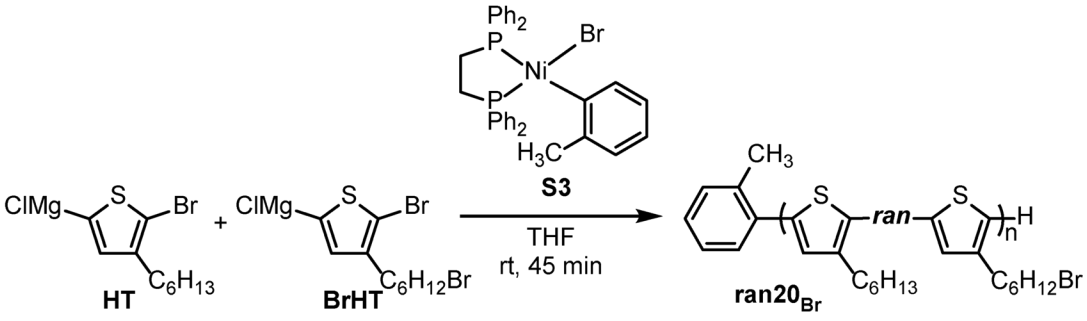

ran20$_{Br}$. In a N_2-filled glovebox, to a 25 mL Schlenk flask equipped with a stir bar was added a 0.089 M solution of **HT** (5.00 mL, 0.445 mmol, 88.0 equiv) in THF, a 0.091 M solution of **BrHT** (1.22 mL, 0.111 mmol, 22.0 equiv) and additional THF (20.6 mL). An aliquot (0.10 mL) was removed for GC analysis. Then to the reaction flask was quickly added a 0.005 M solution of **S3** in THF (1.01 mL, 5.05 μmol, 1.00 equiv) and the solution was stirred for 45 min at rt. The polymerization was removed from the glovebox and quenched with 12 M aq. HCl (6 mL) while stirring. The biphasic mixture was extracted with $CHCl_3$ (3 x 10 mL) and the combined organic layers were dried over $MgSO_4$ and filtered. An aliquot (0.25 mL) was removed and diluted with $CHCl_3$ for GC analysis. The remaining solution was concentrated in vacuo to yield a purple solid. The solid was dissolved in a minimal amount of $CHCl_3$ and precipitated into cold MeOH and centrifuged for 15 min. The supernatant was decanted and the solid was re-suspended in cold MeOH with sonication and centrifuged. This procedure was repeated 3 times. The supernatant was removed a final time and the remaining pellet was dried in vacuo to yield a purple solid (65 mg, 64%). $M_{n,SEC}$ = 18.4 kg/mol, $M_{n,NMR}$ = 14.0 kg/mol, Đ = 1.22, regioregularity = 94%. The M_n obtained by SEC is an overestimation, in reasonable agreement with a previous report.[7]

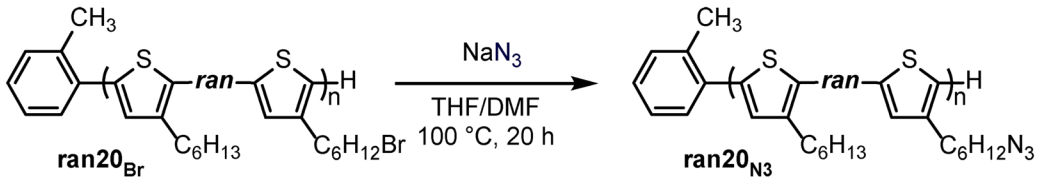

ran20$_{N3}$. To an oven-dried 100 mL RBF was added **ran20Br** (91 mg, 0.10 mmol, 1.0 equiv Br) and dry THF (70 mL). The mixture was stirred for 5 min at 60 °C to dissolve the polymer then to this flask was added DMF (35 mL) and NaN_3 (325 mg, 5.00 mmol, 48.0 equiv wrt Br) in one portion with stirring. The flask was equipped with a reflux condenser and the solution was stirred under N_2 for 20 h at 100 °C. The flask was cooled to rt and the THF was removed in vacuo. The polymer was dissolved in a minimal amount of $CHCl_3$, precipitated into cold MeOH (30 mL), and centrifuged for 15 min. The supernatant was decanted and the polymer was resuspended in MeOH with sonication and centrifuged. This procedure was repeated 3 times. The supernatant was removed a final time and the remaining pellet was dried in vacuo to yield a purple solid (83 mg, 95%). $M_{n,SEC}$ = 19.0 kg/mol, $M_{n,NMR}$ = 14.2, Đ = 1.42, regioregularity = 99%. The M_n obtained by SEC is an overestimation, in reasonable agreement with a previous report.[7]

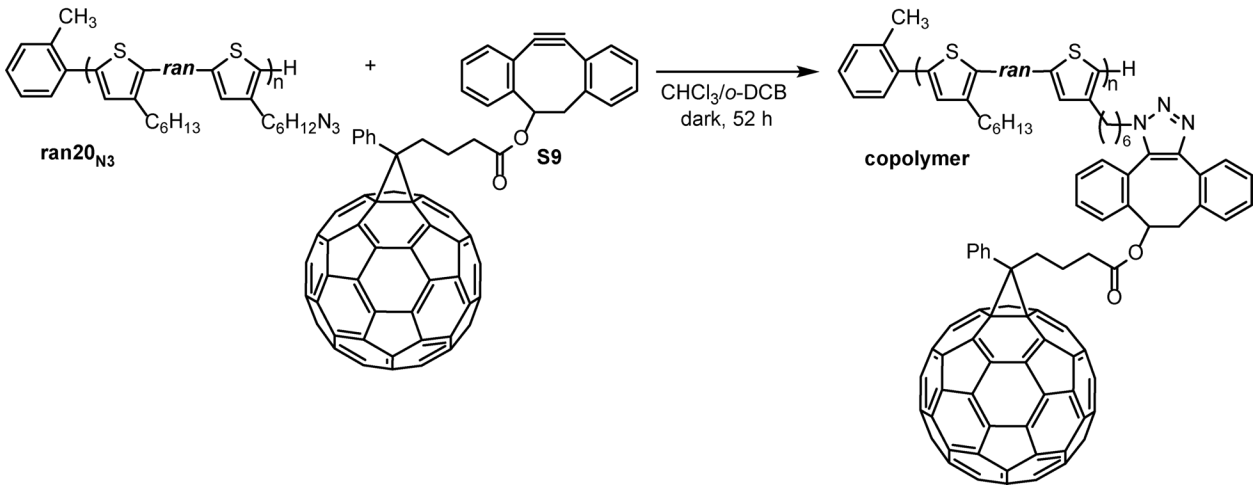

copolymer. To a 100 mL oven-dried round-bottomed flask was added **ran20$_{N3}$** (49.0 mg, 56.0 μmol N_3, 1.00 equiv N_3), $CHCl_3$ (45 mL), *o*-DCB (3 mL), and a stir bar. To this vial was added **S9** (79 mg, 72 μmol, 1.3 equiv wrt N_3). The flask was covered in foil and the solution was stirred under N_2 for 52 h at rt. The $CHCl_3$ was then removed in vacuo until only a minimal amount remained and the polymer was precipitated into cold MeOH. The mixture was cooled for 15 min at –30 °C and the solids were collected via filtration and purified by sequential Soxhlet extraction with DCM (19 h), $CHCl_3$ (6.5 h), and $CHCl_3/CS_2$ (50/50, v/v) (13 h). The polymer was in the $CHCl_3$ fraction and the solvent was removed in vacuo to yield a reddish orange solid (90 mg, 82%). $M_{n,SEC}$ = 21 kg/mol, Đ = 1.15.

Table A1-1. Characterization data for all copolymer syntheses

polymer	functionalization ^{1}H NMR (%)	M_n ^{1}H NMR (kg/mol)	M_n SEC (kg/mol)[a]	Đ	regioregularity (%)	conversion ^{1}H NMR (%)	conversion FTIR (%)	yield (%)
ran20Br	21	14.0	18.4	1.22	94	-	-	64
ran20N3	21	14.2	19.0	1.42	99	quant.	-	95
copolymer	21	-	21.0	1.15		-	quant.	82

[a] The M_n obtained by SEC is an overestimation, in reasonable agreement with a previous report for rod polymers.[7]

A1.6 NMR Spectra

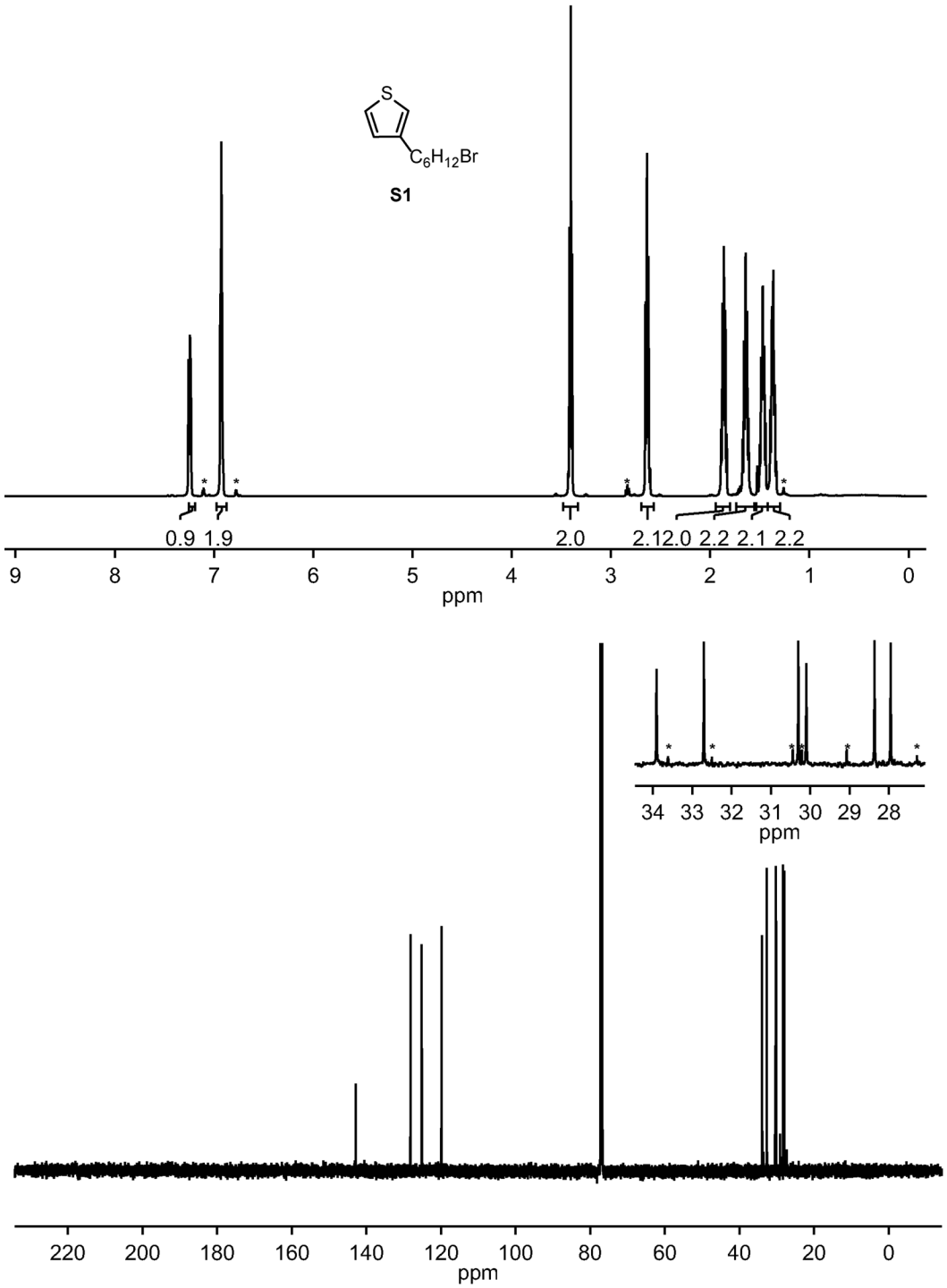

Figure A1.1 ^{1}H and ^{13}C NMR Spectra of S1. ^{1}H NMR (500 MHz, $CDCl_3$) δ 7.25–7.21 (m, 1H), 6.97–6.87 (m, 2H), 3.40 (t, J = 6.8 Hz, 2H), 2.64 (t, J = 7.7 Hz, 2H), 1.86 (p, J = 7.0 Hz, 2H), 1.64 (p, J = 7.6 Hz, 2H), 1.52–1.42 (m, 2H), 1.41–1.32 (m, 2H). ^{13}C NMR (126 MHz, $CDCl_3$) δ 142.84, 128.18, 125.14, 119.88, 33.91, 32.71, 30.30, 30.10, 28.37, 27.95. *unknown impurity

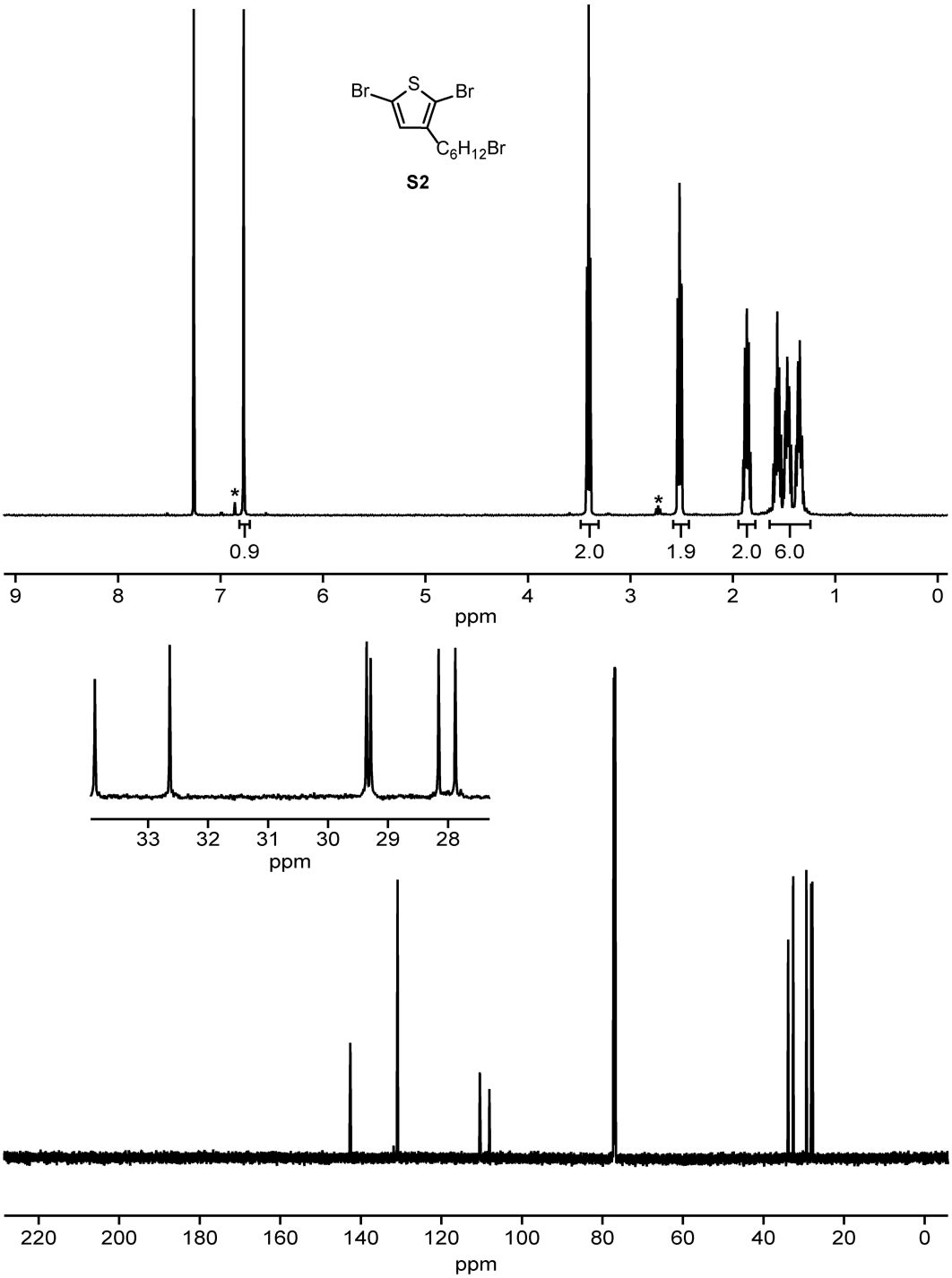

Figure A1.2 ^{1}H and ^{13}C NMR Spectra of S2. ^{1}H NMR (700 MHz, $CDCl_3$) δ 6.77 (s, 1H), 3.41 (t, J = 6.8 Hz, 2H), 2.52 (t, J = 7.6 Hz, 2H), 1.86 (p, J = 7.0 Hz, 2H), 1.56 (p, J = 7.7 Hz, 2H), 1.46 (p, J = 7.7 Hz, 2H), 1.34 (p, J = 7.7 Hz, 2H). ^{13}C NMR (176 MHz, $CDCl_3$) δ 142.60, 130.87, 110.44, 108.87, 33.89, 32.64, 29.36, 29.29, 28.16, 27.88.*unknown impurity

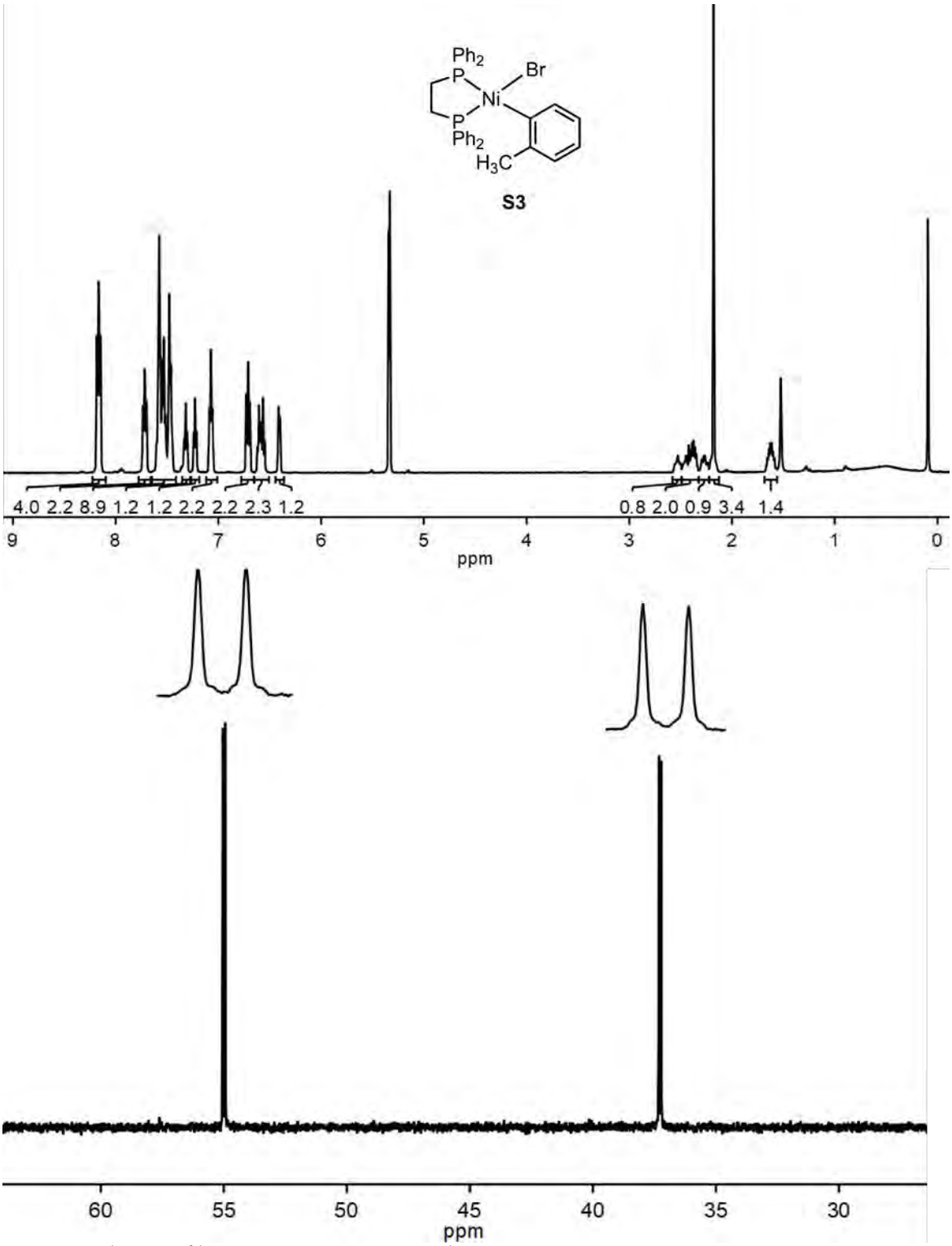

Figure A1.3 ^{1}H and ^{31}P NMR Spectra of S3. ^{1}H NMR (500 MHz, CD_2Cl_2) δ 8.21–8.11 (m, 4H), 7.75–7.68 (m, 2H), 7.63–7.50 (m, 6H), 7.50–7.43 (m, 3H), 7.32 (t, J = 7.6 Hz, 1H), 7.23 (t, J = 6.8 Hz, 1H), 7.07 (t, J = 7.9 Hz, 2H), 6.71 (t, J = 9.3 Hz, 2H), 6.58 (dt, J = 21.0, 7.4 Hz, 2H), 6.41 (d, J = 7.2 Hz, 1H), 2.59–2.49 (m, 1H), 2.49–2.33 (m, 1H), 2.33–2.23 (m, 1H), 2.18 (s, 3H), 1.70–1.56 (m, 1H). ^{31}P NMR (202 MHz, CD_2Cl_2) δ 55.00 (d, J = 18.3 Hz), 37.28 (d, J = 18.3 Hz).

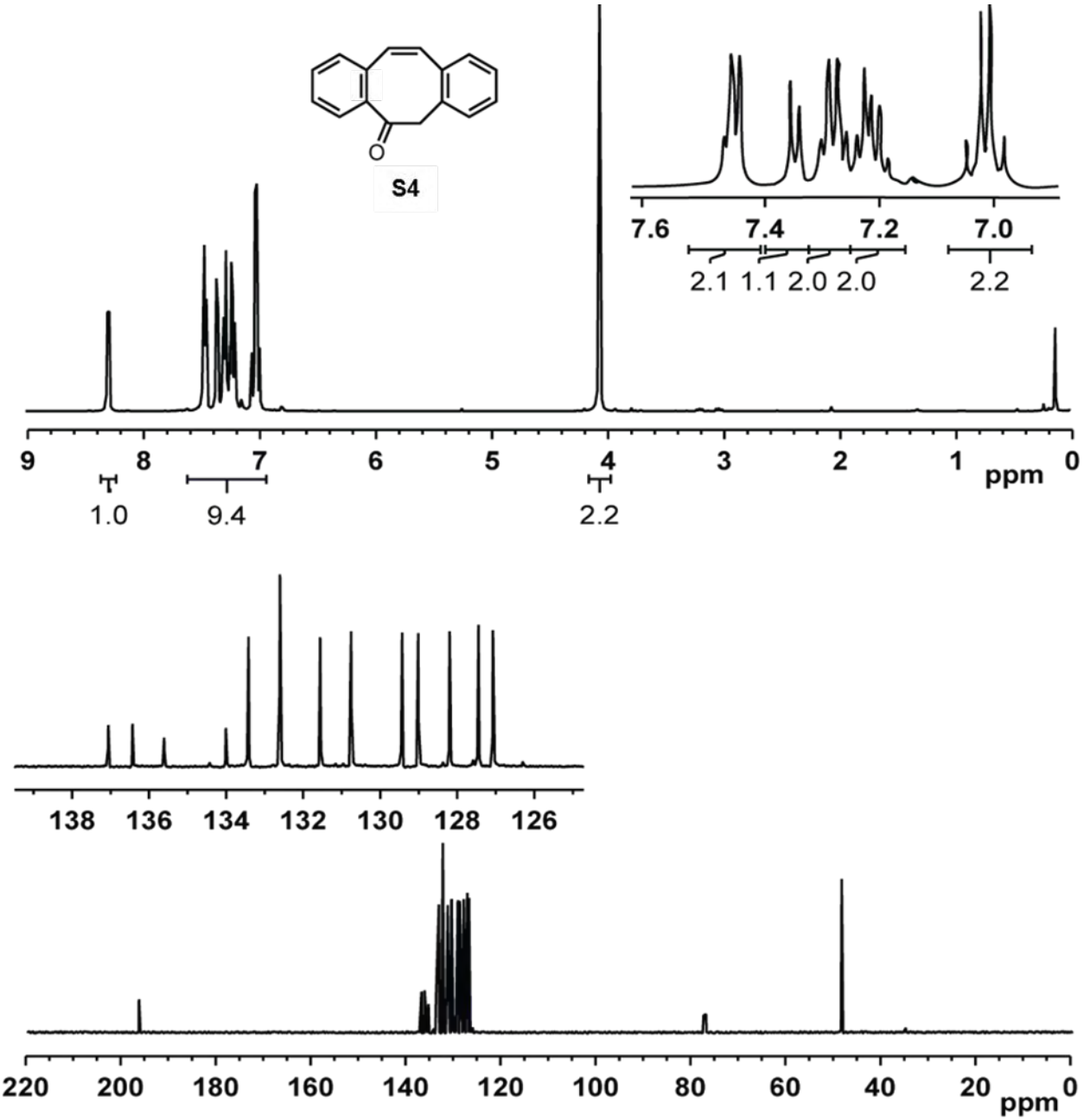

Figure A1.4 ^{1}H and ^{13}C NMR Spectra of S4. ^{1}H NMR (500 MHz, $CDCl_3$) δ 8.29 (d, J = 8.0 Hz, 1H), 7.46 (m, 2H), 7.35 (d, J = 7.7 Hz, 1H), 7.28 (m, 2H), 7.21 (m, 2H), 7.02 (m, 2H), 4.06 (s, 2H). ^{13}C NMR (126 MHz, $CDCl_3$) δ 196.58, 137.06, 136.43, 135.61, 134.01, 133.42, 132.60, 131.56, 130.76, 129.43, 129.01, 128.20, 127.45, 127.07, 48.60.

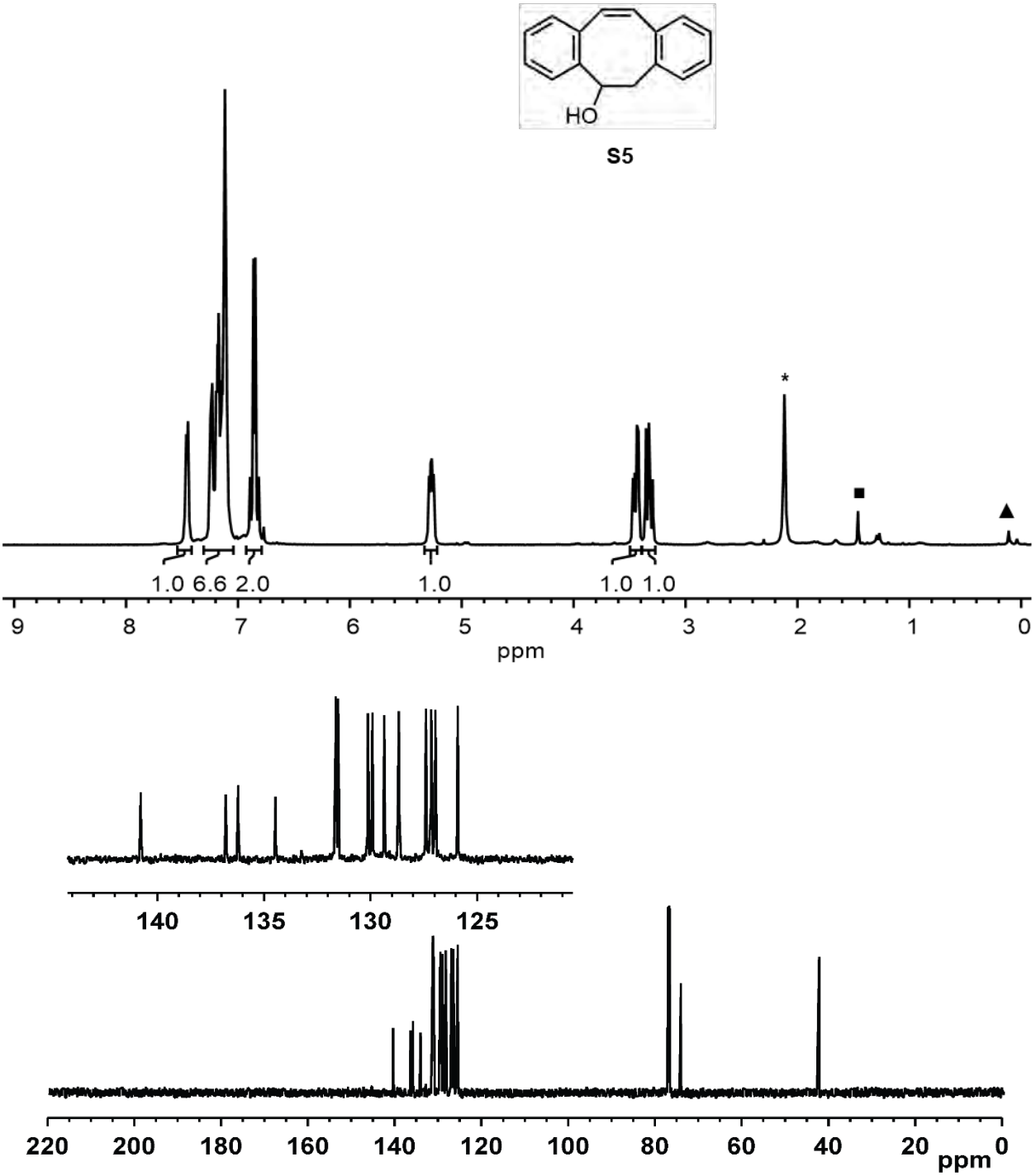

Figure A1.5 ^{1}H and ^{13}C NMR Spectra of S5. ^{1}H NMR (400 MHz, $CDCl_3$) δ 7.48 (m, 1H), 7.17 (m, 7H), 6.84 (m, 2H), 5.27 (dd, *J* = 9.6, 6.3 Hz, 1H), 3.45 (dd, *J* = 13.7, 6.1 Hz, 1H), 3.32 (dd, *J* = 13.6, 10.2 Hz, 1H). *Acetone, ■ H_2O, ▲ grease. ^{13}C NMR (100 MHz, $CDCl_3$) δ 140.78, 136.79, 136.21, 134.46, 131.63, 131.53, 130.12, 129.91, 129.36, 128.67, 127.40, 127.15, 126.96, 125.91, 74.46, 42.59.

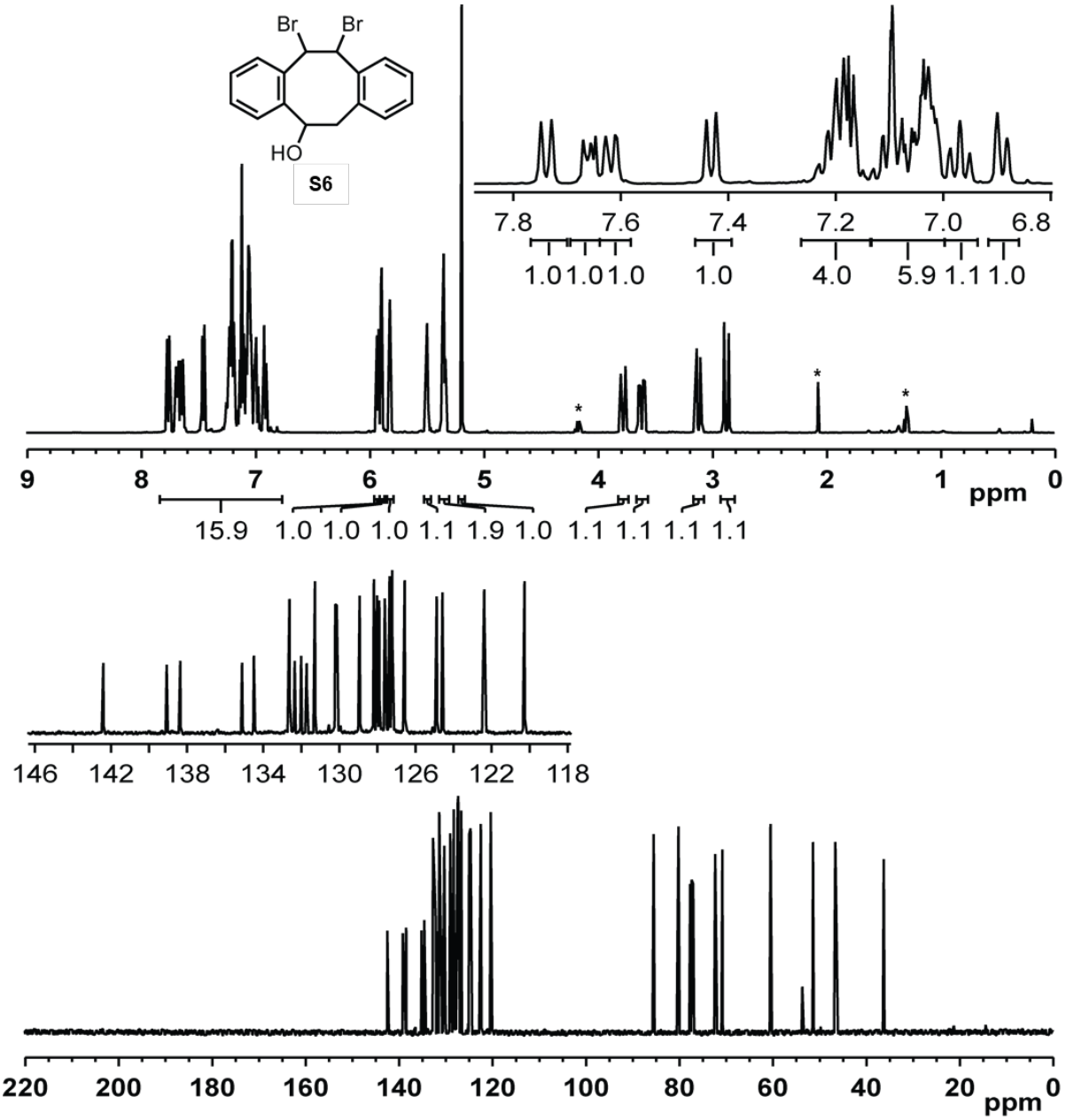

Figure A1.6 ^{1}H and ^{13}C NMR Spectra of S6 (a 1:1 mixture of diastereomers). ^{1}H NMR (400 MHz, CD_2Cl_2) δ 7.74 (d, *J* = 7.8 Hz, 1H), 7.66 (m, 1H), 7.62 (d, *J* = 7.0 Hz, 1H), 7.43 (d, *J* = 7.2 Hz, 1H), 7.23–7.18 (m, 4H), 7.01–7.11 (m, 6H), 6.97 (t, *J* = 7.2 Hz, 1H), 6.89 (d, *J* = 7.4 Hz, 1H), 5.90 (d, *J* = 5.5 Hz, 1H), 5.87 (d, *J* = 2.2 Hz, 1H), 5.80 (s, 1H), 5.47 (t, *J* = 3.2 Hz, 1H), 5.33 (t, *J* = 5.0 Hz, 2H), 5.17 (s, 1H), 3.75 (dd, *J* = 16.1, 1.2 Hz, 1H), 3.59 (dd, *J* = 16.4, 6.2 Hz, 1H), 3.10 (dd, *J* = 16.1, 3.7 Hz, 1H), 2.85 (d, *J* = 16.4 Hz, 1H). ^{13}C NMR (100 MHz, $CDCl_3$) δ 142.40, 139.07, 138.36, 135.11, 134.49, 132.62, 132.35, 132.01, 131.72, 131.28, 130.21, 130.14, 128.93, 128.18, 128.01, 127.90, 127.61, 127.36, 127.22, 126.57, 124.88, 124.58, 122.39, 120.27, 85.40, 80.09, 72.24, 70.70, 60.40, 51.31, 46.53, 36.16. *EtOAc

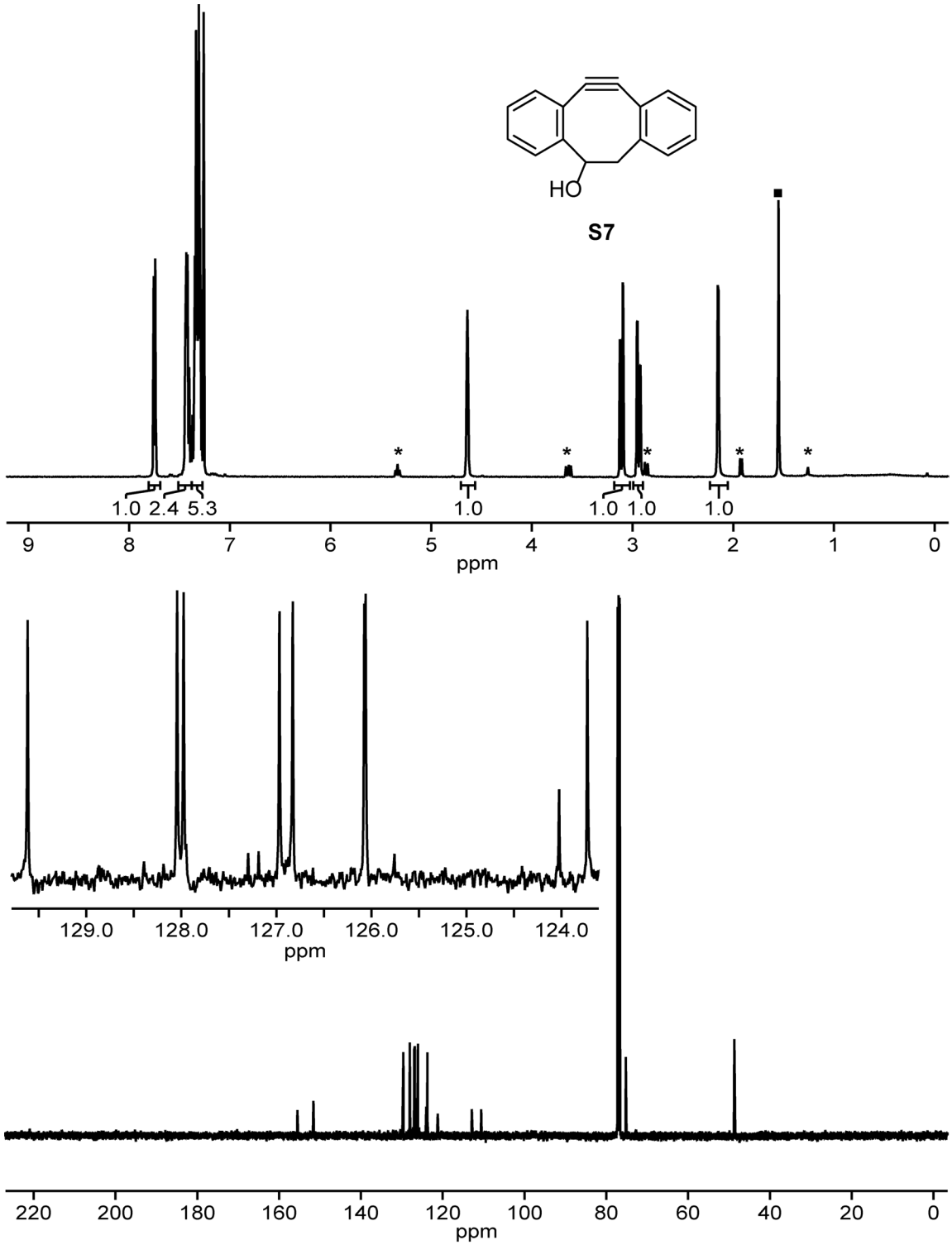

Figure A1.7 ^{1}H and ^{13}C NMR Spectra of S7. ^{1}H NMR (500 MHz, $CDCl_3$) δ 7.75 (d, J = 7.8 Hz, 1H), 7.48–7.38 (m, 2H), 7.38–7.27 (m, 5H), 4.64 (s, 1H), 3.11 (dd, J = 14.8, 2.2 Hz, 1H), 2.94 (dd, J = 14.7, 3.8 Hz, 1H), 2.15 (d, J = 4.4 Hz, 1H). ^{13}C NMR (126 MHz, $CDCl_3$) δ 155.53, 151.61, 129.62, 128.04, 127.98, 126.97, 126.83, 126.07, 126.06, 124.03, 123.73, 121.21, 112.89, 110.58, 75.23, 48.70. *unknown impurity ■H_2O

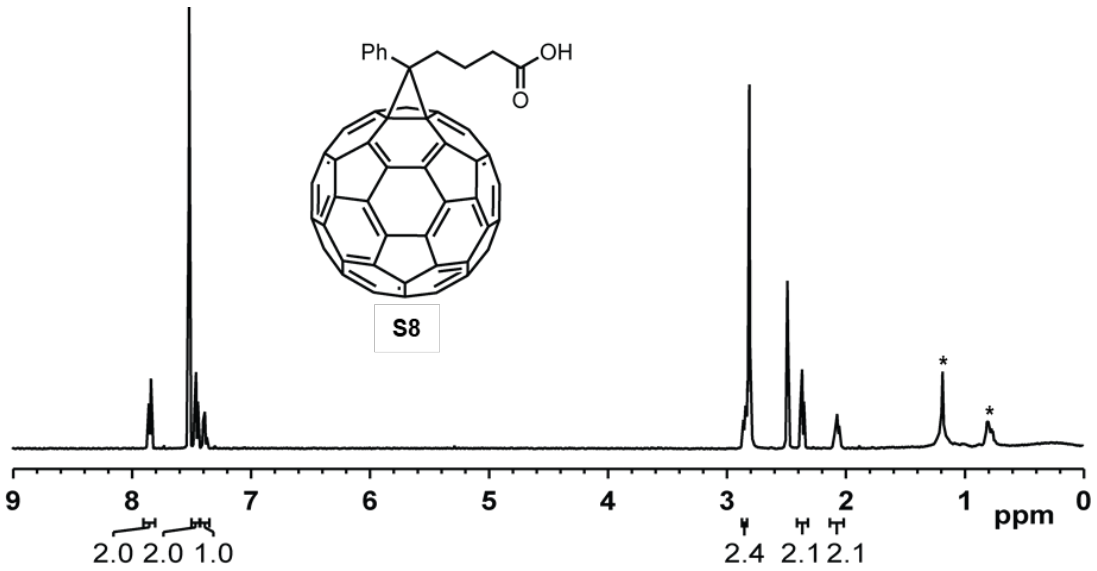

Figure A1.8 ^{1}H NMR Spectrum of S8. ^{1}H NMR (500 MHz, $CDCl_3$/DMSO-d_6/CS_2 3:1:1) δ 7.84 (d, *J* = 7.3 Hz, 2H), 7.46 (m, 2H), 7.38 (m, 1H), 2.84 (m, 2H), 2.36 (t, *J* = 7.6 Hz, 2H), 2.07 (m, 2H). *grease

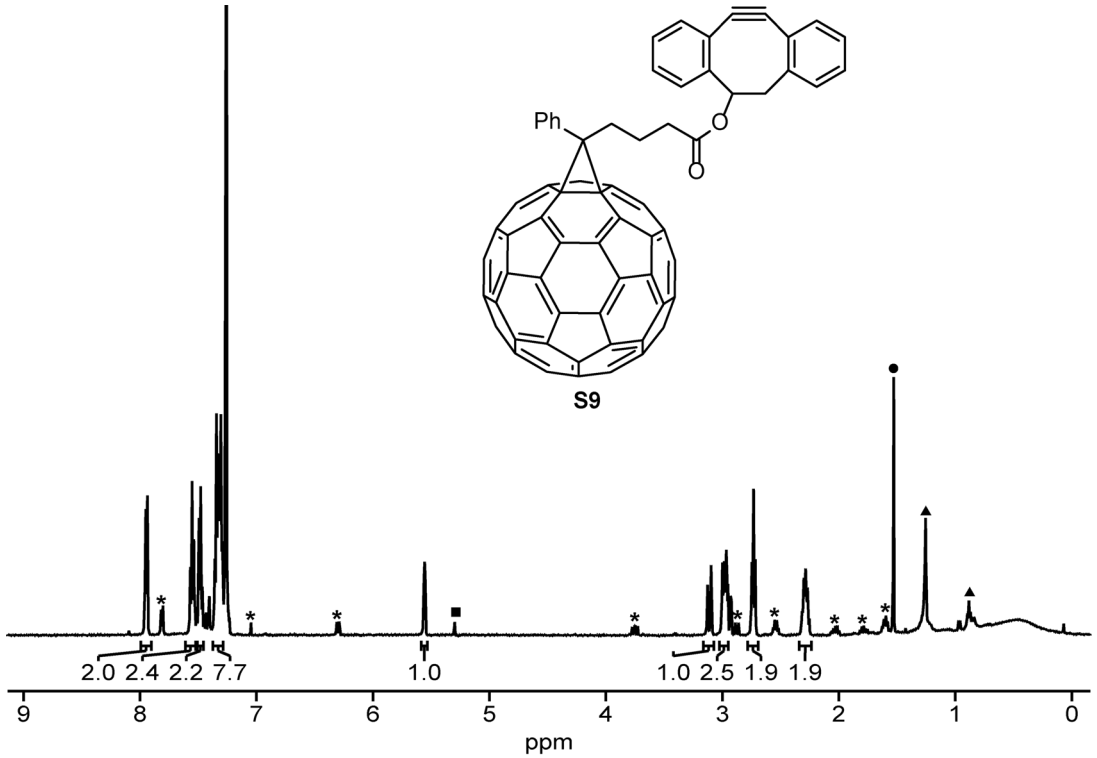

Figure A1.9 ^{1}H NMR Spectrum of S9. ^{1}H NMR ^{1}H NMR (500 MHz, $CDCl_3$) δ 7.99–7.90 (m, 2H), 7.60–7.52 (m, 2H), 7.52–7.46 (m, 2H), 7.37–7.28 (m, 7H), 5.56 (s, 1H), 3.11 (dd, *J* = 15.2, 2.2 Hz, 1H), 3.04 – 2.94 (m, 2H), 2.73 (t, *J* = 7.5 Hz, 2H), 2.35–2.23 (m, 2H). *unknown impurity ■DCM ●H_2O ▲grease

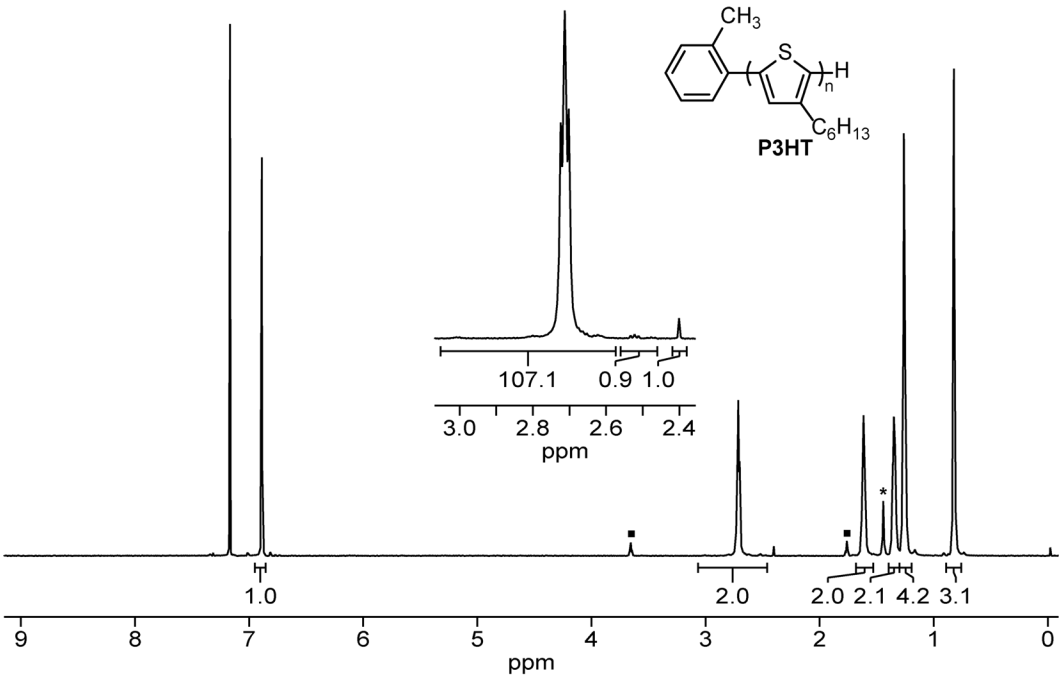

Figure A1.10 ^{1}H NMR Spectrum of P3HT. ^{1}H NMR (700 MHz, $CDCl_3$) δ 6.98 (s, 1H), 2.80 (t, J = 7.9 Hz, 2H), 1.75–1.67 (m, 2H), 1.47–1.41 (m, 2H), 1.39–1.30 (m, 4H), 0.94–0.88 (m, 3H). *cyclohexane, ■ THF. The inset integrals were used to calculate M_n and regioregularity

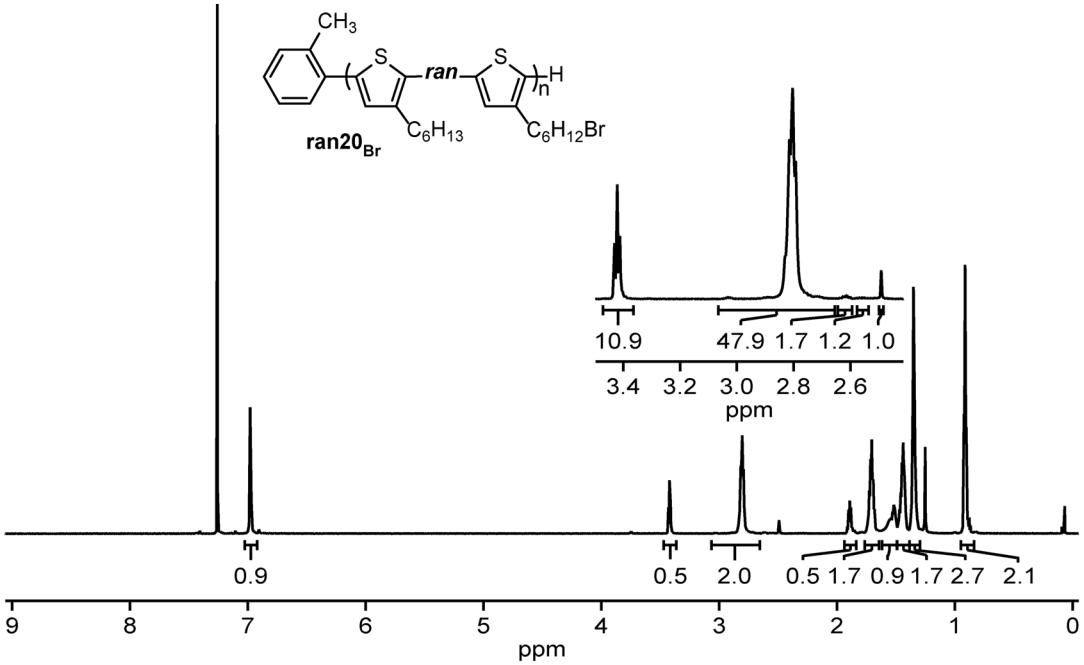

Figure A1.11 ^{1}H NMR Spectrum of ran20$_{Br}$. ^{1}H NMR (700 MHz, $CDCl_3$) δ 6.98 (s, 1H), 3.42 (t, J = 6.8 Hz, 0.5H), 2.80 (t, J = 8.2 Hz, 2H), 1.89 (p, J = 7.0 Hz, 0.5H), 1.78–1.67 (m, 2H), 1.60–1.49 (m, 1H), 1.49–1.39 (m, 2H), 1.38–1.31 (m, 3H), 0.96–0.88 (m, 3H). The inset integrals were used to calculate $M_{n,NMR}$ and to determine regioregularity.

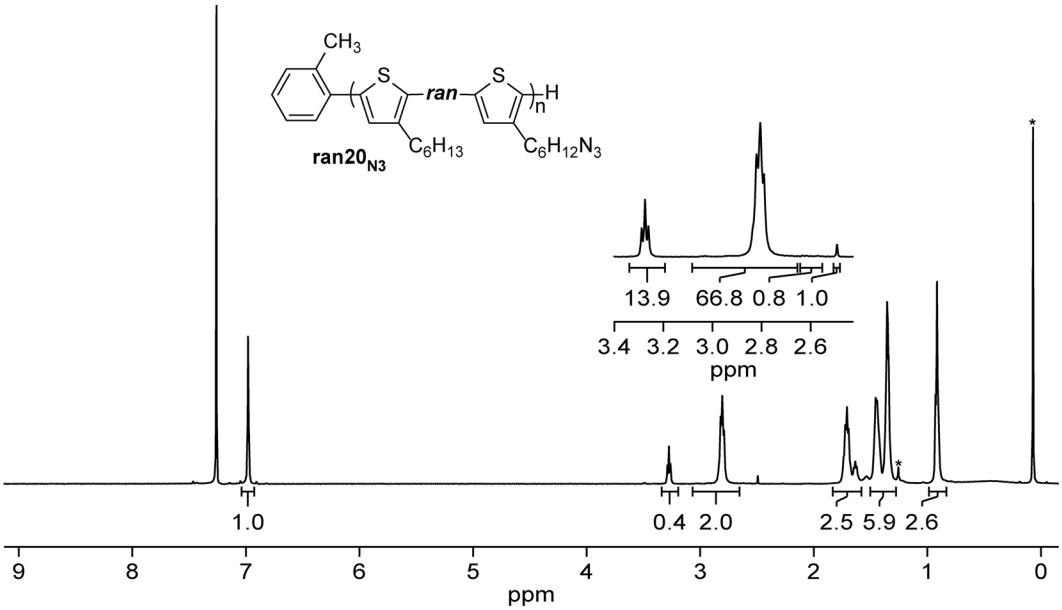

Figure A1.12 ^{1}H NMR Spectrum of ran20$_{N3}$. ^{1}H NMR (500 MHz, $CDCl_3$) δ 6.98 (s, 1H), 3.27 (t, J = 7.0 Hz, 0.5H), 2.80 (t, J = 8.1 Hz, 2H), 1.76–1.60 (m, 2.5H), 1.48–1.29 (m, 6H), 0.98–0.85 (m, 2.5H). *grease. The inset integrals were used to calculate $M_{n,NMR}$ and to determine regioregularity.

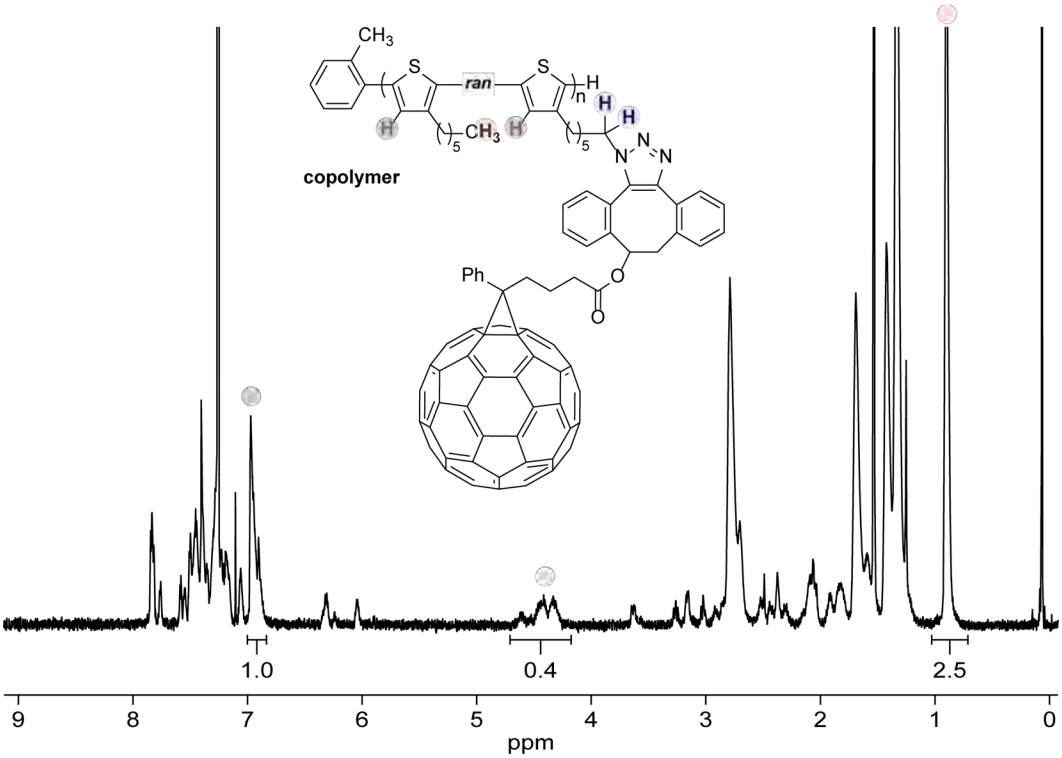

Figure A1.13 ^{1}H NMR Spectrum of copolymer. (700 MHz, $CDCl_3$) δ 7.00–6.85 (m, 1H), 4.70-4.21 (m, 0.4H), 0.96–0.83 (m, 2.5H)

A1.7 Fourier-Transform Infrared Spectroscopy

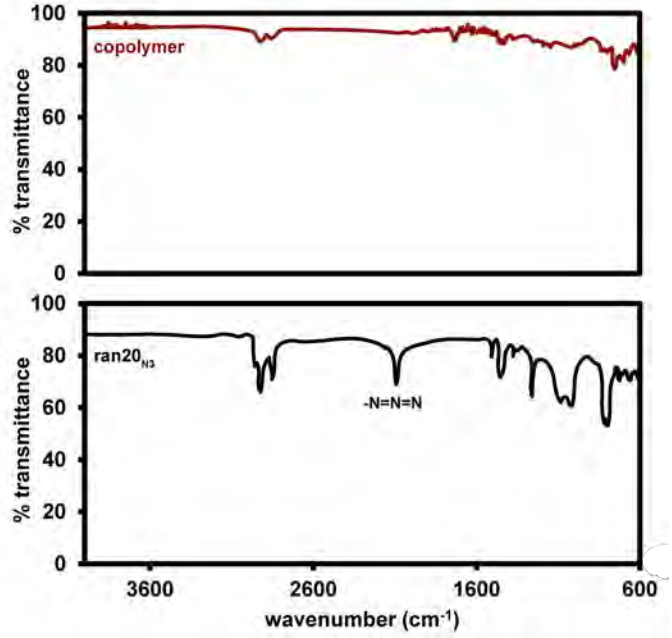

Figure A1.14 Fourier-transform infrared spectra of neat copolymer (red, top) and ran20$_{N3}$ (black, bottom) showing the disappearance of the azide peak at 2092 cm^{-1}

A1.8 Size Exclusion Chromatography Traces

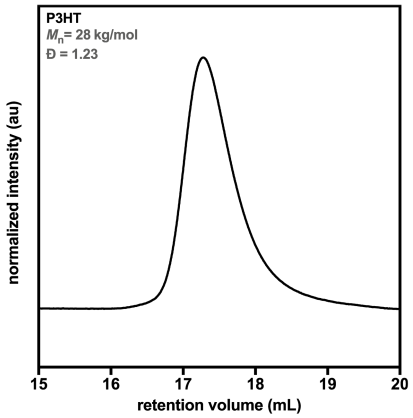

Figure A1.15 Size-exclusion chromatography trace for P3HT

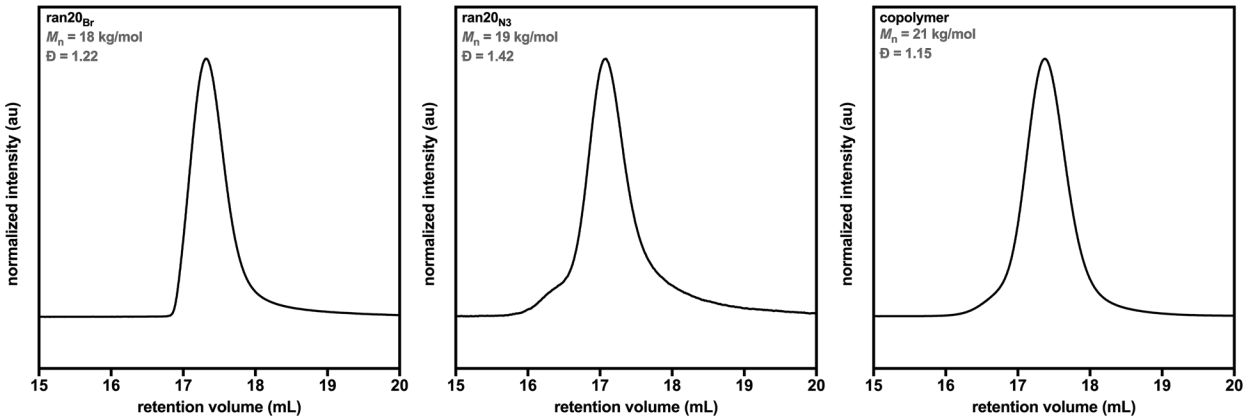

Figure A1.16 Size-exclusion chromatography traces for ran20$_{Br}$, ran20$_{N3}$, and the copolymer

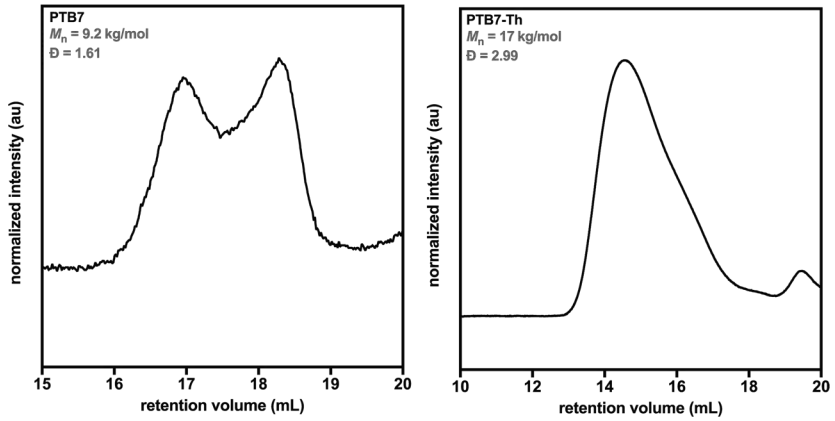

Figure A1.17 Size-exclusion chromatography traces for commercially available polymers PTB7 and PTB7-Th. PffBT4T-2OD was not soluble in THF and was not characterized via SEC.

A1.9 Thin Film Preparation for Optical Microscopy

(A) blends without additives

Table A1-2. Quantities of donor polymers, $PC_{71}BM$, and solvents used to prepare blends without additives

donor	donor mass (mg)	$PC_{71}BM$ mass (mg)	volume o-DCB (μL)	volume CB (μL)
PTB7	7.711	11.569	771	
PTB7-Th	7.585	11.42	759	
PffBT4T-2OD	6.675	7.992	370	370

PTB7 and PTB7-Th. The donor polymer (PTB7 or PTB7-Th) and $PC_{71}BM$ were weighed into a 4 mL vial in a donor:$PC_{71}BM$ ratio 1.0:1.5. To this vial was added a stir bar and *o*-DCB to obtain an overall photoactive solids concentration of 25 mg/mL. The resulting solution was sonicated at rt for 15 min and stirred at 60 °C for 16 h. For each solution, an aliquot (100 μL) was spin-casted onto a glass or fused silica substrate for 120 s at 1000 RPM.

PffBT4T-2OD. PffBT4T-2OD and $PC_{71}BM$ were weighed into a 4 mL vial in a donor:$PC_{71}BM$ ratio of 1.0:1.2. To this vial was added a stir bar and CB/*o*-DCB (50/50 v/v) to obtain an overall photoactive solids concentration of 19.8 mg/mL. The resulting solution was sonicated at rt for 15 min, stirred at 60 °C for 16 h, and stirred an additional 2 h at 110 °C. An aliquot (100 μL) of the solution was spin-cast onto hot glass or fused silica substrates (heated to 110 °C until loading onto spin-coater) for 180 s at 800 RPM.

(B) blends with copolymer

Table A1-3. Quantities of donor polymers, $PC_{71}BM$, and copolymer stock solution used to prepare blends with copolymer

donor	donor mass (mg)	$PC_{71}BM$ mass (mg)	volumer copolymer stock solution (μL)	volume *o*-DCB (μL)
PTB7	4.971	9.347	603	19.5
PTB7-Th	4.851	9.082	588	16.5
PffBT4T-2OD	5.577	8.278	760	

PTB7 and PTB7-Th. The donor polymer (PTB7 or PTB7-Th) and $PC_{71}BM$ were weighed into a 4 mL vial. To this vial was added a stir bar, a 2.06 mg/mL solution of the copolymer in *o*-DCB, and *o*-DCB to obtain a resulting solution with a polymer:$PC_{71}BM$ ratio of 1.0:1.5 and overall photoactive solids concentration of 25 mg/mL. The resulting solution was sonicated at rt for 15 min and stirred at 60 °C for 16 h. For each solution, an aliquot (100 µL) was spin-casted onto a glass or fused silica substrate for 120 s at 1000 RPM.

PffBT4T-2OD. PffBT4T-2OD and $PC_{71}BM$ were weighed into a 4 mL vial. To this vial was added a stir bar and a 1.58 mg/mL solution of the copolymer in *o*-DCB/CB (50/50 v/v) to obtain a solution with a polymer:$PC_{71}BM$ ratio of 1.0:1.2 and an overall photoactive solids concentration of 19.8 mg/mL. The resulting solution was sonicated at rt for 15 min and stirred at 60 °C for 16 h and an additional 2 h at 110 °C. An aliquot (100 µL) of the solution was spin-cast onto hot glass or fused silica substrates (heated to 110 °C until loading onto spin-coater) for 180 s at 800 RPM.

(C) blends with diiodooctane (DIO)

Table A1-4. Quantities of donor polymers, $PC_{71}BM$, and solvents used to prepare blends with DIO

donor	donor mass (mg)	$PC_{71}BM$ mass (mg)	volume o-DCB (µL)	volume CB (µL)	volume DIO (µL)
PTB7	10.115	15.127	979		30.0
PTB7-Th	10.053	15.185	979		30.0
PffBT4T-2OD	6.776	8.143	365	365	19.0

PTB7 and PTB7-Th. The donor polymer (PTB7 or PTB7-Th) and $PC_{71}BM$ were weighed into a 4 mL vial in a donor:$PC_{71}BM$ ratio 1.0:1.5. To this vial was added a stir bar, and *o*-DCB, and DIO to obtain an overall photoactive solids concentration of 25 mg/mL. The resulting solution was sonicated at rt for 15 min and stirred at 60 °C for 16 h. For each solution, an aliquot (100 µL) was spin-casted onto a glass or fused silica substrate for 120 s at 1000 RPM.

PffBT4T-2OD. PffBT4T-2OD and $PC_{71}BM$ were weighed into a 4 mL vial in a PffBT4T-2OD:$PC_{71}BM$ ratio of 1.0:1.2. To this vial was added a stir, *o*-DCB, and CB. The resulting solution was sonicated at rt for 15 min, stirred at 60 °C for 16 h, and stirred for an additional 2 h at 110 °C. To the hot solution was added DIO 10 minutes prior to spin-casting, yielding an overall photoactive

solids concentration of 19.9 mg/mL. An aliquot (100 µL) of the solution was spin-cast onto hot glass or fused silica substrates (heated to 110 °C until loading onto spin-coater) for 180 s at 800 RPM.

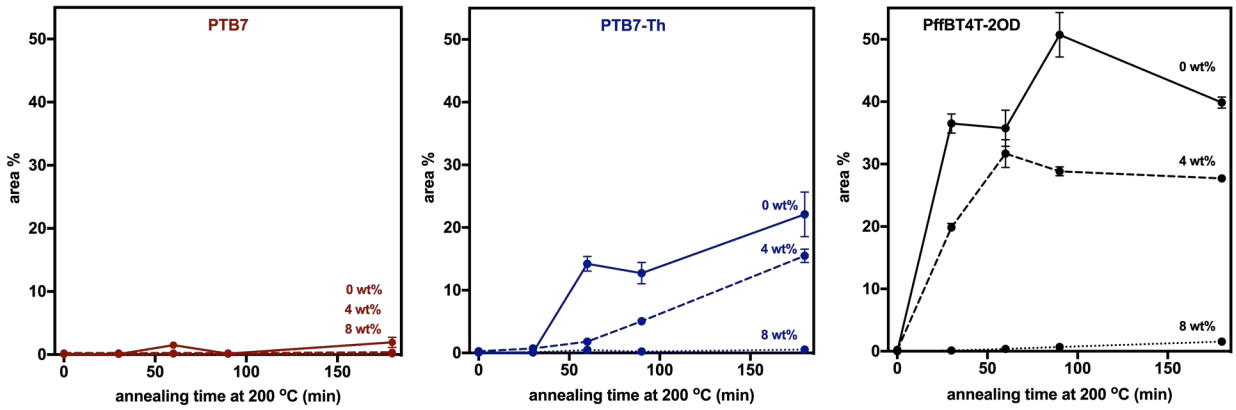

Figure A1.18 The effect of copolymer loading on aggregate area percent for thin film blends of PTB7 (red, left), PTB7-Th (blue, center), or PffBT4T-2OD (black, right) blended with $PC_{71}BM$. The copolymer loading was 0 wt% (solid), 4 wt% (long dashes), or 8 wt% (short dashes) in each case

(D) blends with copolymer and DIO

Table A1-5. Quantities of donor polymers, $PC_{71}BM$, copolymer stock solution, and solvents used to prepare blends with the copolymer and DIO

donor	donor mass (mg)	$PC_{71}BM$ mass (mg)	volume copolymer stock solution (µL)	volume DIO (µL)
PTB7	4.677	8.787	567	18.5
PTB7-Th	4.578	8.568	555	17.0
PffBT4T-2OD	5.561	8.131	729	23.0

PTB7 and PTB7-Th. The donor polymer (PTB7 or PTB7-Th) and $PC_{71}BM$ were weighed into a 4 mL vial. To this vial was added a stir bar and a 2.06 mg/mL solution of copolymer in *o*-DCB to obtain a resulting solution with a polymer:$PC_{71}BM$ ratio of 1.0:1.5. The resulting solution was sonicated at rt for 15 min and stirred at 60 °C for 16 h. To the hot solution was added DIO 10 min prior to spin-casting, yielding an overall photoactive solids concentration of 25 mg/mL. For each

solution, an aliquot (100 μL) was spin-casted onto a glass or fused silica substrate for 120 s at 1000 RPM.

PffBT4T-2OD. PffBT4T-2OD and $PC_{71}BM$ were weighed into a 4 mL vial. To this vial was added a stir bar and a 1.58 mg/mL solution of the copolymer in *o*-DCB/CB (50/50 v/v) to obtain a solution with a polymer:$PC_{71}BM$ ratio of 1.0:1. The resulting solution was sonicated at rt for 15 min and stirred at 60 °C for 16 h and an additional 2 h at 110 °C. To the hot solution was added DIO 10 min prior to spin casting, yielding an overall photoactive solids concentration of 19.8 mg/mL. An aliquot (100 μL) of the solution was spin-cast onto hot glass or fused silica substrates (heated to 110 °C until loading onto spin-coater) for 180 s at 800 RPM.

(E) blends with P3HT

Table A1-6. Quantities of donor polymers, $PC_{71}BM$, and P3HT stock solution used to prepare blends with P3HT

donor	donor mass (mg)	$PC_{71}BM$ mass (mg)	volume P3HT stock solution (μL)	volume *o*-DCB (μL)
PTB7	4.922	9.241	596	19.5
PTB7-Th	4.950	9.284	600	19.0
PffBT4T-2OD	5.519	8.204	753	

PTB7 and PTB7-Th. The donor polymer (PTB7 or PTB7-Th) and $PC_{71}BM$ were weighed into a 4 mL vial. To this vial was added a stir bar, a 2.06 mg/mL solution of P3HT in *o*-DCB, and *o*-DCB to obtain a resulting solution with a polymer:$PC_{71}BM$ ratio of 1.0:1.5 and overall photoactive solids concentration of 25 mg/mL. The resulting solution was sonicated at rt for 15 min and stirred at 60 °C for 16 h. For each solution, an aliquot (100 μL) was spin-casted onto a glass or fused silica substrate for 120 s at 1000 RPM.

PffBT4T-2OD. PffBT4T-2OD and $PC_{71}BM$ were weighed into a 4 mL vial. To this vial was added a stir bar and a 1.58 mg/mL solution of P3HT in *o*-DCB/CB (50/50 v/v) to obtain a solution with a polymer:$PC_{71}BM$ ratio of 1.0:1.2 and an overall photoactive solids concentration of 19.8 mg/mL. The resulting solution was sonicated at rt for 15 min and stirred at 60 °C for 16 h and an additional 2 h at 110 °C. An aliquot (100 μL) of the solution was spin-cast onto hot glass or fused silica substrates (heated to 110 °C until loading onto spin-coater) for 180 s at 800 RPM.

(F) blends with P3HT

Table A1-7. Quantities of donor polymers, $PC_{71}BM$, and P3HT stock solution used to prepare blends with P3HT

donor	donor mass (mg)	$PC_{71}BM$ mass (mg)	volume P3HT stock solution (µL)	volume *o*-DCB (µL)
PTB7	4.922	9.241	596	19.5
PTB7-Th	4.950	9.284	600	19.0
PffBT4T-2OD	5.519	8.204	753	

PTB7 and PTB7-Th. The donor polymer (PTB7 or PTB7-Th) and $PC_{71}BM$ were weighed into a 4 mL vial. To this vial was added a stir bar, a 2.06 mg/mL solution of P3HT in *o*-DCB, and *o*-DCB to obtain a resulting solution with a polymer:$PC_{71}BM$ ratio of 1.0:1.5 and overall photoactive solids concentration of 25 mg/mL. The resulting solution was sonicated at rt for 15 min and stirred at 60 °C for 16 h. For each solution, an aliquot (100 µL) was spin-casted onto a glass or fused silica substrate for 120 s at 1000 RPM.

PffBT4T-2OD. PffBT4T-2OD and $PC_{71}BM$ were weighed into a 4 mL vial. To this vial was added a stir bar and a 1.58 mg/mL solution of P3HT in *o*-DCB/CB (50/50 v/v) to obtain a solution with a polymer:$PC_{71}BM$ ratio of 1.0:1.2 and an overall photoactive solids concentration of 19.8 mg/mL. The resulting solution was sonicated at rt for 15 min and stirred at 60 °C for 16 h and an additional 2 h at 110 °C. An aliquot (100 µL) of the solution was spin-cast onto hot glass or fused silica substrates (heated to 110 °C until loading onto spin-coater) for 180 s at 800 RPM.

Table A1-8. Summary of the blend ratios and solvents used in donor:acceptor thin film blends

additive	donor	polymer:solid additive:$PC_{71}BM$ mass ratio	polymer:$PC_{71}BM$ mass ratio	o-DCB/CB/DIO (v/v/v)	[solids] (mg/mL)
(A) without additives	PTB7	40:0:60	1.0:1.5	100/0/0	25
	PTB7-Th	40:0:60	1.0:1.5	100/0/0	25
	PffBT4T-2OD	45:0:55	1.0:1.2	50/50/0	19.8
(B) copolymer	PTB7	32:8:60	1.0:1.5	100/0/0	25
	PTB7-Th	32:8:60	1.0:1.5	100/0/0	25
	PffBT4T-2OD	37:8:55	1.0:1.2	50/50/0	19.8
(C) DIO	PTB7	40:0:60	1.0:1.5	97/0/3	25
	PTB7-Th	40:0:60	1.0:1.5	97/0/3	25
	PffBT4T-2OD	45:0:55	1.0:1.2	48.5/48.5/3	19.9
(D) copolymer and DIO	PTB7	32:8:60	1.0:1.5	97/0/3	25
	PTB7-Th	32:8:60	1.0:1.5	97/0/3	25
	PffBT4T-2OD	37:8:55	1.0:1.2	48.5/48.5/3	19.8
(E) P3HT	PTB7	32:8:60	1.0:1.5	100/0/0	25
	PTB7-Th	32:8:60	1.0:1.5	100/0/0	25
	PffBT4T-2OD	37:8:55	1.0:1.2	50/50/0	19.8

(F) blends of $PC_{71}BM$ with copolymer or P3HT

copolymer. To a 4 mL vial was added a stir bar, $PC_{71}BM$ (13.413 mg), and a 1.58 mg/mL solution of the copolymer in *o*-DCB/CB (50/50 v/v) (736 μL) to obtain a solution with polymer:$PC_{71}BM$ ratio of 8:92 and an overall photoactive solids concentration of 19.8 mg/mL. The resulting solution was stirred at 60 °C for 18 h. An aliquot (100 μL) of the solution was spin-cast onto a glass substrate for 120 s at 1000 RPM.

P3HT. To a 4 mL vial was added a stir bar, $PC_{71}BM$ (12.556 mg), and a 1.58 mg/mL solution of P3HT in *o*-DCB/CB (50/50 v/v) (689 μL) to obtain a solution with polymer:$PC_{71}BM$ ratio of 8:92 and an overall photoactive solids concentration of 19.8 mg/mL. The resulting solution was stirred at 60 °C for 18 h. An aliquot (100 μL) of the solution was spin-cast onto a glass substrate for 120 s at 1000 RPM.

Thin film annealing

After spin-casting, all films were dried in vacuo for 24 h. The films were then annealed at 200 °C in vacuo, unless otherwise noted.

A1.10 Optical Microscopy Images of Thin Films

(A) without copolymer

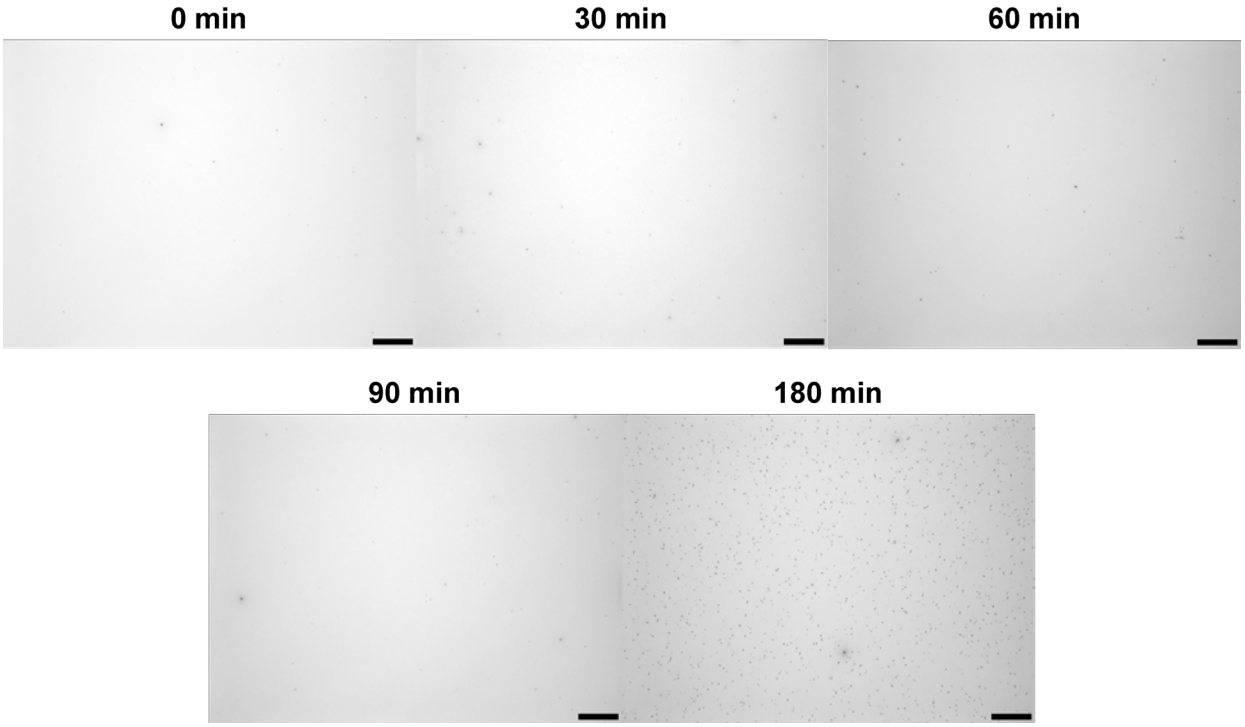

Figure A1.19 Optical microscopy images of PTB7:$PC_{71}BM$ films annealed at 200 °C for a given time. Scale bars represent 30 μm.

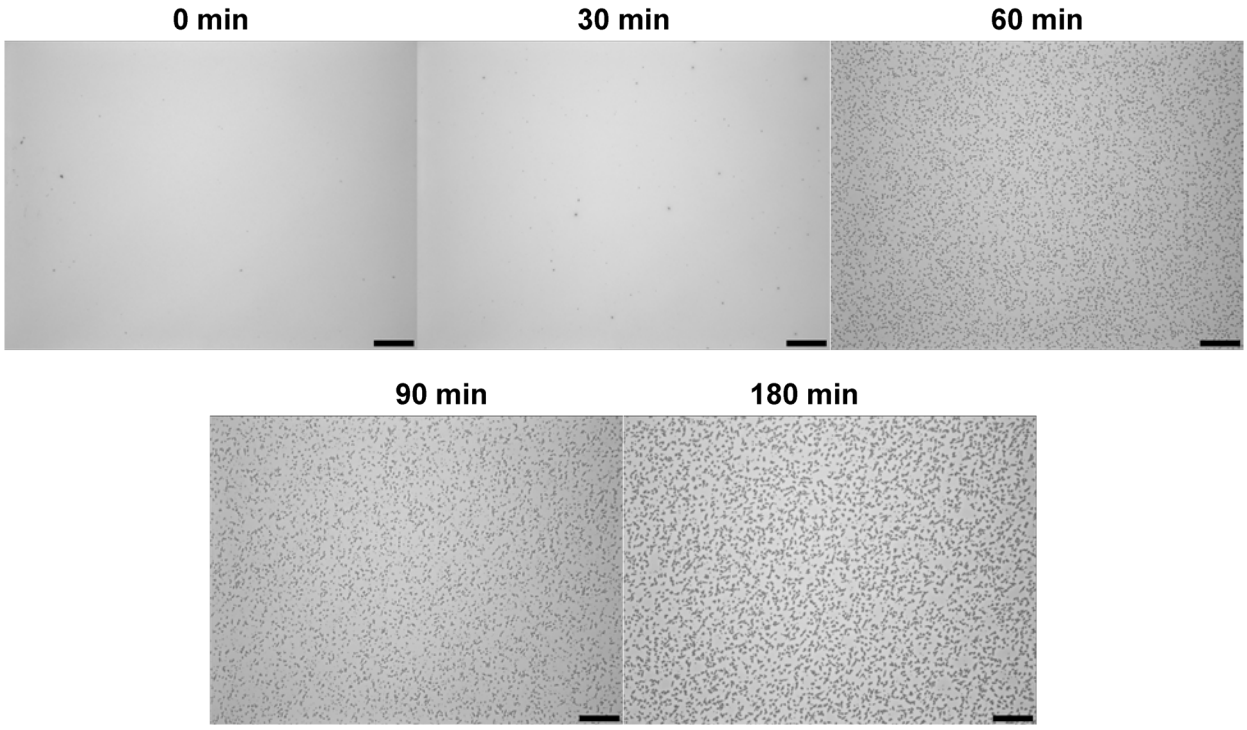

Figure A1.20 Optical microscopy images of PTB7-Th:$PC_{71}BM$ films annealed at 200 °C for a given time. Scale bars represent 30 μm

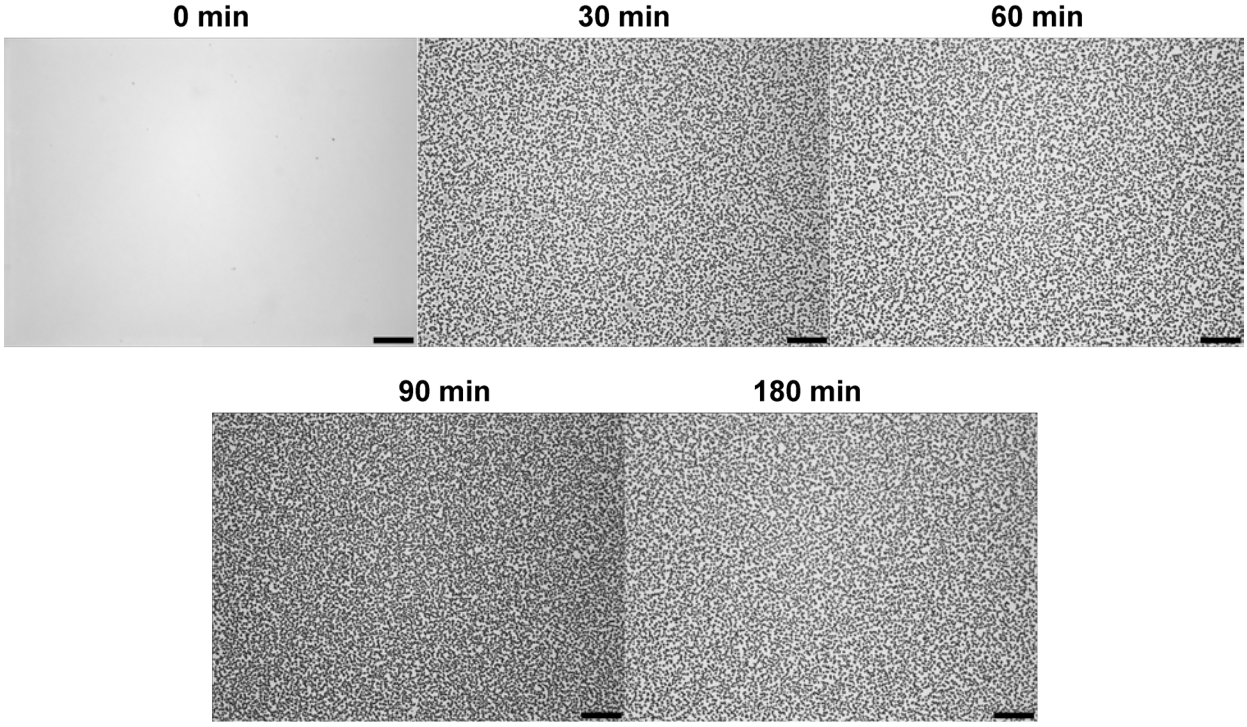

Figure A1.21 Optical microscopy images of PffBT4T-2OD:$PC_{71}BM$ films annealed at 200 °C for a given time. Scale bars represent 30 μm

(B) films with 8 wt% copolymer

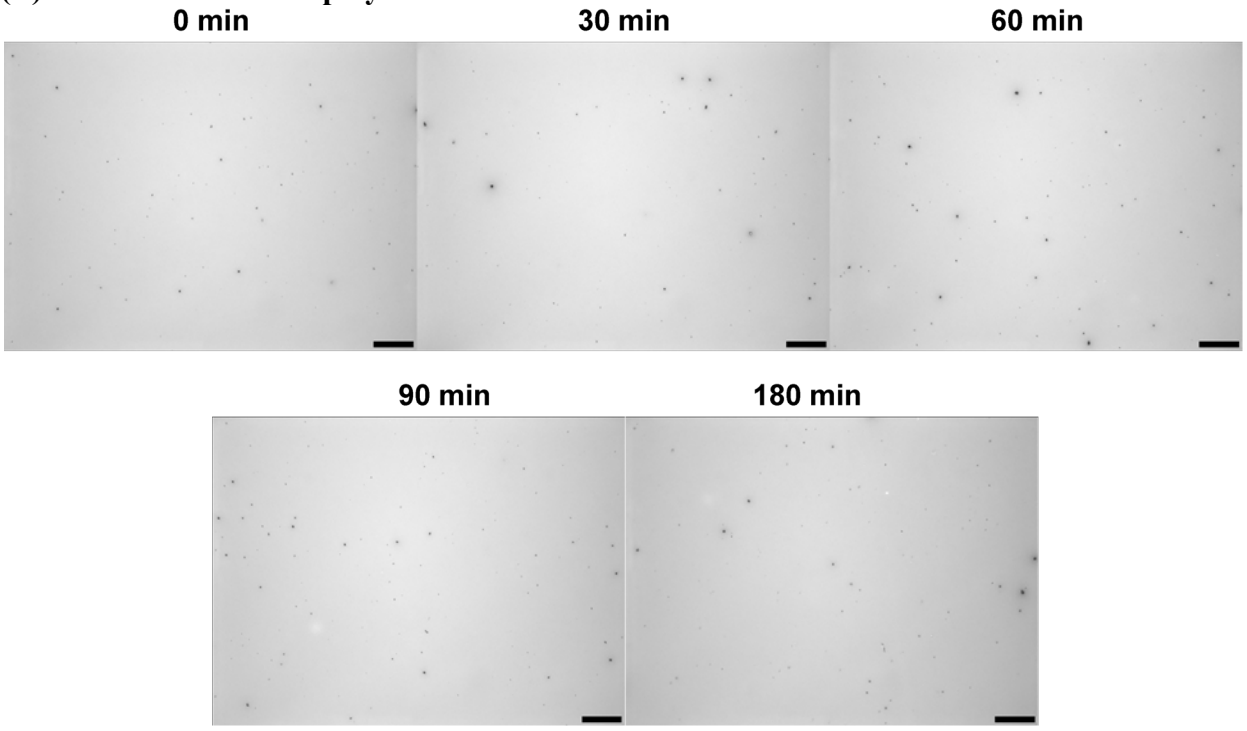

Figure A1.22 Optical microscopy images of PTB7:$PC_{71}BM$ films with 8 wt% copolymer annealed at 200 °C for a given time. Scale bars represent 30 μm

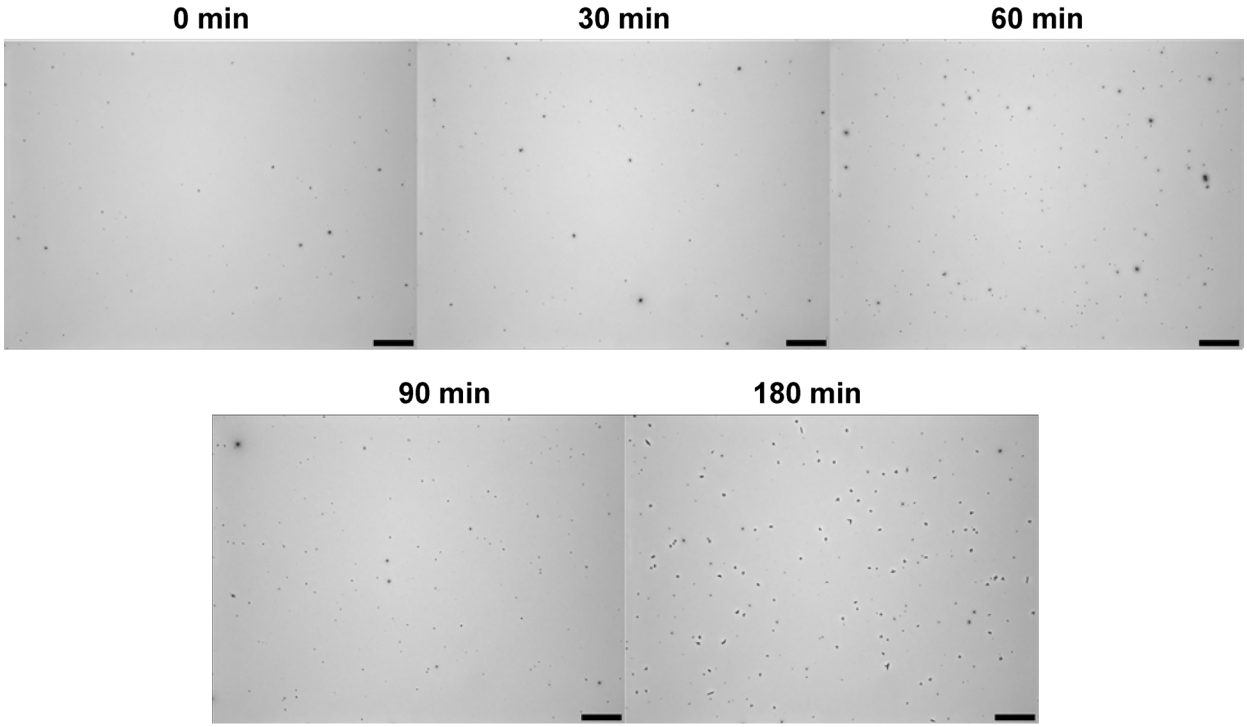

Figure A1.23 Optical microscopy images of PTB7-Th:$PC_{71}BM$ films with 8 wt% copolymer annealed at 200 °C for a given time. Scale bars represent 30 μm

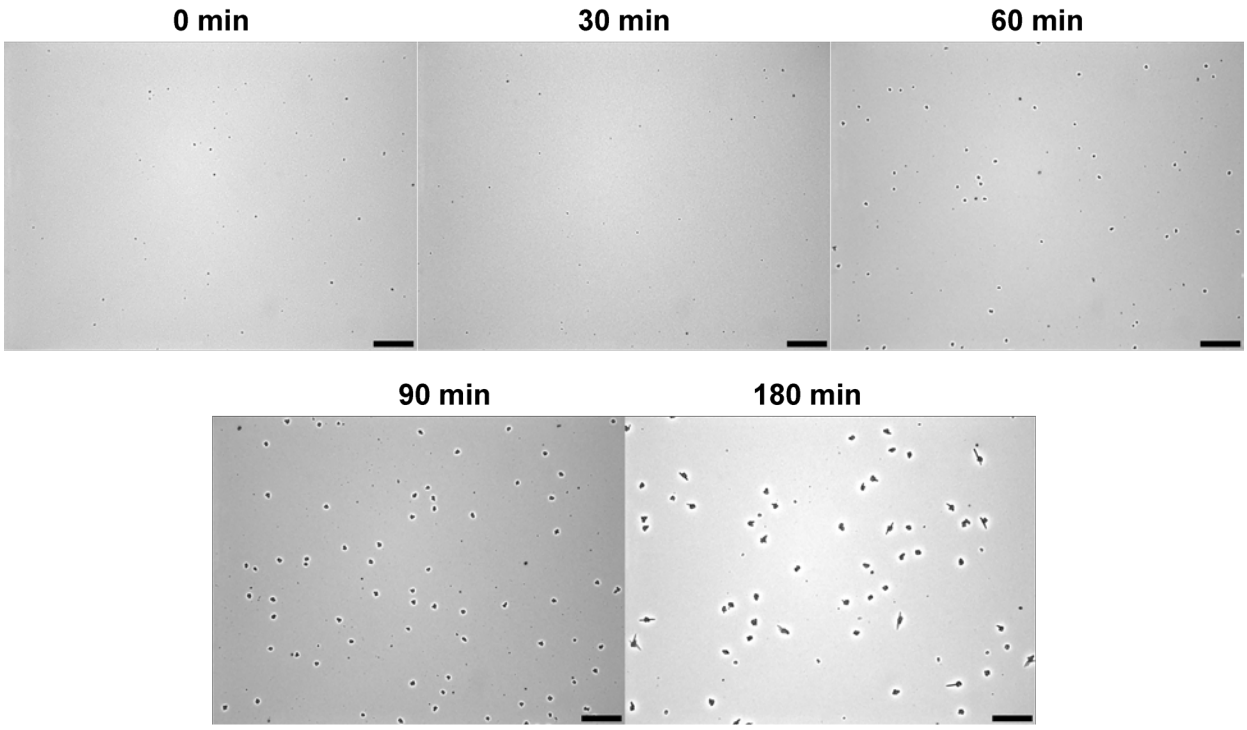

Figure A1.24 Optical microscopy images of PffBT4T-2OD:$PC_{71}BM$ films with 8 wt% copolymer annealed at 200 °C for a given time. Scale bars represent 30 μm

(C) films with 4 wt% copolymer

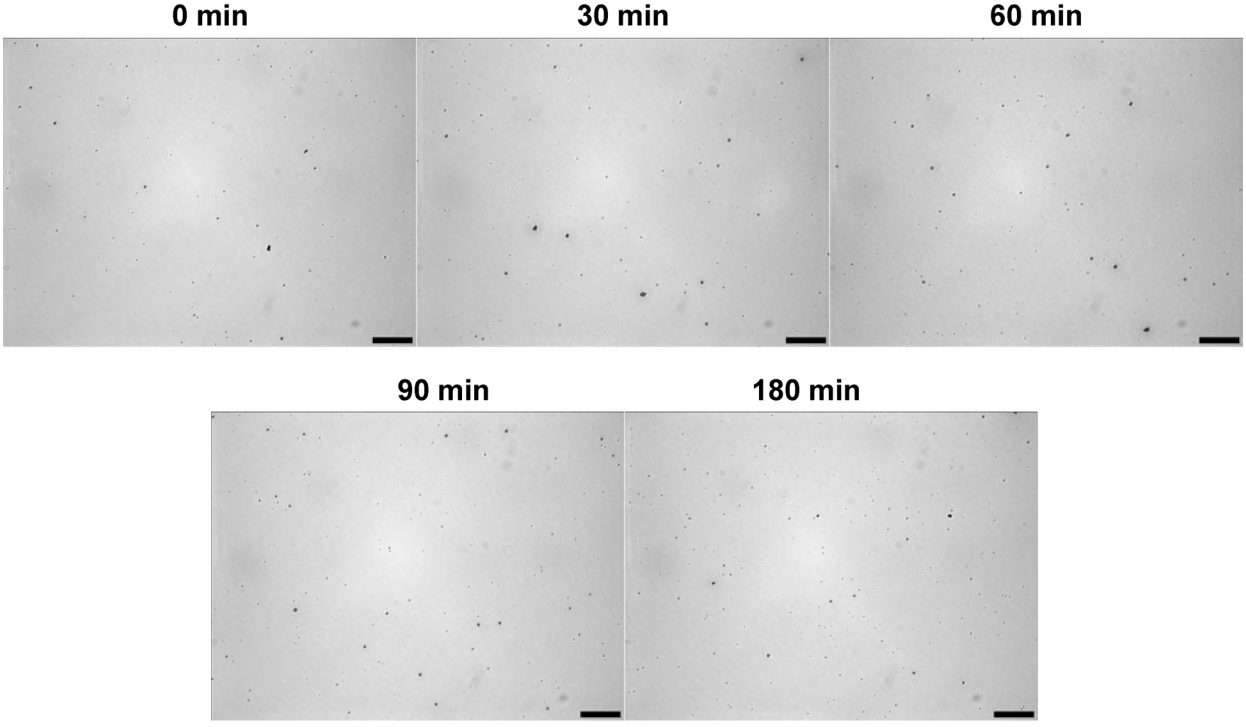

Figure A1.25 Optical microscopy images of PTB7:$PC_{71}BM$ films with 4 wt% copolymer annealed at 200 °C for a given time. Scale bars represent 30 μm

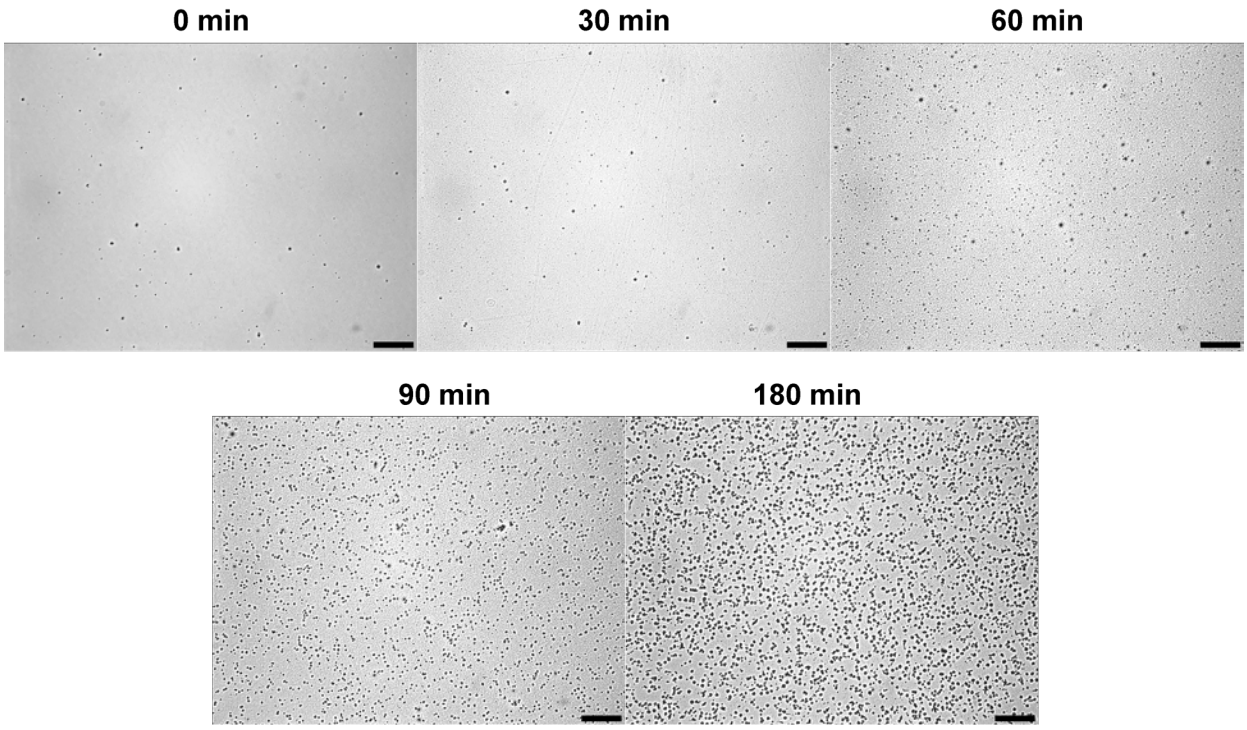

Figure A1.26 Optical microscopy images of PTB7-Th:$PC_{71}BM$ films with 4 wt% copolymer annealed at 200 °C for a given time. Scale bars represent 30 μm

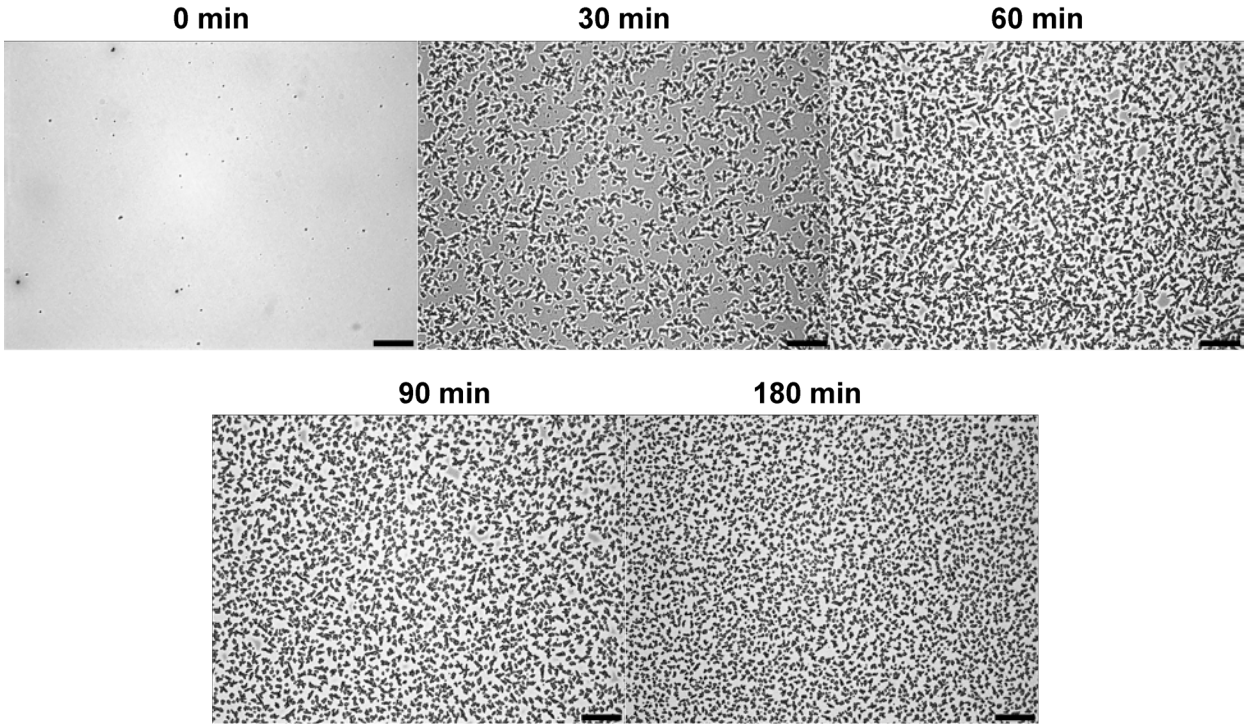

Figure A1.27 Optical microscopy images of PffBT4T-2OD:$PC_{71}BM$ films with 4 wt% copolymer annealed at 200 °C for a given time. Scale bars represent 30 μm.

(D) films with DIO

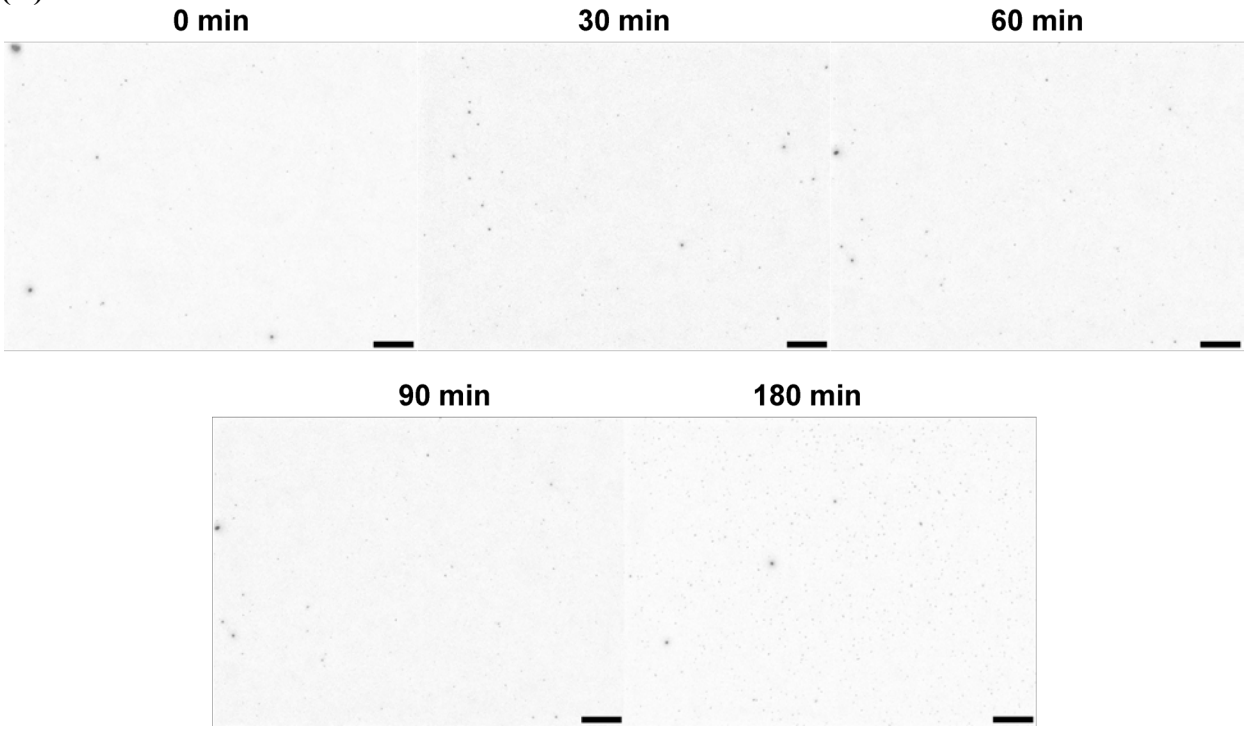

Figure A1.28 Optical microscopy images of PTB7:$PC_{71}BM$ films with 3 vol% DIO annealed at 200 °C for a given time. Scale bars represent 30 μm

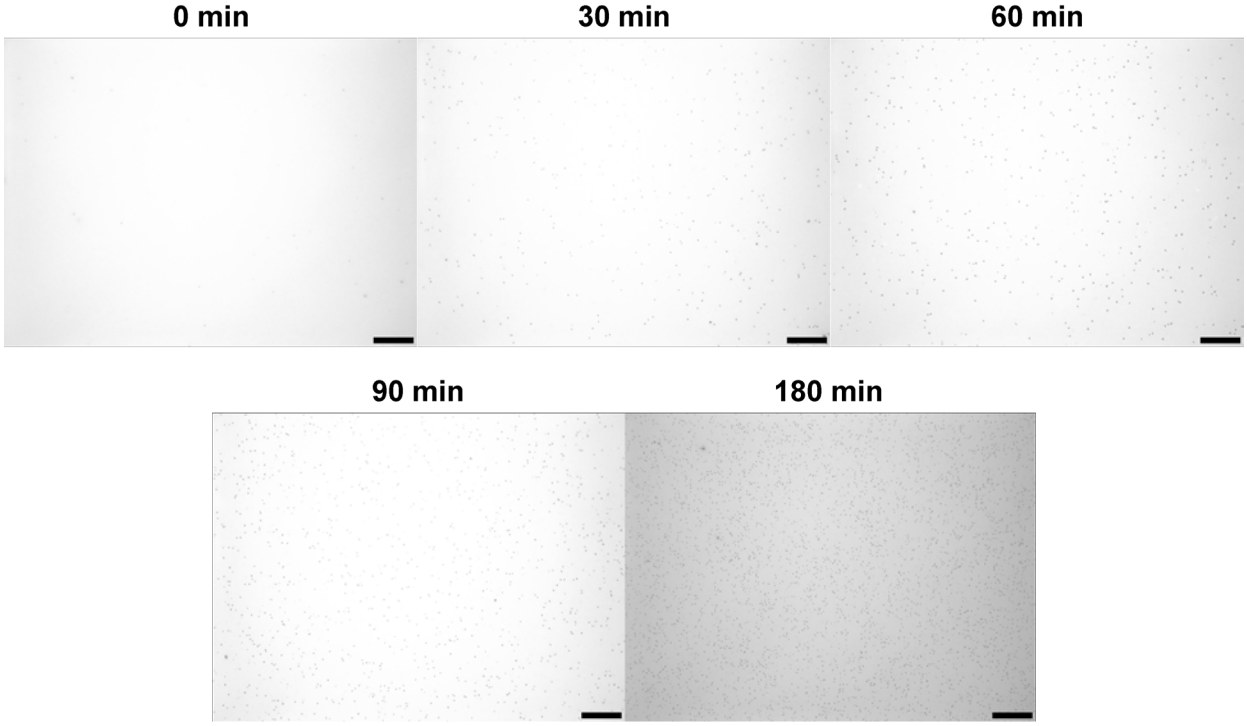

Figure A1.29 Optical microscopy images of PTB7-Th:$PC_{71}BM$ films with 3 vol% DIO annealed at 200 °C for a given time. Scale bars represent 30 μm.

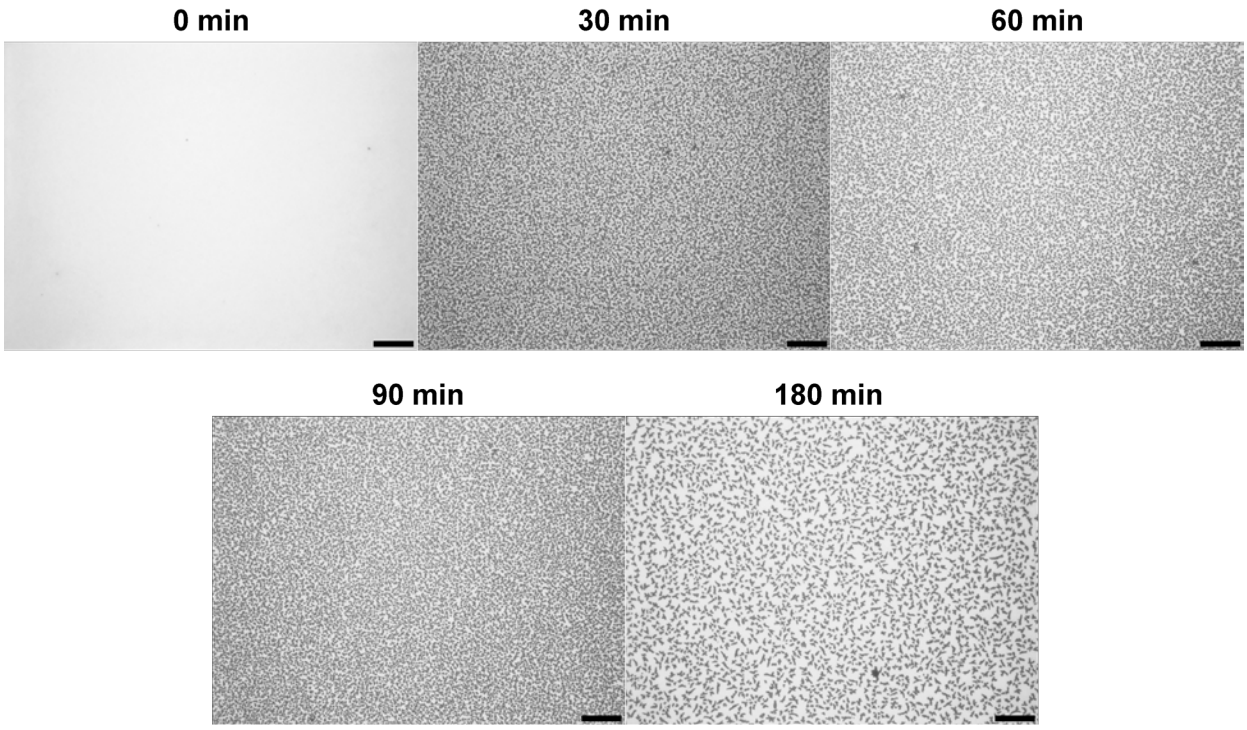

Figure A1.30 Optical microscopy images of PffBT4T-2OD:$PC_{71}BM$ films with 3 vol% DIO annealed at 200 °C for a given time. Scale bars represent 30 μm

(D) films with copolymer and DIO

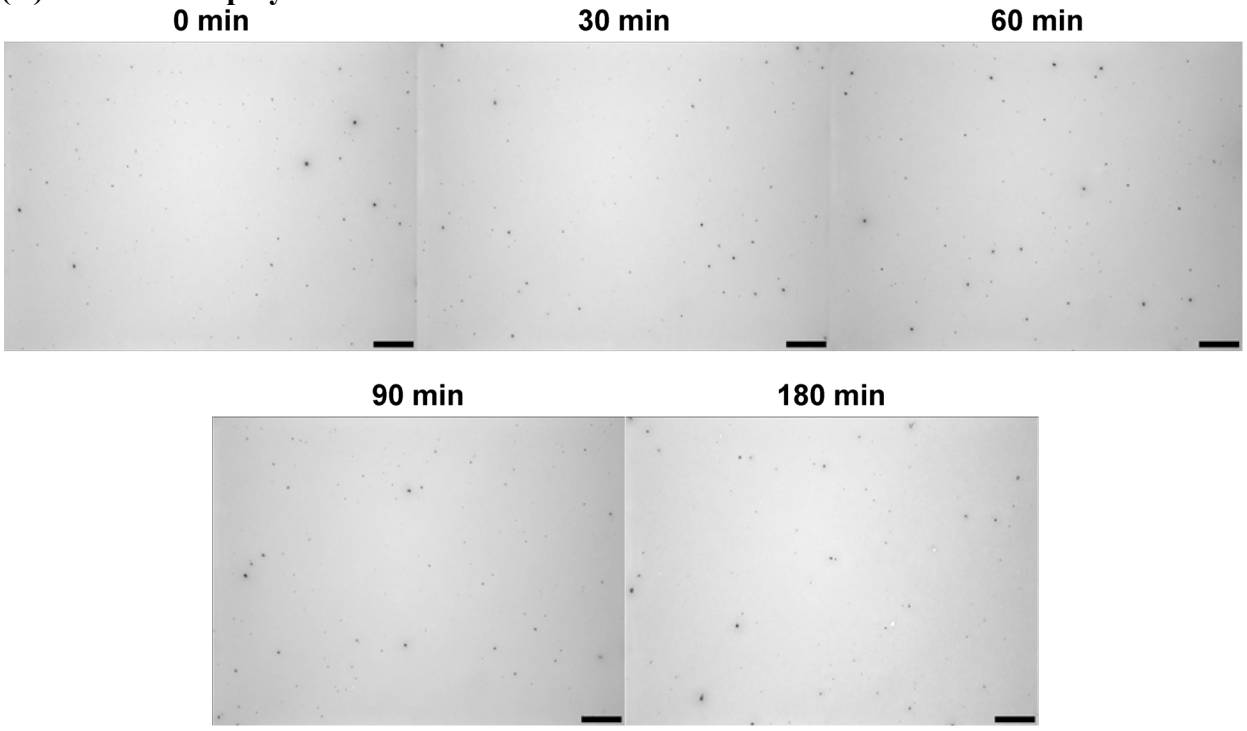

Figure A1.31 Optical microscopy images of PTB7:$PC_{71}BM$ films with 8 wt% copolymer and 3 vol% DIO annealed at 200 °C for a given time. Scale bars represent 30 μm

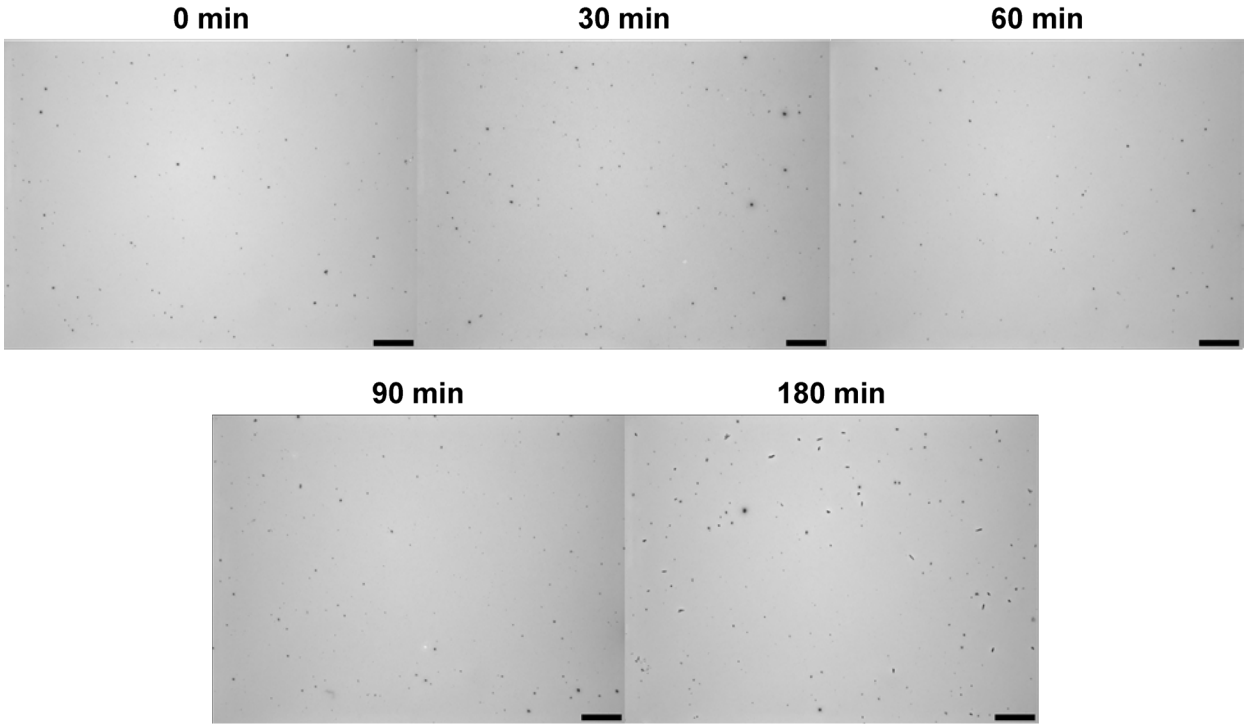

Figure A1.32 Optical microscopy images of PTB7-Th:$PC_{71}BM$ films with 8 wt% copolymer and 3 vol% DIO annealed at 200 °C for a given time. Scale bars represent 30 μm

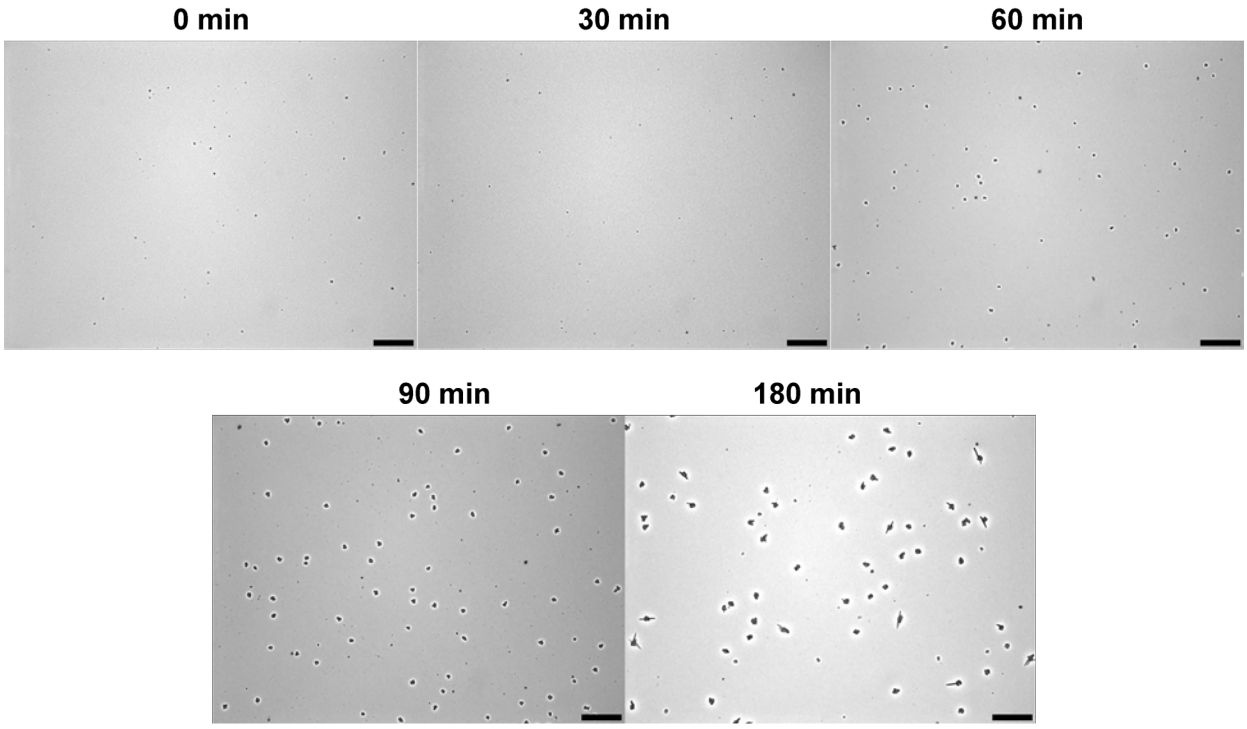

Figure A1.33 Optical microscopy images of PffBT4T-2OD:$PC_{71}BM$ films with 8 wt% copolymer and 3 vol% DIO annealed at 200 °C for a given time. Scale bars represent 30 μm

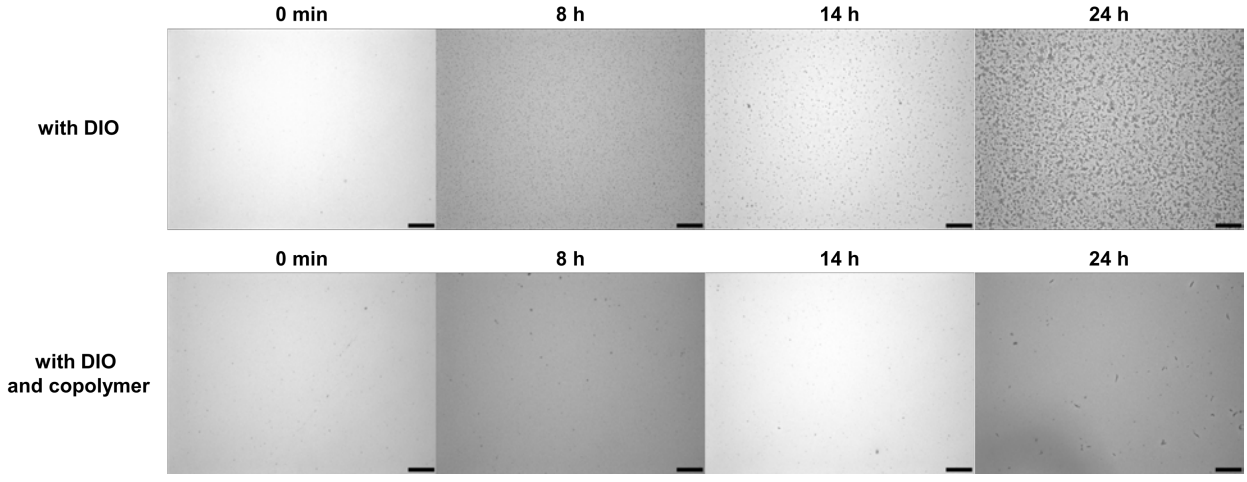

Figure A1.34 Optical microscopy images of PffBT4T-2OD:$PC_{71}BM$ films with 3 vol% DIO (top) and with 3 vol% DIO and 8 wt% copolymer (bottom) annealed at 150 °C under N_2. Scale bars represent 30 μm

(F) films with P3HT

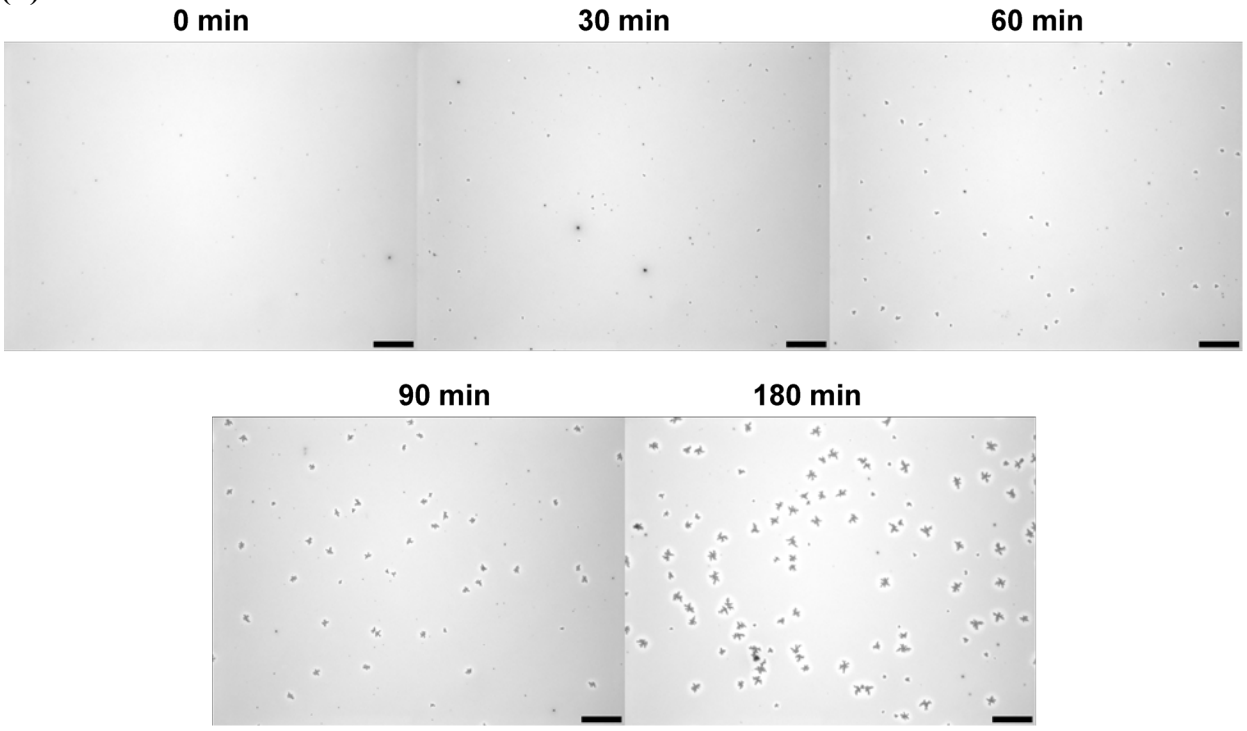

Figure A1.35 Optical microscopy images of PTB7:$PC_{71}BM$ films with 8 wt% P3HT annealed at 200 °C for a given time. Scale bars represent 30 μm

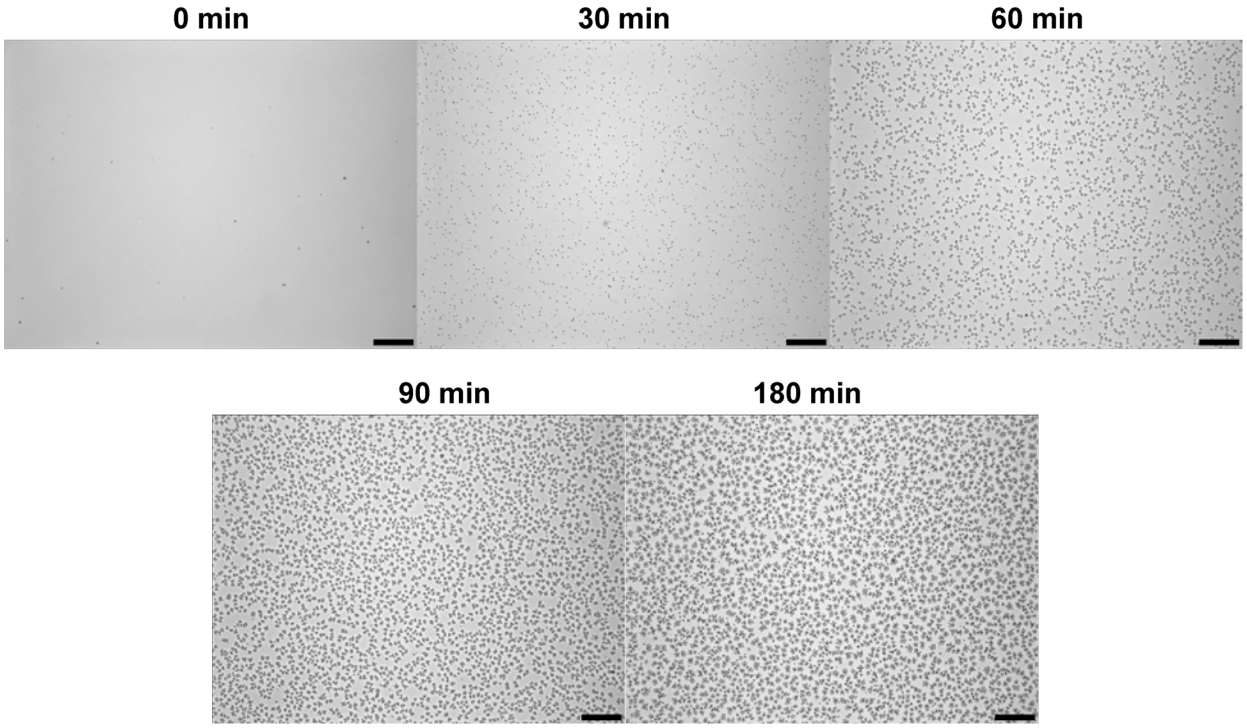

Figure A1.36 Optical microscopy images of PTB7-Th:$PC_{71}BM$ films with 8 wt% P3HT annealed at 200 °C for a given time. Scale bars represent 30 μm

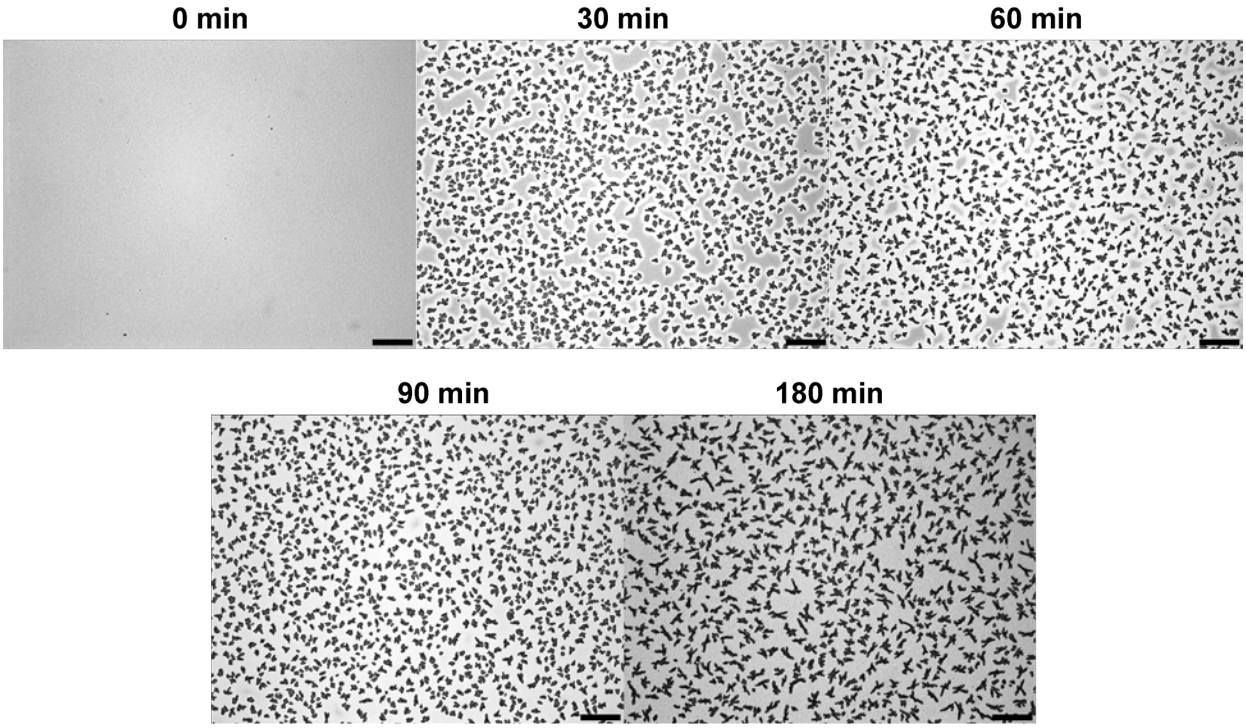

Figure A1.37 Optical microscopy images of PffBT4T-2OD:$PC_{71}BM$ films with 8 wt% P3HT annealed at 200 °C for a given time. Scale bars represent 30 μm

(G) blends of $PC_{71}BM$ with copolymer or P3HT

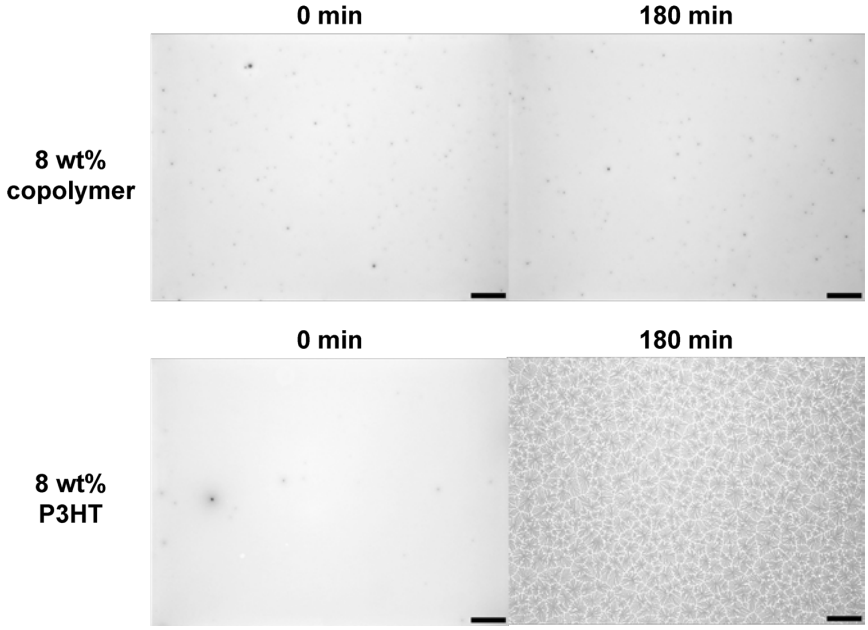

Figure A1.38 Optical microscopy images of $PC_{71}BM$ films with 8 wt% copolymer (top) or P3HT (bottom) annealed at 200 °C for a given time. Scale bars represent 30 μm

A1.11 Surface Contact Angle Data

Thin film preparation

PTB7. To a 4 mL vial equipped with a stir bar was added PTB7 (6.917 mg) and *o*-DCB (277 µL) to yield a final solution with a concentration of 25 mg/mL. The resulting solution was stirred at 60 °C for 18 h. An aliquot of hot solution (100 µL) was spin-cast onto a fused silica substrate at 1000 RPM for 120 s.

PTB7-Th. To a 4 mL vial equipped with a stir bar was added PTB7-Th (6.530 mg) and *o*-DCB (261 µL) to yield a final solution with a concentration of 25 mg/mL. The resulting solution was stirred at 60 °C for 18 h. An aliquot of hot solution (100 µL) was spin-cast onto a fused silica substrate at 1000 RPM for 120 s.

*PffBT4T-2OD.*To a 4 mL vial equipped with a stir bar was added PffBT4T-2OD (6.013 mg) and *o*-DCB (300 µL) to yield a final solution with a concentration of 20 mg/mL. The resulting solution was stirred at 60 °C for 18 h and at 110 °C for an additional 1.5 h. An aliquot of hot solution (100 µL) was spin-cast onto a fused silica substrate at 1500 RPM for 120 s.

$PC_{71}BM$. To a 4 mL vial equipped with a stir bar was added $PC_{71}BM$ (6.397 mg) and $CHCl_3$ (256 µL) to yield a final concentration of 25 mg/mL. The resulting solution was stirred at 60 °C for 18 h. An aliquot of hot solution (100 µL) was spin-cast onto a fused silica substrate at 1000 RPM for 120 s.

Copolymer. To a 4 mL vial equipped with a stir bar was added the copolymer (3.204 mg) and *o*-DCB (214 µL) to yield a final concentration of 15 mg/mL. The resulting solution was stirred at 60 °C for 18 h. An aliquot of hot solution (100 µL) was spin-cast onto a fused silica substrate at 1000 RPM for 120 s.

P3HT. To a 4 mL vial was added P3HT (0.551 mg) and *o*-DCB (344 µL) to give a 1.60 mg/mL solution. This solution was stirred for 16 h at 60 °C starting at 18:30.

Surface contact angle measurements

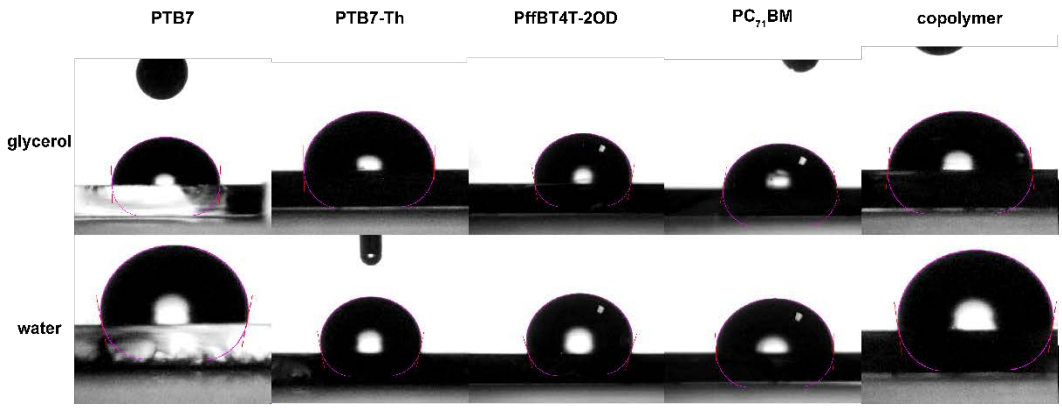

Figure A1.39 Surface contact angles for PTB7, PTB7-Th, PffBT4T-2OD, $PC_{71}BM$, and the copolymer.

Table A1-9 Water and glycerol contact angles for thin films of the donor polymers, the copolymer, and $PC_{71}BM$.

compound	water contact angle	glycerol contact angle
PTB7	99 ± 2°	91 ± 1°
PTB7-Th	101 ± 3°	91 ± 2°
PffBT4T-2OD	108 ± 2°	97 ± 2°
$PC_{71}BM$	90 ± 2°	78 ± 2°
copolymer	98 ± 1°	84 ± 1°
P3HT	108.3 ± 0.5°	96.4 ± 0.7°

Table A1-10 Surface energies for thin films of the donor polymers the copolymer, and $PC_{71}BM$

compound	γ_i^d (mj/m^2)	γ_i^p(mj/m^2)	γ_i^{total}(mj/m^2)
PTB7	14	7.9	21.9
PTB7-Th	15	6.4	21.4
PffBT4T-2OD	15	4.2	19.2
$PC_{71}BM$	18	10	28.0
copolymer	23	4.8	27.8
P3HT	18	2.8	20.7

Surface energy calculations

The polar and dispersive components of the surface energy for each material (*i*) were calculated with the Wu harmonic mean method (Eq 1).[3,4] Literature values were used for the surface energy of water and glycerol.[8]

$$\begin{cases} \gamma_1(\cos\theta+1)=\frac{4\gamma_1^d\gamma_i^d}{\gamma_1^d+\gamma_i^d}+\frac{4\gamma_1^p\gamma_i^p}{\gamma_1^p+\gamma_i^p} \\ \gamma_2(\cos\theta+1)=\frac{4\gamma_2^d\gamma_i^d}{\gamma_2^d+\gamma_i^d}+\frac{4\gamma_2^p\gamma_i^p}{\gamma_2^p+\gamma_i^p} \end{cases} \quad (1)$$

where γ_1 = 72.8 mJ/m^2 (water), and γ_2 = 64.0 mJ/m^2 (glycerol)

The polar and dispersive components of the surface energy were used to calculate the total surface energy with Eq 2:[9]

$$\gamma_i=\gamma_i^d+\gamma_i^p \quad (2)$$

Table A1-11 Interfacial surface energies for each donor polymer, $PC_{71}BM$, or the copolymer with each of the other blend components

compound	$\gamma_{polymer\text{-}PCBM}$ (mj/m^2)	$\gamma_{donor\text{-}copolymer}$ (mj/m^2)	$\gamma_{PCBM\text{-}copolymer}$ (mj/m^2)
PTB7	0.586	0.548	-
PTB7-Th	0.688	0.647	-
PffBT4T-2OD	1.24	1.18	-
$PC_{71}BM$	-	-	0.000615

Table A1-12 Interfacial surface energies for each donor polymer, $PC_{71}BM$, or P3HT with each of the other blend components

compound	$\gamma_{polymer\text{-}PCBM}$ (mj/m^2)	$\gamma_{donor\text{-}P3HT}$ (mj/m^2)	$\gamma_{PCBM\text{-}P3HT}$ (mj/m^2)
PTB7	0.586	0.0201	-
PTB7-Th	0.688	0.00601	-
PffBT4T-2OD	1.24	0.0438	-
$PC_{71}BM$	-	-	0.821

Interfacial surface energy calculations

The interfacial surface energy between two components (i, j) was calculated with Eq 3:[9]

$$\gamma_{i-j}=\gamma_i+\gamma_j-2\sqrt{\gamma_i\gamma_j}e^{-\beta\left(\gamma_i-\gamma_j\right)^2} \quad \beta=1.15\times10^{-4} \tag{3}$$

Table A1-13 Wetting coefficients for the copolymer in various donor:$PC_{71}BM$ blends

donor	copolymer ω_c	P3HT ω_c
PTB7	-0.94	1.37
PTB7-Th	-0.94	1.19
PffBT4T-2OD	-0.96	0.63

Wetting coefficient calculations

The wetting coefficient for the copolymer as the third component (k) in a three-component mixture (i, j, k) was calculated with Eq 4:[10]

$$\omega_k=\frac{(\gamma_{k-j}-\gamma_{k-i})}{\gamma_{i-j}} \tag{4}$$

Table A1-14 Flory-Huggins interaction parameters calculated from surface energies of the copolymer with various donors and acceptors

material	γ_i^{total}(mj/m^2)	$\chi_{i,copolymer}$K
PTB7	21.9	0.36
PTB7-Th	21.4	0.50
PffBT4T-2OD	19.2	0.87
$PC_{71}BM$	28.0	0.0036
copolymer	27.8	-

Flory-Huggins interaction parameter (χ) calculations

The Flory-Huggins interaction parameter (χ) between the copolymer and the different blend components can be estimated by taking advantage of the relationship between the surface energy (γ) and the Hildebrand solubility parameter (δ) (Eq 5):

$$\delta = A\sqrt{\gamma} \tag{5}$$

where A is a proportionality constant (e.g., 116 $\times 10^3$ $m^{-1/2}$ for P3HT).[11,12]

The relationship between the Flory-Huggins interaction parameter (χ) and Hildebrandt solubility parameters of the copolymer and a blend component, *i*, is shown in Eq 6:

$$\chi_{copolymer,i} = \frac{V_0}{RT}\left(\delta_{copolymer} - \delta_i\right)^2 \quad (6)$$

where V_0 is the molar volume of the copolymer.

Substituting Eq 5 into Eq 6 yields Eq 7:[12]

$$X = K\left(\sqrt{\gamma_{copolymer}} - \sqrt{\gamma_i}\right)^2 \quad (7)$$

where $K = \frac{V_o A^2}{RT}$. Reporting the Flory-Huggins interaction parameter in terms of K enables numerical values to be generated without determining the molar volume of the copolymer segment (V_0).

A1.12 Differential Scanning Calorimetry

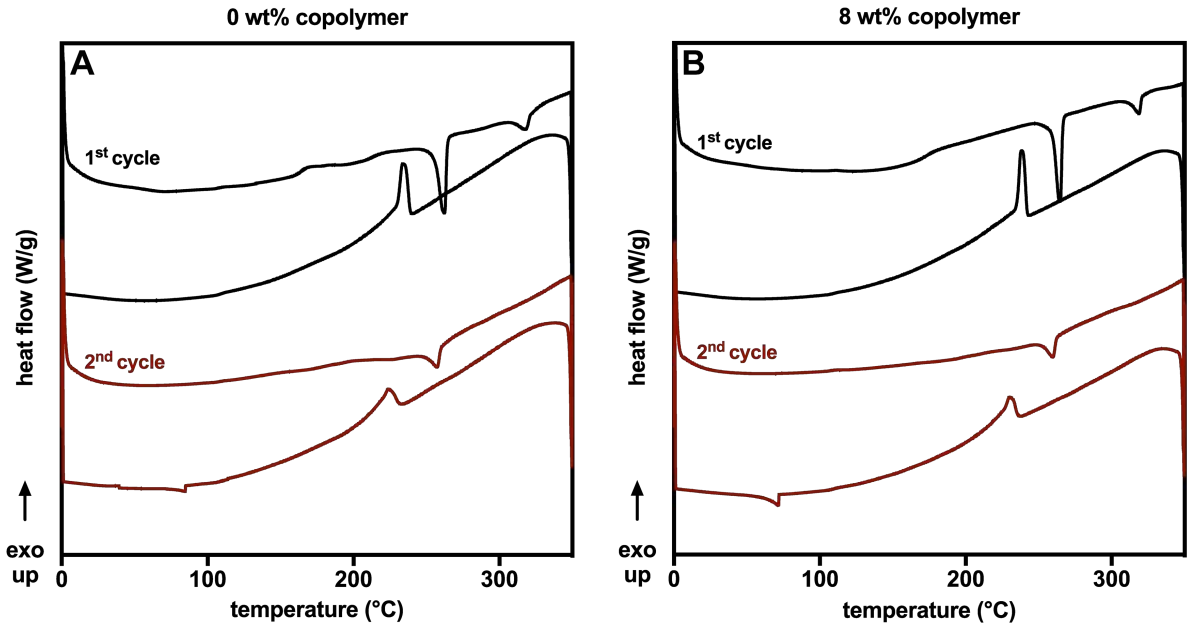

Figure A1.40 DSC thermograms PffBT4T-2OD:$PC_{71}BM$ blends with (A) 0 wt% or (B) 8 wt% copolymer showing both the first cycle (black) and the second cycle (red). The melting point for $PC_{71}BM$ (T_m = 318 °C) is evident only on the 1st heating cycle and $PC_{71}BM$ crystallization is not observed from the melt

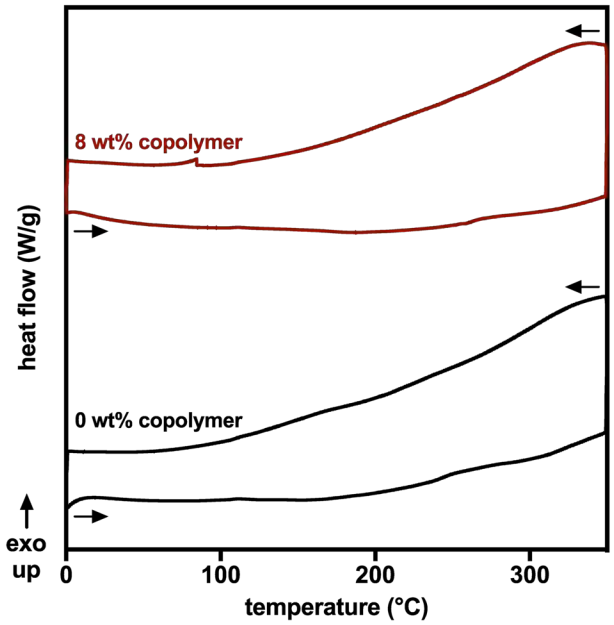

Figure A1.41 Thermogram of the 2nd cycle for $PC_{71}BM$ blended with 0 wt% (black) or 8 wt% (red) copolymer. Arrows indicate direction of heating (pointing right) and cooling (pointing left). No $PC_{71}BM$ crystallization is observed

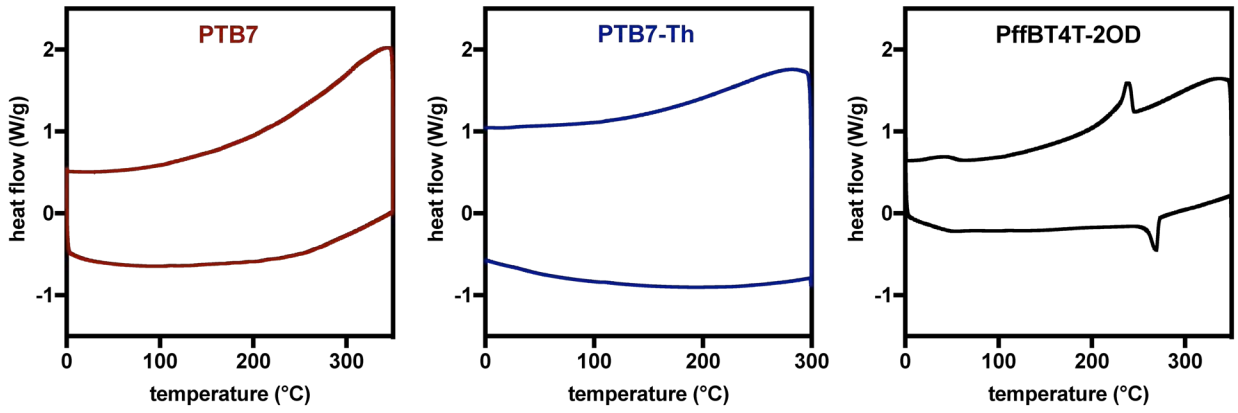

Figure A1.42 Thermograms of the 2nd cycle for neat PTB7 (left), PTB7-Th (middle), and PffBT4T-2OD (right)

A1.13 Photocurrent and Device Performance Data

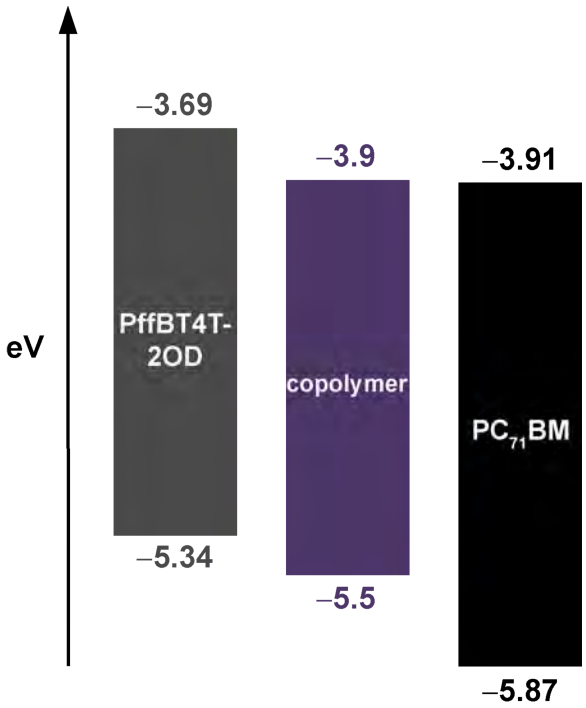

Figure A1.43 Energy level diagram for the active layer materials PffBT4T-2OD (grey),[13] copolymer (purple),[1] and $PC_{71}BM$ (black).[14]

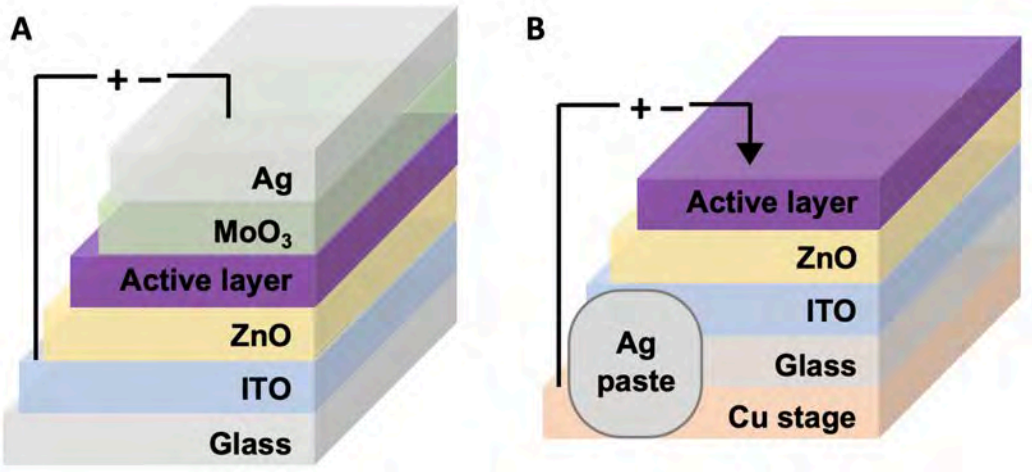

Figure A1.44 (A) Inverted structure of bulk heterojunction solar cell device and (B) structure of samples for triboindentation measurements; Ag paste connects the ITO layer to the copper stage.

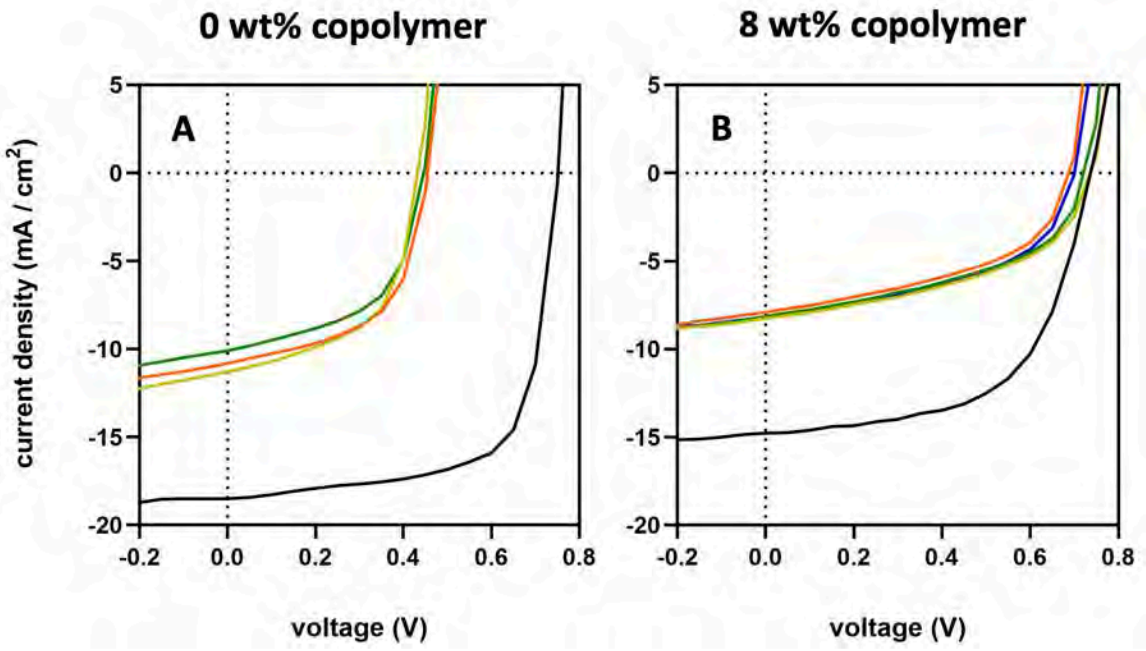

Figure A1.45 Representative current-voltage data for the bulk he terojunction devices. The device active layer is composed of PffBT4T-2OD:$PC_{71}BM$ blend with (A) 0 wt% and (B) 8 wt% copolymer additives. Thermal annealing at 150 °C for 0 min (black), 30 min (orange), 60 min (yellow), 90 min (green), 180 min (blue, B only)

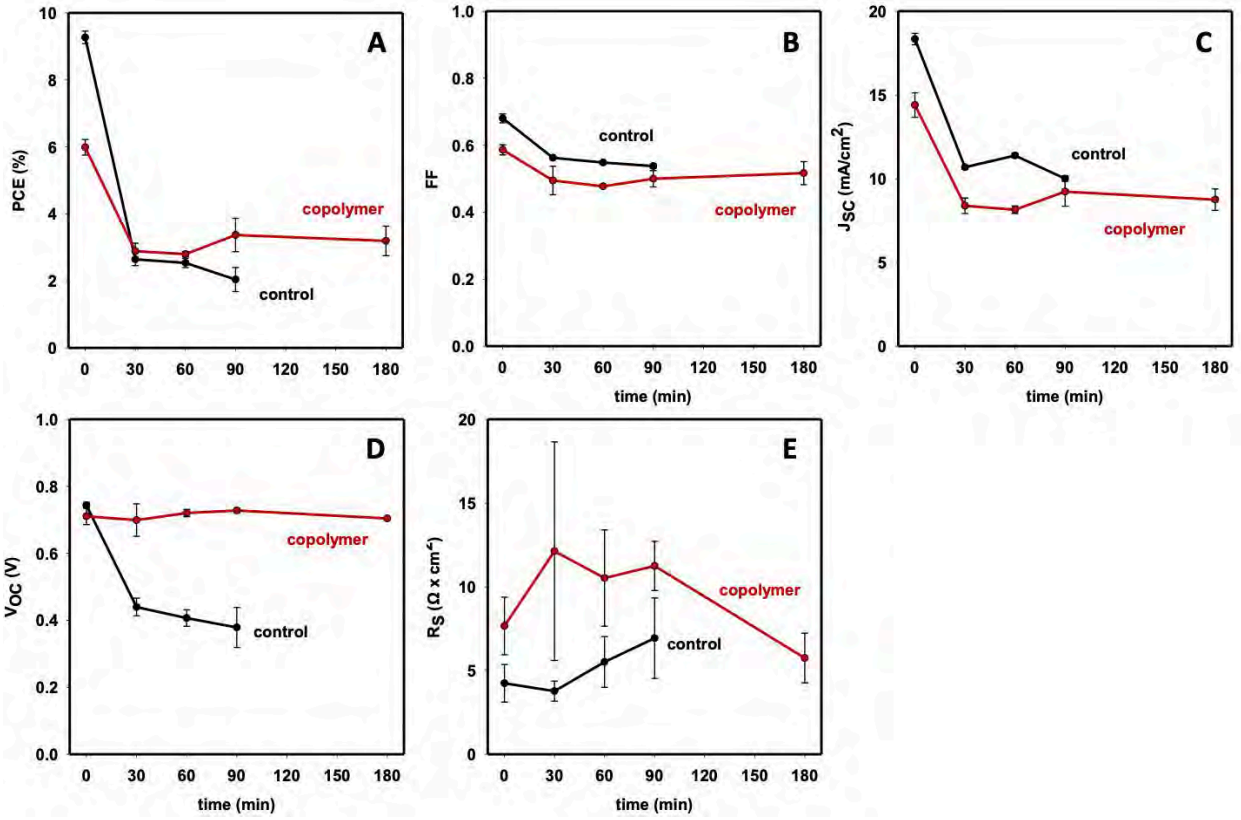

Figure A1.46 Performance data for bulk heterojunction devices with active layers composed PffBT4T-2OD:$PC_{71}BM$ blend with 0 wt% (black circles) or 8 wt% (red circles) copolymer. (A) power conversion efficiency (PCE), (B) fill factor (FF) (C) short circuit current (J_{SC}), (D) open circuit voltage (V_{OC}) (E) series resistance (R_S) as a function of annealing time at 150 °C. Each data point represents an average of six measurements obtained from three different devices fabricated on two different substrates

Table A1-15 All measured parameters for annealed bulk heterojunction devices with active layers composed PffBT4T-2OD:$PC_{71}BM$ blend with or without copolymer

copolymer	Annealing temp & time	PCE (%)	FF	J_{SC} (mA/cm^2)	V_{OC} (V)	R_S ($\Omega \times cm^2$)	R_{sh} ($\Omega \times cm^2$)
0 wt%	not annealed	9.3 ± 0.2	0.7 ± 0.0	18.3 ± 0.3	0.7 ± 0.0	4.2 ± 1.1	808.8 ± 360.8
	150 °C, 30min	2.6 ± 0.2	0.6 ± 0.0	10.7 ± 0.1	0.4 ± 0.0	3.8 ± 0.6	199.5 ± 7.4
	150 °C, 60min	2.5 ± 0.1	0.5 ± 0.0	11.4 ± 0.1	0.4 ± 0.0	5.5 ± 1.5	166.0 ± 17.7
	150 °C, 90min	2.0 ± 0.4	0.5 ± 0.0	10.0 ± 0.2	0.4 ± 0.1	6.9 ± 2.4	168.9 ± 26.6
	150 °C, 180min	fully degraded					
8 wt%	not annealed	6.0 ± 0.2	0.6 ± 0.0	14.4 ± 0.7	0.7 ± 0.0	7.7 ± 1.7	454.4 ± 52.3
	150 °C, 30min	2.9 ± 0.2	0.5 ± 0.0	8.4 ± 0.5	0.7 ± 0.0	12.1 ± 6.5	279.8 ± 12.9
	150 °C, 60min	2.8 ± 0.1	0.5 ± 0.0	8.1 ± 0.2	0.7 ± 0.0	10.5 ± 2.9	281.3 ± 20.1
	150 °C, 90min	3.4 ± 0.5	0.5 ± 0.0	9.2 ± 0.9	0.7 ± 0.0	11.2 ± 1.5	256.7 ± 13.3
	150 °C, 180min	3.2 ± 0.4	0.5 ± 0.0	8.7 ± 0.6	0.7 ± 0.0	5.7 ± 1.5	306.1 ± 11.1
0 wt%	200 °C, 90min	0.6 ± 0.1	0.6 ± 0.0	1.8 ± 0.3	0.6 ± 0.0	55.3 ± 12.3	-
8 wt%		0.5 ± 0.0	0.5 ± 0.0	2.3 ± 0.2	0.5 ± 0.0	46.8 ± 4.6	-

A1.14 Optical Microscopy Images of Devices

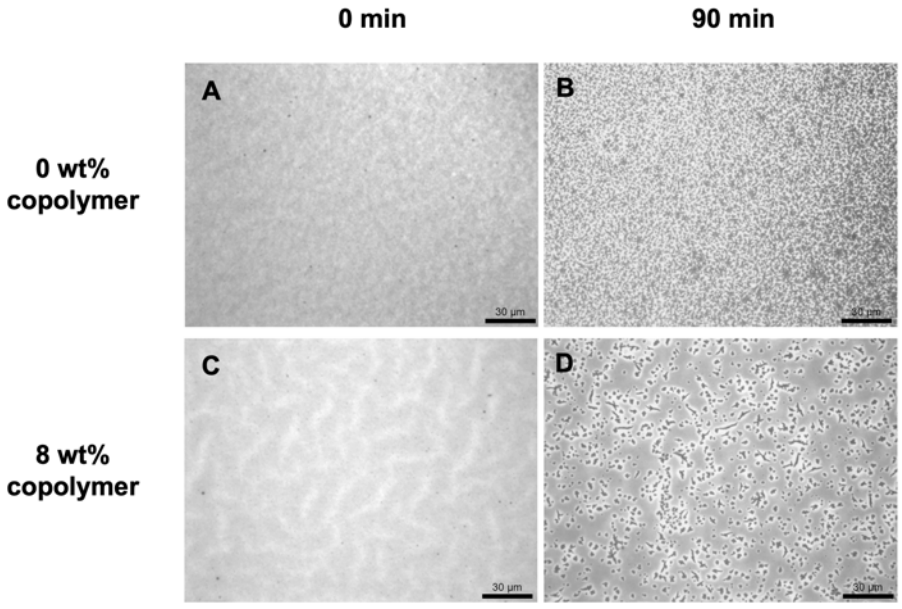

Figure A1.47 Optical microscopy images of PffBT4T-2OD:$PC_{71}BM$ devices with 3 vol% DIO annealed for 0 min (A, C) or 90 min (B, D) at 200 °C with 0 wt% (top) or 8 wt% (bottom) copolymer.

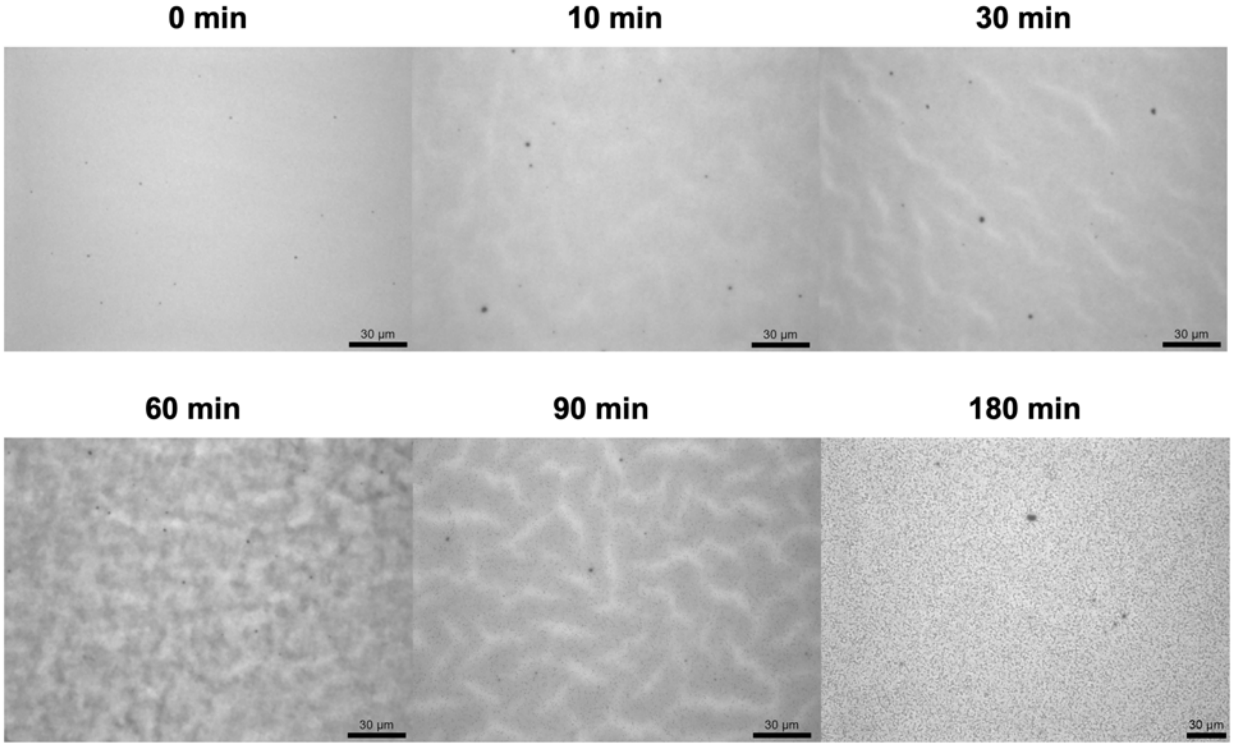

Figure A1.48 Optical microscopy images of PffBT4T-2OD:$PC_{71}BM$ devices with 3 vol% DIO annealed at 150 °C for a given time. Scale bars represent 30 µm

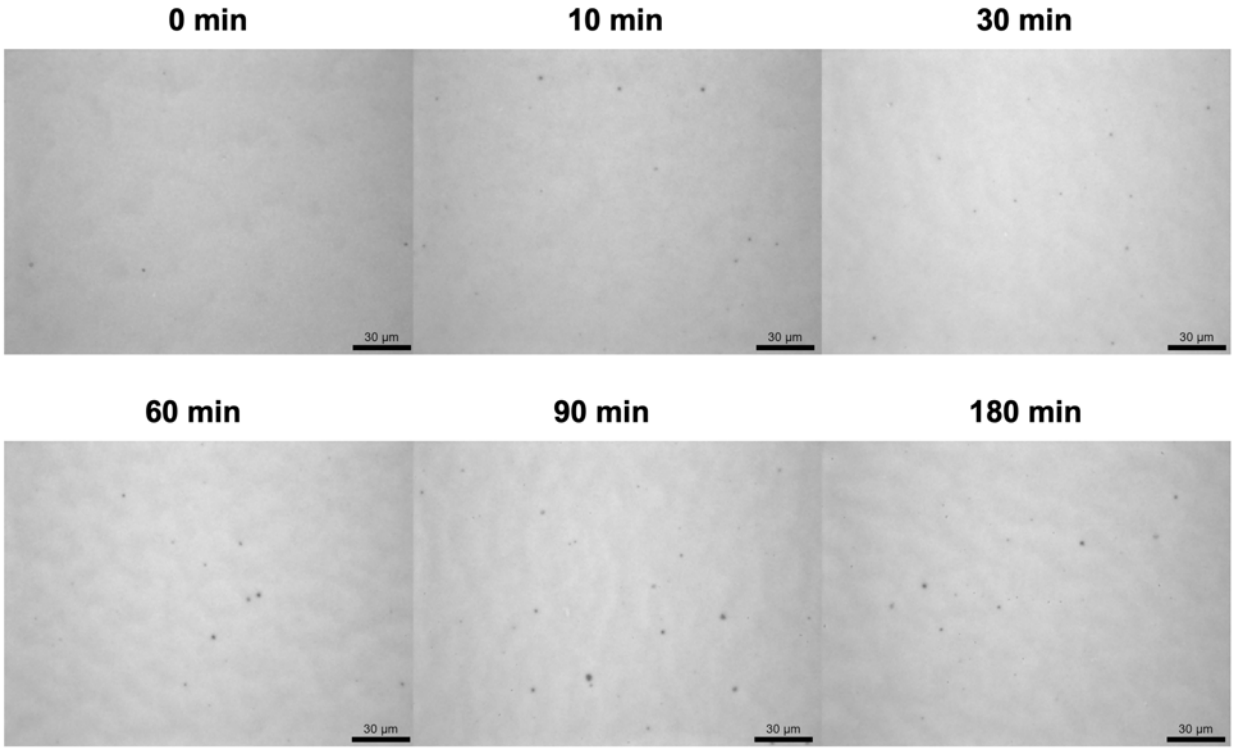

Figure A1.49 Optical microscopy images of PffBT4T-2OD:$PC_{71}BM$ devices with 8 wt% copolymer and 3 vol% DIO annealed at 150 °C for a given time. Scale bars represent 30 µm

A1.15 UV-vis Spectroscopic Data

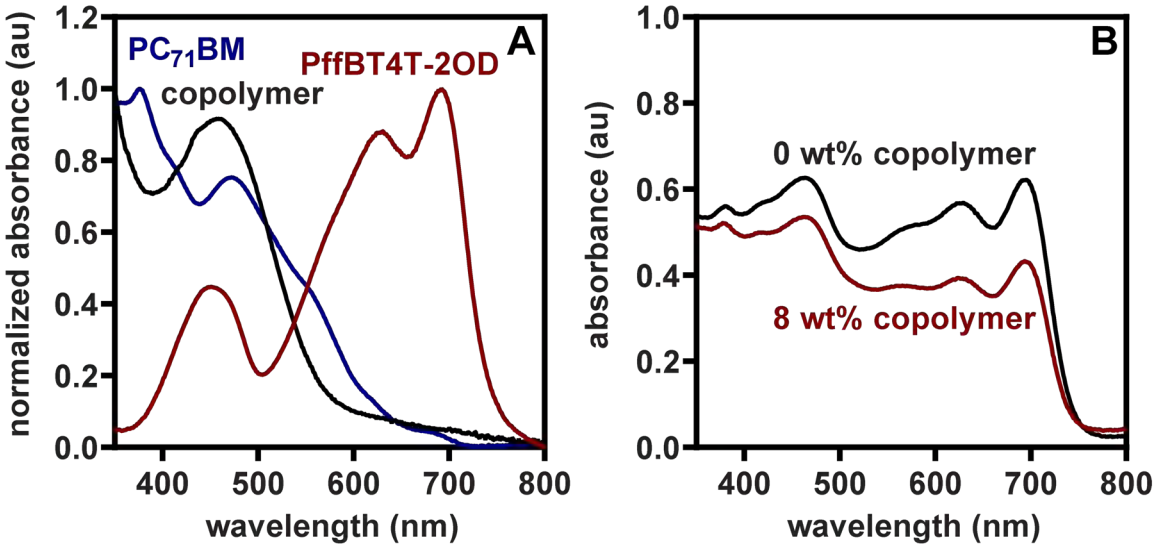

Figure A1.50 A) UV-vis spectra of films of PffBT4T-2OD (red), $PC_{71}BM$ (blue), and copolymer (black). B) Uncorrected UV-vis spectra of films of PffBT4T-2OD:$PC_{71}BM$ with 0 (black) or 8 (red) wt% copolymer

A1.16 Energy-Filtered Transmission Electron Microscopy (EF-TEM) Images

Thin film preparation

PEDOT:PSS coated substrates. An aliquot of PEDOT:PSS (100 µL, 3–4% suspension in H_2O) was spin-cast onto a glass substrate at 2000 RPM for 120 s.

Blends with DIO or DIO and copolymer. Blend solutions were prepared as described for optical microscopy (S27–S28). Solutions were spin-cast onto hot PEDOT:PSS-coated substrates (heated to 110 °C before loading onto spin-coater) at 800 RPM for 180 s. Immediately after spin-casting the films were delaminated from the substrates by removing a section of film at substrate edge with a razor blade then submerging the scraped substrate in deionized water at a ~15° angle. The delaminated film was lifted onto a 400-mesh Pure-C on copper TEM grid and dried for 24 h in vacuo before analysis.

EF-TEM images

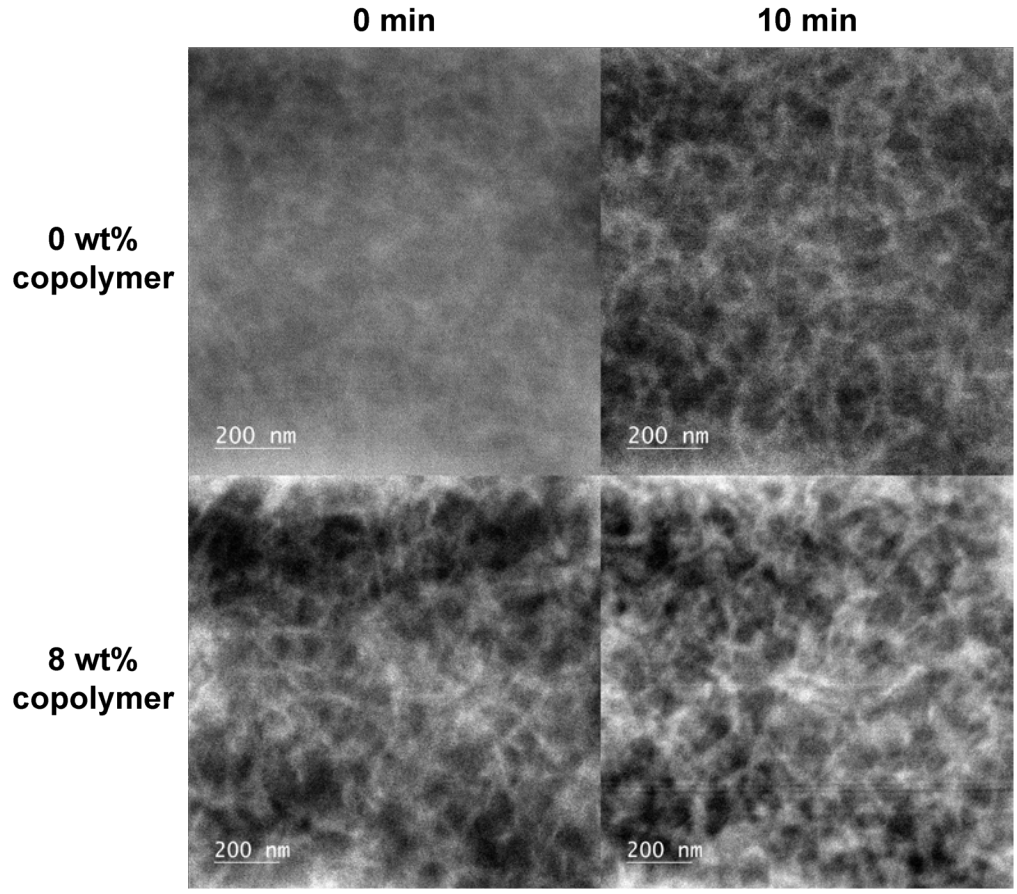

Figure A1.51 EF-TEM images for PffBT4T-2OD:$PC_{71}BM$ thin film blends with 0% (top) or with (bottom) 8 wt% copolymer and before (left) or after (right) annealing at 150 °C for 10 min

A1.17 References

(1) Kong, C.; Song, B.; Mueller, E. A.; Kim, J.; McNeil, A. J. Random Copolymers Outperform Gradient and Block Copolymers in Stabilizing Organic Photovoltaics. *Adv. Funct. Mater.* **2019**, 1900467.

(2) Love, B. E.; Jones, E. G. The Use of Salicylaldehyde Phenylhydrazone as an Indicator for the Titration of Organometallic Reagents. *J. Org. Chem.* **1999**, 64, 3755–3756.

(3) Wu, S. Calculation of Interfacial Tension in Polymer Systems. *J. Polym. Sci.: Part C* **1971**, 34, 19–30.

(4) Wu, S. Polar and Nonpolar Interactions in Adhesion. *J. Adhesion* **1973**, 5, 39–55.

(5) White, M. S.; Olson, D. C.; Shaheen, S. E.; Kopidakis, N.; Ginley, D. S. Inverted Bulk-heterojunction Organic Photovoltaic Device Using a Solution-derived ZnO Underlayer. *Appl. Phys. Lett.* **2006,** 89, 143517.

(6) Kozub, D. R.; Vakhshouri, K.; Orme, L. M.; Wang, C.; Hexemer, A.; Gomez, E. D. Polymer Crystallization of Partially Miscible Polythiophene/Fullerene Mixtures Controls Morphology. *Macromolecules* **2011,** 44, 5722–5726.

(7) Wong, M.; Hollinger, J.; Kozycz, L. M.; McCormick, T. M.; Lu, Y.; Burns, C. D.; Seferos, D. S. An Apparent Size-Exclusion Quantification Limit Reveals a Molecular Weight Limit in the Synthesis of Externally Initiated Polythiophenes. *ACS Macro Lett.* **2012,** 1, 1266–1269.

(8) van Oss, C. J. Interfacial Forces in Aqueous Media, 2nd Ed. 2006, Taylor & Frances Group: Boca Raton, FL, pp 96, 146.

(9) Li, D.; Neumann, A. W. Equation of State for Interfacial Tensions of Solid-liquid Systems. *Adv. Colloid Interface Sci.* **1992**, 39, 299–345.

(10) Sumita, M.; Sakata, K.; Asai, S.; Miyasaka, K.; Nakagawa, H. Dispersion of Fillers and the Electrical Conductivity of Polymer Blends Filled with Carbon Black. *Polym. Bull.* **1991**, 25, 265–271.

(11) Clark, M. D.; Jespersen, M. L.; Patel, R. J.; Leever, B. J. Predicting Vertical Phase Segregation in Polymer-Fullerene Bulk Heterojunction Solar Cells by Free Energy Analysis. *ACS Appl. Mater. Interfaces* **2013**, 5, 4799−4807.

(12) Nilsson, S.; Bernasik, A.; Budkowski, A.; Moons, E. Morphology and Phase Segregation of Spin-Casted Films of Polyfluorene/PCBM Blends. *Macromolecules* **2007**, 40, 8291−8301.

(13) Liu, Y.; Zhao, J.; Li, Z.; Mu, C.; Ma, W.; Hu, H.; Jiang, K.; Lin, H.; Ade, H.; Yan, H. Aggregation and Morphology Control Enables Multiple Cases of High-Efficiency Polymer Solar Cells. *Nat. Commun.* **2014**, 5, 5293.

(14) He, Y.; Zhao, G.; Peng, B.; Li, Y. High-Yield Synthesis and Electrochemical and Photovoltaic Properties of Indene-C70 Bisadduct. *Adv. Funct. Mater.* **2010**, 20, 3383–3389.

Appendix 2: Supporting Information for Chapter 3

A2.1 Structures and Abbreviations

Soluble Mediators

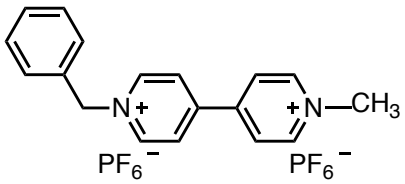

[Bn-bpy-Me^{2+}][PF$_6^-$]$_2$

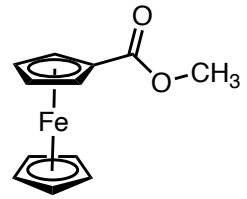

FcR

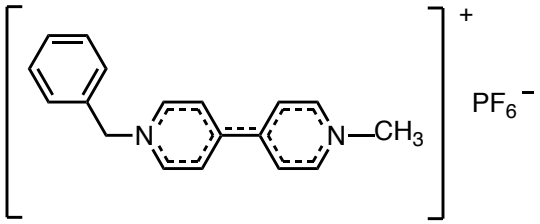

[Bn-bpy-Me$^+$][PF$_6^-$]

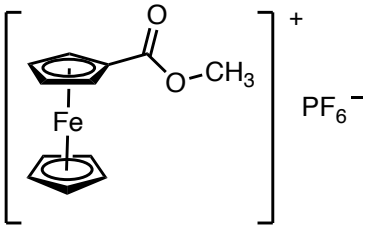

[FcR$^+$][PF$_6^-$]

Insoluble beads

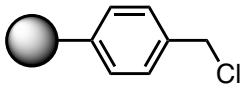

xPS-Cl

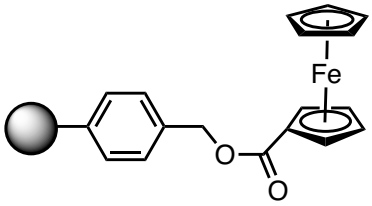

xPS-FcR

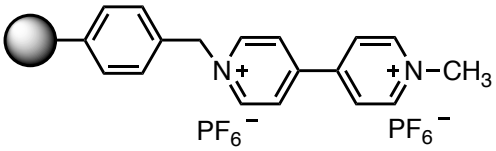

[xPS-bpy-Me^{2+}][PF$_6^-$]$_2$

A2.2 Materials

4,4′-Dipyridyl, iodomethane, benzyl bromide, ammonium hexafluorophosphate (NH_4PF_6), ferrocene carboxylic acid, diisopropylethylamine, and silver hexafluorophosphate were purchased from Sigma Aldrich and used without further purification. Methyl ferrocenecarboxylate (**FcR**) was purchased from Ambeed and used after sublimation. Merrifield resin (poly(chloromethylstyrene-*co*-styrene-*co*-divinylbenzene) (200–400 mesh, 3.5–4.5 mmol/g Cl^-, 1% cross-linked) (**xPS-Cl**) was purchased from Sigma Aldrich. Dichloromethane (DCM), ethyl acetate (EtOAc), methanol (MeOH), acetonitrile (MeCN), dimethylformamide (DMF), and diethyl ether (Et_2O) were purchased from Sigma Aldrich or Fisher and used without purification.

A2.3 Materials Characterization

NMR Spectroscopy – ^1H and ^{13}C NMR spectra for all compounds were acquired at rt. Chemical shift data are reported in units of δ (ppm) relative to tetramethylsilane (TMS) and referenced with residual solvent. Multiplicities are reported as follows: singlet (s), doublet (d), doublet of doublets (dd), triplet (t), quartet (q), multiplet (m).

Element Analysis (EA) – EA was performed by Midwest Microlab. EA for **xPS-Cl** was C: 78.27%, H: 6.66%, Cl: 14.87%, indicating that 1 g of **xPS-Cl** has 4.2 mmol of Cl. This number was used for further measurements of functionalized beads.

Infrared Spectroscopy (IR) – IR data were recorded using a Thermo Scientific Nicolet IS50 FT-IR spectrometer.

Raman Spectroscopy – Raman data were recorded using a Renishaw inVia Raman microscope equipped with a RenCam CCD detector, a 785 nm diode laser, 1200 lines/mm grating, and a 65 μm slit. Spectra were analyzed using the WiRE 3.4 software package and calibrated using a silicon standard.

Swelling Measurement – Optical Microscopy – Before measurements, the beads were dried under vacuum. The crosslinked polymer beads were soaked in MeCN or DMF for 60 min then examined while still in the solvent, using a microscope slide and a cover slip to contain the solvent, using a Leica DMCB optical microscope with a 10x objective lens. Images were recorded with an attached QICAM Fast 1394 digital video camera. Similar images of pristine beads were collected. The average diameter was calculated by ImageJ from over 300 beads before and after soaking.

Swelling Measurement – Volumetric Change – In an NMR tube, a precisely measured mass (~100 mg) of polymer beads was added, and the height was measured and used for calculating the volume change upon swelling using conversion factor 1 cm height = 130 μL. The height of the beads was recorded before and after soaking in MeCN or DMF for 60 min.

A2.4 Synthetic Procedures

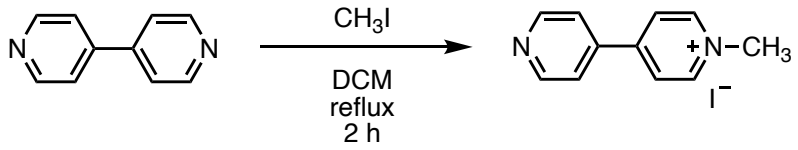

[bpy-Me$^+$][I$^-$]

[bpy-Me$^+$][I$^-$]. (This is a slight modification of a reported procedure.[1]) In an oven-dried 100 mL round-bottom flask, a mixture of 4,4'-dipyridyl (784 mg, 5.02 mmol) and iodomethane (0.41 mL, 6.6 mmol, 1.3 equiv.) in DCM (10 mL) was stirred at reflux under N_2 for 2 h, during which time a yellow precipitate formed. After cooling to rt, the yellow precipitate was collected and washed with EtOAc (2 x 50 mL) and Et_2O (2 x 50 mL). The solid was recrystallized from MeOH to yield **[bpy-Me$^+$][I$^-$]** as a yellow powder (1.13 g, 75% yield). ^{1}H NMR (401 MHz, DMSO-d_6) δ 9.15 (d, J = 6.5 Hz, 2H), 8.91 – 8.82 (m, 2H), 8.67 – 8.58 (m, 2H), 8.08 – 8.00 (m, 2H), 4.39 (s, 3H). ^{13}C NMR (126 MHz, DMSO-d_6) δ 152.29, 151.48, 146.61, 141.29, 125.40, 122.32, 48.05.

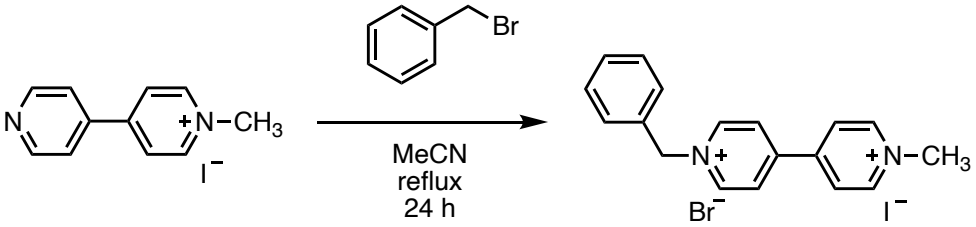

[bpy-Me$^+$][I$^-$] **[Bn-bpy-Me^{2+}][Br$^-$][I$^-$]**

[Bn-bpy-Me^{2+}][Br$^-$][I$^-$]. (This is a modified version of a reported procedure.[2]) In an oven-dried 100 mL round-bottom flask, a mixture of **[bpy-Me$^+$][I$^-$]** (415.7 mg, 1.395 mmol) and benzyl bromide (285 mg, 1.67 mmol, 1.2 equiv.) in MeCN (20.0 mL) was stirred at reflux for 24 h, during which time a red precipitate formed. After cooling to rt, the red precipitate was collected and washed with EtOAc (2 x 100 mL). The red powder was collected to yield **[Bn-bpy-Me^{2+}][Br$^-$][I$^-$**

] (561 mg, 86% yield). ^{1}H NMR (401 MHz, DMSO-d_6) δ 9.60 (d, *J* = 6.7 Hz, 2H), 9.33 (d, *J* = 6.6 Hz, 2H), 8.90 – 8.72 (m, 4H), 7.72 – 7.60 (m, 2H), 7.52 – 7.40 (m, 3H), 6.01 (s, 2H), 4.46 (s, 3H). ^{13}C NMR (126 MHz, DMSO) δ 149.54, 148.60, 147.04, 146.19, 134.70, 129.97, 129.73, 129.49, 127.55, 126.67, 63.65, 48.49.

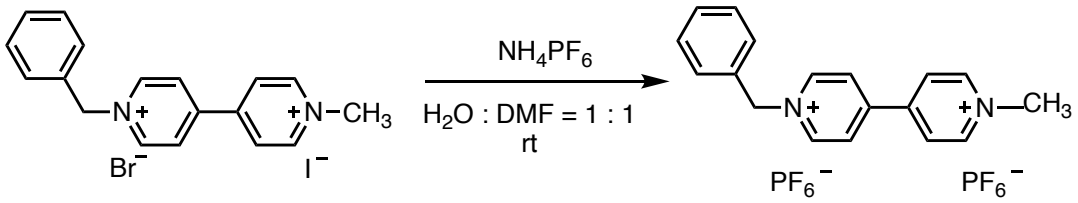

[Bn-bpy-Me^{2+}][Br^{-}][I^{-}] **[Bn-bpy-Me^{2+}][PF$_6^{-}$]$_2$**

[Bn-bpy-Me^{2+}][PF$_6^{-}$]$_2$. In a 20 mL vial, **[Bn-bpy-Me^{2+}][Br^{-}][I^{-}] (**100 mg, 0.214 mmol) was dissolved in a 1:1 mixture of deionized water (2.5 mL) and DMF (2.5 mL). This homogenous solution was added dropwise via syringe into another 20 mL vial containing excess NH_4PF_6 (192 mg, 1.18 mmol, 5.5 equiv.) in water (10 mL). A yellow precipitate formed instantly. The yellow solid was collected by filtration and then washed with water (2 x 50 mL). The solid was dried under vacuum to obtain **[Bn-bpy-Me^{2+}][PF$_6^{-}$]$_2$** as a yellow solid (118 mg, 97% yield). ^{1}H NMR (401 MHz, DMSO-d_6) δ 9.50 (d, *J* = 5.1 Hz, 2H), 9.26 (d, *J* = 6.6 Hz, 2H), 8.81 – 8.67 (m, 4H), 7.60 (d, *J* = 6.5 Hz, 2H), 7.47 (m, *J* = 7.8 Hz, 3H), 5.94 (s, *J* = 3.9 Hz, 2H), 4.51 – 4.36 (s, 3H). ^{13}C NMR (126 MHz, DMSO) δ 149.67, 148.73, 147.02, 146.18, 134.58, 130.00, 129.76, 129.34, 127.54, 126.66, 63.95, 48.51.

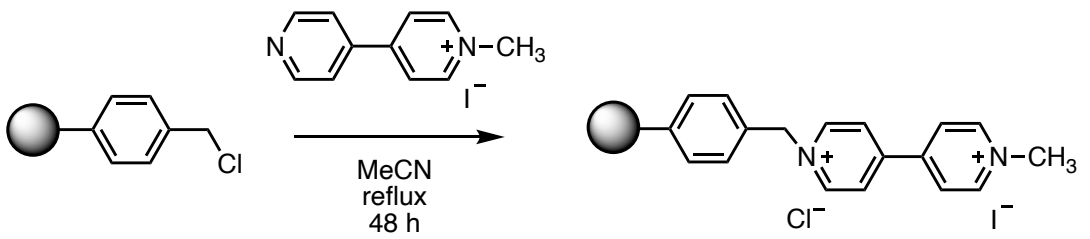

xPS-Cl **[xPS-bpy-Me^{2+}][Cl$^-$][I$^-$]**

[xPS-bpy-Me^{2+}][Cl$^-$][I$^-$]. In an oven-dried 100 mL round-bottom flask**,** a mixture of **[bpy-Me$^+$][I$^-$]** (197 mg, 0.66 mmol) and **xPS-Cl** (100 mg, 0.42 mmol Cl) in MeCN (30 mL) was heated to reflux for 48 h, during which time the beads turned red. After cooling to rt, the red beads were collected by filtration and then washed with MeCN (30 mL). The beads were transferred to a centrifuge tube using MeCN and soaked in MeCN (30 mL) for 30 min. The MeCN was decanted, then fresh MeCN was added (30 mL) and soaked for another 30 min. The MeCN was decanted. The red solid was dried and collected (75% conversion of the chloromethyl groups). (EA: C 65.48%, H 5.73%, N 2.51%, Cl 9.07%, I 13.77%) (theoretical EA for 75% conversion of the chloromethyl groups with 0.50 equiv of MeCN present: C 61.71%, H 5.36%, N 6.76%, Cl 7.10%, I 19.07%).

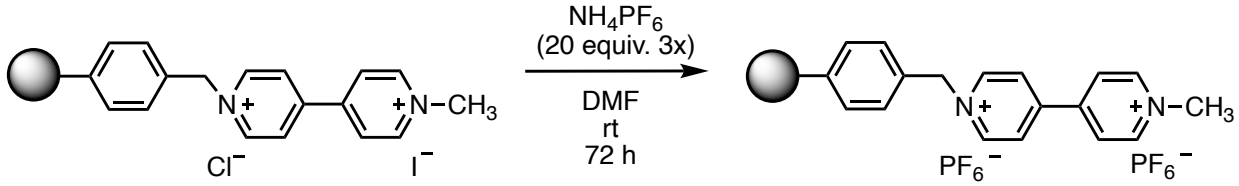

[xPS-bpy-Me^{2+}][Cl$^-$][I$^-$] **[xPS-bpy-Me^{2+}][PF$_6^-$]$_2$**

[xPS-bpy-Me^{2+}][PF$_6^-$]$_2$. In a 20 mL vial, **[xPS-bpy-Me^{2+}][Cl$^-$][I$^-$]** (100 mg, 0.256 mmol Cl$^-$, I$^-$ each) and NH_4PF_6 (835 mg, 5.12 mmol, 20 equiv.) were added into DMF (15 mL) in a centrifuge tube. The mixture was agitated using a shaker (Sonics SHK-COCK2) for 24 h. Then, the supernatant was decanted, and NH_4PF_6 (835 mg, 5.12 mmol, 20 equiv.) in DMF (10 mL) solution

was added. The mixture was shaken for another 24 h. The supernatant was decanted, and the procedure was repeated (for a total of three times). The beads were soaked for 30 min in neat DMF (50 mL) and the DMF then decanted. The beads were soaked for 30 min in neat MeCN (50 mL) and the MeCN then decanted. The yellow solid was vacuum dried and collected (95% ion exchange based on EA) (EA: C 57.37%, H 5.14%, N 3.44%, Cl 1.69%, I 0.93%, F 21.15%) (theoretical EA for 95% ion exchange and 75% conversion of chloromethyl groups in reaction above): C 51.78%, H 4.35%, N 3.80%, Cl 1.84%, I 0.86%, P 7.98%, F 29.38%).

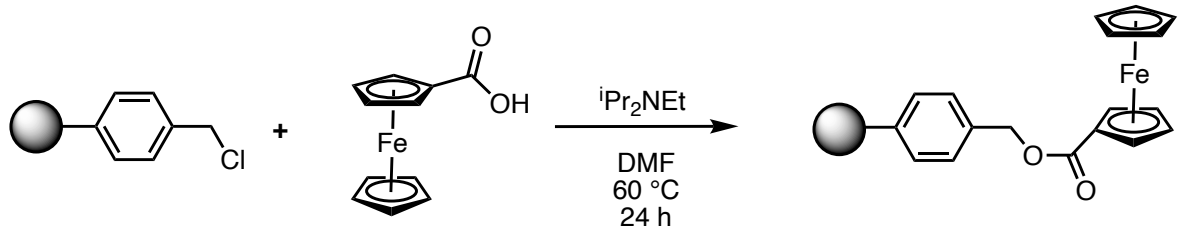

xPS-Cl **xPS-FcR**

xPS-FcR. In an oven-dried 100 mL round-bottom flask, a mixture of **xPS-Cl** (200 mg, 0.840 mmol Cl), ferrocene carboxylic acid (242 mg, 1.05 mmol), and diisopropylethylamine (0.183 mL, 1.05 mmol) was stirred in DMF (30 mL) for 24 h at 60 °C. After cooling to rt, the dark brown beads were collected by filtration and washed with DMF (30 mL). Then the beads were transferred to a centrifuge tube using DMF and soaked in DMF (30 mL) for 30 min. The DMF was decanted, and fresh DMF (30 mL) was added and soaking repeated for another 30 min. The DMF was decanted, and MeCN (30 mL) was added soaking repeated for 30 min. The MeCN was decanted, and the MeCN wash was repeated for a total of 3 MeCN washes. The brown solid was vacuum dried and collected (70% conversion of the chloromethyl groups based on EA) (EA: C 72.26%, H 6.52%, N 1.05%, Cl 2.66%) (theoretical EA for 70% conversion of the chloromethyl groups with 0.16 equiv of DMF present: C 73.43%, H 6.10%, N 1.03%, Cl 2.69%, Fe 9.89%).

A2.5 NMR Spectra

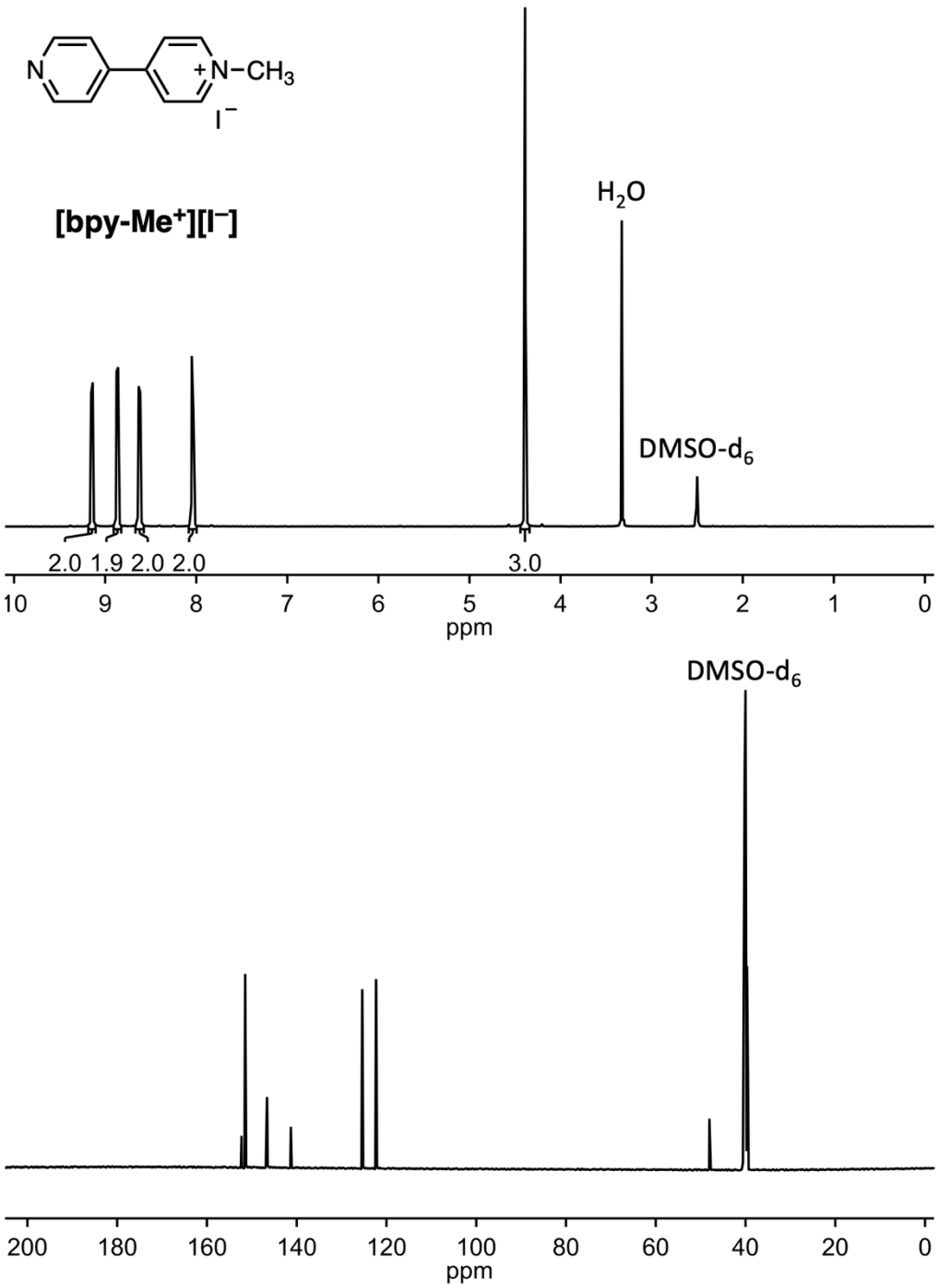

Figure A2.1 ^{1}H and ^{13}C NMR Spectra of [bpy-Me^{+}][I^{-}].

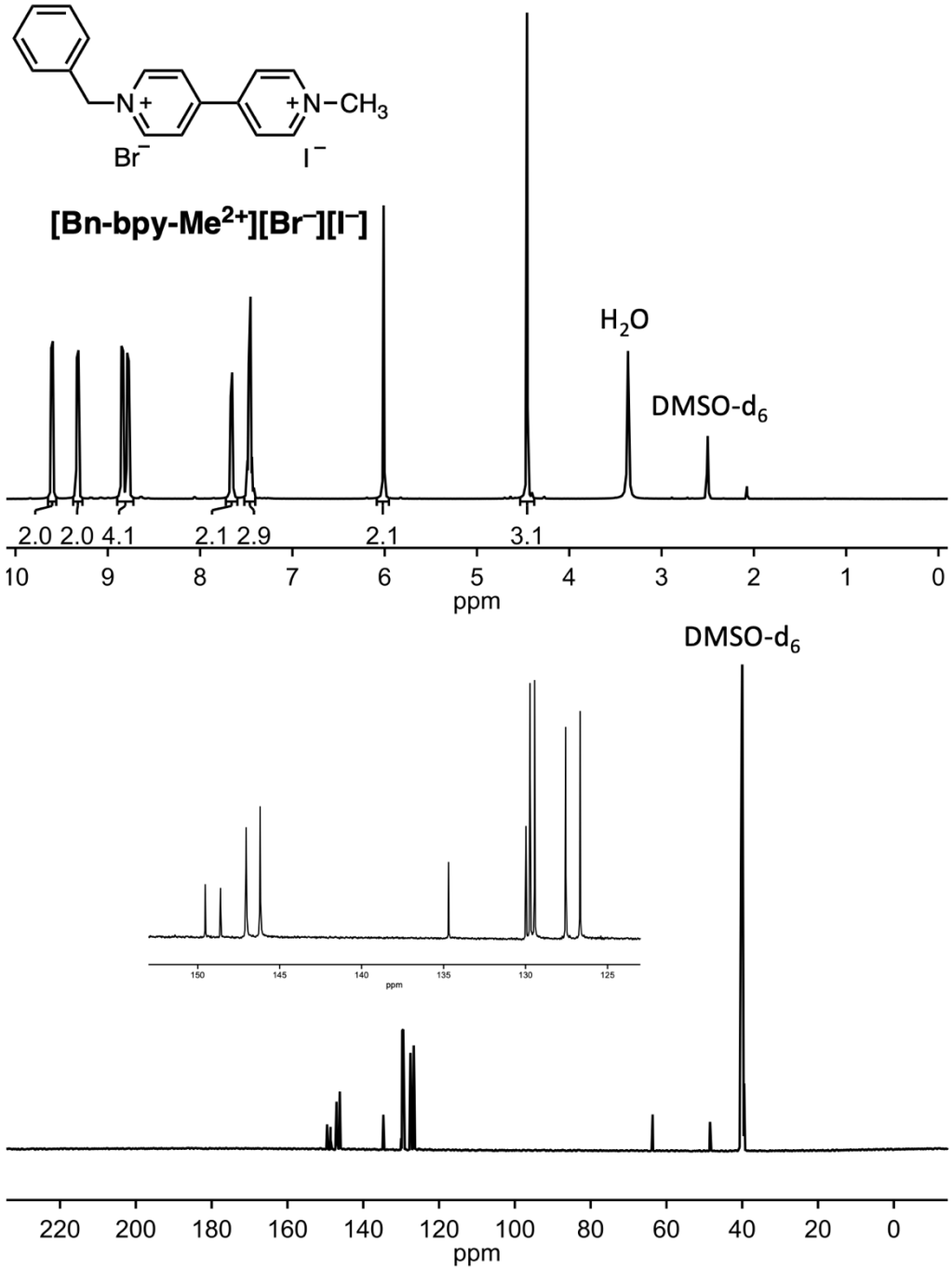

Figure A2.2 ^{1}H and ^{13}C NMR Spectra of [Bn-bpy-Me^{2+}][Br^{-}][I^{-}].

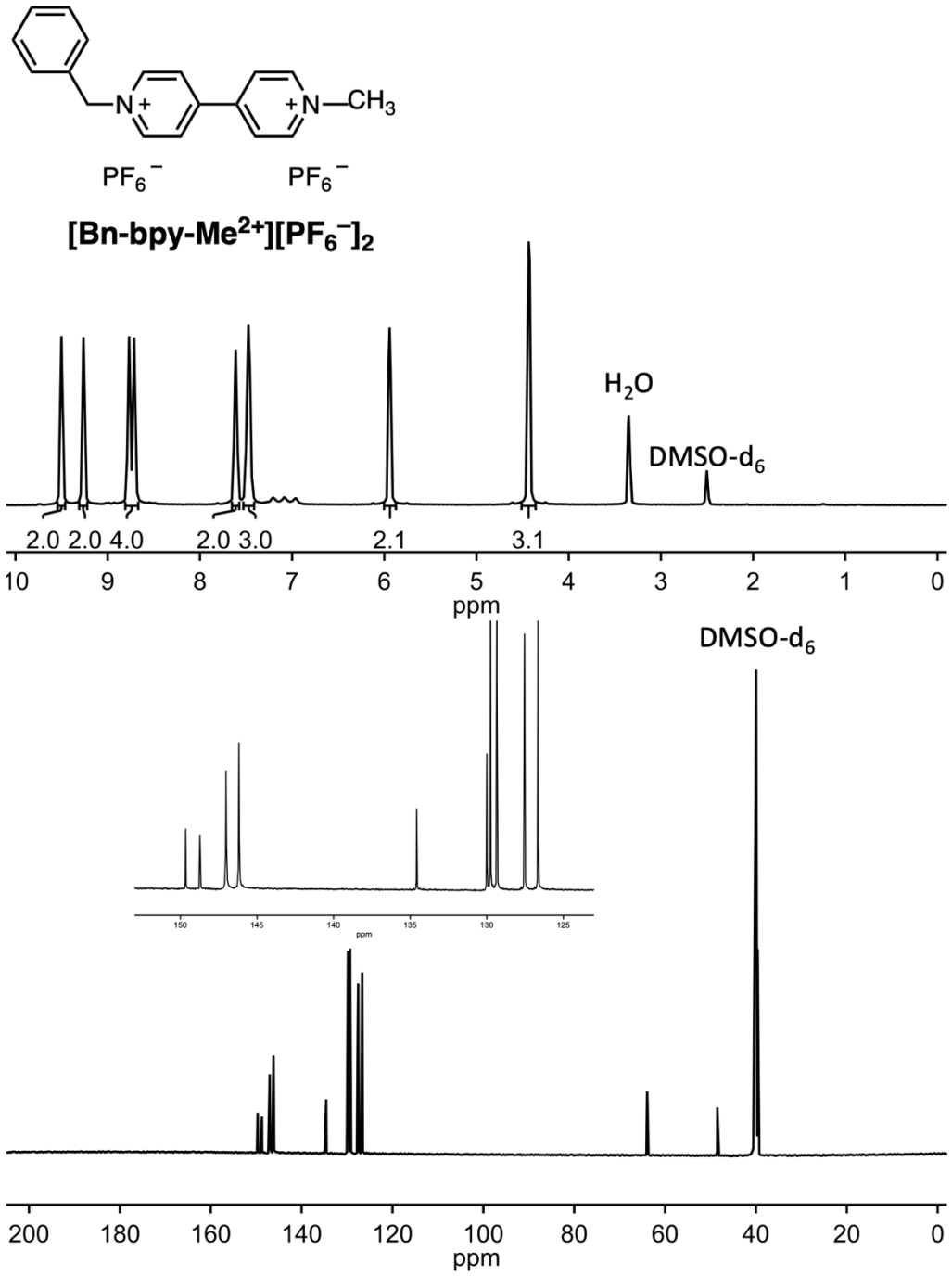

Figure A2.3 ^{1}H and ^{13}C NMR Spectra of [Bn-bpy-Me^{2+}][PF_6^-]$_2$.

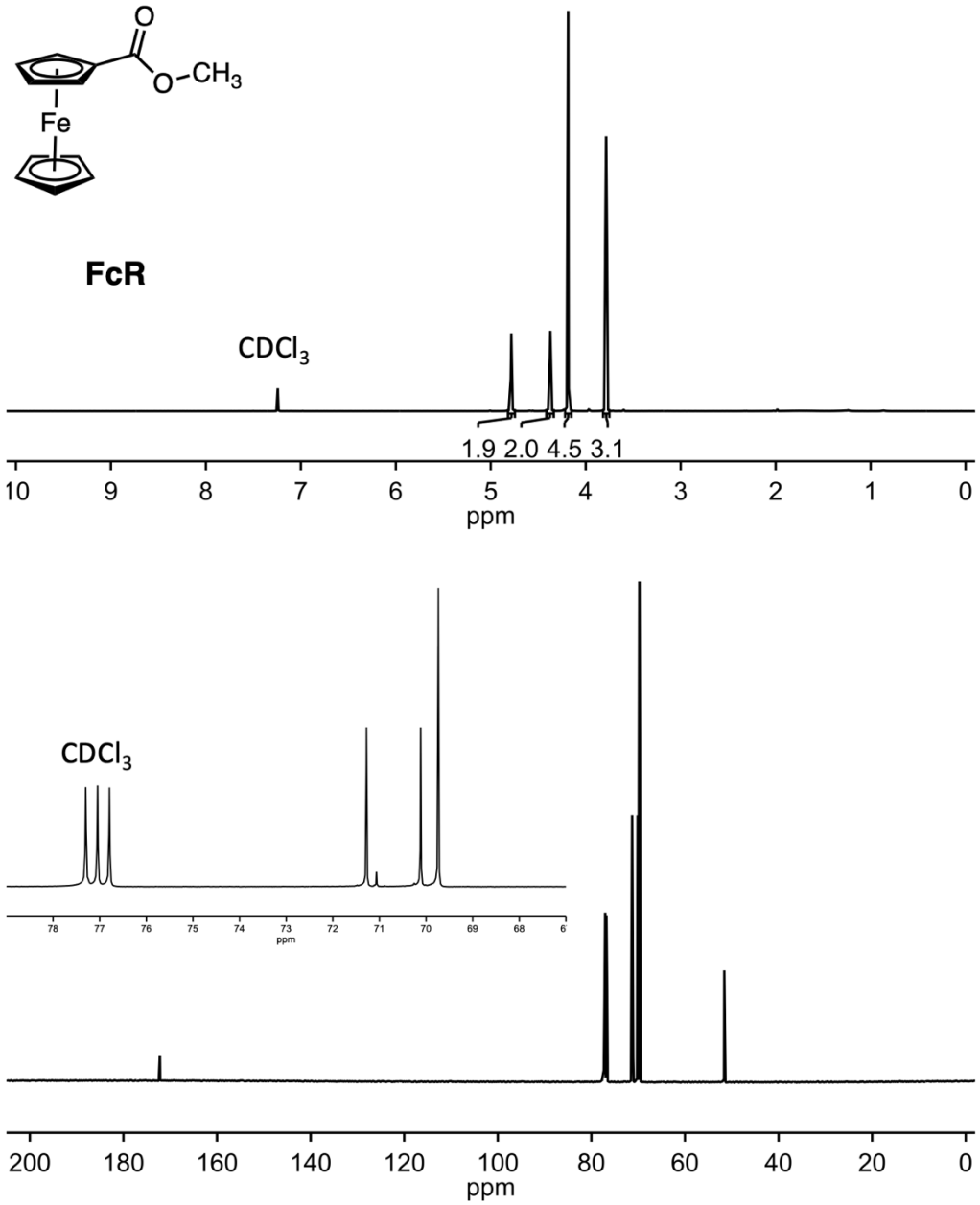

Figure A2.4 ^{1}H and ^{13}C NMR Spectra of FcR. ^{1}H NMR (401 MHz, $CDCl_3$) δ 4.78 (s, J = 1.9 Hz, 2H), 4.37 (s, J = 2.0 Hz, 2H), 4.19 (s, 5H), 3.79 (s, 3H). ^{13}C NMR (126 MHz, $CDCl_3$) δ 172.22, 71.28, 71.06, 70.25, 69.85, 51.60

A2.6 IR and Raman Spectra

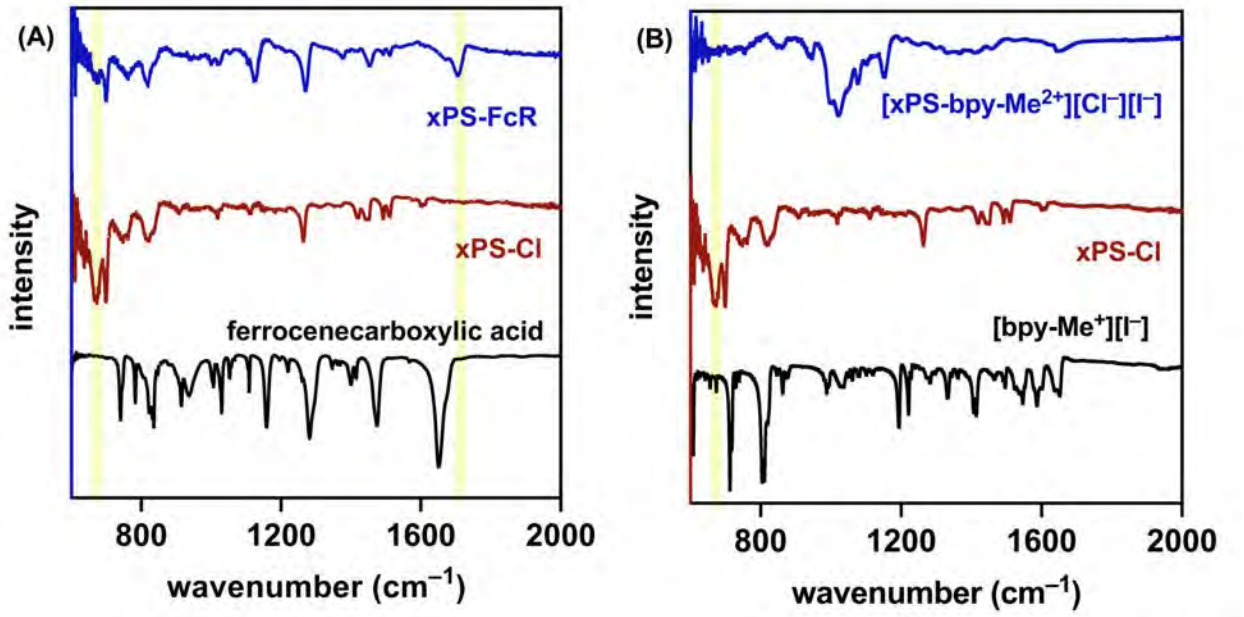

Figure A2.5 IR spectra of (A) xPS-FcR, xPS-Cl and ferrocene carboxylic acid, and (B) [xPS-bpy-Me^{2+}][Cl^-][I^-], xPS-Cl, and [bpy-Me^+][I^-]. C-Cl band at 672 cm^{-1} and C=O band at 1714 cm^{-1}

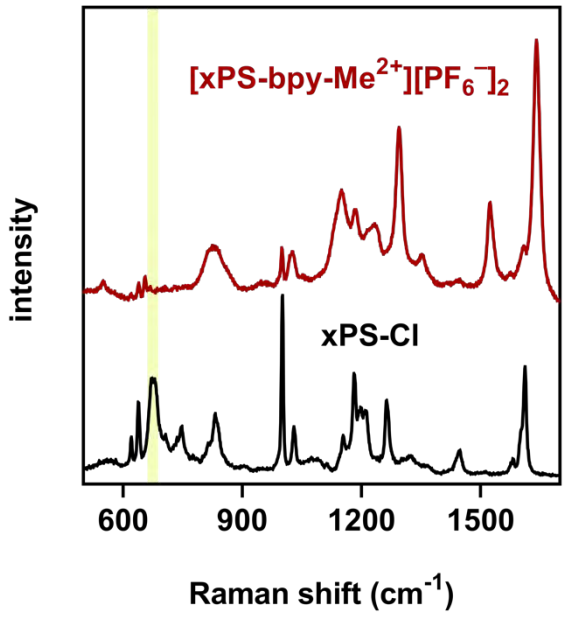

Figure A2.6 Raman spectra of [xPS-bpy-Me^{2+}][PF_6^-]$_2$ and xPS-Cl. C-Cl band at 665 cm^{-1}.

A2.7 Swelling Measurements

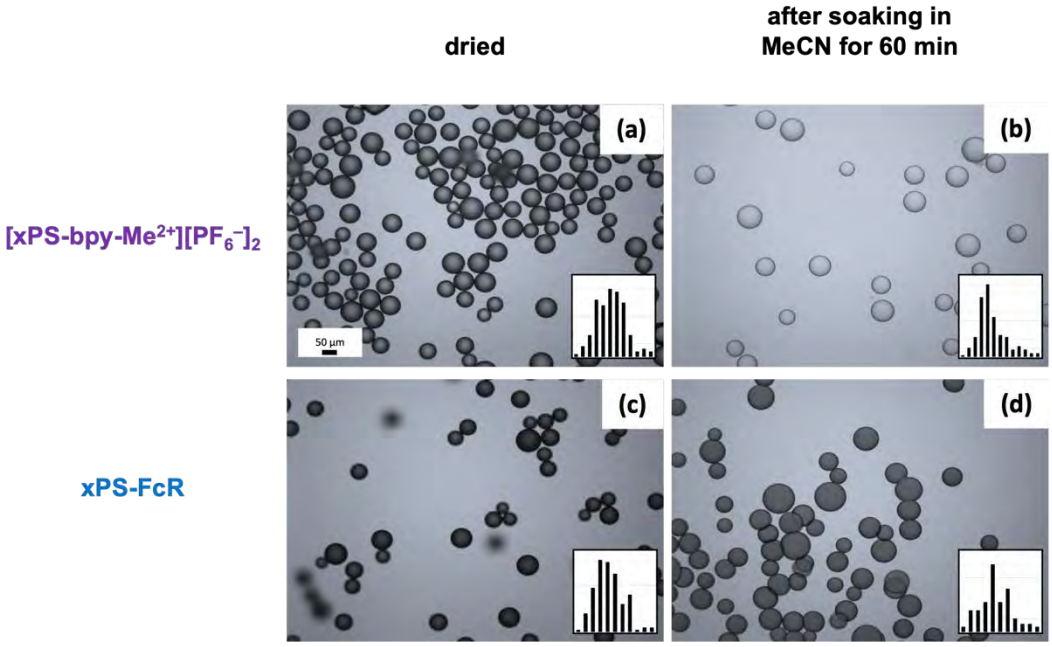

Figure A2.7 Optical microscope images of (a) dried [xPS-bpy-Me^{2+}][PF_6^-]$_2$ and (b) after soaking in MeCN for 60 min, (c) dried xPS-FcR and (d) after soaking in MeCN for 60 min. Each inset (bar charts) indicates the distribution of diameter of the beads

Table A2-1 Swelling data of crosslinked beads

method	calculated volume of each bead from radius measured by optical microscope			measured volume per 100 mg of each bead using NMR tube		
	dry	in MeCN	in DMF	dry	in MeCN	in DMF
xPS-Cl	52 pL	57 pL	194 pL	143 µL	169 µL	312 µL
xPS-FcR	81 pL	121 pL	269 pL	143 µL	247 µL	390 µL
[xPS-bpy-Me^{2+}][PF_6^-]$_2$	82 pL	144 pL	211 pL	143 µL	273 µL	299 µL

A2.8 Electrochemical Materials and Methods

General – Acetonitrile (MeCN) (99.8%, anhydrous) was obtained from Sigma Aldrich and used as received. Tetrabutylammonium hexafluorophosphate ($TBAPF_6$, electrochemical grade) and silver hexafluorophosphate ($AgPF_6$) were obtained from Sigma Aldrich and dried under high vacuum for 48 h before being transferred to a N_2-filled glovebox. A 0.50 M stock solution of the $TBAPF_6$ in MeCN was prepared in a N_2-filled glovebox (Mbraun Labmaster) with water < 4 ppm and oxygen < 0.5 ppm and dried over 3 Å molecular sieves for at least 2 days prior to use.

Cyclic Voltammetry – Cyclic voltammetry was performed in a N_2-filled glovebox with a Biologic VSP multichannel potentiostat/galvanostat and a three-electrode electrochemical cell, consisting of a glassy carbon disk working electrode (3.0 mm diameter, area 0.071 cm^2, BASi), an Ag/Ag^+ reference electrode (BASi) with 0.010 M $AgPF_6$ in MeCN, and a platinum wire counter electrode (BASi). All experiments were conducted in a 0.50 M $TBAPF_6$/MeCN solution.

Ultramicroelectrode (UME) Experiments – UME experiments were performed in a N_2-filled glovebox with a Biologic VSP multichannel potentiostat/galvanostat and a three-electrode electrochemical cell, consisting of an UME platinum disk working electrode (10 μm diameter, BASi), a silver wire quasi-reference electrode (BASi), and a platinum wire counter electrode (BASi). All experiments were conducted in a 0.50 M $TBAPF_6$/MeCN solution. Plateau currents in the CVs were used to calculate the concentrations of neutral and charged mediators.

Flow Cell Cycling[3] – Cycling under flow conditions was performed with a zero-gap flow cell comprised of graphite charge collecting plates containing an interdigitated flow field in

combination with two layers of non-woven carbon felt electrodes (Sicracet 29AA) on each side. ePTFE gaskets were used to achieve ~20% compression of the felt. A membrane separated the two half cells, and the exposed area of the membrane in the gasket window was used as the active area (2.55 cm^2). After assembly, both the catholyte side and anolyte side of the cell were loaded with a 15 mM (in each mediator) solution (12 mL) of 1:1 mixed **FcR**:**[Bn-bpy-Me^{2+}][PF$_6^-$]$_2$** in 0.50 M $TBAPF_6$/MeCN. The cell was pretreated by continuously flowing the solution above at 10 mL/min for 30 min without any charging process using a peristaltic pump (Cole-Parmer) with Solveflex and PFA tubing. After this step, using the same flow rate, galvanostatic charge/discharge cycling was performed using a BioLogic VSP galvanostat employing a charging current of 10 mA (3.92 mA/cm^2) and a discharging current of -10 mA (-3.92 mA/cm^2) with +1.6 V and +0.4 V voltage cut-off. After running the battery without beads, cycling and circulation were stopped. A targeted amount of **xPS-FcR** was added into catholyte reservoir and **[xPS-bpy-Me^{2+}][PF$_6^-$]$_2$** was added into anolyte reservoir. After this step, using the same flow rate, galvanostatic charge/discharge cycling was restarted.

Membranes

Celgard 2500 membranes were received from Asahi Kasei, Daramic 175 membranes were received from Daramic, LLC, and Fumasep (FAP-375-PP) ion-exchange membranes were received from Fuel Cell Store

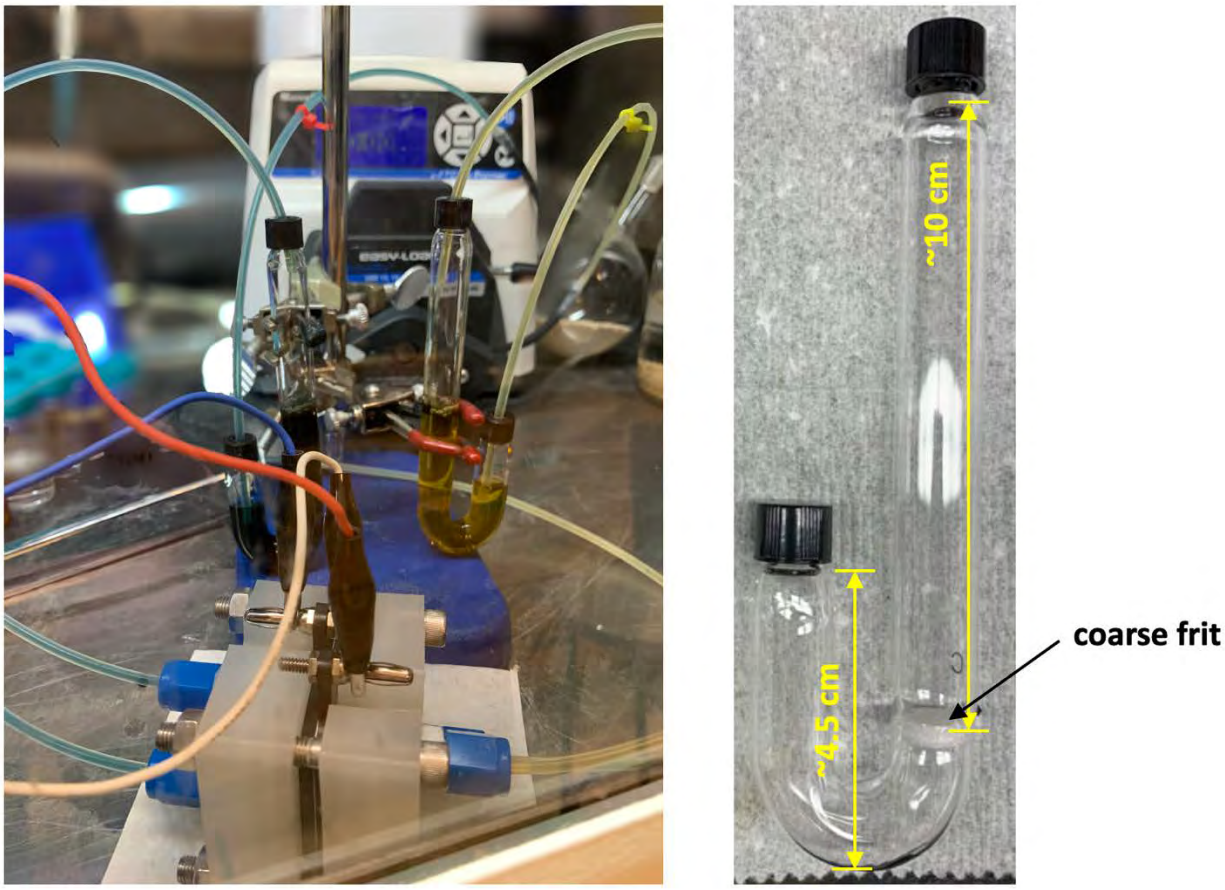

Figure A2.8 Redox-Matched Flow Battery setup with customized reservoirs

A2.9 Materials Preparation via Bulk Electrolysis

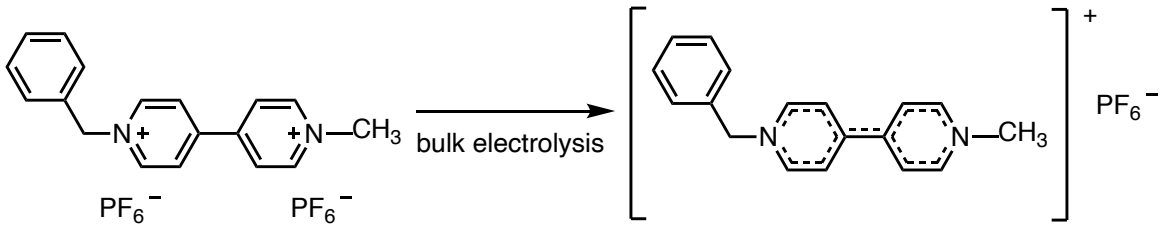

[Bn-bpy-Me^{2+}][PF$_6^-$]$_2$ **[Bn-bpy-Me^{+}][PF$_6^-$]**

[Bn-bpy-Me$^+$][PF$_6^-$]. Bulk electrolysis was performed in an H-cell with an ultrafine fritted glass separator (P5, Adams and Chittenden). The experiments were performed in 0.50 M $TBAPF_6$ in MeCN with 5.0 mM of **[Bn-bpy-Me^{2+}][PF$_6^-$]$_2$.** The working and counter electrode were reticulated vitreous carbon 2" long (McMaster 100 PPI, ~0.25 inches diameter), and the reference electrode was Ag wire in 10 mM $AgPF_6$ + 0.50 M $TBAPF_6$ in MeCN in a glass tube separated by a 0.50 mm BASi CoralPore frit. The working chamber was charged against 5 mL of blank solution (0.50 M $TBAPF_6$ in MeCN), and the current was set to -5 mA under a predetermined voltaic cut-off of -1.5 V. When the potential reached the voltaic cut-off after 15 min, the charging was stopped and the solution in working side was collected.

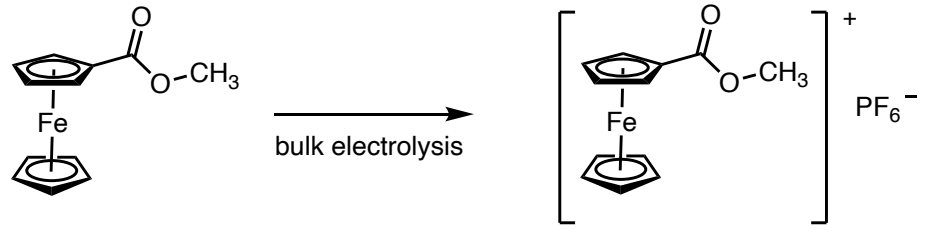

FcR **[FcR$^+$][PF$_6^-$]**

[FcR$^+$][PF$_6^-$]. Bulk electrolysis as described above, except using a 5.0 mM solution of FcR and an oxidative current with a cutoff of +1.5 V.

A2.10 Cyclic Voltammograms of Electrolyte over Beads vs Mediators Solution

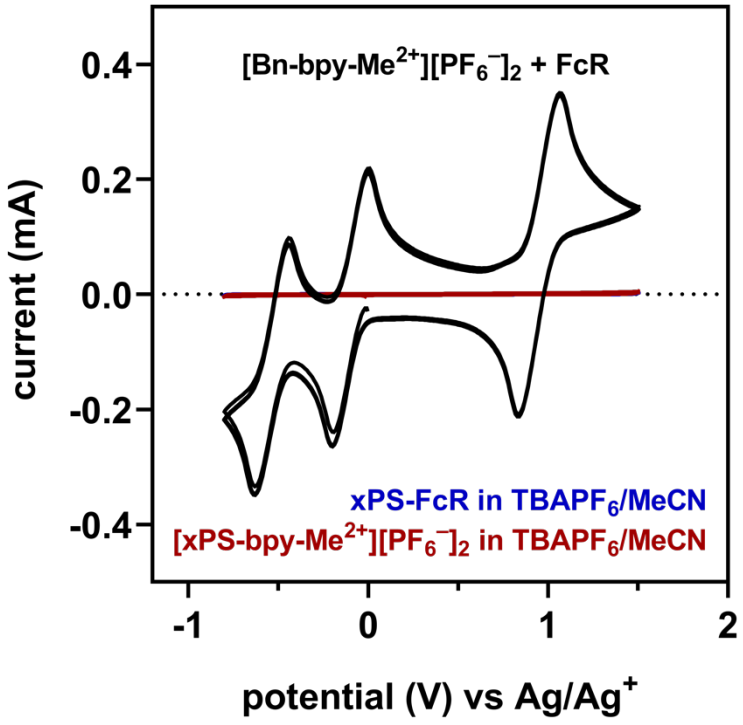

Figure A2.9 Cyclic voltammetry of 1:1 mixed solution of 5.0 mM FcR + 5.0 mM [Bn-bpy-Me^{2+}][PF$_6^-$]$_2$ (black), xPS-FcR (blue, overlapped with red line), and [xPS-bpy-Me^{2+}][PF$_6^-$]$_2$ (red) in 0.5 M TBAPF$_6$ in MeCN (showing no electroactive species are released from beads into a blank supporting electrolyte solution in MeCN)

A2.11 Bead-Mediator Redox Exchange Rate in Reservoir with Flow

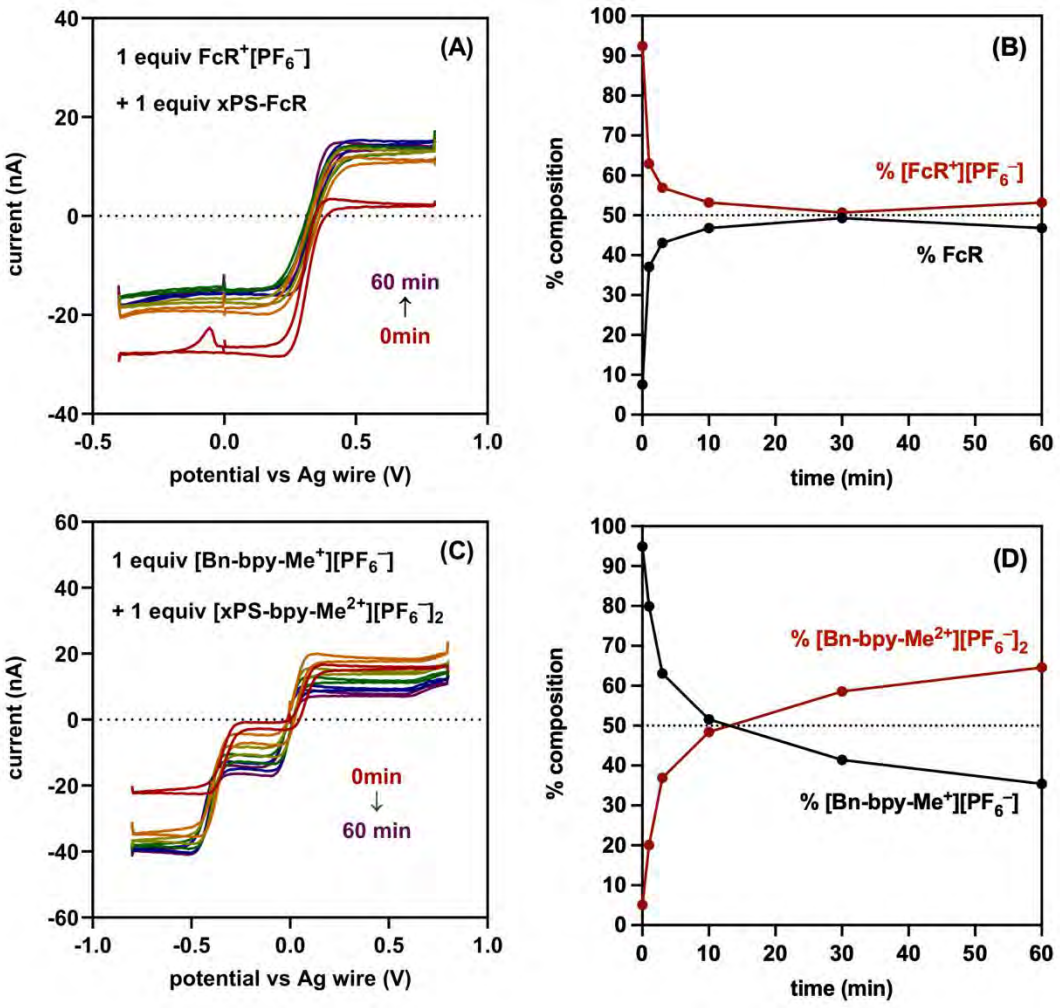

Figure A2.10 (A) Ultramicroelectrode cyclic voltammograms of $[FcR^+][PF_6^-]$ solution in contact with 1 equiv of xPS-FcR in the reservoir with recirculation by the pump (bypassing the cell stack). (B) Percentage of $[FcR^+][PF_6^-]$ and FcR present in solution over time. (C) Ultramicroelectrode cyclic voltammograms of $[Bn\text{-}bpy\text{-}Me^+][PF_6^-]$ solution in contact with 1 equiv of $[xPS\text{-}bpy\text{-}Me^{2+}][PF_6^-]_2$ in the reservoir with recirculation by the pump. (D) Percentage of $[Bn\text{-}bpy\text{-}Me^+][PF_6^-]$ and $[Bn\text{-}bpy\text{-}Me^{2+}][PF_6^-]_2$ present in solution over time

A2.12 Screening Crossover Rates with Various Membranes

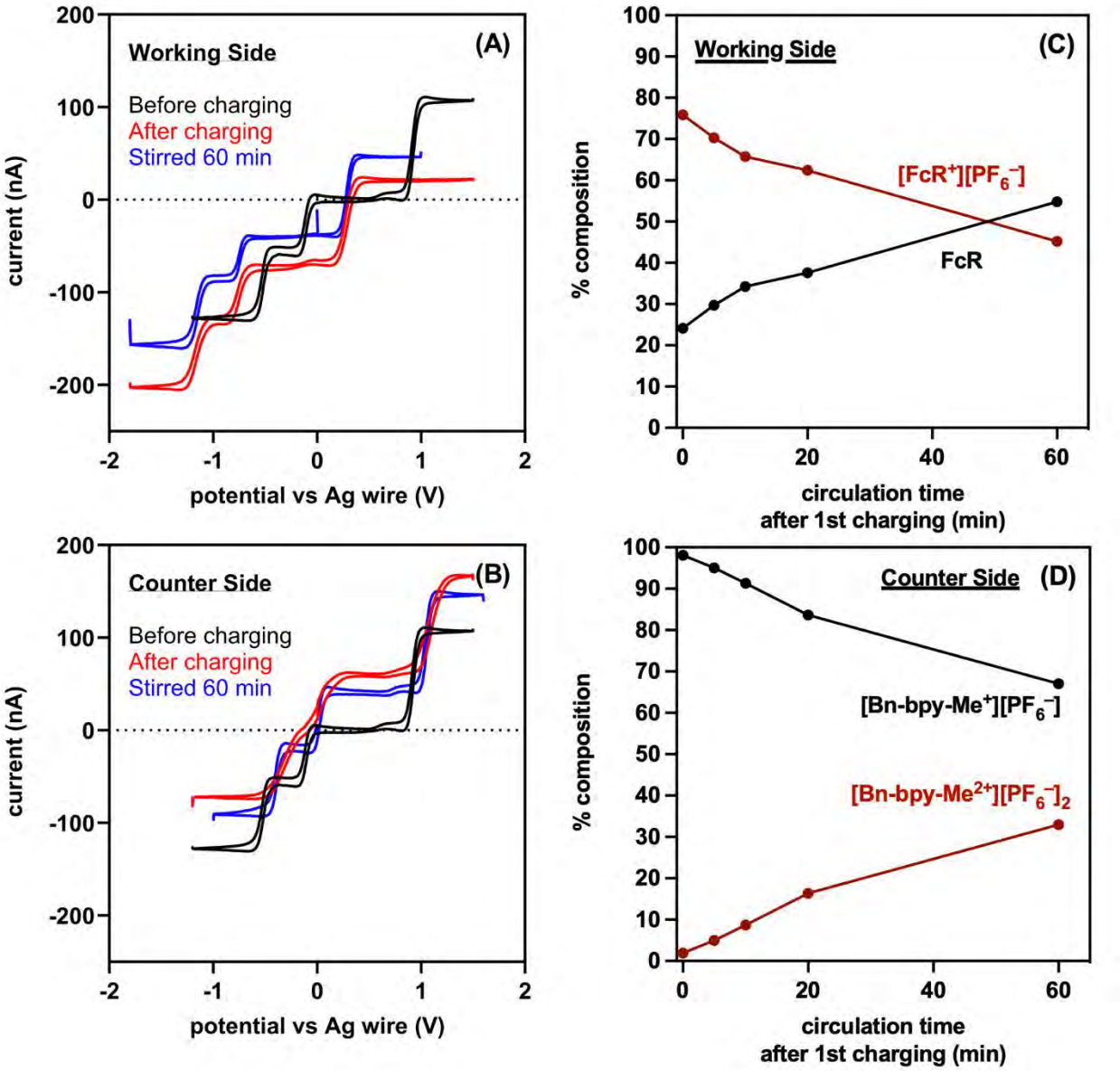

Figure A2.11 (A) Ultramicroelectrode cyclic voltammetry of working side before charging (black), after charging (red), and stirred for 60 min after charging monitored by a microelectrode with 2 sheets of Celgard membrane. (B) Cyclic voltammetry of counter side for the same experiment. (C) Calculated percentages of FcR and $[FcR^+][PF_6^-]$ over circulation time after charging. (D) Calculated percentages of $[Bn\text{-}bpy\text{-}Me^{2+}][PF_6^-]_2$ and $[Bn\text{-}bpy\text{-}Me^+][PF_6^-]$ over circulation time after charging.

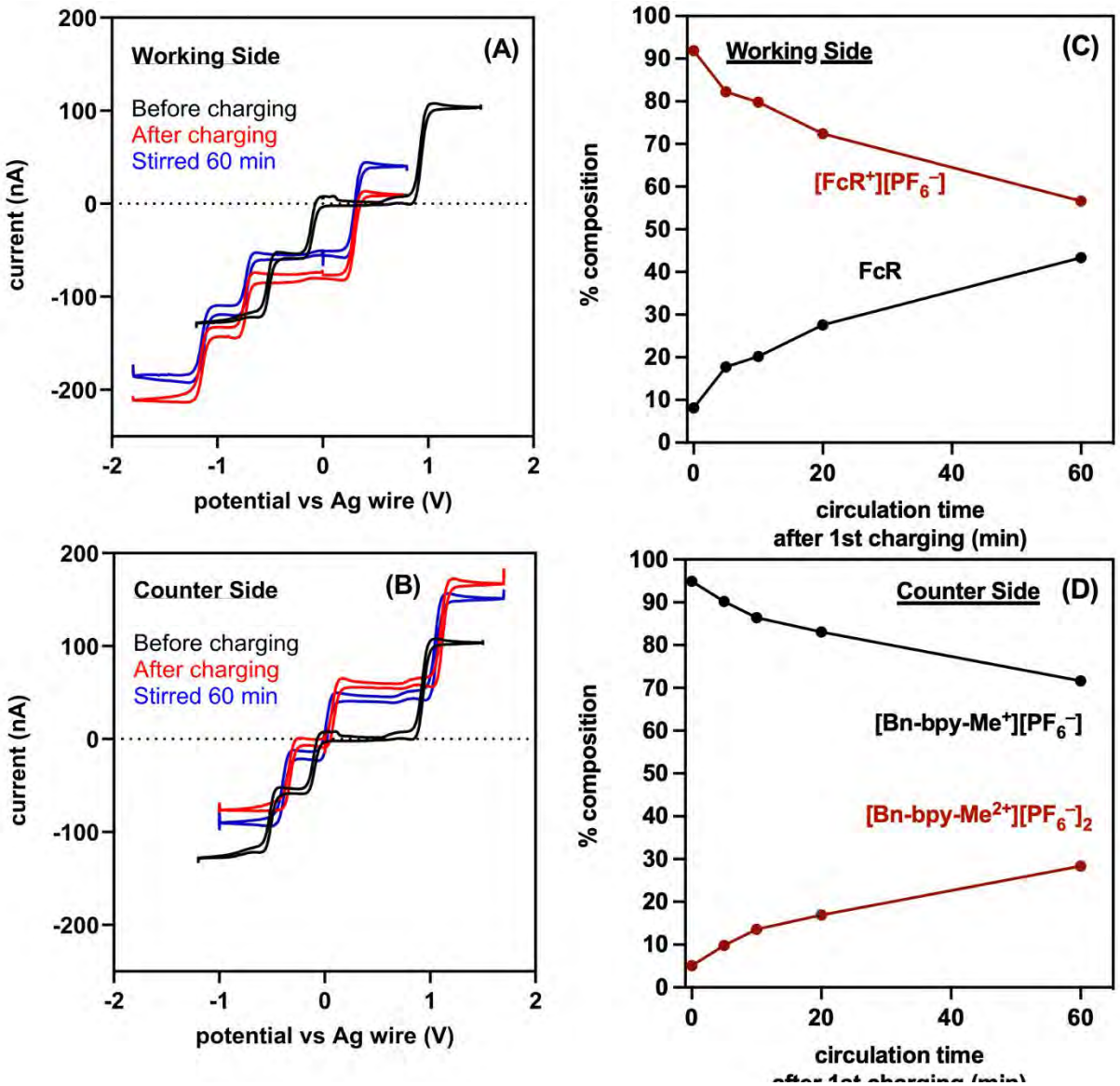

Figure A2.12 (A) Ultramicroelectrode cyclic voltammetry of working side before charging (black), after charging (red), and stirred for 60 min after charging monitored by a microelectrode with 1 sheet of Daramic membrane. (B) Cyclic voltammetry of counter side for the same experiment. (C) Calculated percentages of FcR and $[FcR^+][PF_6^-]$ over circulation time after charging. (D) Calculated percentages of $[Bn\text{-}bpy\text{-}Me^{2+}][PF_6^-]_2$ and $[Bn\text{-}bpy\text{-}Me^+][PF_6^-]$ over circulation time after charging

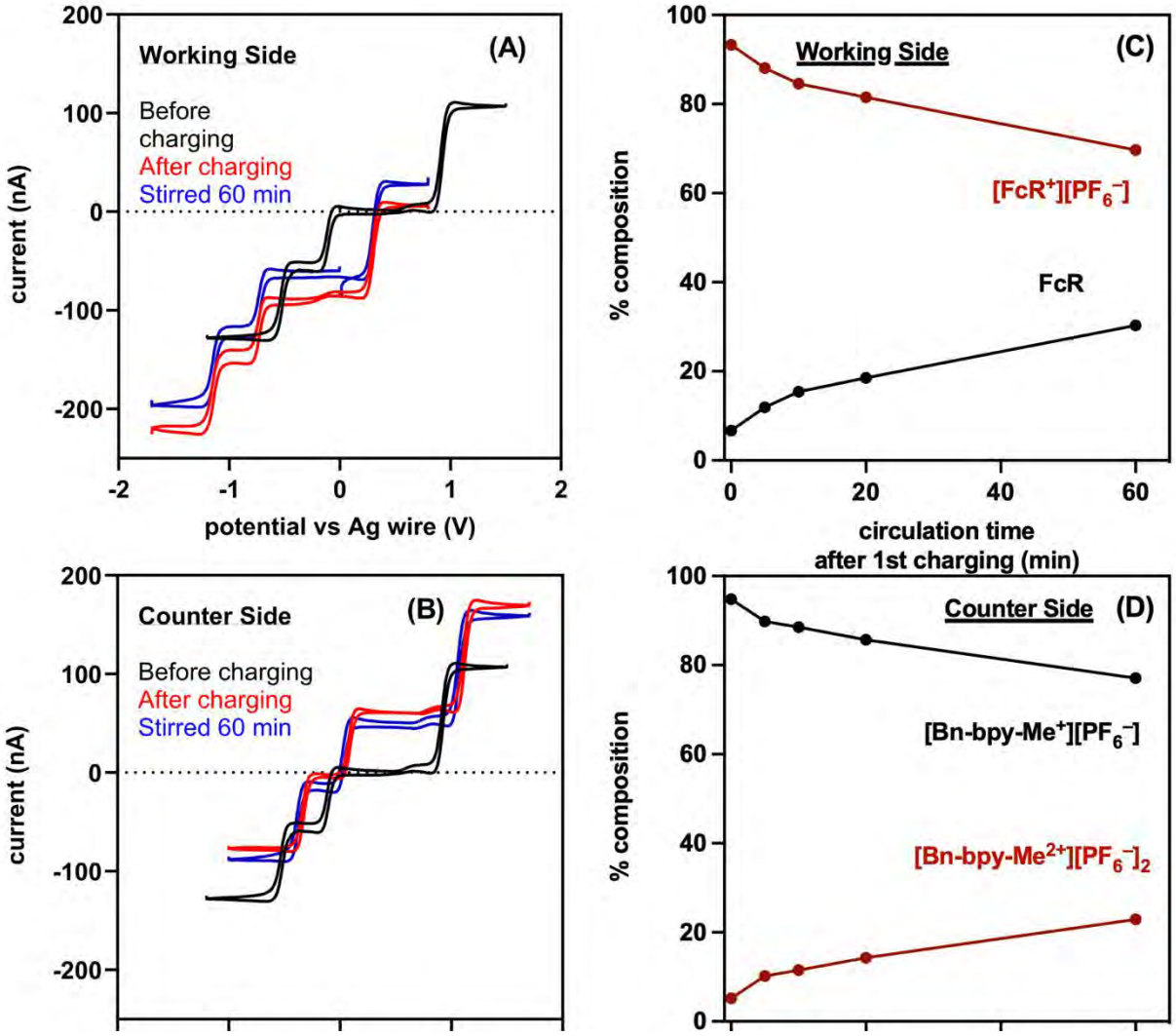

Figure A2.13 (A) Ultramicroelectrode cyclic voltammetry of working side before charging (black), after charging (red), and stirred for 60 min after charging monitored by a microelectrode with 2 sheets of Daramic membrane. (B) Cyclic voltammetry of counter side for the same experiment. (C) Calculated percentages of FcR and $[FcR^+][PF_6^-]$ over circulation time after charging. (D) Calculated percentages of $[Bn\text{-}bpy\text{-}Me^{2+}][PF_6^-]_2$ and $[Bn\text{-}bpy\text{-}Me^+][PF_6^-]$ over circulation time after charging.

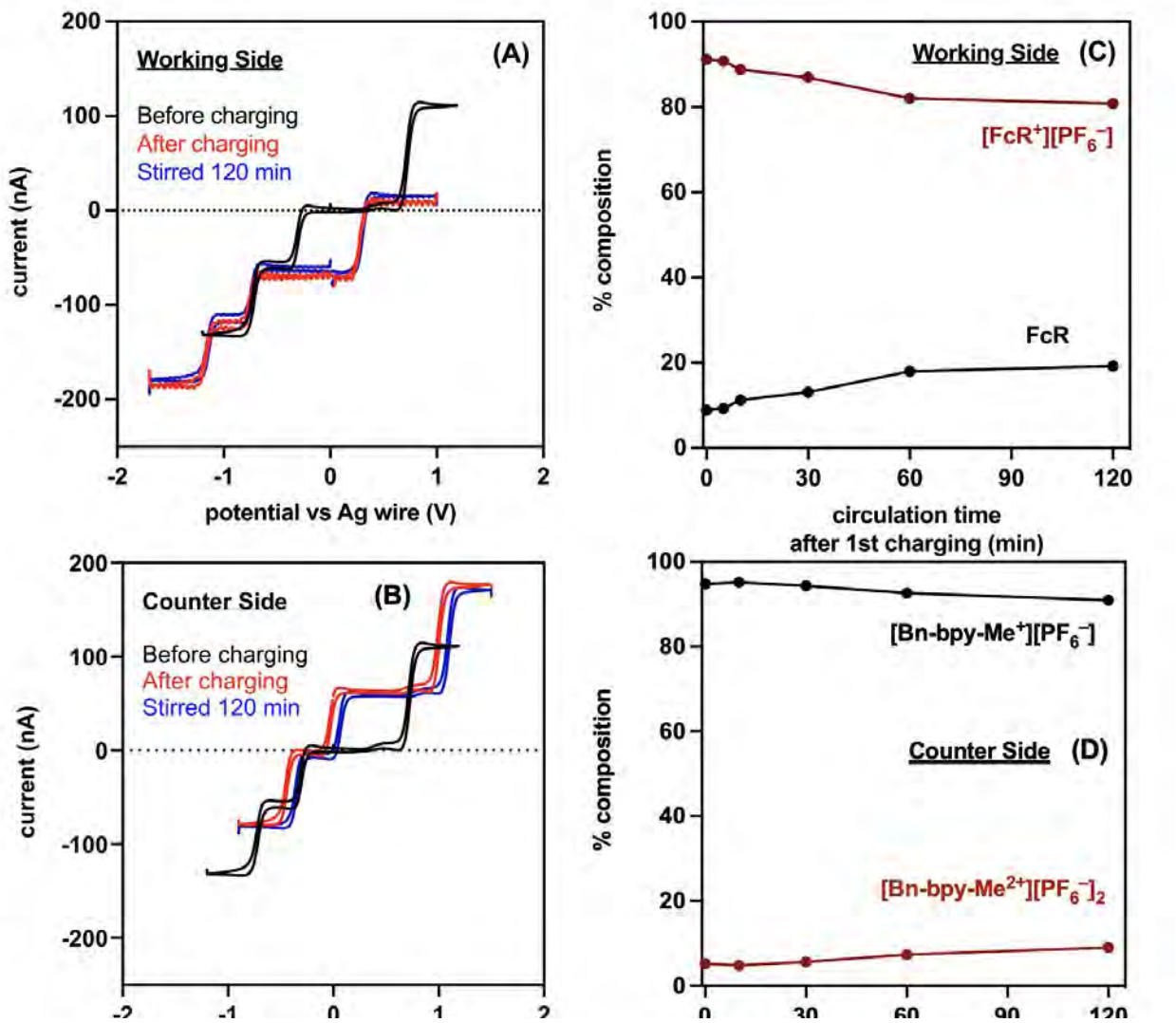

Figure A2.14 (A) Ultramicroelectrode cyclic voltammetry of working side before charging (black), after charging (red), and stirred for 60 min after charging monitored by a microelectrode with 1 sheet of Fumasep membrane. (B) Cyclic voltammetry of counter side for the same experiment. (C) Calculated percentages of FcR and $[FcR^+][PF_6^-]$ over circulation time after charging. (D) Calculated percentages of $[Bn\text{-}bpy\text{-}Me^{2+}][PF_6^-]_2$ and $[Bn\text{-}bpy\text{-}Me^+][PF_6^-]$ over circulation time after charging.

A2.13 Flow Cell Cycling

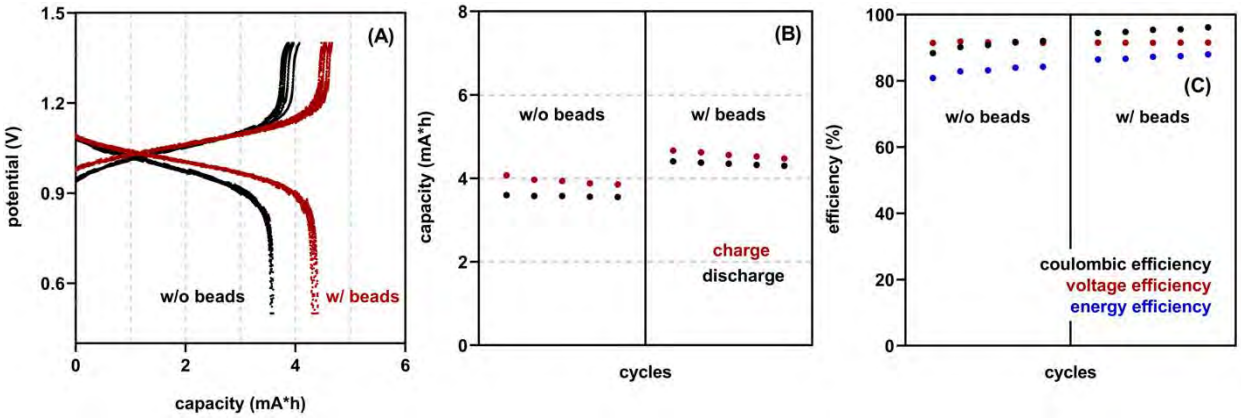

Figure A2.15 RMFB data with or without 1 equiv. functionalized beads using 2 sheets of Celgard membrane. Plots of (A) potential versus capacity, (B) capacity versus cycles, and (C) efficiency versus cycles.

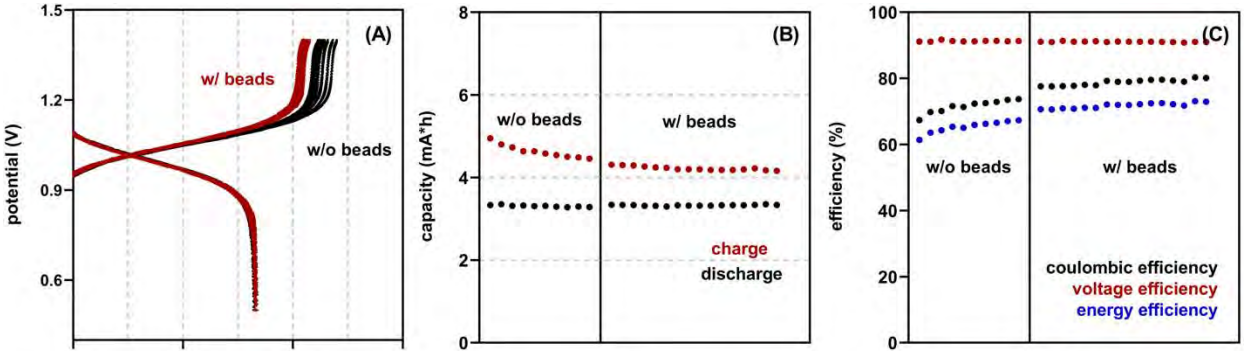

Figure A2.16 RFB data with or without 1 equiv. xPS-Cl (unfunctionalized beads) with 2 sheets of Celgard membrane. Plots of (A) potential versus capacity, (B) capacity versus cycles, and (C) efficiency versus cycles. Data indicated that unfunctionalized beads had no impact on RFB

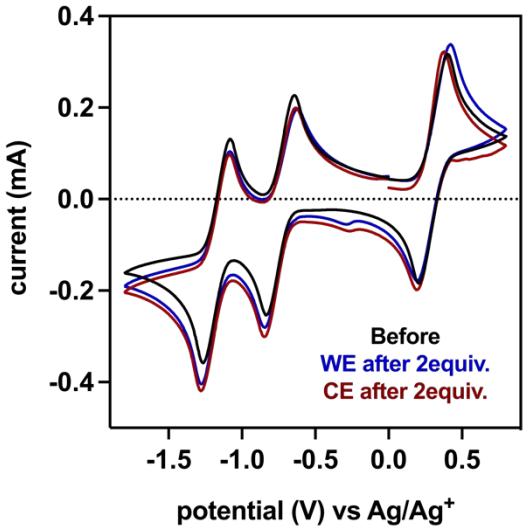

Figure A2.17 Post-run cyclic voltammetry of electrolyte solutions of RMFB (with 2 equiv of beads) before and after cycling. Black CV is before cycling, blue CV ("WE") is catholyte after cycling, red CV ("CE") is anolyte after cycling

A2.14 References

(1) Xiao, Y.; Chu, L.; Sanakis, Y.; Liu, P. Revisiting the IspH catalytic system in the deoxyxylulose phosphate pathway: achieving high activity. *J. Am. Chem. Soc.* **2009**, *131*, 9931–9933.

(2) Nchimi-Nono, K.; Dalvand, P.; Wadhwa, K.; Nuryyeva, S.; Alneyadi, S.; Prakasam, T.; Trabolsi, A. Radical-Cation Dimerization Overwhelms Inclusion in [n] Pseudorotaxanes. *Chem. Eur. J.* **2014**, *20*, 7334–7344.

(3) Milshtein, J. D.; Kaur, A. P.; Casselman, M. D.; Kowalski, J. A.; Modekrutti, S.; Zhang, P. L.; Attanayake, N. H.; Elliott, C. F.; Parkin, S. R.; Risko, C.; Brushett, F. R.; Odom, S. A. High Current Density, Long Duration Cycling of Soluble Organic Active Species for Non-Aqueous Redox Flow Batteries. *Energy Environ. Sci.* **2016**, *9*, 3531–3543.

Appendix 3: Supporting Information for Chapter 4

A3.1 Materials

Poly(vinyl chloride) (PVC) was obtained from Sigma Aldrich and Tygon Tubing ®. Sigma Aldrich: PVC listed: M_w: ~233,000, M_n: ~99,000 (product #: 346764, lot # MKBW2191V), PVC listed: M_w: ~80,000, M_n: ~47,000 (product #: 389323, lot # MKCC7597), PVC listed: M_w: ~43,000, M_n: ~22,000 (product #: 389293, lot # MKCH4545). Tygon Tubing ®: PVC tubing (Formulation: B-44-3, product #: 389293, lot # MKCH4545, inner diameter: 1/8 inch, outer diameter: 1/4 inch, wall thickness: 1/16 inch.

The following reagents were used as received. From Sigma Aldrich: di(2-ethylhexyl) phthalate (lot # MKCK4506), ethoxybenzene, tridecane, 4'-chloroacetanilide, 1,3,5-triethylbenzene, caffeine, 2-chlorophenol, 4-chlorophenol, 4-phenylphenol, diisopropyl azodicarboxylate, triphenylphosphine, hydrochloric acid. From Oakwood Chemical: 1-phenylimidazole, 1-methyl-1H-indole, methyl phenoxyacetate, *N*,*N*-dimethylaminoethanol, (2,2,6,6-tetramethylpiperidin-1-yl)oxyl. From TCI: 3-methylbenzo[b]thiophene, 3-hexylthiophene, 2-phenyl[1,2-a]pyridine, 1-phenylpyrazole. From Fisher: triethylamine.

A3.2 Experimental techniques

Nuclear Magnetic Resonance (NMR) Spectroscopy

Unless otherwise noted, ^{1}H and ^{13}C NMR spectra were acquired at rt. Chemical shift data are reported in units of δ (ppm) relative to tetramethylsilane (TMS). Spectra are referenced to residual solvent. Multiplicities are reported as follows: singlet (s), doublet (d), doublet of doublets (dd), triplet (t), quartet (q), multiplet (m).

High-Resolution Mass Spectrometry (HRMS)

High-resolution mass spectrometry data were obtained on a Micromass AutoSpec Ultima Magnetic Sector mass spectrometer.

Gas Chromatography–Mass Spectrometry (GC-MS)

GC-MS data was collected on Shimadzu GC-2010 gas chromatograph containing a Restek™ Rtx™-5 capillary columns with 15 m length, 0.25 mm inner diameter, 0.25 μm df (film thickness) with 5% diphenyl, 95% dimethsiloxane as the stationary phase, equipped with a Shimadzu GC-MS-QP2010S mass spectrometer. GC-MS data were analyzed using Shimadzu Corporation LabSolutions GC-MS solution Version 2.70 software. GC method: start and hold at 55 °C for 1 min, ramp 10 °C/min to 270 °C, hold at 270 °C for 10 min, total time = 32.5 min.

Sample work-up for GC-MS

A ~0.05 mL aliquot of crude reaction mixture was diluted with ~2 mL diethyl ether (Et_2O) and filtered through a silica gel plug and a PTFE filter (0.2 μm) into a GC vial.

Size-Exclusion Chromatography (SEC)

For SEC analysis, all polymers were dried under vacuum overnight, dissolved (~0.5 mg polymer/mL) in THF spiked with trace toluene as a flow marker (<1 vol%), and filtered through a PTFE filter (0.2 μm). Polymer molar masses were determined by comparison with polystyrene standards (Varian, EasiCal PS-2 MW 580–377, 400) at 40 °C in THF on a Malvern Viscotek GPCMax VE2001 equipped with two Viscotek LT-5000L 8 mm (ID) × 300 mm (L) columns and analyzed with Viscotek TDA 305, or on a Shimadzu LC-20AD equipped with two Styragel HT 7.8 mm (ID) x 300 mm (L) columns and a PSS Gram column 8 mm (ID) x 300 mm (L) and analyzed with Shimadzu SPD-M20A. Data presented corresponds to the refractive index (RI) response normalized to the highest peak, and data were obtained at a flow rate of 1 mL/min.

Fourier-Transform Infrared (FTIR) Spectroscopy

FTIR spectroscopy data were obtained on neat samples using a Thermo-Nicolet IS-50 using the attenuated total reflectance (ATR) accessory.

Elemental Analysis (EA)

EA was performed by Atlantic Microlab, Inc.

Automatic Column Chromatography

Column chromatography was performed using a Biotage® Isolera™ One system and Biotage® Sfär Duo columns.

Thermogravimetric Analysis (TGA)

Thermogravimetric analysis (TGA) thermograms were recorded on a TA Instruments Q50 TGA. All experiments were conducted on platinum TGA sample pans under a nitrogen purge of 50 mL/min with a heating rate of 10 °C/min, covering a temperature range of 27 °C to 550 °C. The instrument was calibrated using the Curie points of alumel and nickel standards.

A3.3 Characterization of PVC sources

Molar mass of PVC samples

The number-average (M_n) and weight-average (M_w) molar masses of each PVC source were measured by SEC. The measured values were different from the manufacturer listed values, and used to describe each PVC source herein, as highlighted in Table S1.

Table A3-1 List of PVC sources used in this work and the molar masses measured by SEC

PVC	Source and Product Info	measured M_n (kg/mol)	measured M_w (kg/mol)	dispersity, $Đ_M$
PVC_{100k}	Sigma Aldrich listed: M_w: ~233,000; M_n: ~99,000	100	318	2.57
PVC_{47k}	Sigma Aldrich listed: M_w: ~80,000; M_n: ~47,000	47	100	2.08
PVC_{35k}	Sigma Aldrich listed: M_w: ~43,000; M_n: ~22,000	35	67	2.08
PVC_{tubing}, PVC_{solid}	Tygon Tubing	83	191	2.42

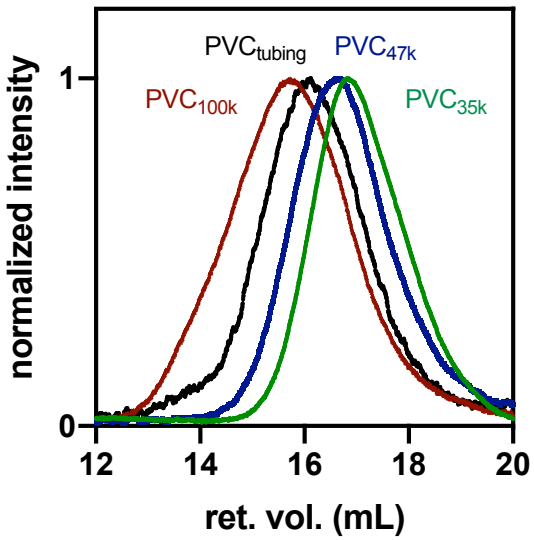

Figure A3.1 Normalized SEC traces of PVC samples

Characterization of PVC$_{tubing}$

Extraction of plasticizer from Tygon tubing. A strip of Tygon tubing (4.145 g) was cut into small pieces (~0.5 cm length) and stirred in THF (~50 mL) at rt until fully dissolved (~30 min). The polymer was precipitated by pouring into cold methanol (~200 mL) while stirring. The polymer was collected by filtration, and the filtrate was concentrated under reduced pressure. This dissolution and precipitation process was repeated on the filtered polymer 2 more times. The combined filtrates were concentrated under reduced pressured and further dried under vacuum overnight to remove residual solvent. A colorless oil was obtained (1.308 g, 32% mass rel. to tubing input, 1:14 mol ratio DEHP:PVC repeat unit). NMR signals and GC retention times of extract matched commercial DEHP standard. Note, the commercial DEHP standard purchased from Sigma Aldrich is labeled "di(octyl) phthalate" by the supplier, but it is actually di(2-ethylhexyl) phthalate (see NMR evidence below).

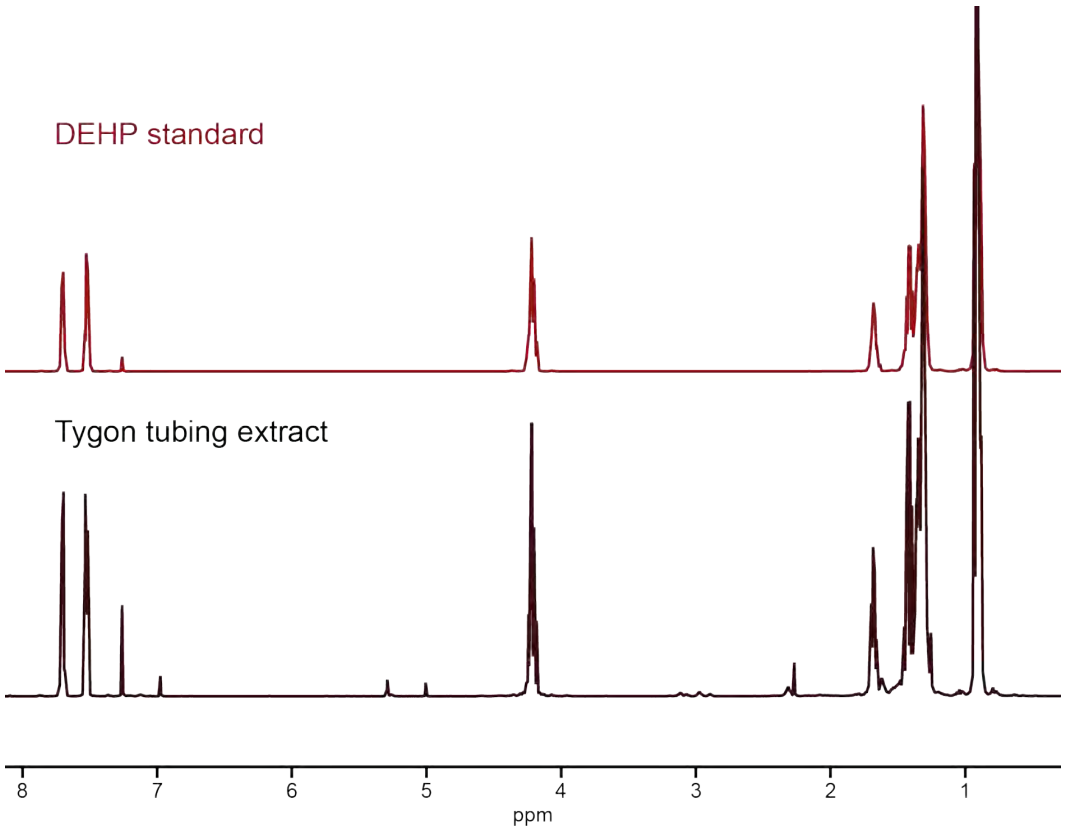

Figure A3.2 Stacked ^{1}H NMR spectra of DEHP standard (Sigma Aldrich) and liquid extracted from Tygon tubing sample. DEHP standard ^{1}H NMR (500 MHz, $CDCl_3$) δ 7.74 – 7.67 (m, 2H), 7.55 – 7.49 (m, 2H), 4.28 – 4.16 (m, 4H), 1.74 – 1.61 (m, 2H), 1.49 – 1.24 (m, 16H), 0.97 – 0.84 (m, 12H). ^{1}H NMR (500 MHz, $CDCl_3$) δ 7.74 – 7.68 (m, 2H), 7.56 – 7.49 (m, 2H), 4.27 – 4.16 (m, 4H), 1.76 – 1.63 (m, 2H), 1.51 – 1.24 (m, 16H), 0.96 – 0.85 (m, 12H)

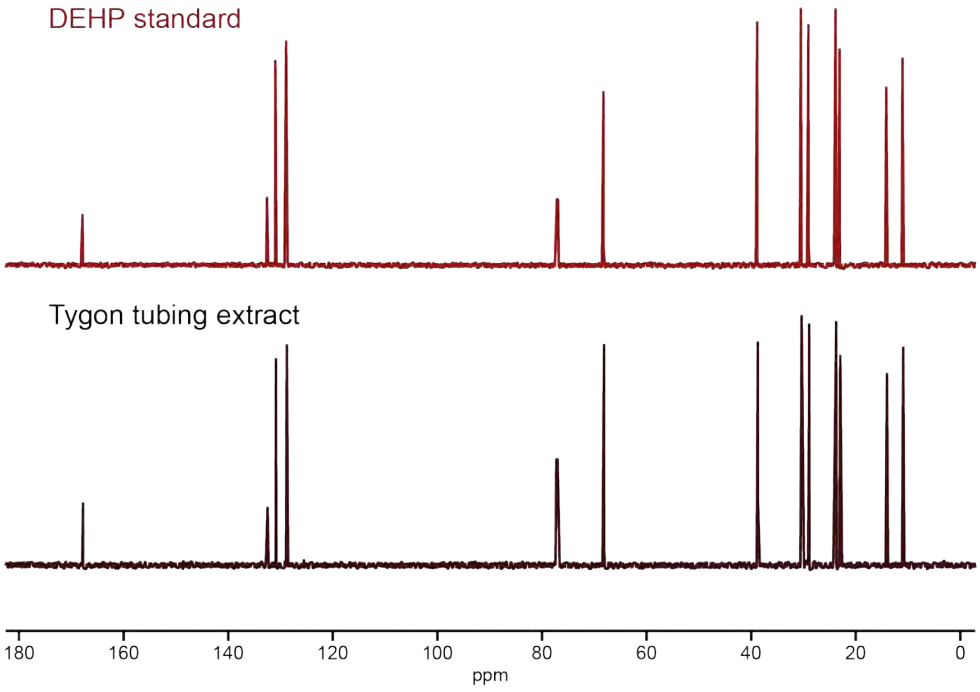

Figure A3.3 Stacked ^{13}C NMR spectra of DEHP standard (Sigma Aldrich) and liquid extracted from Tygon tubing sample. DEHP standard ^{13}C NMR (126 MHz, $CDCl_3$) δ 167.85, 132.58, 130.98, 128.91, 68.26, 38.86, 30.49, 29.05, 23.88, 23.11, 14.17, 11.08. Tygon tubing extract ^{13}C NMR (126 MHz, $CDCl_3$) δ 167.88, 132.60, 131.01, 128.93, 68.28, 38.87, 30.50, 29.06, 23.88, 23.12, 14.18, 11.09

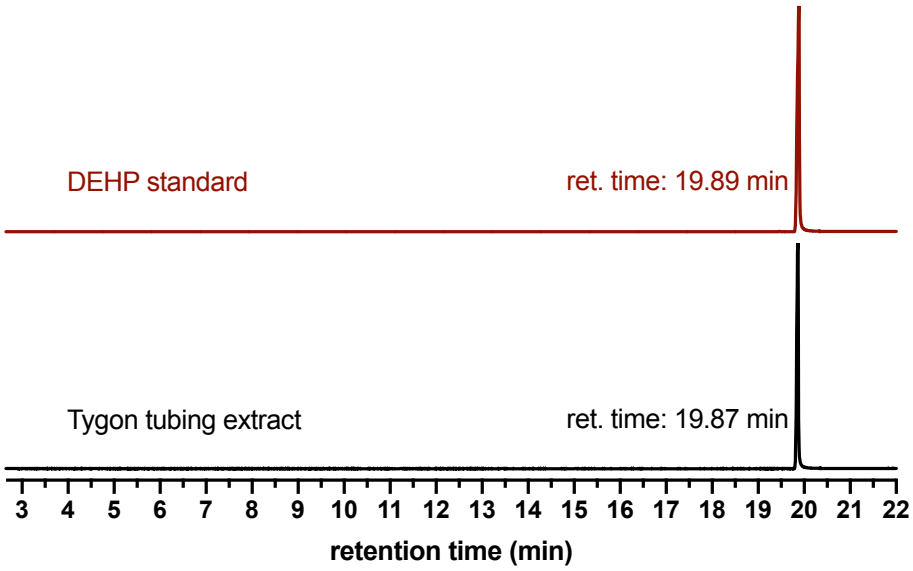

Figure A3.4 Stacked GC-MS chromatograms of DEHP standard (Sigma Aldrich) and liquid extracted from Tygon tubing sample

A3.4 Optimization of paired dehydrochlorination–chlorination reaction

General Procedure A (undivided cell paired electrolysis, constant current, 3 mL scale)

PVC (65 mg, 1.0 mmol (repeat unit), 8.0 equiv. (repeat unit)), NBu_4BF_4 (314 mg, 0.95 mmol), DEHP (0.050 mL, 0.13 mmol, 1.0 equiv.), ethoxybenzene (0.015 mL, 0.13 mmol, 1.0 equiv.), tridecane internal standard (0.010 mL), and DMF (3 mL) were added to a 5 mL *ElectraSyn*® reaction vessel equipped with Teflon coated magnetic stir bar (cylindrical, 12.7 mm length) and two graphite electrodes (0.8 x 0.2 x 5.20 cm). All reagents were dissolved by stirring for at least 15 min, then the reaction mixture was subjected to constant current electrolysis (3 or 7 mA, as specified) with alternating polarity (15 min) at rt. The reaction was stirred at 400 rpm for 5–10 h.

General Procedure B (undivided cell paired electrolysis, constant voltage, 3 mL scale)

PVC (65 mg, 1.0 mmol (repeat unit), 8.0 equiv. (repeat unit)), NBu_4BF_4 (314 mg, 0.95 mmol), DEHP (0.050 mL, 0.13 mmol, 1.0 equiv.), ethoxybenzene (0.015 mL, 0.13 mmol, 1 equiv.), tridecane internal standard (0.010 mL), and DMF (3 mL) were added to a 5 mL *ElectraSyn*® reaction vessel equipped with Teflon coated magnetic stir bar (cylindrical, 12.7 mm length), two graphite electrodes (0.8 x 0.2 x 5.20 cm), and a silver wire reference electrode stored in 3 M KCl in water. All reagents were dissolved by stirring for at least 15 min, then the reaction mixture was subjected to constant voltage electrolysis (−1.1, −1.2, −1.3, or −2.0 V) with alternating polarity (15 min) at rt. The reaction was stirred at 400 rpm for 8 h.

General Procedure C (undivided cell paired electrolysis, constant current, 8 mL scale)

PVC (200 mg, 3.2 mmol (repeat unit), 8.1 equiv. (repeat unit)), NBu_4BF_4 (264 mg, 0.80 mmol), DEHP (0.157 mL, 0.4 mmol, 1.0 equiv.), ethoxybenzene (0.051 mL, 0.4 mmol), tridecane internal standard (0.050 mL), and DMF (8 mL) were added to a 10 mL *ElectraSyn*® reaction vessel equipped with Teflon coated magnetic stir bar (egg-shaped, 16 mm length) and two graphite electrodes (0.8 x 0.2 x 5.20 cm). All reagents were dissolved by stirring for at least 15 min, then the reaction mixture was subjected to constant current electrolysis (10 mA) with alternating polarity (15 min) at rt. The reaction was stirred at 400 rpm for 16 h.

General Procedure D (undivided cell paired electrolysis, constant voltage, 8 mL scale)

PVC (200 mg, 3.2 mmol (repeat unit), 8.1 equiv. (repeat unit)), NBu_4BF_4 (264 g, 0.80 mmol), DEHP (0.157 mL, 0.4 mmol, 1.0 equiv.), ethoxybenzene (0.4 mmol), tridecane internal standard (0.050 mL), and DMF (8 mL) were added to a 10 mL *ElectraSyn*® reaction vessel equipped with Teflon coated magnetic stir bar (egg-shaped, 16 mm length), two graphite electrodes (0.8 x 0.2 x 5.20 cm), and a silver wire reference electrode stored in 3 M KCl in water. All reagents were dissolved (or swelled) by stirring for at least 15 min, then the reaction mixture was subjected to constant voltage electrolysis (−1.3 V) with alternating polarity (15 min) at rt. The reaction was stirred at 400 rpm for 16 h.

Survey of current strength (smaller scale)

The reactions were set up according to General Procedure A and monitored by GC-MS. Details on the GC-MS analysis are described at the end of this section. As shown in Figure S5, once DEHP is consumed, the paired oxidative chlorination reaction tapers off. This information suggests that the rates of each half reaction (reduction and oxidation) should be matched. Note, the effect of operating currents varies with reaction scale. For example, the influence of 7 mA on a 3 mL reaction is different than 7 mA would be a on a larger scale. In forthcoming reactions on a larger scale (8 mL), 10 mA current was used.

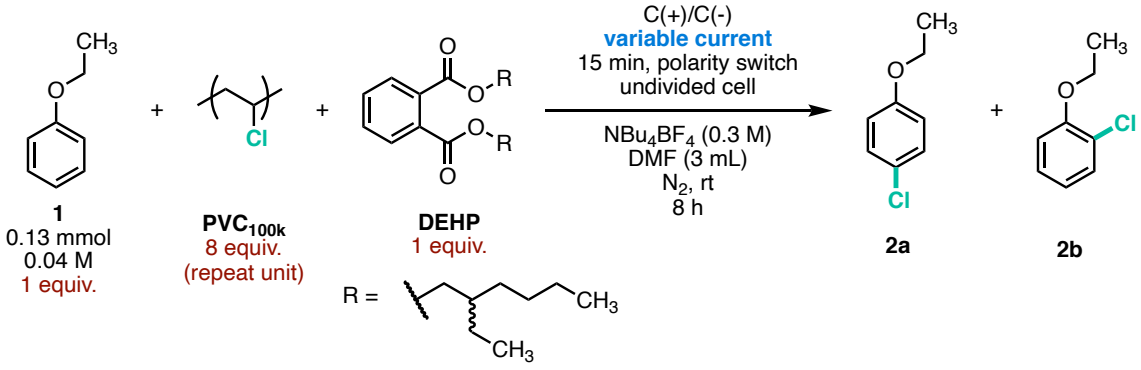

Table A3-2 Survey of current strength on a 3 mL scale paired-electrolysis reaction

entry	conditions	conversion of **1** (%)	consumption of DEHP (%)	yield of **2** (%)
1	3 mA, 10 h	67	89	53
2	7 mA, 5 h	56	95	35

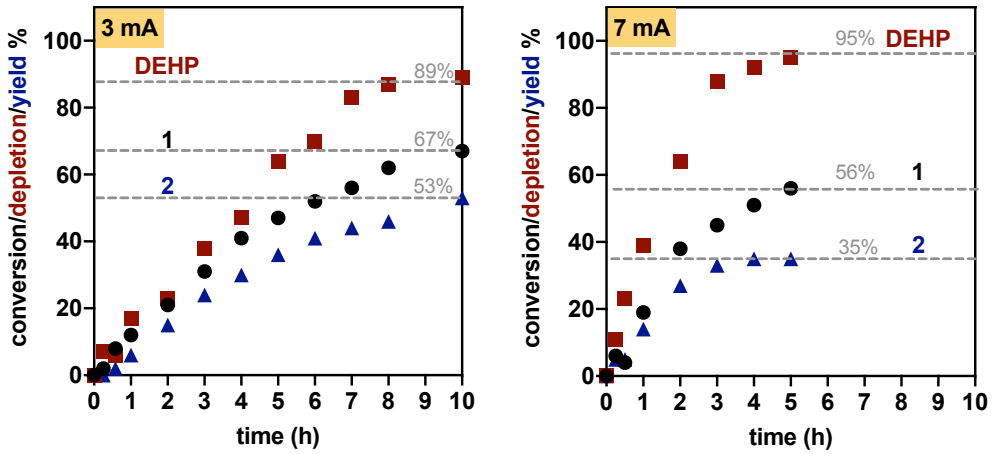

Figure A3.5 Monitoring conversion of 1 (●), consumption of DEHP (■), and yield of 2 (▲) over time under 3 mA (left) and 7 mA (right) constant current. Reactions were performed on a 3 mL scale under N_2

Survey of voltages (smaller scale)

The reactions were set up according to General Procedure B and monitored by GC-MS. −1.3 V is the smallest voltage at which the reaction proceeds and is used in forthcoming constant voltage experiments. Note, this voltage is achieved using the potentiostat built into the IKA ElectraSyn, which differs from the potentiostat used in the cyclic voltammetry and bulk electrolysis studies.

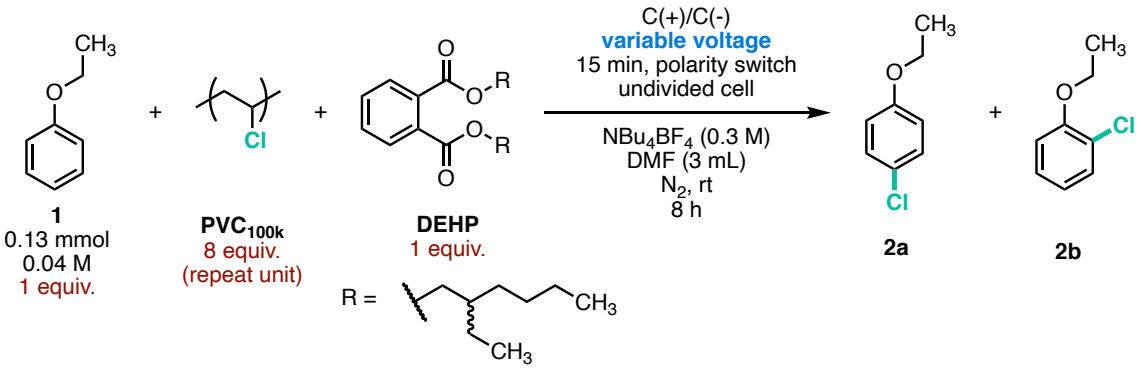

Table A3-3 Survey of voltage strength on a 3 mL scale paired-electrolysis reaction

entry	conditions	conversion of **1** (%)	consumption of DEHP (%)	yield of **2** (%)
1	−1.1 V[a]	n.r.	n.r.	n.r.
2	−1.2 V[a]	n.r.	n.r.	n.r.
3	−1.3 V, 8 h	76	89	55
4	−2.0 V[b], 2 h	43	44	0

[a] Reaction auto shutdown in less than 15 min because the resistance was too high.
[b] Reaction was turned off after 2 h because no product was observed although starting material was being consumed.
n.r. = no reaction occurred

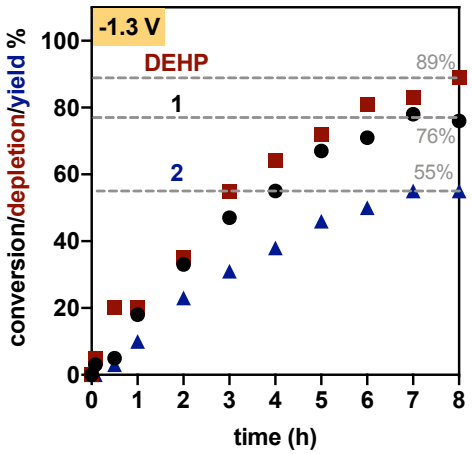

Figure A3.6 Monitoring conversion of 1(●), consumption of DEHP (■), and yield of 2 (▲) over time under -1.3 V constant voltage. Reaction was performed on a 3 mL scale under N_2

Survey of air vs. N_2

The reactions were set up according to General Procedure C and monitored by GC-MS. Each set of conditions were run in duplicate. This data shows that this reaction proceeds to higher yields under air.

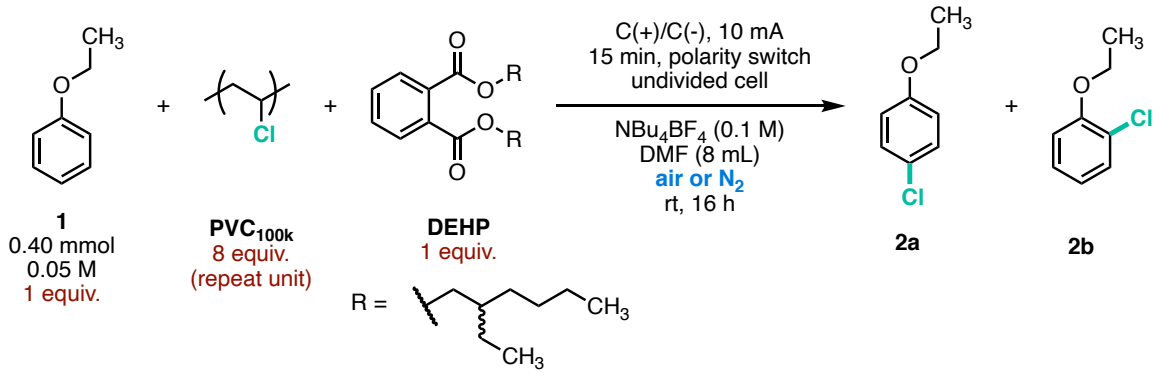

Table A3-4 Survey of air vs N_2 atmosphere on the paired-electrolysis reaction

entry	conditions	conversion of **1** (%)	consumption of **DEHP** (%)	yield of **2** (%)
1	wet[a] DMF air	85, 93	99, 100	68, 77
2	anhydrous[b] DMF N_2	73, 79	97, 98	53, 54

[a] "Wet" DMF was stored in an opened bottle

[b] "Anhydrous" DMF was stored in sure/seal bottle

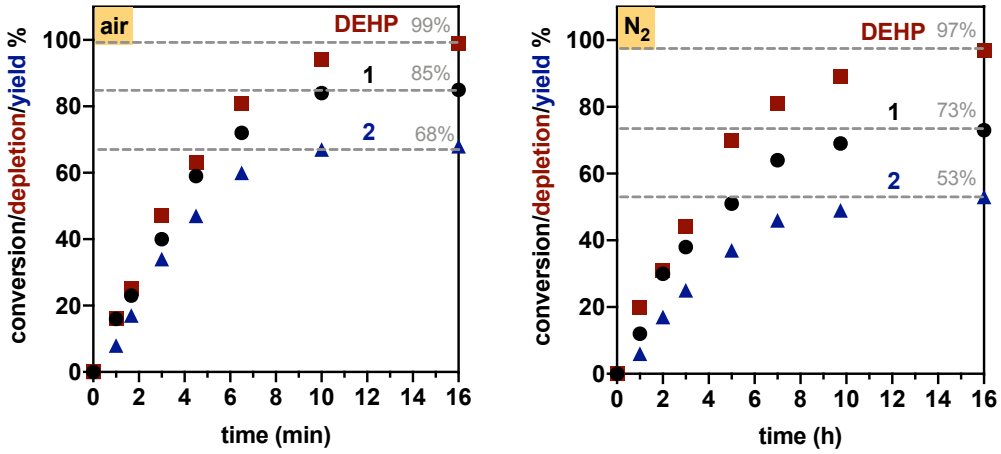

Figure A3.7 Monitoring conversion of (●), consumption of DEHP (■), and yield of 2 (▲) over time under air (left) and a N_2 atmosphere (right). Reactions were performed on an 8 mL scale

Survey of PVC molecular weight and DEHP equivalents under galvanostatic conditions

The reactions were set up according to General Procedure C and monitored by GC-MS. Each set of conditions were run in duplicate. Tributylamine was only observed in the GC-MS traces of reactions performed without DEHP.

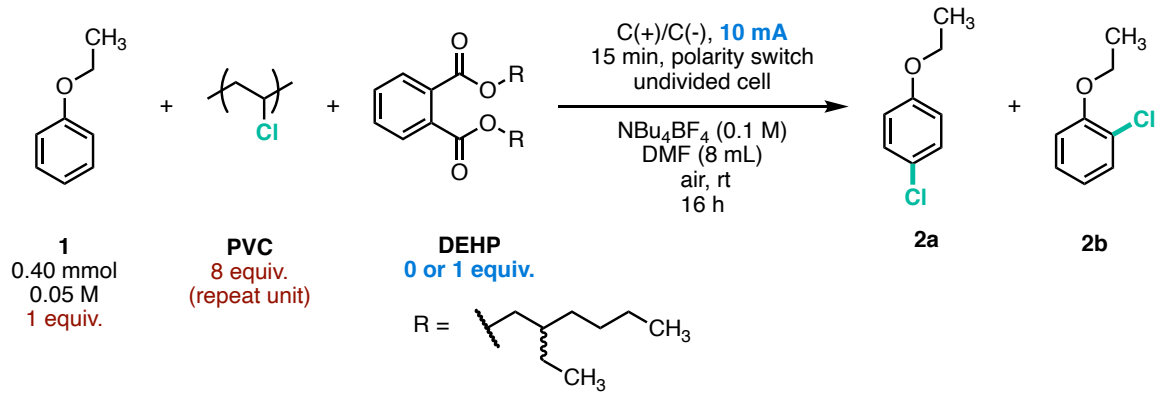

Table A3-5 Survey of effect of PVC molecular weight and presence of DEHP under constant current

entry	**PVC** source	**PVC** equiv.	**DEHP** equiv.	conversion of **1** (%)	consumption of **DEHP** (%)	yield of **2** (%)	NBu_3
1	PVC_{100k}	8	0	53, 51	n/a	26, 31	y, y
2	PVC_{100k}	8	1	85, 93	99, 100	68, 77	n, n
3	PVC_{47k}	8	0	76, 71	n/a	52, 59	y, y
4	PVC_{47k}	8	1	97, 99	96, 99	78, 92	n, n
5	PVC_{35k}	8	0	95, 100	n/a	86, 89	y, y
6	PVC_{35k}	8	1	99, 99	94, 97	74, 75	n, n

n/a = not applicable because reagent was not used in this reaction

Survey of PVC molecular weight and DEHP equivalents under potentiostatic conditions

The reactions were set up according to General Procedure D and monitored by GC-MS. Each set of conditions were run in duplicate. Reactions auto shutdown when there was no DEHP present in the reaction mixture because the resistance was too high. Tributyl amine was observed in the GC-MS traces of all reactions where conversion is observed.

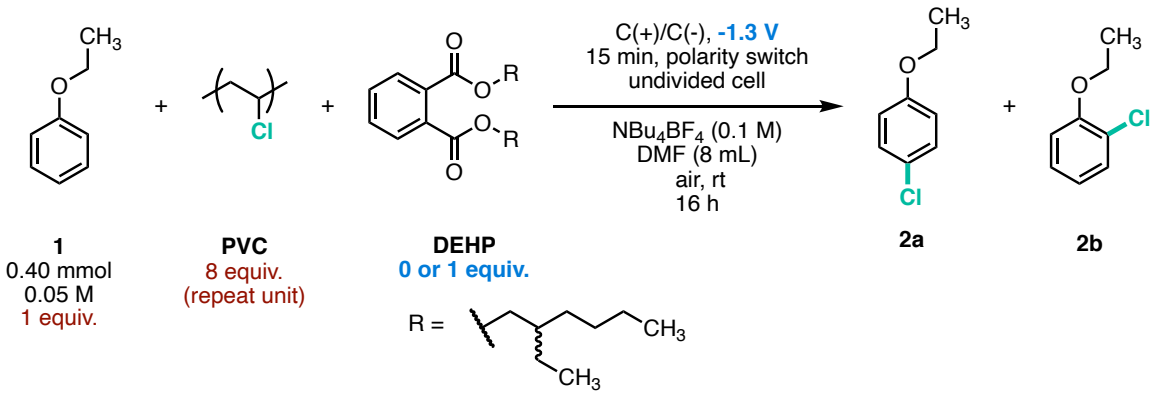

Table A3-6 Survey of effect of PVC molecular weight and presence of DEHP under constant voltage

entry	**PVC** source	**PVC** equiv.	**DEHP** equiv.	conversion of **1** (%)	consumption of **DEHP** (%)	yield of **2** (%)	NBu_3
1	PVC_{100k}	8	0	n.r.	n/a	n.r.	n.r.
2	PVC_{100k}	8	1	84, 73	83, 77	54, 41	y, y
3	PVC_{47k}	8	0	n.r.	n/a	n.r.	n.r.
4	PVC_{47k}	8	1	88, 81	98, 94	57, 46	y, y
5	PVC_{35k}	8	0	n.r.	n/a	n.r.	n.r.
6	PVC_{35k}	8	1	73, 82	94, 99	36, 48	y, y

n.r. = no reaction occurred

n/a = not applicable because reagent was not used in this reaction

GC-MS Analysis

GC-MS data was collected for several chemical standards and used as references for retention times. The mass spectrum of each sample matched >90% with spectra in Shimadzu mass-spec library.

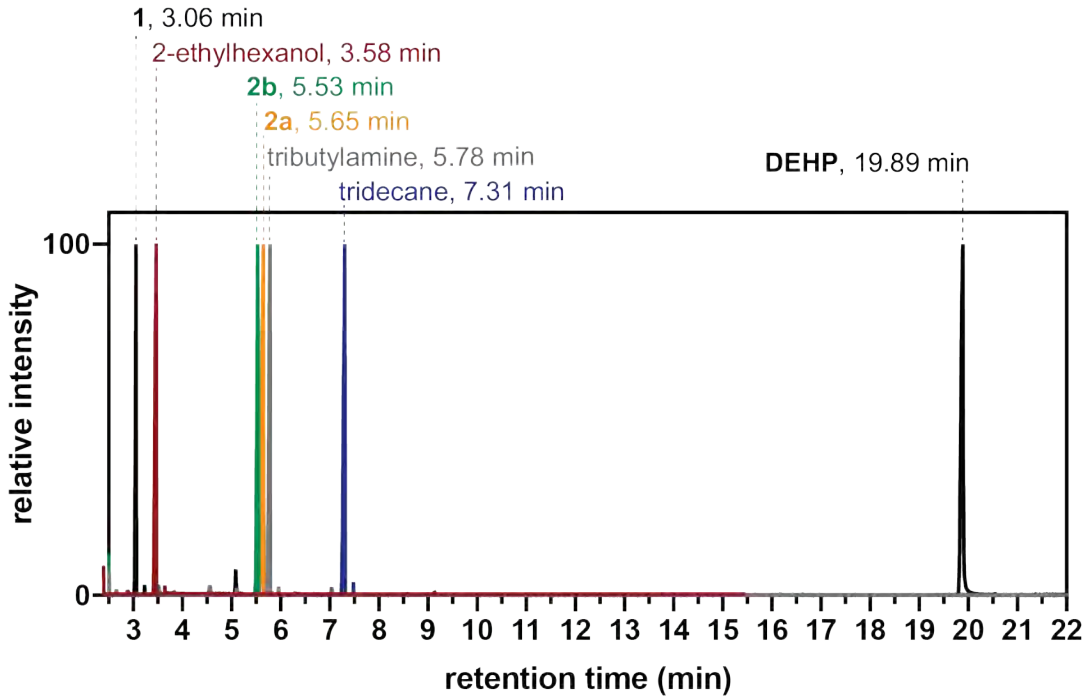

Figure A3.8 Overlaid GC-MS chromatograms of chemical standards relevant to this work

GC-MS response factors of products 4-chloro-1-ethoxybenzene (**2a**) and 4-chloro-1-ethoxybenzene (**2b**) vs. starting material ethoxybenzene (**1**) were calculated using the molar response measured from the GC peak areas of known solution concentrations (eq. 1).

$$response\ factor = \frac{molar\ response\ of\ 2a\ or\ 2b}{molar\ response\ of 1} = \frac{area/concentration}{area/concentration} \qquad (eq.\ 1)$$

Six solutions of known concentrations were prepared according to volumes listed in the table below. For each, the indicated amount of analyte **1**, **2a**, or **2b** was dispensed from a micropipette into a 25 mL volumetric flask and then diluted with acetone. Two GC-MS traces were taken for

each solution, generating 12 total molar response data points for each analyte. These data points were used calculate average response factors for **2a** vs. **1** and **2b** vs. **1**.

response factor of **2a** vs. **1** = **1.17 ± 0.07**

response factor of **2b** vs. **1** = **1.16 ± 0.05**

Table A3-7 Data used to calculate GC-MS response factors, including sample preparation measurements and data extracted from chromatograms

solution	analyte	vol. added (μL)	concentration (M)[a]	trial	GC peak area	molar response	response factor vs. 1
1	1	10	0.00315	1	6753561	2146416616	1.00
				2	7862605	2498892957	1.00
	2a	10	0.00286	1	6660478	2327511290	1.08
				2	7598539	2655317728	1.06
	2b	10	0.00288	1	6923597	2401454036	1.12
				2	7875972	2731785912	1.09
2	1	12	0.00378	1	8167544	2163173887	1.00
				2	7462957	1976564032	1.00
	2a	12	0.00343	1	9236690	2689809482	1.24
				2	8002472	2330393795	1.18
	2b	12	0.00346	1	8717753	2519798491	1.17
				2	7684397	2221115001	1.12
3	1	14	0.00441	1	6785241	1540346538	1.00
				2	7603729	1726154995	1.00
	2a	14	0.00401	1	7755426	1935815758	1.26
				2	8100810	2022026340	1.17
	2b	14	0.00404	1	7443360	1844095831	1.20
				2	8026028	1988452094	1.15
4	1	16	0.00503	1	10251061	2036244996	1.00
				2	11508964	2286111687	1.00

	2a	16	0.00458	1	10215492	2231134252	1.10
				2	11783768	2573656599	1.13
	2b	16	0.00461	1	10468225	2269319074	1.11
				2	12033682	2608681423	1.14
5	1	18	0.00566	1	11447268	2021205821	1.00
				2	10998116	1941900555	1.00
	2a	18	0.00515	1	13374301	2596480026	1.29
				2	12206113	2369688599	1.22
	2b	18	0.00519	1	13184267	2540539677	1.26
				2	11978904	2308272496	1.19
6	1	20	0.00629	1	10923164	1735799878	1.00
				2	9146106	1453407609	1.00
	2a	20	0.00572	1	11357821	1984501458	1.14
				2	10118519	1767963741	1.22
	2b	20	0.00577	1	11581444	2008515619	1.16
				2	10135133	1757688673	1.21

[a] Concentrations were calculated for a total volume of 25 mL. The densities of **1**, **2a**, and **2b** (0.961, 1.1204, and 1.1288 g/mL, respectively) were taken from the literature and used to calculate concentration.[1] The molecular weights of **1**, **2a**, and **2b** (122.17, 156.61, and 156.61 g/mol, respectively) were also used to calculate concentration.

For each reaction, GC-MS was taken before electrolysis (0 min) and after electrolysis (typically 16 h). Representative chromatograms and peak integration area data is shown below. Tridecane was used as an internal standard.

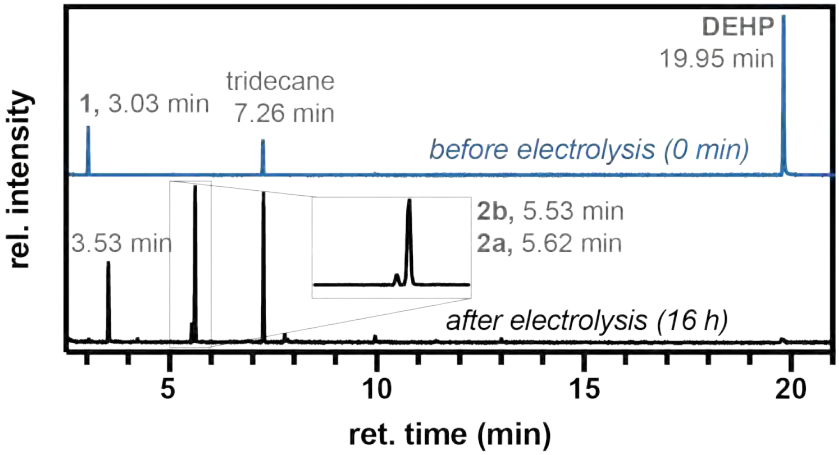

Figure A3.9 Representative GC-MS collected before and after the electrochemical reaction performed according to General Procedure C, using PVC_{47k} and 1 equiv. of DEHP under 10 mA constant current. GC-MS peak at 3.53 min matches with 2-ethylhexanol

Table A3-8 Raw data extracted from representative GC-MS chromatograms from 10 mA constant current electrolysis with PVC_{47k} and 1 equiv. of DEHP

	GC-MS peak area	
compound	**0 min**	**16 h**
1	2295449	25293
2b	0	264078
2a	0	2126567
tributyl amine	0	0
tridecane	2061868	2007309
DEHP	12497710	107637

The fraction of each analyte (**1**, **2a**, **2b**, and **DEHP**) relative to the internal standard (tridecane) was calculated for each using the following equation:

$$fraction\ relative\ to\ standard = \frac{area_{analyte}}{area_{internal\ standard}} \qquad (eq.\ 2)$$

Table A3-9 Representative GC-MS data normalized to tridecane internal standard

	fraction relative to standard	
compound	**0 min**	**16 h**
1	1.113	0.013
DEHP	6.061	0.054
2b	0.000	0.132
2a	0.000	1.059

The percent of **1** converted during electrolysis was determined using the following equation:

$$\%\ of\ 1\ converted = \left(1 - \frac{fraction\ of\ 1\ at\ 16\ h}{fraction\ of\ 1\ at\ 0\ min}\right) \times 100\% \qquad (eq.\ 3)$$

The percent of **DEHP** consumed during electrolysis was determined using the following equation:

$$\%\ of\ DEHP\ consumed = \left(1 - \frac{fraction\ of\ DEHP\ at\ 16h}{fraction\ of\ DEHP\ at\ 0\ min}\right) \times 100\% \qquad (eq.\ 4)$$

The relative percent of **2a** generated during electrolysis (% yield) was determined using the following equation, in which 1.17 is used as the response factor for **2a** vs. **1**:

$$\%\ yield\ of\ 2a = \left(\frac{fraction\ of\ 2a\ at\ 16\ h}{1.17 * fraction\ of\ 1\ at\ 0\ min}\right) \times 100\% \qquad (eq.\ 5)$$

The relative percent of **2b** generated during electrolysis (% yield) was determined using the following equation, in which 1.16 is included as the response factor for **2b** vs. **1**:

$$\%\ yield\ of\ 2b = \left(\frac{fraction\ of\ 2b\ at\ 16h}{1.16 * fraction\ of\ 1\ at\ 0\ min}\right) \times 100\% \qquad \textit{(eq. 6)}$$

The total yield of **2** was determined by adding the individual yields of **2a** and **2b**.

$$total\ \%\ yield\ of\ 2 = \%\ yield\ of\ 2a + \%\ yield\ of\ 2b \qquad \textit{(eq. 7)}$$

Table A3-10 Final values determined from representative GC-MS data from 10 mA constant current electrolysis with PVC_{47k} and 1 equiv. of DEHP

	% converted, consumed, or generated	
compound	**0 min**	**16 h**
1	0	99
DEHP	0	99
2b	0	10
2a	0	81
total yield of 2	**-**	**92**

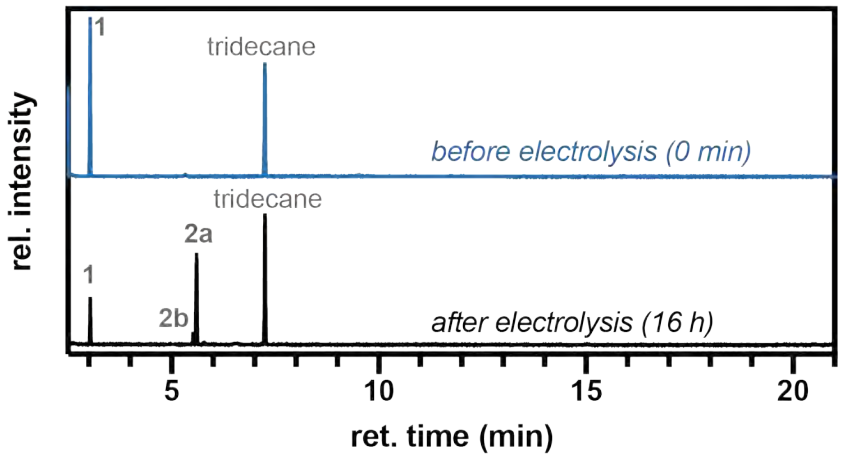

Figure A3.10 Representative GC-MS collected before and after the electrochemical reaction performed according to General Procedure C, using PVC_{47k} and 0 equiv. of DEHP under 10 mA constant current. Note, no material eluted after 21 min

Table A3-11 Raw data extracted from representative GC-MS chromatograms from 10 mA constant current electrolysis with PVC_{47k} and no DEHP

	GC-MS peak area	
compound	**0 min**	**16 h**
1	3332164	541219
2b	0	168956
2a	0	1178574
tributyl amine	0	40544
tridecane	2818302	1872548
DEHP	0	0

Table A3-12 Final values determined from representative GC-MS data from 10 mA constant current electrolysis with PVC_{47k} and no DEHP

	% converted, consumed, or generated	
compound	**0 min**	**16 h**
1	0	76
DEHP	-	-
2b	0	7
2a	0	45
total yield of 2	**-**	**52**

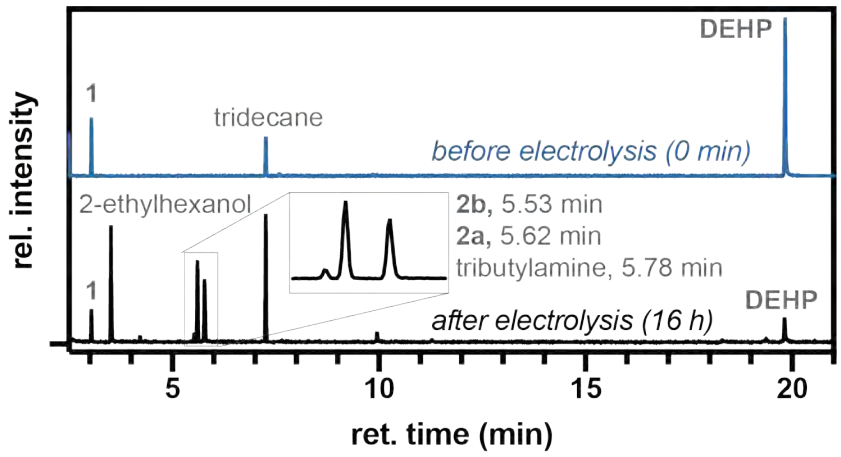

Figure A3.11 Representative GC-MS collected before and after the electrochemical reaction performed according to general procedure D, using PVC_{47k} and 1 equiv. of DEHP under −1.3 V constant voltage. Note, no material eluted after 21 min

Table A3-13 Raw data extracted from representative GC-MS chromatograms from −1.3 V constant voltage electrolysis with PVC_{47k} and 1 equiv. DEHP

	GC-MS peak area	
compound	**0 min**	**16 h**
1	2675738	418466
2b	0	123465
2a	0	1064898
tributyl amine	0	926672
tridecane	2178672	1793189
DEHP	10665027	521906

Table A3-14 Final values determined from representative GC-MS data from −1.3 V constant voltage electrolysis with PVC_{47k} and 1 equiv. DEHP

	% converted, consumed, or generated	
compound	**0 min**	**16 h**
1	0	81
DEHP	0	94
2b	0	5
2a	0	41
total yield of 2	**-**	**46**

A3.5 Cyclic voltammetry

Analysis of individual components

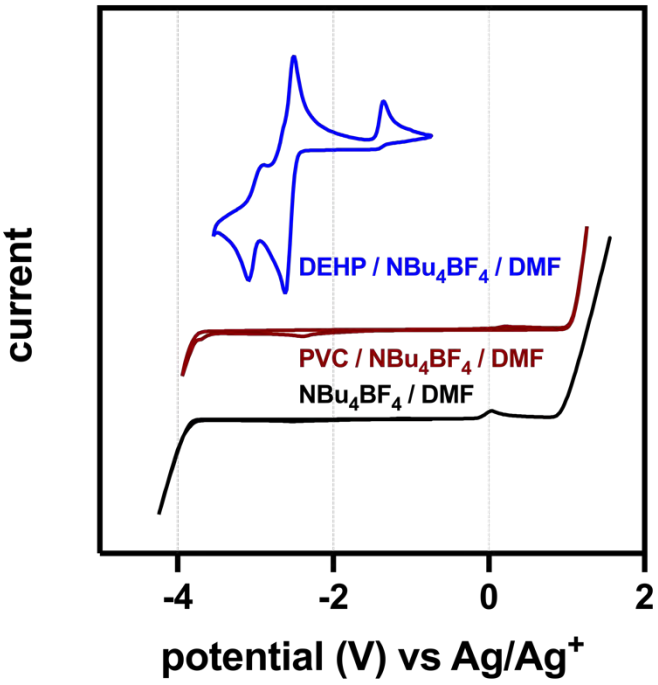

Figure A3.12 CVs of a blank solution (black —), 10 mM PVC_{35k} calculated per repeat unit (red —), and 10 mM DEHP (blue —). CVs were collected in 0.1 M NBu_4BF_4 in DMF using a 100 mV/s scan rate.

Analysis of mixed components

CVs of the first $1e^-$ redox couple of DEHP were collected in the presence of increasing equivalents of PVC. Equivalents were calculated by repeat unit mass and are effectively the same the number of C–Cl bonds. CVs were initially collected using a 10 mM concentration of DEHP. The concentration was reduced by 10-fold (1 mM DEHP) to minimize viscosity/diffusivity effects upon addition of excess polymer. Although attenuated at lower net concentrations, PVC still affected the reversibility of the $1e^-$ redox couple observed for DEHP. Control studies using polystyrene (average M_w: 35,000 g/mol, lot # MKCD6541) showed a

negligible effect on the $1e^-$ redox couple observed for DEHP, suggesting changes in solution viscosity were not significant.

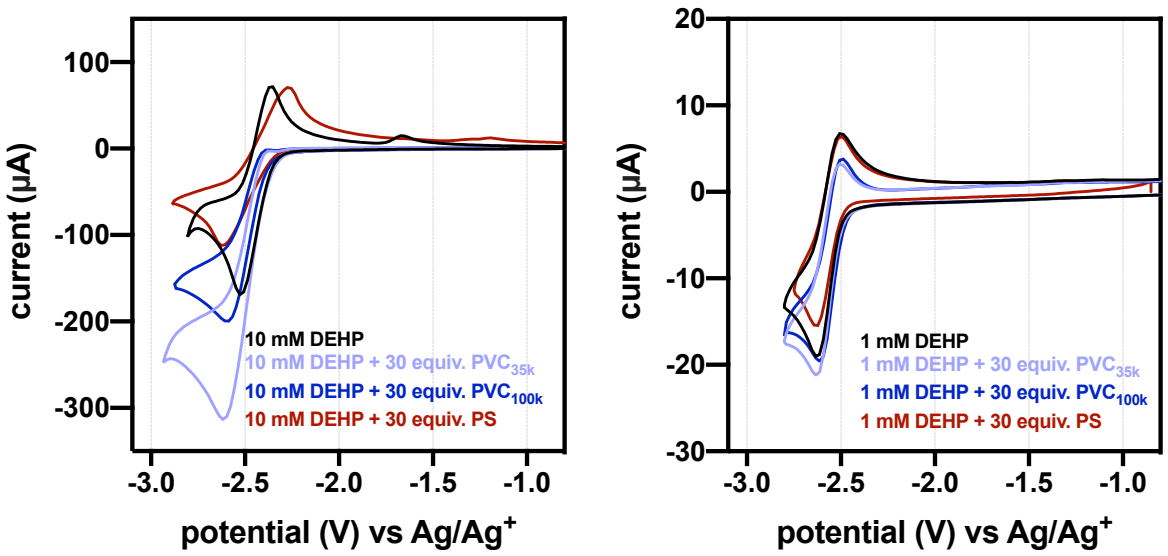

Figure A3.13 CVs of DEHP at 10 mM (left) and 1 mM (right) and DEHP mixed with 30 equiv. PVC_{35k}, PVC_{100k}, or PS. CVs were collected in 0.1 M NBu_4BF_4 in DMF using 100 mV/s scan rate.

Table A3-15 Raw data extracted from CV measurements of DEHP mixed with 30 equiv. PVC_{35k}, PVC_{100k}, or PS

polymer added	10 mM DEHP			1 mM DEHP		
	i_{pa} (μA) oxidation	**i_{pc} (μA) reduction**	**i_{pa} / i_{pc}**	**i_{pa} (μA) oxidation**	**i_{pc} (μA) reduction**	**i_{pa} / i_{pc}**
none	92.0	168.8	0.54	10.3	17.3	0.59
PVC_{35k} (30 equiv.)	-	314.3	-	7.8	19.5	0.40
PVC_{100k} (30 equiv.)	-	199.1	-	7.9	18.0	0.44
PS (30 equiv.)	71.4	112.5	0.63	9.2	13.8	0.67

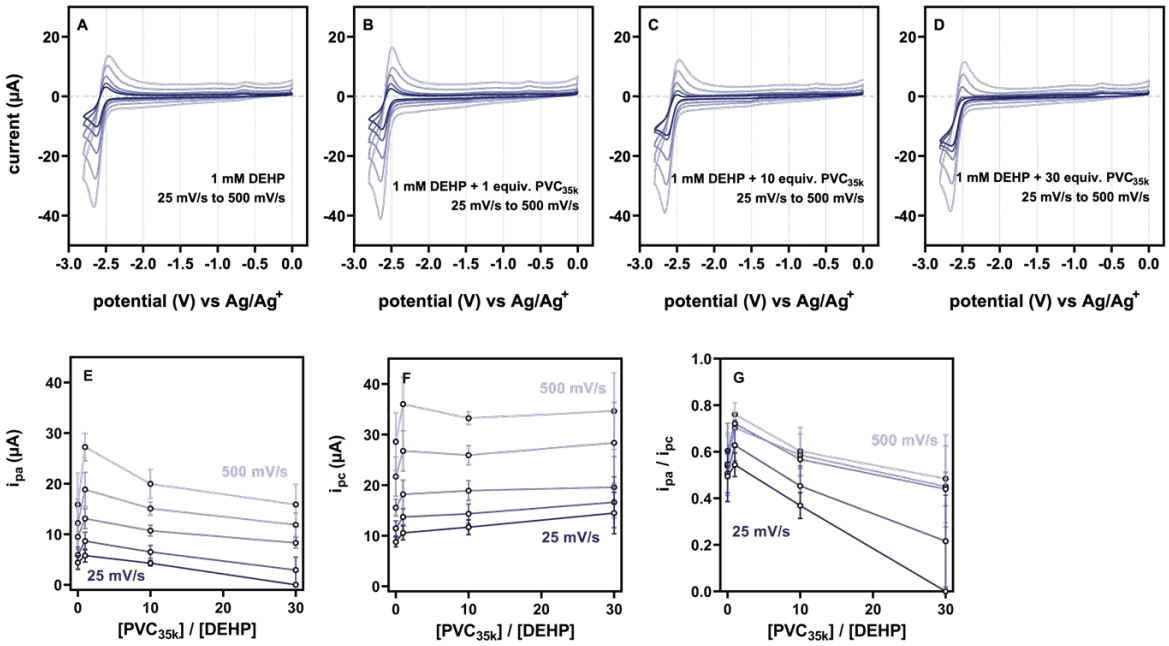

Figure A3.154 (A–D) Cyclic voltammetry of 1 mM DEHP in the presence of (A) 0 equiv. (B) 1 equiv. (C) 10 equiv. (D) 30 equiv. of PVC_{35k} with scan rates of 25, 50, 100, 250, 500 mV/s (darkest blue = 25 and lightest blue = 500 mV/s) (E) oxidation current (F) reduction current (G) oxidation/reduction

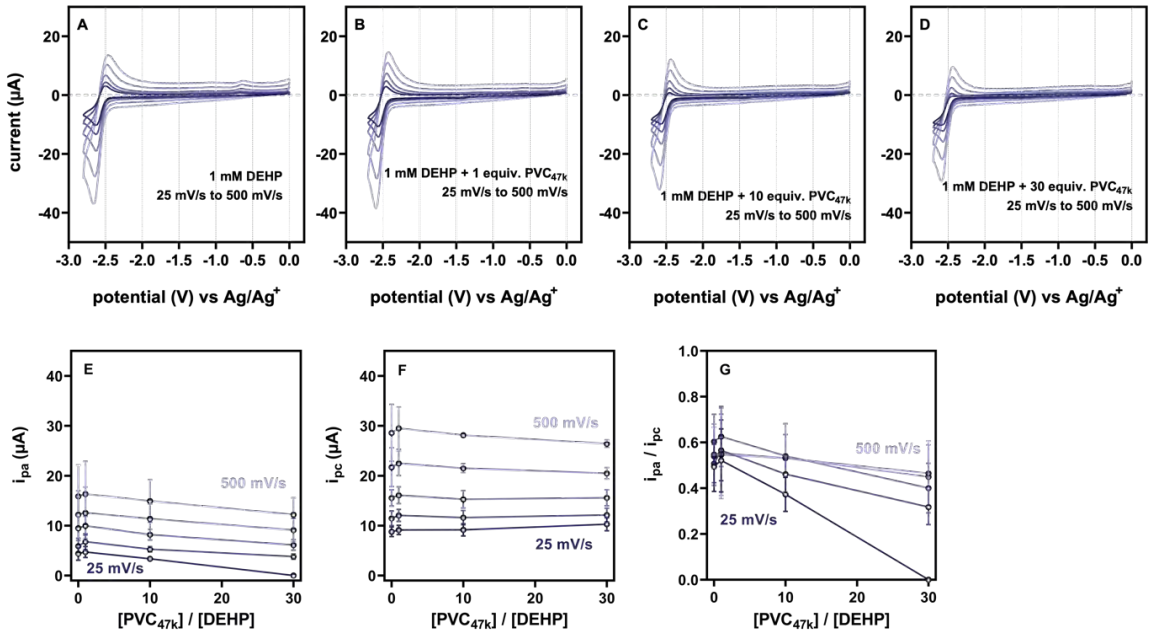

Figure A3.145 (A–D) Cyclic voltammetry of 1 mM DEHP in the presence of (A) 0 equiv. (B) 1 equiv. (C) 10 equiv. (D) 30 equiv. of PVC_{47k} with scan rates of 25, 50, 100, 250, 500 mV/s (darkest blue = 25 and lightest blue = 500 mV/s) (E) oxidation current (F) reduction current (G) oxidation/reduction

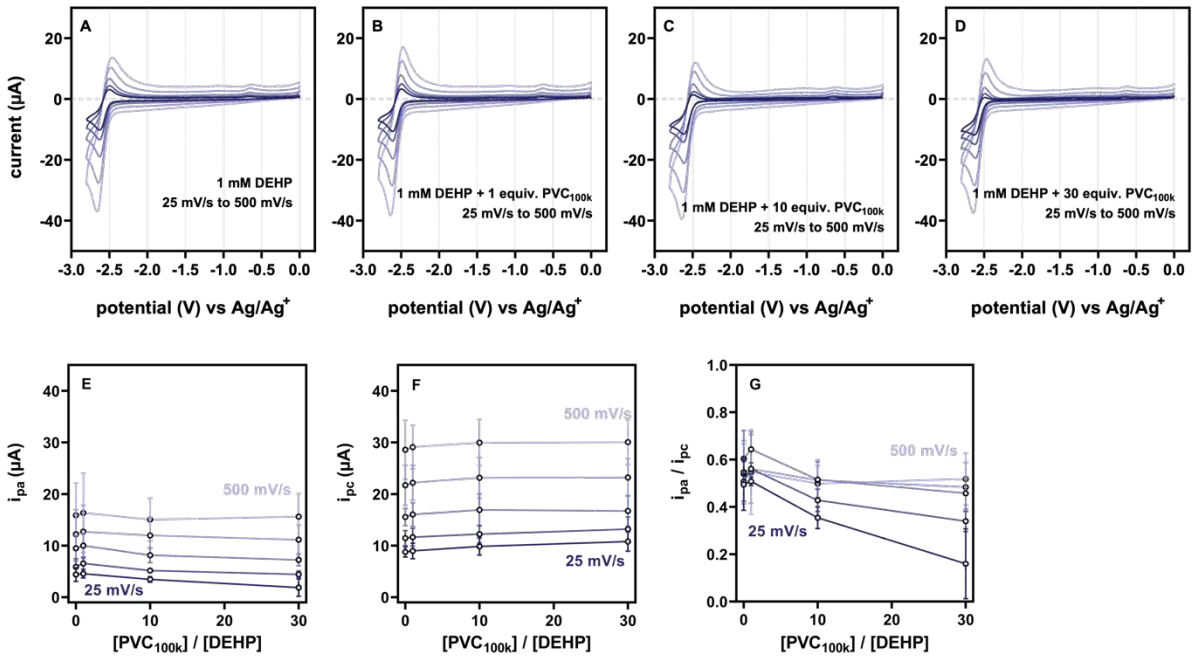

Figure A3.16 (A–D) Cyclic voltammetry of 1 mM DEHP in the presence of (A) 0 equiv. (B) 1 equiv. (C) 10 equiv. (D) 30 equiv. of PVC_{100k} with scan rates of 25, 50, 100, 250, 500 mV/s (darkest blue = 25 and lightest blue = 500 mV/s (E) oxidation current (F) reduction current (G) oxidation/reduction

Table A3-16 Raw data extracted from CV measurements, measured in triplicate using PVC_{35k} as the PVC source.

equiv. of PVC_{35k}	scan rate (mV/s)	i_{pa} (μA), oxidation					i_{pc} (μA), reduction					i_{pa} / i_{pc}				
		trial 1	trial 2	trial 3	avg.	std. dev.	trial 1	trial 2	trial 3	avg.	std. dev.	trial 1	trial 2	trial 3	avg.	std. dev.
0	25	5.0	2.9	5.4	4.4	1.34	9.6	7.7	9.1	8.8	0.97	0.52	0.37	0.59	0.50	0.11
	50	6.7	4.1	6.8	5.9	1.55	12.7	9.9	11.8	11.5	1.46	0.53	0.41	0.58	0.51	0.08
	100	10.7	5.9	9.8	9.5	2.49	17.3	13.4	15.6	15.5	1.63	0.62	0.44	0.63	0.60	0.12
	250	16.0	6.9	13.8	12.2	4.76	25.0	17.4	22.7	21.7	3.89	0.64	0.39	0.61	0.55	0.13
	500	20.3	8.7	18.6	15.9	6.26	33.3	22.2	30.3	28.6	5.71	0.61	0.39	0.62	0.54	0.13
1	25	5.0	7.3	5.1	5.8	1.28	10.0	12.1	9.5	10.6	1.38	0.50	0.60	0.54	0.54	0.05
	50	7.4	10.7	7.8	8.7	1.78	13.4	15.5	12.3	13.7	1.59	0.56	0.69	0.63	0.63	0.07
	100	12.8	16.0	11.9	13.1	1.96	18.3	22.1	16.2	18.2	2.81	0.70	0.72	0.74	0.72	0.02
	250	16.0	22.6	17.9	18.8	3.38	25.5	31.2	23.6	26.8	3.99	0.63	0.72	0.76	0.70	0.07
	500	26.3	30.3	25.2	27.3	2.73	36.0	41.4	30.7	36.0	5.32	0.73	0.73	0.82	0.76	0.05
10	25	3.8	4.8	4.3	4.3	0.50	12.0	13.0	10.1	11.7	1.47	0.31	0.37	0.42	0.37	0.06
	50	5.0	7.5	7.0	6.5	1.32	13.6	16.5	12.9	14.4	1.92	0.37	0.45	0.54	0.45	0.09
	100	10.1	12.3	10.5	10.7	1.06	19.0	21.6	17.0	18.9	1.96	0.53	0.57	0.62	0.57	0.04
	250	15.1	13.8	16.4	15.1	1.29	27.3	26.7	23.8	25.9	1.91	0.55	0.52	0.69	0.59	0.09
	500	19.6	17.3	23.0	20.0	2.84	34.5	33.3	32.0	33.2	1.26	0.57	0.52	0.72	0.60	0.10
30	25	0	0	0	0	0	15.4	18.0	10.0	14.5	4.10	0	0	0	0	0
	50	4.0	0	4.7	2.9	2.56	15.6	22.1	12.2	16.6	5.03	0.26	0	0.39	0.22	0.20
	100	8.5	9.6	8.0	8.3	1.03	19.4	28.2	15.9	19.6	6.07	0.44	0.34	0.50	0.44	0.07
	250	13.9	9.4	12.3	11.9	2.32	26.9	37.0	21.2	28.4	8.02	0.52	0.25	0.58	0.45	0.17
	500	19.1	11.4	17.0	15.9	3.99	34.6	42.2	27.1	34.6	7.56	0.55	0.27	0.63	0.48	0.19

Table A3-17 Raw data extracted from CV measurements, measured in triplicate using PVC_{47k} as the PVC source

equiv. of PVC_{47k}	scan rate (mV/s)	i_{pa} (μA), oxidation					i_{pc} (μA), reduction					i_{pa} / i_{pc}				
		trial 1	trial 2	trial 3	avg.	std. dev.	trial 1	trial 2	trial 3	avg.	std. dev.	trial 1	trial 2	trial 3	avg.	std. dev.
1	25	3.6	5.8	4.7	4.7	1.10	9.9	9.4	8.1	9.1	0.92	0.36	0.62	0.58	0.52	0.14
	50	5.3	8.4	6.7	6.8	1.56	12.7	12.8	10.7	12.0	1.21	0.41	0.66	0.63	0.57	0.13
	100	8.0	11.8	10.1	10.0	1.89	17.0	17.1	14.2	16.1	1.68	0.47	0.69	0.71	0.63	0.13
	250	6.9	17.1	13.7	12.6	5.16	21.3	25.3	20.8	22.5	2.45	0.32	0.67	0.66	0.55	0.20
	500	9.1	21.7	18.3	16.3	6.52	26.6	34.4	27.5	29.5	4.25	0.34	0.63	0.66	0.55	0.18
10	25	3.1	3.8	3.2	3.4	0.38	10.6	8.7	8.2	9.2	1.24	0.29	0.44	0.39	0.37	0.07
	50	4.9	5.9	5.1	5.3	0.52	13.2	11.1	10.5	11.6	1.43	0.37	0.53	0.49	0.46	0.08
	100	7.7	9.4	7.4	8.2	1.07	17.2	14.8	13.8	15.3	1.73	0.45	0.64	0.54	0.54	0.09
	250	8.1	14.0	12.0	11.4	2.98	22.3	21.6	20.6	21.5	0.87	0.36	0.65	0.58	0.53	0.15
	500	10.3	18.6	15.9	14.9	4.26	28.1	28.3	28.0	28.1	0.14	0.37	0.66	0.57	0.53	0.15
30	25	0	0	0	0	0	11.7	9.2	10.0	10.3	1.30	0	0	0	0	0
	50	3.2	4.2	3.9	3.8	0.52	13.7	11.0	11.7	12.1	1.38	0.24	0.39	0.33	0.32	0.08
	100	5.2	7.2	6.0	6.1	1.04	17.3	14.1	15.4	15.6	1.62	0.30	0.51	0.39	0.40	0.11
	250	6.7	11.4	9.3	9.1	2.34	21.7	19.4	20.3	20.5	1.17	0.31	0.58	0.46	0.45	0.14
	500	8.8	15.5	12.3	12.2	3.38	27.1	25.6	26.6	26.4	0.78	0.32	0.61	0.46	0.46	0.14

Table A3-18 Raw data extracted from CV measurements, measured in triplicate using PVC_{100k} as the PVC source

equiv. of PVC_{100k}	scan rate (mV/s)	i_{pa} (μA), oxidation					i_{pc} (μA), reduction					i_{pa} / i_{pc}				
		trial 1	trial 2	trial 3	avg.	std. dev.	trial 1	trial 2	trial 3	avg.	std. dev.	trial 1	trial 2	trial 3	avg.	std. dev.
1	25	5.3	4.7	3.7	4.6	0.81	10.1	9.5	7.3	9.0	1.50	0.53	0.49	0.51	0.51	0.02
	50	7.6	6.9	5.2	6.6	1.24	12.9	12.4	9.7	11.6	1.72	0.59	0.56	0.53	0.56	0.03
	100	12.2	10.4	7.4	10.0	2.45	18.0	16.6	13.5	16.0	2.31	0.68	0.62	0.55	0.64	0.07
	250	18.6	10.2	9.3	12.7	5.14	25.6	22.2	18.8	22.2	3.39	0.73	0.46	0.49	0.56	0.15
	500	25.1	12.4	11.5	16.3	7.63	33.4	28.9	25.0	29.1	4.20	0.75	0.43	0.46	0.55	0.18
10	25	4.1	3.2	3.1	3.5	0.54	11.0	10.6	7.9	9.8	1.66	0.37	0.30	0.39	0.35	0.05
	50	5.5	5.1	4.9	5.2	0.29	13.4	13.0	10.3	12.2	1.70	0.41	0.39	0.48	0.43	0.05
	100	9.8	7.6	7.1	8.1	1.44	19.6	17.6	13.6	16.9	3.08	0.50	0.43	0.52	0.52	0.08
	250	16.0	9.5	10.5	12.0	3.51	27.4	22.6	19.5	23.2	3.97	0.58	0.42	0.54	0.51	0.09
	500	19.8	12.0	13.5	15.1	4.14	34.9	28.7	26.3	30.0	4.47	0.57	0.42	0.51	0.50	0.08
30	25	3.3	2.3	0	1.9	1.69	11.3	12.4	8.7	10.8	1.87	0.29	0.19	0	0.16	0.15
	50	5.1	4.4	3.8	4.4	0.66	14.0	15.0	10.5	13.2	2.37	0.37	0.29	0.36	0.34	0.04
	100	8.5	6.8	6.4	7.2	1.12	18.0	18.9	13.3	16.7	2.96	0.47	0.36	0.48	0.46	0.07
	250	14.4	9.1	10.0	11.2	2.81	25.6	25.0	19.0	23.2	3.64	0.56	0.36	0.52	0.48	0.10
	500	20.7	13.1	13.0	15.6	4.42	33.0	32.1	25.1	30.1	4.31	0.63	0.41	0.52	0.52	0.11

A3.6 Bulk Electrolysis

Bulk electrolysis under constant current was performed to monitor the voltage readout of the reaction. After constant current bulk electrolysis, each half-reaction was analyzed by GC-MS. The voltages (vs. Ag/Ag^{+}) were read at capacity 0 mA*h, see Figure 3B in the manuscript.

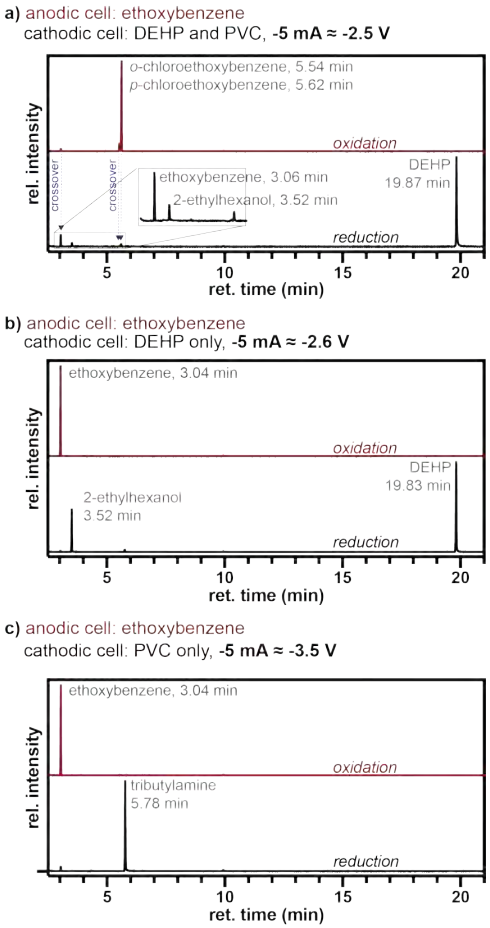

Figure A3.17 GC-MS traces of each half-reaction after constant current bulk electrolysis

The theoretical capacity of 5 mL of a 50 mM DEHP solution (0.25 mmol) was calculated to be 6.70 mA*h using the following conversion, in which 96485 C/mol is the Faraday constant.

$$0.25\ mmol\ DEHP * \frac{1\ mol}{1000\ mmol} * \frac{96485\ C}{1\ mol} * \frac{1\ A * s}{1\ C} * \frac{1000\ mA}{1\ A} * \frac{1\ h}{3600\ s} = 6.7\ mA * h$$

A3.7 Oxidative chlorination mechanism

The pH of the electrolysis reaction was monitored using pH strips. The electrolysis was performed following General Procedure C using PVC_{47k} and DEHP. The arene substrate was not included in the reaction, to remove effects of the arene chlorination on the pH. The pH strips indicated that the reaction became more acidic during electrolysis. The change in pH is attributed to the degradation of PVC during electrolysis, likely releasing HCl.

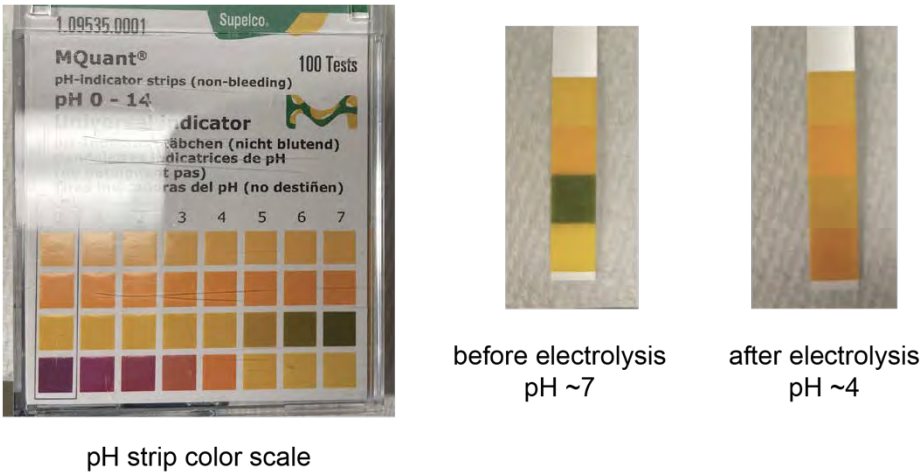

Figure A3.18 Photos of the pH strip color scale and pH strips immediately after being wetted with the reaction mixture

Control reactions were performed to identify the possible chlorine species in solution. The chlorination reaction did not proceed when PVC was not included in the reaction (entry 2), supporting the role of PVC as the chloride source. The reaction proceeded cleanly when HCl was used as the chloride source (entry 3), supporting the notion that PVC degrades into HCl, and then HCl undergoes further reactivity. The reaction with PVC/DEHP did not generate any product when TEMPO was included in the reaction (entry 4), suggesting that radicals are involved in the

paired-electrolysis reaction, either during reduction processes, oxidation processes, or both. Likewise, the HCl control reaction did not proceed when TEMPO was included in the reaction (entry 5), suggesting that radical intermediates are involved in the oxidative chlorination half-reaction, either to convert Cl^- into an active chloride species or in the arene chlorination step. The reaction proceeded with NaOCl as the chloride source without any electrical potential (entry 6), suggesting that hypochlorite could be the active chloride species in this reaction. The fact that the PVC/DEHP reaction proceeds better under air, in which O_2 can serve as oxygen source to generate hypochlorite (OCl^-), further supports involvement of hypochlorite as the active chloride species. Taken together, this data supports the possible reaction pathway in which PVC is reductively degraded into HCl, and then Cl^- is converted into OCl^-, which reacts with arene **1** to generate product **2**.

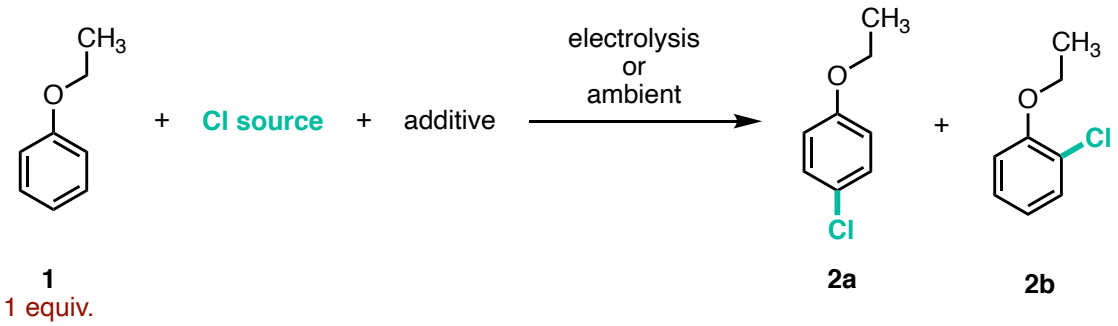

Table A3-19 Reactions performed to vary the possible chloride source

entry	Cl source	additive	conditions	yield of **2** (%)
1	PVC_{47k} (8 equiv.)	DEHP (1 equiv.)	electrolysis[a]	85%
2	none	DEHP (1 equiv.)	electrolysis[a]	0%
3	HCl (3.2 equiv.)[b]	none	electrolysis[a]	quant.
4	PVC_{47k} (8 equiv.)	DEHP (1 equiv.), TEMPO (3.5 equiv.)[c]	electrolysis[a]	0%
5	HCl (3.2 equiv.)[b]	TEMPO (3.5 equiv.)[c]	electrolysis[a]	0%
6	NaOCl (3.2 equiv.)	none	ambient[d]	33%

[a] Electrolysis conditions: performed according to General Procedure C.

[b] Concentrated HCl (37 %w/w, 0.100 mL, 1.3 mmol) was used in place of PVC and DEHP and added to the reaction after dilution with DMF.

[c] (2,2,6,6-Tetramethylpiperidin-1-yl)oxyl (TEMPO, 0.219 g, 1.4 mmol) was added to the to the reaction before electrolysis.

[d] Ambient conditions: Ethoxybenzene (0.051 mL, 0.4 mmol) and tridecane (0.050 mL) were dispensed in a 20 mL vial and dissolved in DMF (6 mL). NaOCl solution (2.21 mL, 4.00–4.99% active chlorine) was added and the reaction stirred at rt for 16 h.

A3.8 Real plastics scenarios

Reaction with PVC_{solid}

This reaction was performed according to General Procedure C, using 0.20 g of PVC_{solid}. The reaction was performed twice.

Reaction with PVC_{tubing}

This reaction was performed according to General Procedure C, using 0.30 g of PVC_{tubing} (~67% by wt PVC = ~0.20 g PVC_{solid}). A ~2 inch piece of tubing was cut up in half lengthwise and then cut into smaller pieces that were added to the reaction (photo below). The PVC_{tubing} pieces did not fully dissolve in the reaction mixture. The reaction was performed twice.

Figure A3.19 PVC_{tubing} and PVC_{tubing} cut up into smaller pieces

Reaction with PVC_{tubing} and mixed plastics

This reaction was performed according to General Procedure C, using 0.30 g of PVC_{tubing} (~67% by wt PVC = ~0.20 g PVC_{solid}). Other plastics were collected from household items (water bottle, food container lids, medicine container, Styrofoam cup) and the polymer type was identified by the recycling code information listed on the item. Each plastic item cleaned with water, wiped dry, and cut into a small piece that was added into the reaction mixture. The reaction was performed once. The masses of each plastic piece were: 63 mg PET, 84 mg HDPE, 96 mg LDPE, 56 mg LLDPE, 80 mg PP, and 58 mg PS.

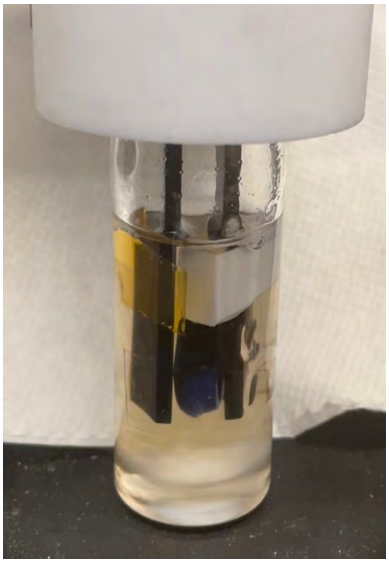

Figure A3.20 Reaction mixture containing PVC_{tubing} and pieces of mixed plastic items

Table A3-20 Summary of data collected from reactions using real plastic items

entry	**PVC** source	**possible contaminant(s)**	conversion of **1** (%)	consumption of **DEHP** (%)	yield of **2** (%)	NBu_3
1	PVC_{solid}	none	66	-	30	y
2	PVC_{solid}	none	55	-	33	y
3	PVC_{tubing}	none	85	95	62	n
4	PVC_{tubing}	none	89	91	64	n
5	PVC_{tubing}	mixed plastics	76	100	67	n

A3.9 Characterization of dPVC after electrolysis

Isolation of dechlorinated PVC (dPVC)

After performing the electrolysis reaction according to General Procedure C, dPVC was recovered using the following protocol: The reaction mixture was poured into 200 mL methanol while stirring to precipitate the polymer. The polymer was collected by filtration and then redissolved in 5 mL THF. The solution was poured into 200 mL methanol while stirring to precipitate the polymer, again. The polymer was collected by filtration, and the dissolution and precipitation processes were repeated one more time. The polymer was collected by filtration and dried under vacuum overnight.

Figure A3.21 Photo of dPVC recovered from reactions performed using PVC_{47k} with 1 equiv. of DEHP (left) and with no DEHP (right)

Thermogravimetric analysis (TGA)

TGA was used to estimate the relative amount of chlorine-containing repeat units in each dPVC sample. The thermal mass loss profile of PVC shows two major steps. The first step occurs at ~300 °C and generates mostly HCl along with some hydrocarbon degradation products.[2] The second step occurs at ~450 °C and degrades the remaining hydrocarbon content of the material. PVC_{47k} retains 36% of its mass after the first thermal step (64% mass loss). Samples of dPVC are expected to show less mass loss during the first stage because some HCl has already been removed from the polymer. This change in mass is observed. Recovered dPVC from reactions performed with DEHP retains 45% mass (55% mass loss), while dPVC recovered from reaction without DEHP retains 40% mass (60% mass loss). In both cases, less mass is lost from dPVC, further supporting that some HCl was emitted during electrolysis. This data suggests that more HCl was lost when DEHP was included in the reaction, which agrees with the higher chlorination yields observed under these conditions.

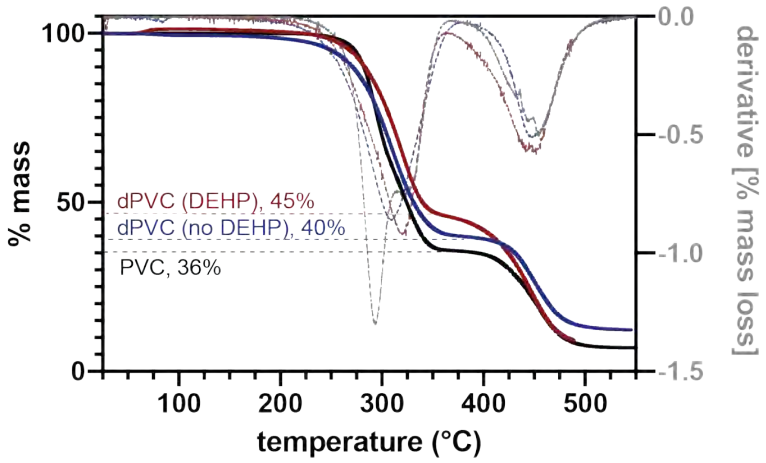

Figure A3.22 TGA mass loss profiles collected from PVC_{47k} (black) and dPVC recovered from reactions performed using PVC_{47k} with 1 equiv. of DEHP (red) and with no DEHP (blue). The % mass remaining after the first stage is indicated on the plot. The first derivative was used to identify the completion of the first mass loss stage, designated when the first derivative reached zero.

Elemental analysis

Elemental analysis indicated that both dPVC samples contained chlorinated repeat units, but dPVC recovered from reactions that include DEHP show a higher degree of dechlorination. An estimate of % dechlorination was calculated using the equation below.

$$\%\ dechlorination\ = \left(1 - \frac{\%\ Cl\ \text{dPVC}}{\%\ Cl\ \text{PVC}}\right) * 100\%$$

Table A3-21 Summary of elemental analysis data collected on PVC and dPVC recovered from reactions performed using PVC_{47k} with 1 equiv. of DEHP and with no DEHP

element	mass %			
	PVC (theoretical)	**PVC (experimental)**	**dPVC, DEHP**	**dPVC, no DEHP**
C	38.44	38.7	46.0	39.0
H	4.84	5.0	5.8	4.9
N	0.00	0.0	0.0	0.0
Cl	56.72	56.5	43.5	53.4
total	100	100.2	95.3	97.3
% dechlorination			***23.0 %***	***5.5%***

Infrared spectroscopy (IR)

The IR spectrum of dPVC recovered from reactions performed with DEHP shows weak C_{sp3}–H stretching from 2850–2900 cm^{-1} and a strong carbonyl stretch at 1726 cm^{-1}, which may be from oxidation of the polymer backbone or from residual DEHP. Otherwise, the IR spectra of both dPVC samples do not vary qualitatively from PVC starting material, suggesting the polymer contains a significant portion of unreacted PVC repeat units.

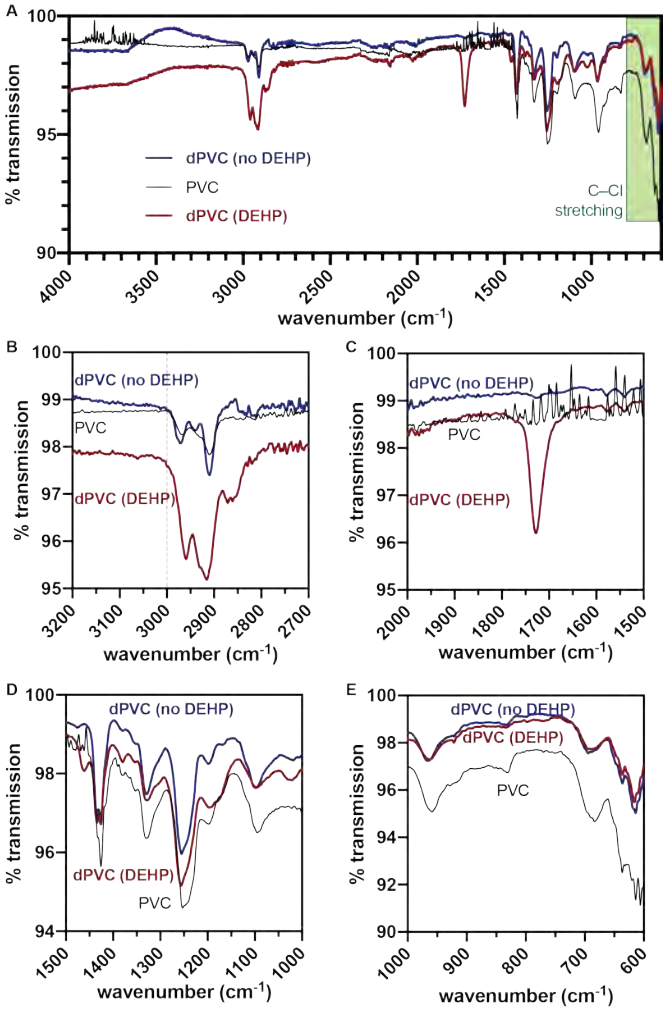

Figure A3.23 Full IR spectra of (A) PVC_{47k} (black —), dPVC recovered from reactions performed with DEHP (red —) and without DEHP (blue —) and (B–E) the same IR spectra zoomed into smaller wavenumber regions

A3.10 ElectraSyn setup guide

Undivided cell

step 1: Equip ElectraSyn® cap with graphite electrodes and reference electrode (optional*).

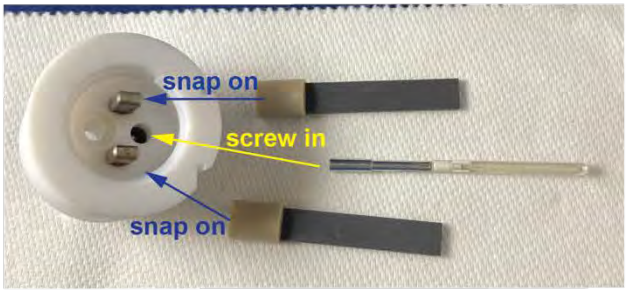

disassembled ElectraSyn® cap, graphite electrodes, and Ag wire reference electrode in 3 M KCl (bottom of cap shown)

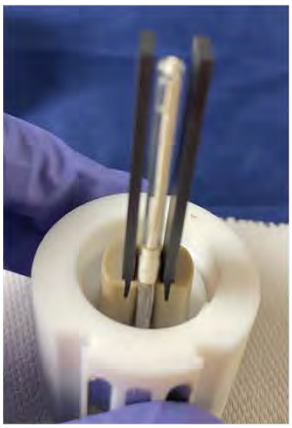

graphite electrodes plugged into W and C electrode positions and reference electrode screwed in on ElectraSyn® cap

* reference electrode was not used in constant current reactions

step 2: Measure required amounts of each reagent and dispense into 10 mL ElectraSyn® vial.

chemical reagents used in reaction

reagents added to 10 mL vial

step 3: Add stir bar and dispense DMF into the vial and then screw on ElectraSyn® cap. Stir reaction solution until for 15 min, until fully dissolved.

reaction after stirring for 15 minutes (front of cap shown)

step 4: Connect vial+cap to the ElectraSyn® potentiostat.

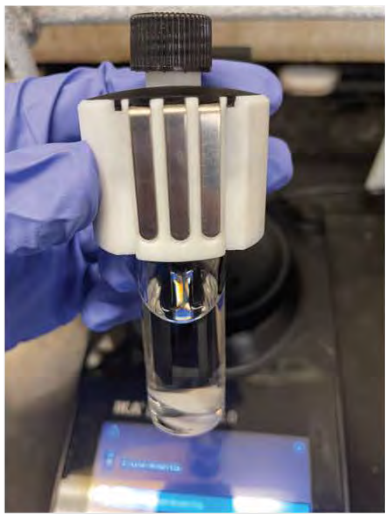

connection ports on ElectraSyn® cap (back of cap shown)

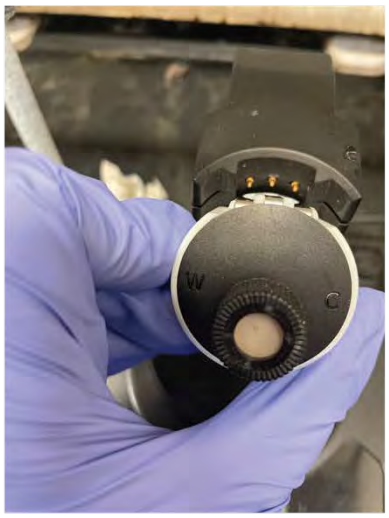

connecting cap to potentiostat

Divided cell

step 1: Gently place pre-soaked AEM on frit and secure with o-ring.

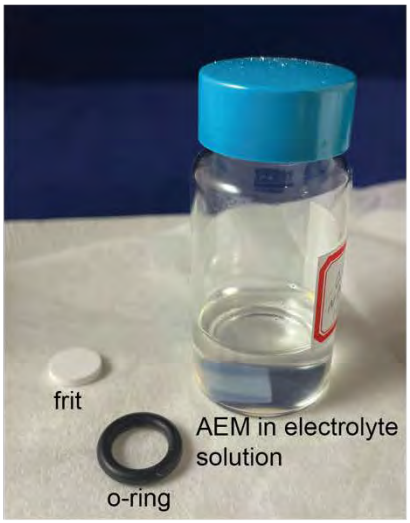

AEM = anion exchange membrane

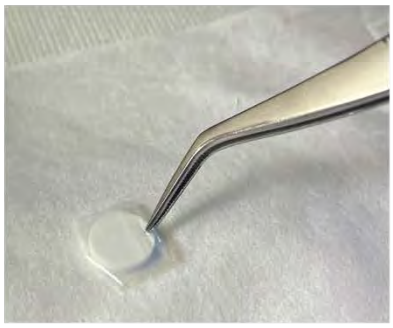

placing AEM on top of frit

secure o-ring around frit to hold AEM in place

step 2: Assemble IKA Pro-Divide cell.

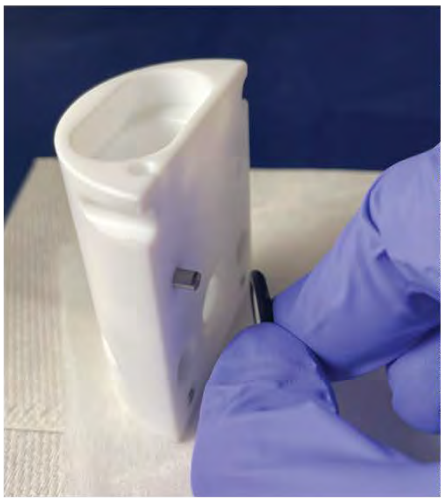

place the frit on the half-cell, the AEM should face the half-cell that will contain the polymer solution to avoid polymer clogging the frit

align both half-cells around frit

rotate thumb screws as tight as possible

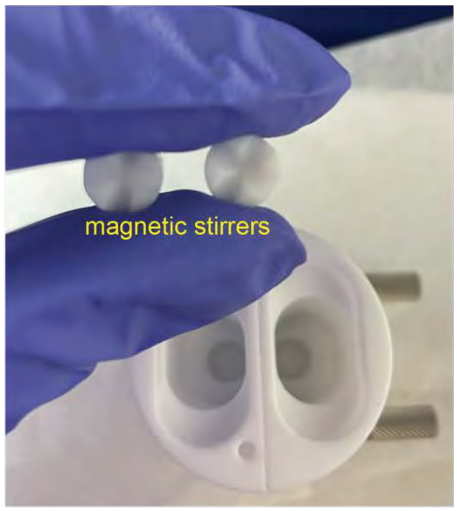

place a magnet stirrer in each half-cell

step 3: Assemble IKA Pro-Divide cap with electrodes.

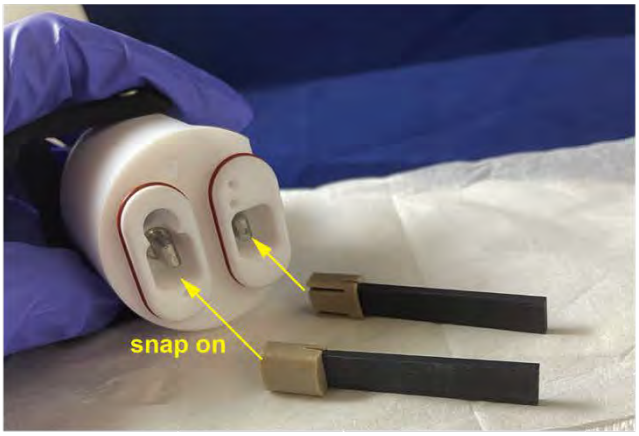

disassembled Pro-Divide cap and graphite electrodes (bottom of cap shown)

step 4: Add reagents and secure cap on a cell.

add reagents (not shown) and Pro-Divide cap with electrodes

connect cap to cell but clamping down the latch

assembled reaction vessel

step 5: Connect Pro-Divide to ElectraSyn® potentiostat, configure settings, and start reaction.

“ready-to-run” reaction setup

<u>example of settings:</u>
constant current
10 mA
no reference electrode
0.5 mmol substrate
total reaction time of 4 h
no alternating current
stir at 700 rpm

A3.11 Life cycle assessment

Functional Unit: 1 kg of chloroethoxybenzene (**2**)

Scope: Process Flow Diagrams

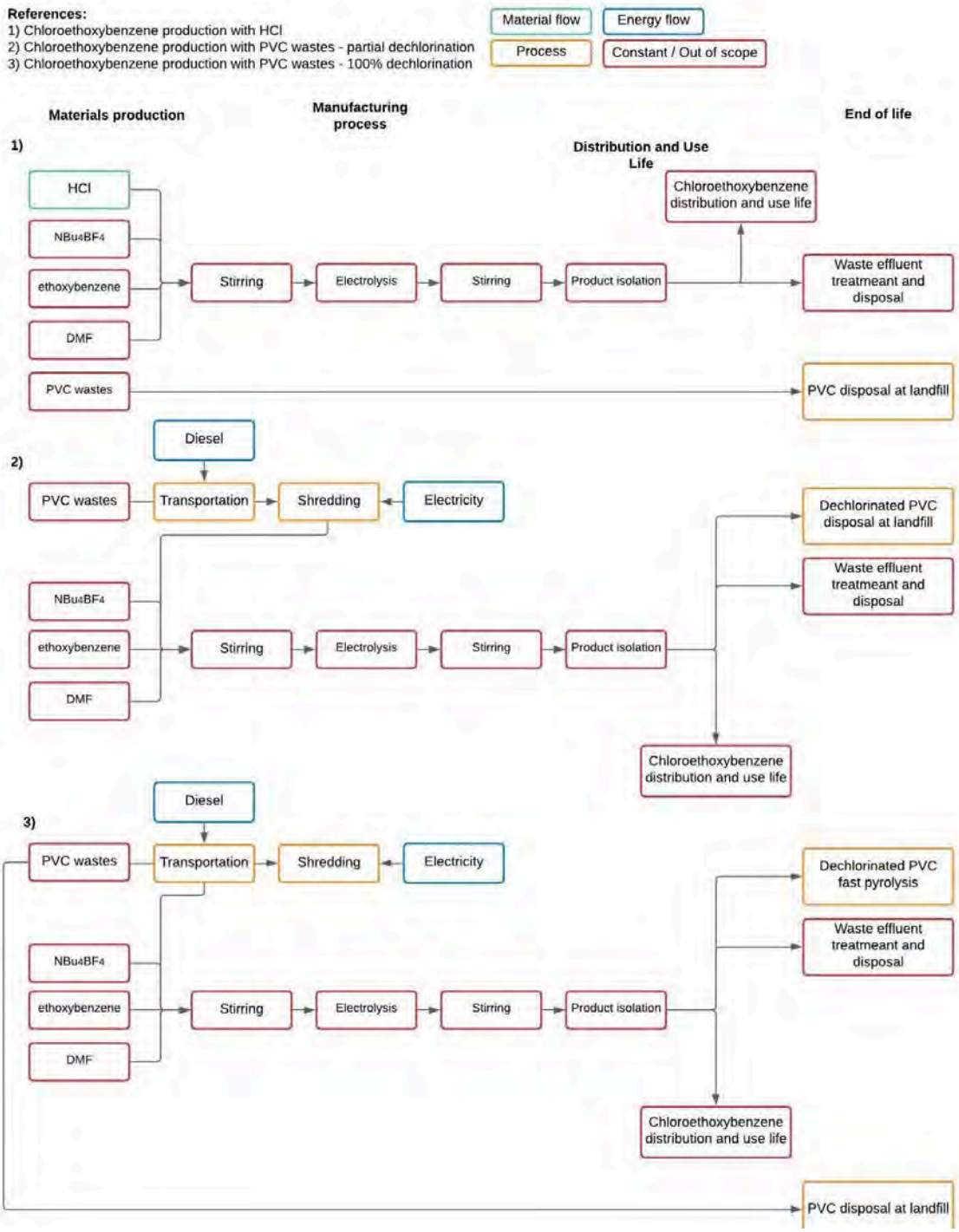

Figure A3.24 Process flow diagram of each scenario studied by life cycle assessment

Assumptions:

PVC production is left out of scope, because it is waste and therefore produced independently from this process.

PVC wastes acquisition supply chain is assumed to be 100 km of transportation and shredding.

Shredding process consumes 0.085 MJ/kg.[3]

Because General Procedure C was followed for HCl and PVC reaction, the following items are considered to be constant, and are thus left out of scope:

repeated reagents

energy consumption during product synthesis and isolation

equipment required

electrode change/discard frequency

PVC weight change with dechlorination is negligible.

Use life of chloroethoxybenzene (**2**) is constant, and are thus left out of scope.

PVC and partially dechlorinated PVC have the same impact when sent to landfill.

Waste effluents are assumed to undergo the same treatment in any case, thus are left out of scope.

Total impact of chemical recycling of plastics via pyrolysis: 0.739 kg CO_2 eq per kg of plastics (including displaced fossil fuels with the resulting products).[4]

The disposal of a fixed amount of PVC wastes equivalent to the amount of PVC wastes required to produce 1 kg of chloroethoxybenzene (**2**) in scenario 2, is considered for all scenarios.

Table A3-22 Life cycle inventories used with each scenario

Item	Units	Scenario 1	Scenario 2	Scenario 3
Materials Production				
HCl	kg	0.740	0	0
PVC wastes supply chain	tkm	0	0.373	0.040
PVC shredding	kWh	0	0.088	0.009
End of Life				
PVC to landfill	kg	3.732	3.732	3.335
Chemical recycling of dechlorinated PVC	kg	0	0	0.397

Table A3-23 Life cycle impact assessments. CO_2 equivalents are per unit of item listed

Item	SimaPro: Ecoinvent library	SimaPro: Method	Units	Impact
Materials Production				
HCl	*Hydrochloric acid, from the reaction of hydrogen with chlorine, at plant/RER S*	*IPCC 2013 gwp 100a*	kg CO_2 eq/kg	1.320
PVC wastes supply chain	*Transport, combination truck, long-haul, diesel powered/tkm/RNA*	*IPCC 2013 gwp 100a*	kg CO_2 eq/tkm	0.0965
PVC shredding	*Electricity, high voltage {US}| market for electricity, high voltage | Cut-off, S*	*IPCC 2013 gwp 100a*	kg CO_2 eq/kWh	0.557
End of Life				
PVC to landfill	*Municipal Solid Waste (waste scenario) (RoW)*	*IPCC 2013 gwp 100a*	kg CO_2 eq/kg	0.074
Chemical recycling of dechlorinated PVC	*Values sourced from Jeswani et al., 2021[4]		kg CO_2 eq/kg	0.739

Table A3-24 Results of the life cycle impact assessment (LCIA) of global warming potential (GWP) for each scenario. CO_2 equivalents are per kg of chloroethoxybenzene (2)

	Units	Scenario 1	Scenario 2	Scenario 3
LCIA - GWP	kg CO_2 eq	1.252	0.360	0.548

A3.12 Synthetic procedures

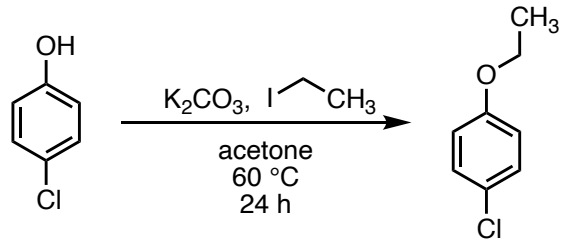

2a

4-chloro-1-ethoxybenzene (2a). Potassium carbonate (2.57g, 18.6 mmol, 1.2 equiv.) and 4-chlorophenol (1.99 g, 15.5 mmol, 1.0 equiv.) were added to a 50 mL round-bottom flask equipped with reflux condenser and dissolved in acetone (30 mL). Ethyl iodide (1.49 mL, 18.6 mmol, 1.2 equiv.) was added and the resulting solution was stirred at 60 °C. After 24 h, the reaction was cooled to rt and concentrated under reduced pressure. The crude reaction mixture was directly purified by silica gel column chromatography (0–100% ethyl acetate in hexanes) to obtain a viscous, colorless oil (2.01 g, 83%). HRMS (APCI+) calc'd for $C_9H_{10}ClO$ [$M+H^+$]: 157.0415; found: 157.0423.

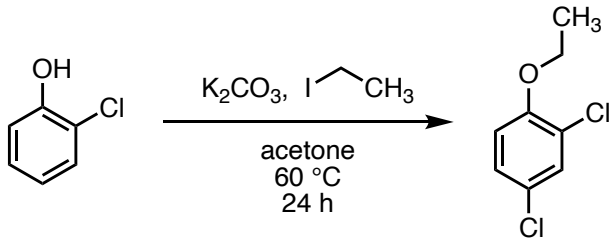

2b

2-chloro-1-ethoxybenzene (2b). Potassium carbonate (2.57g, 18.6 mmol, 1.2 equiv.) and 2-chlorophenol (1.99 g, 15.5 mmol, 1.0 equiv.) were added to a 50 mL round-bottom flask equipped with reflux condenser and dissolved in acetone (30 mL). Ethyl iodide (1.49 mL, 18.6 mmol, 1.2 equiv.) was added and the resulting solution was stirred at 60 °C. After 24 h, the reaction was cooled to rt and concentrated under reduced pressure. The crude reaction mixture was directly purified by silica gel column chromatography (0–100% ethyl acetate in hexanes) to

obtain and viscous, colorless oil (1.85 g, 76%). HRMS (APCI+) calc'd for $C_9H_{10}ClO$ [$M+H^+$]: 157.0415; found: 157.0424.

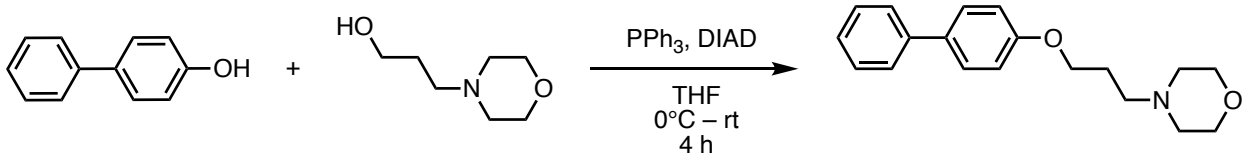

4-(3-([1,1'-biphenyl]-4-yloxy)propyl)morpholine. 4-Phenylphenol (1.00 g, 5.88 mmol), triphenylphosphine (1.85 g, 7.05 mmol), and 4-(3-hydroxypropyl)morpholine (0.975 mL, 7.05 mmol) were added to a round-bottom flask under N_2 and dissolved in anhydrous THF (17 mL). The reaction was cooled to 0 °C in an ice-bath and then diisopropyl azodicarboxylate (1.38 mL, 7.05 mmol) was added dropwise. The reaction was warmed for room temperature and stirred for a total of 4 h. After the reaction was complete, 50 mL of H_2O was added and then extracted 3 x 100 mL ethyl acetate. The combined organic layers were dried with $MgSO_4$, filtered, and concentrated under reduced pressure. The crude material was further purified by silica gel column chromatography (0–80% (ethyl acetate + 5% triethylamine) in hexanes) to obtain a white solid (0.714 g, 2.40 mmol, 41%). HRMS (EI+) calc'd for $C_{19}H_{23}NO_2$ [M^+]: 297.1729; found: 297.1726.

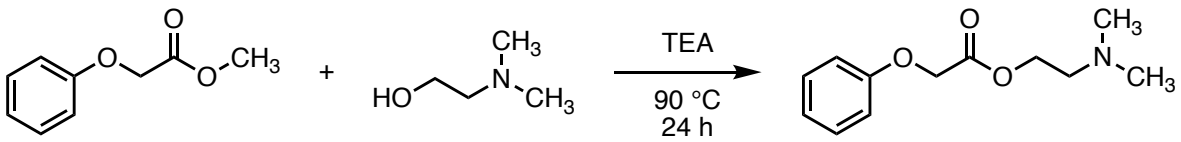

2-(dimethylamino)ethyl 2-phenoxyacetate. Methyl phenoxyacetate (1.00 mL, 1.15 g, 6.91 mmol), *N*,*N*-dimethylethanol amine (1.04 mL, 0.924 g, 10.4 mmol), and triethylamine (1 mL) were dispensed into an 8 mL glass vial. The reaction was stirred at 90 °C for 24 h. The crude

reaction mixture was cooled to rt and directly purified by silicia gel chromatography (0–50% (ethyl acetate + 5% triethylamine) in hexanes) to obtain a colorless oil (1.23 g, 5.53 mmol, 80%). HRMS (EI+) calc'd for $C_{12}H_{17}NO_3$ [M^+]: 223.1208; found: 223.1212.

General Procedure E (divided cell paired electrolysis, constant current)

The *ElectraSyn® Pro-Divide* reaction vessel was assembled using graphite electrodes (0.8 x 0.2 x 5.20 cm) and a 5 micron frit separator layered with a PiperION anion-exchange membrane (pre-soaked in 0.1 M NBu_4BF_4 in DMF). The aromatic substrate (0.5 mmol), NBu_4BF_4 (231 mg, 0.70 mmol), and DMF (7 mL) were added to the working (anodic) chamber. PVC_{47k} (200 mg, 3.2 mmol (repeat unit), 6.4 equiv. (repeat unit)), NBu_4BF_4 (231 g, 0.70 mmol), DEHP (0.20 mL, 0.50 mmol, 1.0 equiv.), and DMF (7 mL) were added to the counter (cathodic) chamber. All reagents were added under air and then dissolved by stirring for at least 15 min. Then the reaction mixture was subjected to constant current electrolysis (10 mA) at rt. The anodic reaction was monitored by GC and stirred until all the aromatic substrate was consumed. The working (anodic) chamber was poured into ~250 mL of ethyl acetate and washed with H_2O (5 × 40 mL) and brine (1 × 50 mL) to remove DMF. The organic layer was dried with $MgSO_4$, filtered, and concentrated under reduced pressure. The crude reaction was further purified by column chromatography and the final product dried under reduced pressure.

chloro-1-ethoxybenzene (2). 1-Ethoxybenzene (63 μL, 61 mg, 0.50 mmol) was reacted

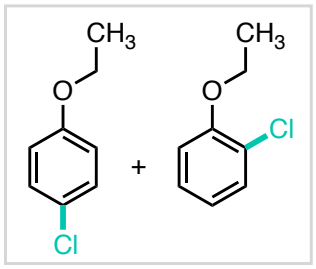

according to General Procedure E for a total of 8 h. The crude product was purified by chromatography (mobile phase: 100% hexanes) to obtain a colorless oil (41 mg, 52% yield). NMR analysis indicated that the product was formed as a 4:1 mixture of regioisomers (4-chloro-1-ethoxybenzene: 2-chloro-1-ethoxybenzene). HRMS (APCI+) calc'd for $C_9H_{10}ClO$ [M+H$^+$]: 157.0415; found: 157.0422.

***N*-(2,4-dichlorophenyl)acetamide (3).** *N*-(4-chlorophenyl)acetamide (85 mg, 0.50 mmol) was

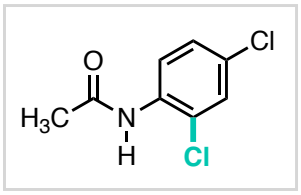

reacted according to General Procedure E for a total of 10 h. The crude product was purified by chromatography (mobile phase: 0–100% gradient ethyl acetate in hexanes) to obtain an off-white solid (69 mg, 67% yield). HRMS (APCI+) calc'd for $C_8H_8Cl_2NO$ [M+H$^+$]: 203.9977; found: 203.9984.

chloro-1,3,5-triethylbenzene (4). 1,3,5-Triethylbenzene (94 μL, 81 mg, 0.50 mmol) was reacted

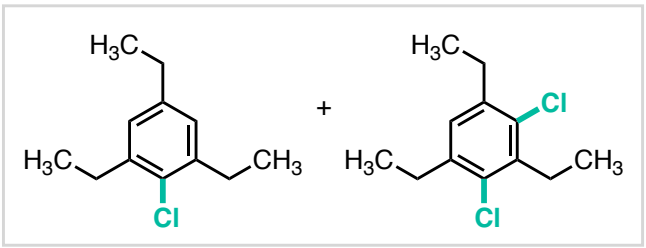

according to General Procedure E for a total of 8 h. The crude product was purified by chromatography (mobile phase: 100% hexanes) to obtain a colorless liquid (77 mg, 76% yield). NMR analysis indicated that the product was formed as a 5:1 mixture of products (2-chloro-1,3-5-triethylbenzene: 2,4-dichloro-1,3,5-triethylbenzene). HRMS (EI+)

calc'd for $C_{12}H_{17}Cl$: 196.1019 [M^+]; found: 196.1022; calc'd for $C_{12}H_{16}Cl_2$ [M^+]: 230.0629; found: 230.0629.

methyl 2-(4-chlorophenoxy)acetate (5). Methyl phenoxy acetate (72 μL, 83 mg, 0.50 mmol) 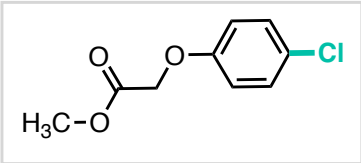 was reacted according to General Procedure E for a total of 7 h. The crude product was purified by chromatography (mobile phase: 15% ethyl acetate in hexanes) to obtain a yellow oil (72 mg, 72% yield). HRMS (APCI+) calc'd for $C_9H_{10}ClO_3$ [$M+H^+$]: 201.0313; found: 201.0322.

4-chloro-1-phenyl-1*H*-pyrazole (6). 1-Phenyl-1*H*-pyrazole (66 μL, 72 mg, 0.50 mmol) was 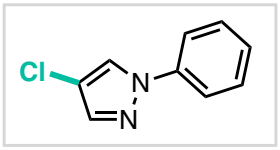 reacted according to General Procedure E for a total of 8 h. The crude product was purified by chromatography (mobile phase: 0–30% gradient ethyl acetate in hexanes) to obtain an off-white solid (64 mg, 71% yield). HRMS (EI+) calc'd for $C_9H_7ClN_2$ [M^+]: 178.0298; found: 178.0300.

8-chloro-1,3,7-trimethyl-3,7-dihydro-1*H*-purine-2,6-dione (7). Caffeine (97 mg, 0.50 mmol) 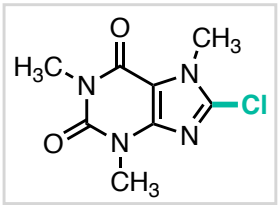 was reacted according to General Procedure E for a total of 8 h. The crude product was purified by chromatography (mobile phase: 0–50% ethyl acetate in hexanes) to obtain a white solid (41 mg, 36% yield). HRMS (APCI+) calc'd for $C_8H_{10}ClN_4O_2$ [$M+H^+$]: 229.0487; found: 229.0482.

3-chloro-1-methyl-2-phenyl-1*H*-indole (8). 1-Methyl-2-phenyl-1*H*-indole (104 mg, 0.50 mmol)

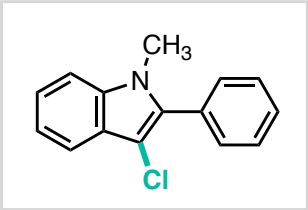

was reacted according to General Procedure E for a total of 4 h. The crude product was purified by chromatography (mobile phase: 100% hexanes) to obtain a white solid (6.1 mg, 5% yield). HRMS (EI+) calc'd for $C_{15}H_{12}ClN$ [M^+]: 241.0658; found: 241.0664.

4,5-dichloro-1-phenyl-1*H*-imidazole (9). 1-Phenyl-1*H*-imidazole (63 µL, 72 mg, 0.50 mmol)

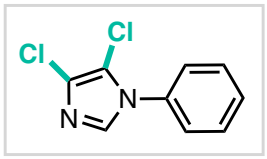

was reacted according to General Procedure E for a total of 4 hours. The crude product was purified by chromatography (mobile phase: 0–100% gradient ethyl acetate in hexanes) to obtain a white solid (14 mg, 13% yield). HRMS (EI+) calc'd for $C_9H_6Cl_2N_2$ [M^+]: 211.9908; found: 211.9907.

3-chloro-2-phenylimidazo[1,2-*a*]pyridine (10). 2-Phenylimidazo[1,2-*a*]pyridine (97 mg, 0.50

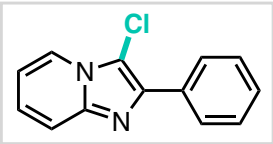

mmol) was reacted according to General Procedure E for a total of 4 h. The crude product was purified by chromatography (mobile phase: 0–100% gradient ethyl acetate in hexanes) to obtain an off-white solid (27 mg, 24% yield). HRMS (APCI+) calc'd for $C_{13}H_{10}ClN_2$ [$M+H^+$]: 229.0527; found: 229.0526.

chloro-3-hexylthiophene (11). 3-Hexylthiophene (89 µL, 84 mg, 0.50 mmol) was reacted

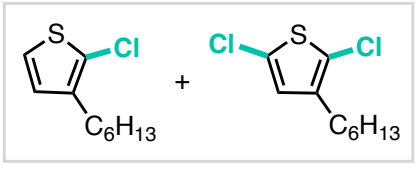

according to General Procedure E for a total of 8 h. The crude product was purified by chromatography (mobile phase: 100% hexanes) to obtain a colorless oil (37 mg, 33% yield).

NMR analysis indicated that the product was formed as a 1:1.8 mixture of products (2-chloro-3-hexylthiophene: 2,5-dichloro-3-hexylthiophene). HRMS (APCI+) calc'd for $C_{10}H_{16}ClS$ [$M+H^+$]: 203.0656; found: 203.0655; $C_{10}H_{15}Cl_2S$ [$M+H^+$]: 237.0266; found: 237.0263.

2-chloro-3-methylbenzo[*b*]thiophene (12). 3-Methylbenzo[*b*]thiophene (67 µL, 74 mg, 0.50 mmol) was reacted according to General Procedure E for a total of 10 h. The crude product was purified by chromatography (mobile phase: 100% hexanes) to obtain a colorless oil (50 mg, 55 % yield. HRMS (EI+) calc'd for C_9H_7ClS [M^+]: 181.9957; found: 181.9888.

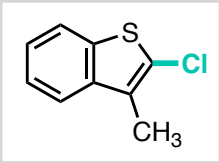

4-(3-((3-chloro-[1,1'-biphenyl]-4-yl)oxy)propyl)morpholine (13). 4-(3-([1,1'-Biphenyl]-4-yloxy)propyl)morpholine (0.149 g, 0.50 mmol) was reacted according to General Procedure E for a total of 8 h. The crude product was purified by chromatography (mobile phase: 0–80% (ethyl acetate + 5% triethylamine)) to obtain and off-white solid (73 mg, 44% yield). HRMS (EI+) calc'd for $C_{19}H_{22}ClNO_2$ [M^+]: 331.1339; found: 331.1336.

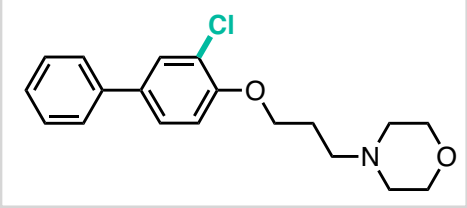

2-(dimethylamino)ethyl 2-(4-chlorophenoxy)acetate (14). 2-(Dimethylamino)ethyl 2-phenoxyacetate (107 µL, 0.112 g, 0.5 mmol) was reacted according to General Procedure E for a total of 8 h. The crude product was purified by chromatography (mobile

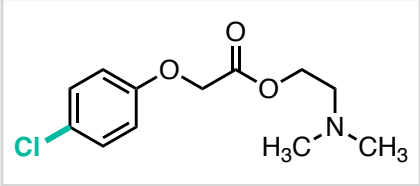

phase: 0–60% (ethyl acetate + 5% triethylamine)) to obtain a yellow oil (44 mg, 29% yield). NMR analysis indicated that the obtained oil contained 1:0.2 mixture of product and unreacted starting material, which were not separated chromatographically. HRMS (ESI+) calc'd for $C_{12}H_{17}ClNO_3$ [$M+H^+$]: 258.0891; found: 258.0894.

A3.13 ^{1}H and ^{13}C NMR spectra

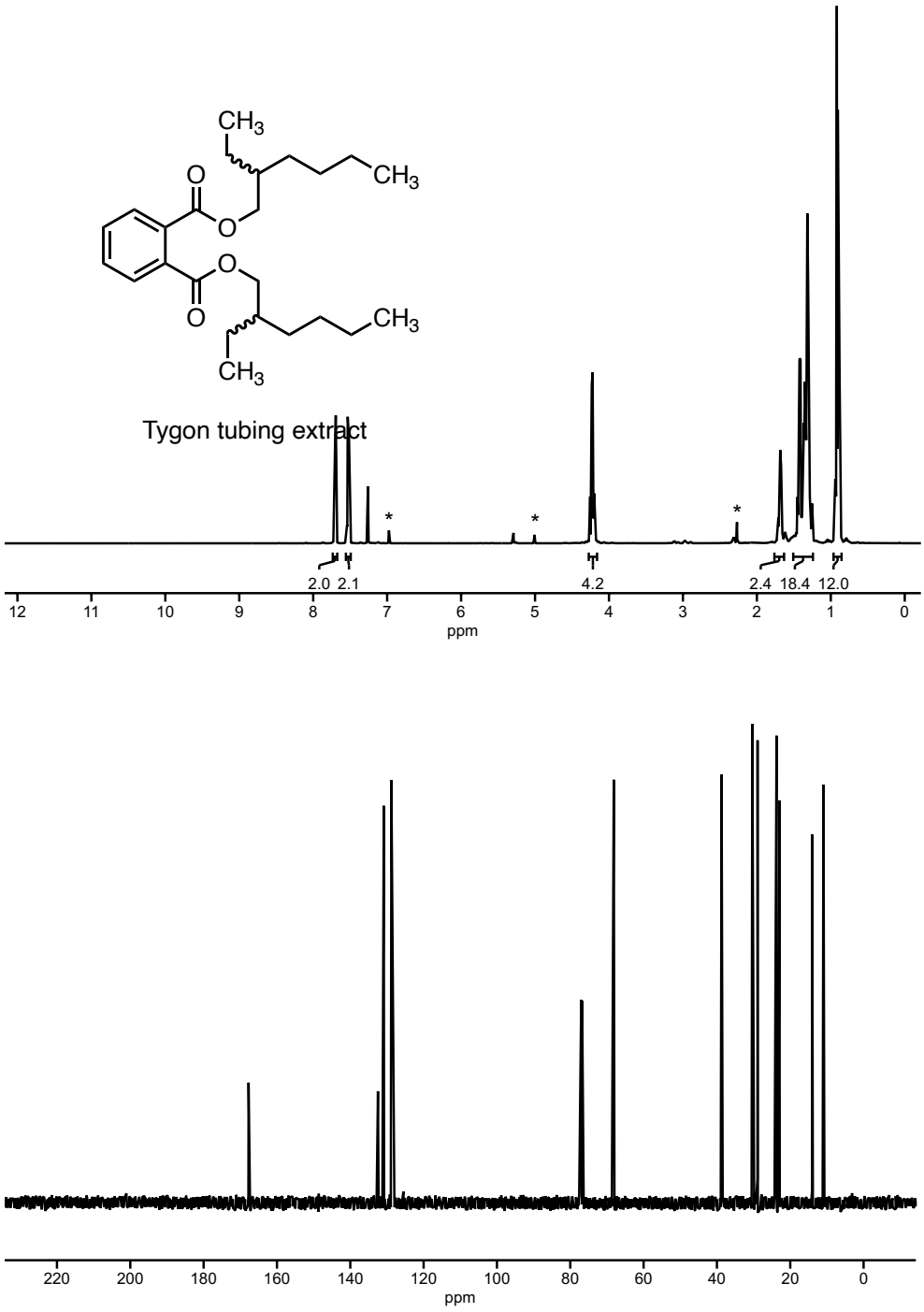

Figure A3.25 ^{1}H and ^{13}C NMR spectra of Tygon tubing extract. ^{1}H NMR (500 MHz, $CDCl_3$) δ 7.74 – 7.68 (m, 2H), 7.56 – 7.49 (m, 2H), 4.27 – 4.16 (m, 4H), 1.76 – 1.63 (m, 2H), 1.51 – 1.24 (m, 16H), 0.96 – 0.85 (m, 12H). ^{13}C NMR (126 MHz, $CDCl_3$) δ 167.88, 132.60, 131.01, 128.93, 68.28, 38.87, 30.50, 29.06, 23.88, 23.12, 14.18, 11.09. *butylated hydroxytoluene (BHT)

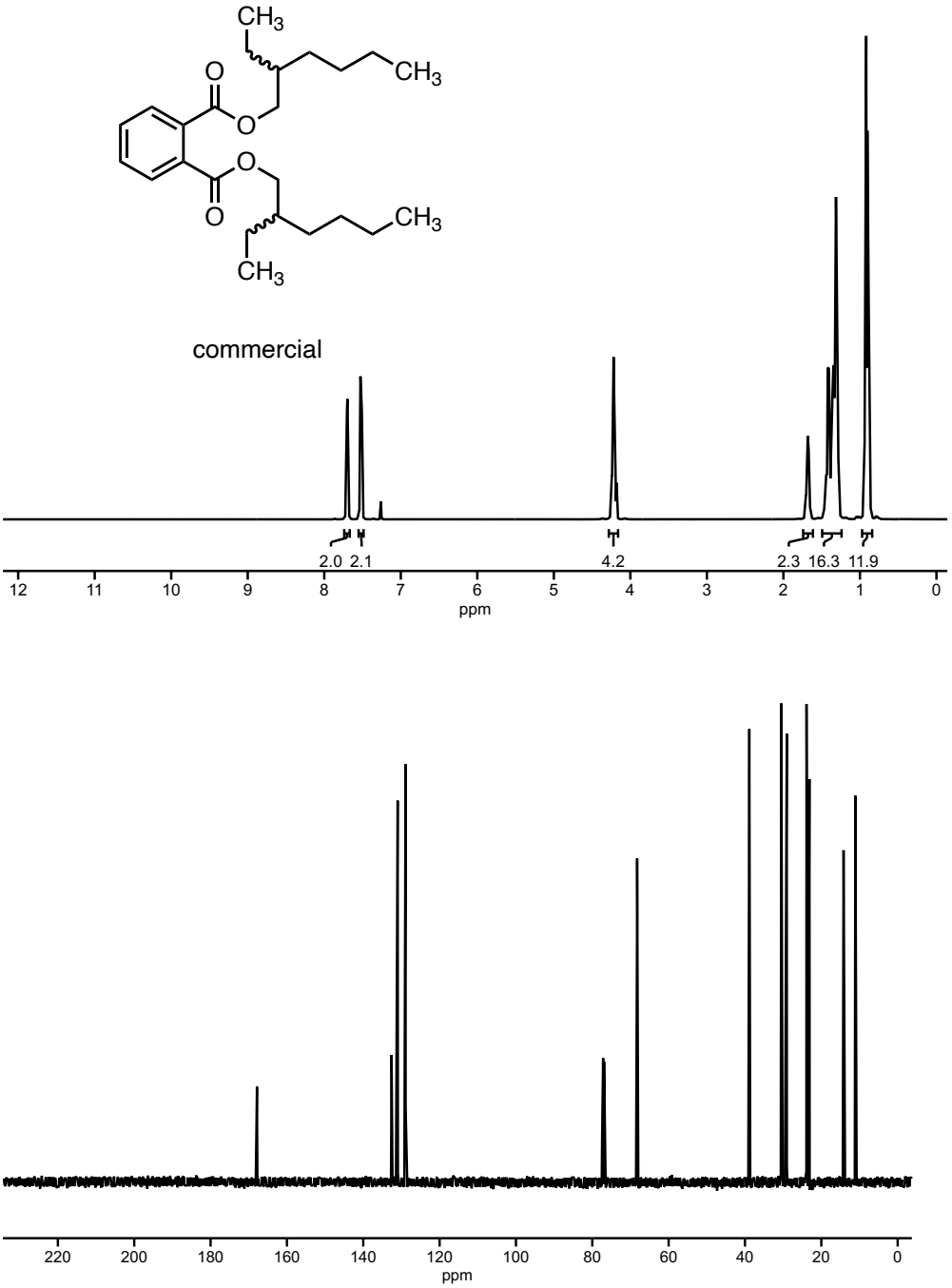

Figure A3.26 ^{1}H and ^{13}C NMR spectra of commercial DEHP. ^{1}H NMR (500 MHz, $CDCl_3$) δ 7.74 – 7.67 (m, 2H), 7.55 – 7.49 (m, 2H), 4.28 – 4.16 (m, 4H), 1.74 – 1.61 (m, 2H), 1.49 – 1.24 (m, 16H), 0.97 – 0.84 (m, 12H). ^{13}C NMR (126 MHz, $CDCl_3$) δ 167.85, 132.58, 130.98, 128.91, 68.26, 38.86, 30.49, 29.05, 23.88, 23.11, 14.17, 11.08.

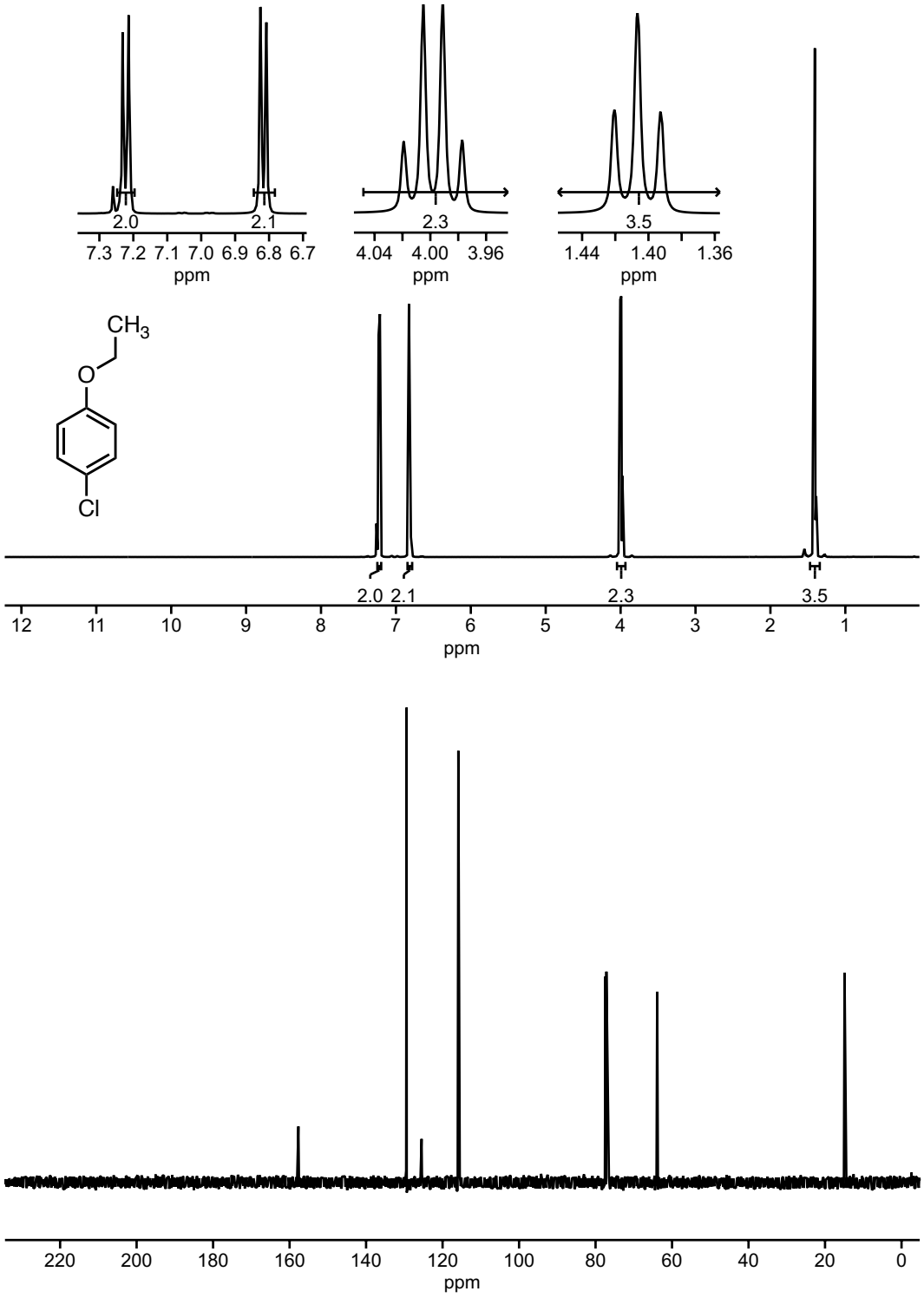

Figure A3.27 ^{1}H and ^{13}C NMR spectra of 4-chloro-1-ethoxy benzene (2a). ^{1}H NMR (500 MHz, $CDCl_3$) δ 7.22 (d, J = 8.8 Hz, 2H), 6.82 (d, J = 8.8 Hz, 2H), 4.00 (q, J = 7.0 Hz, 2H), 1.41 (t, J = 7.0 Hz, 3H).^{13}C NMR (126 MHz, $CDCl_3$) δ 157.70, 129.41, 125.49, 115.88, 63.89, 14.89

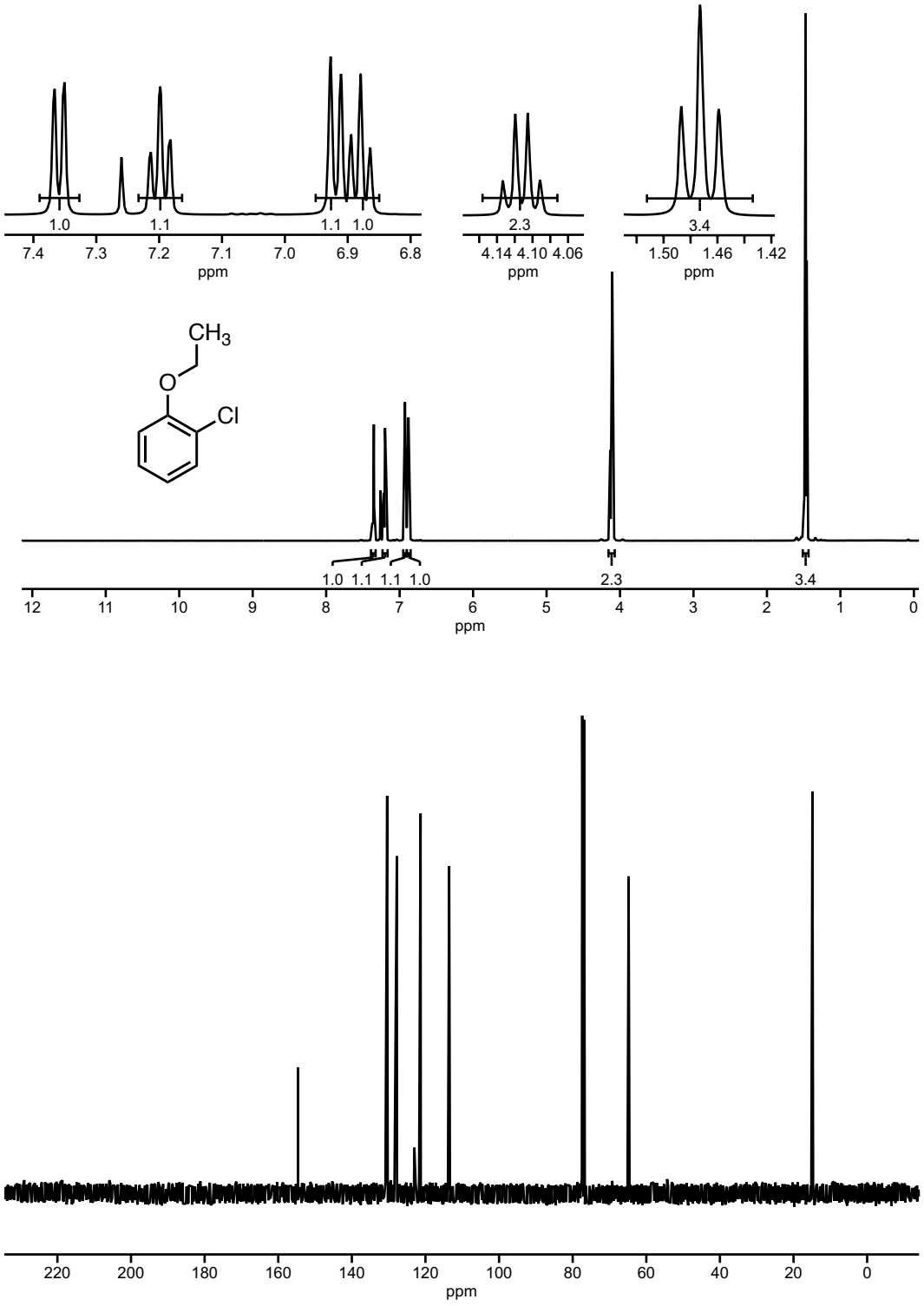

Figure A3.28 ^{1}H and ^{13}C NMR spectra of 2-chloro-1-ethoxy benzene (2b). ^{1}H NMR (500 MHz, $CDCl_3$) δ 7.36 (d, J = 7.8 Hz, 1H), 7.20 (t, J = 7.8 Hz, 1H), 6.92 (d, J = 8.2 Hz, 1H), 6.88 (t, J = 7.7 Hz, 1H), 4.11 (q, J = 7.0 Hz, 2H), 1.47 (t, J = 7.0 Hz, 3H). ^{13}C NMR (126 MHz, $CDCl_3$) δ 154.62, 130.41, 127.78, 123.01, 121.33, 113.56, 64.81, 14.87.

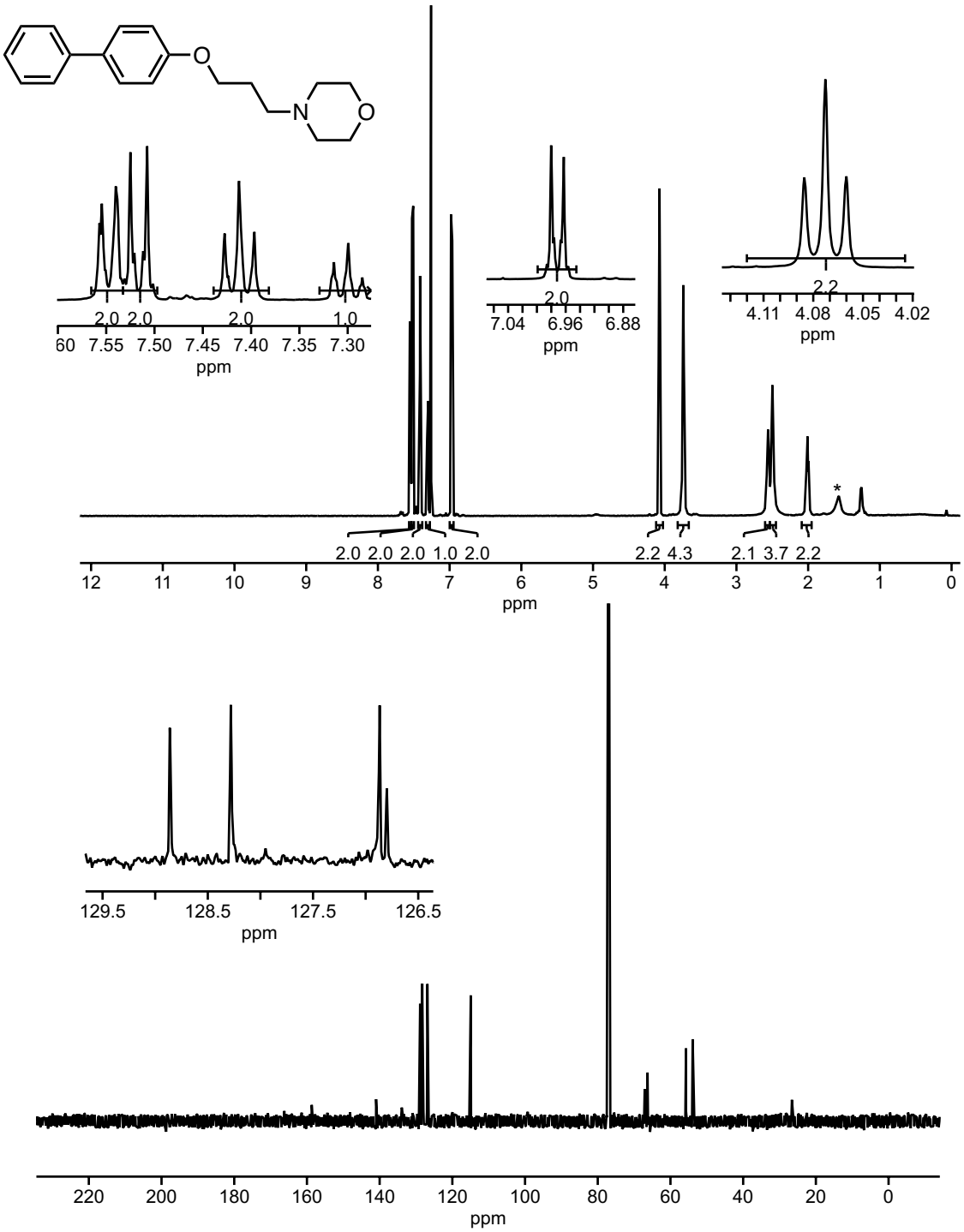

Figure A3.29 1H and 13C NMR spectra of 4-(3-([1,1'-biphenyl]-4-yloxy)propyl)morpholine. 1H NMR (500 MHz, CDCl3) δ 7.55 (dd, J = 8.2, 1.0 Hz, 2H), 7.53 – 7.50 (m, 2H), 7.41 (t, J = 7.7 Hz, 2H), 7.30 (t, J = 7.4 Hz, 1H), 7.00 – 6.95 (m, 2H), 4.07 (t, J = 6.3 Hz, 2H), 3.74 (s, 4H), 2.60 – 2.54 (m, 2H), 2.50 (s, 4H), 2.09 – 1.95 (m, 2H). 13C NMR (126 MHz, CDCl3) δ 158.68, 140.97, 133.91, 128.86, 128.28, 126.87, 126.80, 114.93, 67.10, 66.30, 55.73, 53.89, 26.59. *water

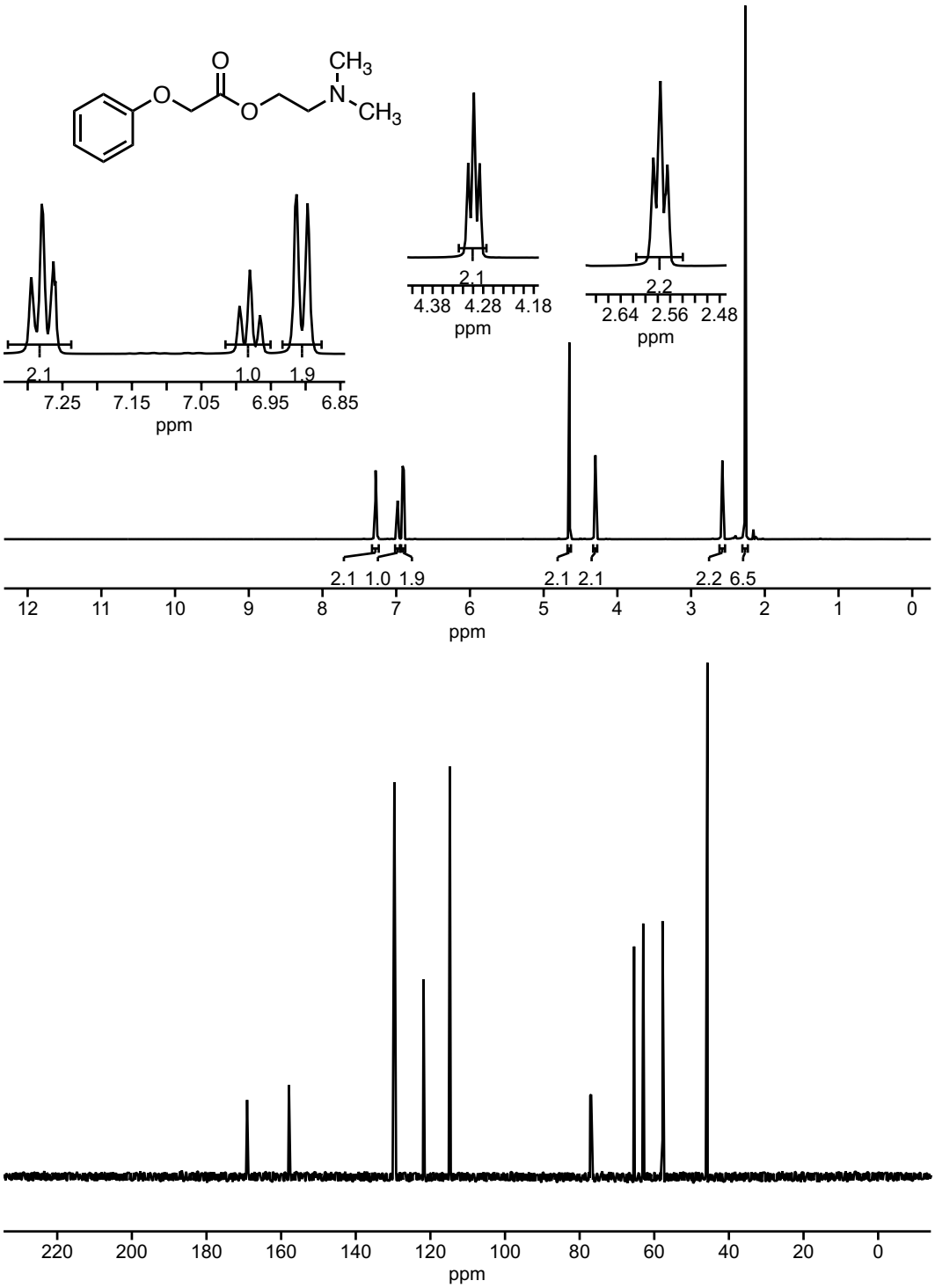

Figure A3.30 ^{1}H and ^{13}C NMR spectra of 2-(dimethylamino)ethyl 2-phenoxyacetate. ^{1}H NMR (500 MHz, $CDCl_3$) δ 7.28 (t, J = 8.0 Hz, 2H), 6.98 (t, J = 7.4 Hz, 1H), 6.91 (d, J = 8.6 Hz, 2H), 4.65 (s, 2H), 4.30 (t, J = 5.7 Hz, 2H), 2.58 (t, J = 5.7 Hz, 2H), 2.26 (s, 6H). ^{13}C NMR (126 MHz, $CDCl_3$) δ 169.11, 157.90, 129.65, 121.82, 114.78, 65.40, 62.95, 57.78, 45.75.

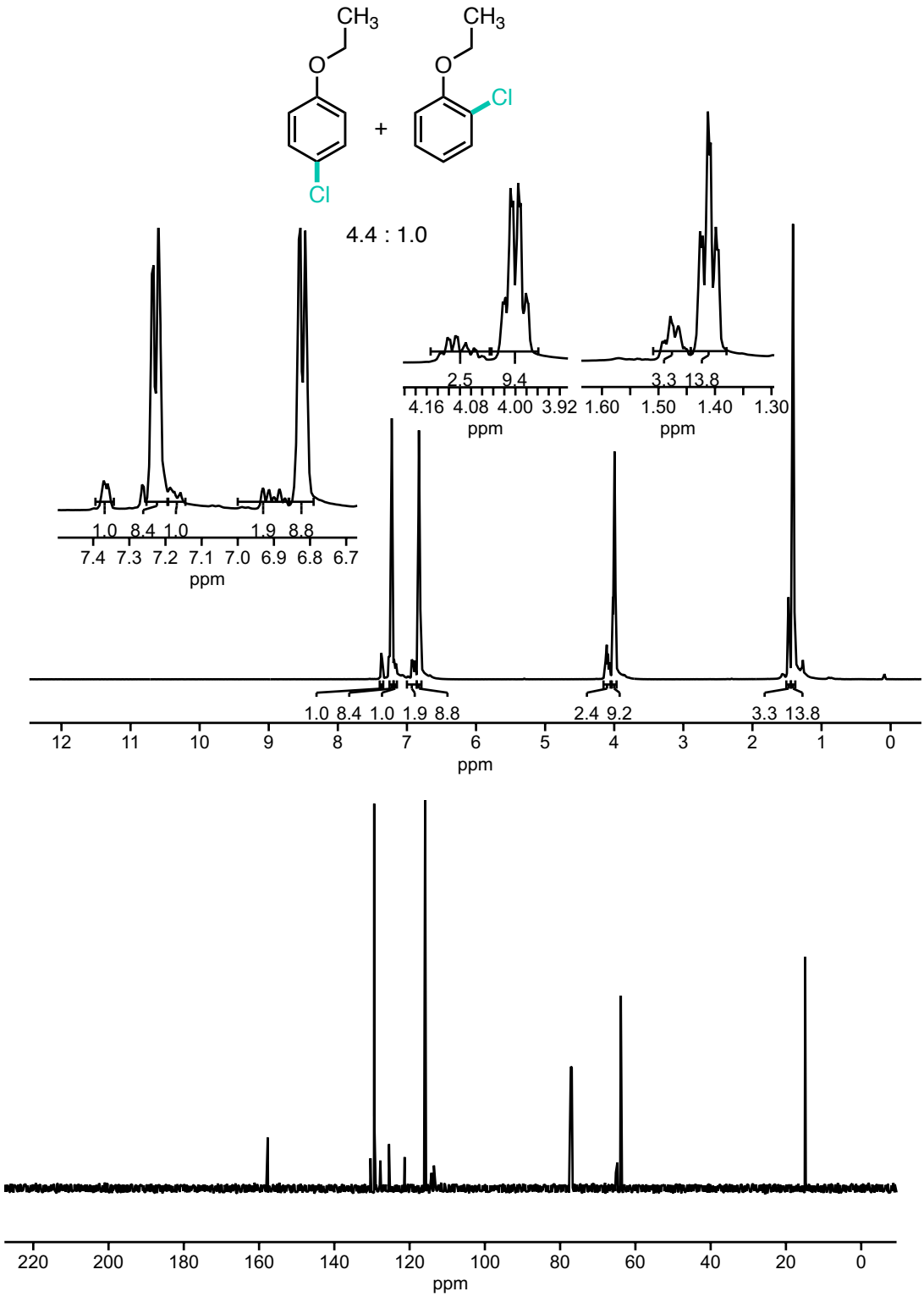

Figure A3.31 ^{1}H and ^{13}C NMR spectra of 4.4:1 mixture of 4-chloro-1-ethoxy benzene: 2-chloro-1-ethoxy benzene (2). ^{1}H NMR (500 MHz, $CDCl_3$) δ 7.36 (m, 1H), 7.25 – 7.19 (m, 8H), 7.19 – 7.14 (m, 1H), 7.00 – 6.86 (m, 2H), 6.86 – 6.79 (m, 9H), 4.15 – 4.05 (m, 2H), 4.02 – 3.98 (m 9H), 1.47 (7, J = 7 3H), 1.41 (t, J = 7.0 Hz, 13H). ^{13}C NMR (126 MHz, $CDCl_3$) δ157.69, 130.40, 129.40, 127.77, 125.47, 121.32, 115.87, 113.54, 64.79, 63.88, 14.88.

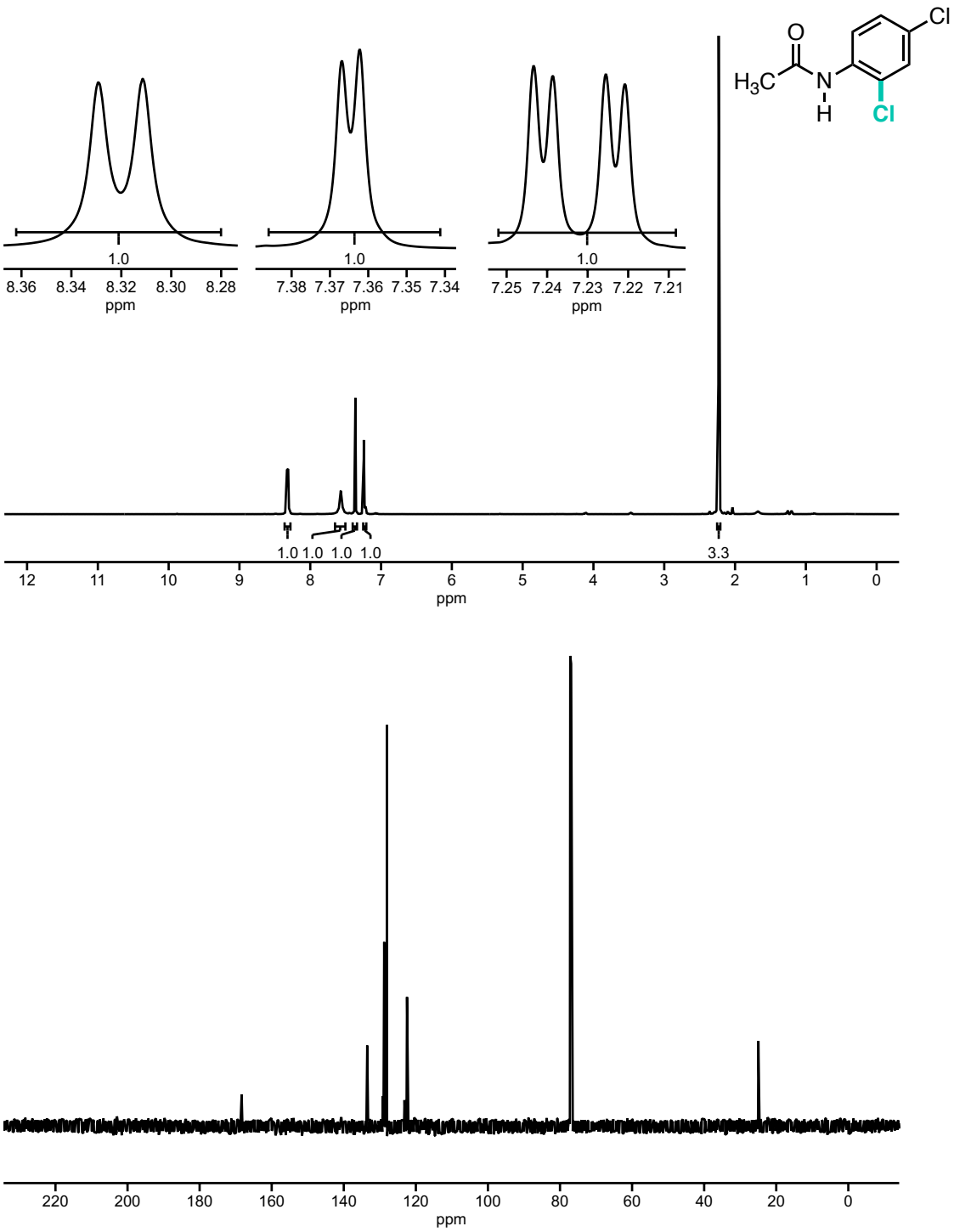

Figure A3.32 ^{1}H and ^{13}C NMR spectra of *N*-(2,4-dichlorophenyl)acetamide (3). ^{1}H NMR (500 MHz, $CDCl_3$) δ 8.32 (d, *J* = 8.9 Hz, 1H), 7.57 (s, 1H), 7.36 (d, *J* = 2.3 Hz, 1H), 7.23 (dd, *J* = 8.9, 2.4 Hz, 1H), 2.23 (s, 3H). ^{13}C NMR (126 MHz, $CDCl_3$) δ 168.34, 133.49, 129.17, 128.78, 128.01, 123.16, 122.46, 24.95.

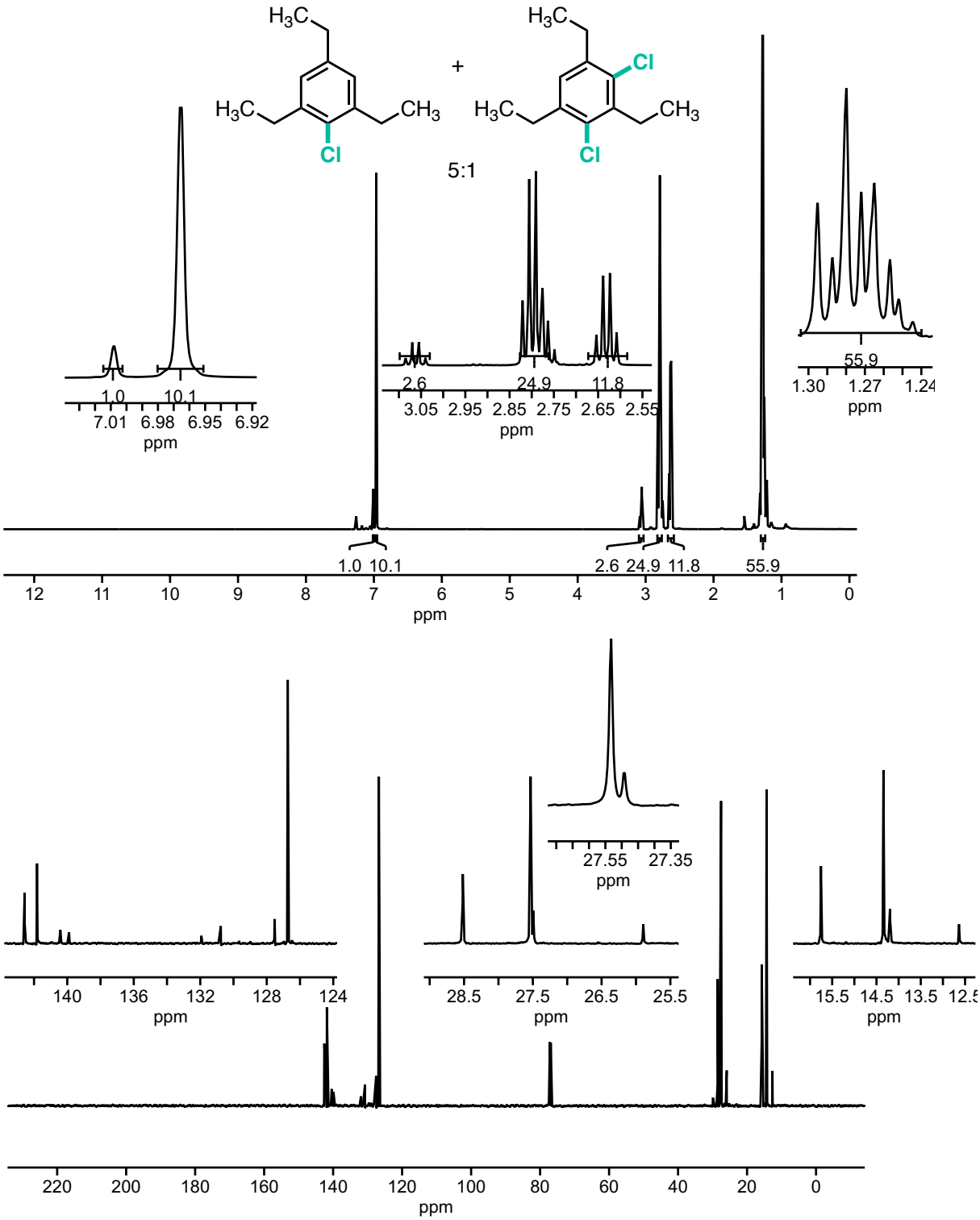

Figure A3.33 1H and 13C NMR spectra of 5:1 mixture of 2-chloro-1,3-5-triethylbenzene: 2,4-dichloro-1,3,5-triethylbenzene (4). 1H NMR (500 MHz, CDCl3) δ 7.01 (s, 1H), 6.97 (s, 10H), 3.06 (q, J = 7.5 Hz, 2H), 2.80 (q, J = 7.5 Hz, 24H), 2.63 (q, J = 7.6 Hz, 10H), 1.28 (m, 54 H). 13C NMR (126 MHz, CDCl3) δ 142.56, 141.82, 140.41, 139.89, 131.93, 130.76, 127.53, 126.74, 28.52, 27.53, 27.49, 25.89, 15.75, 14.34, 14.20, 12.64.

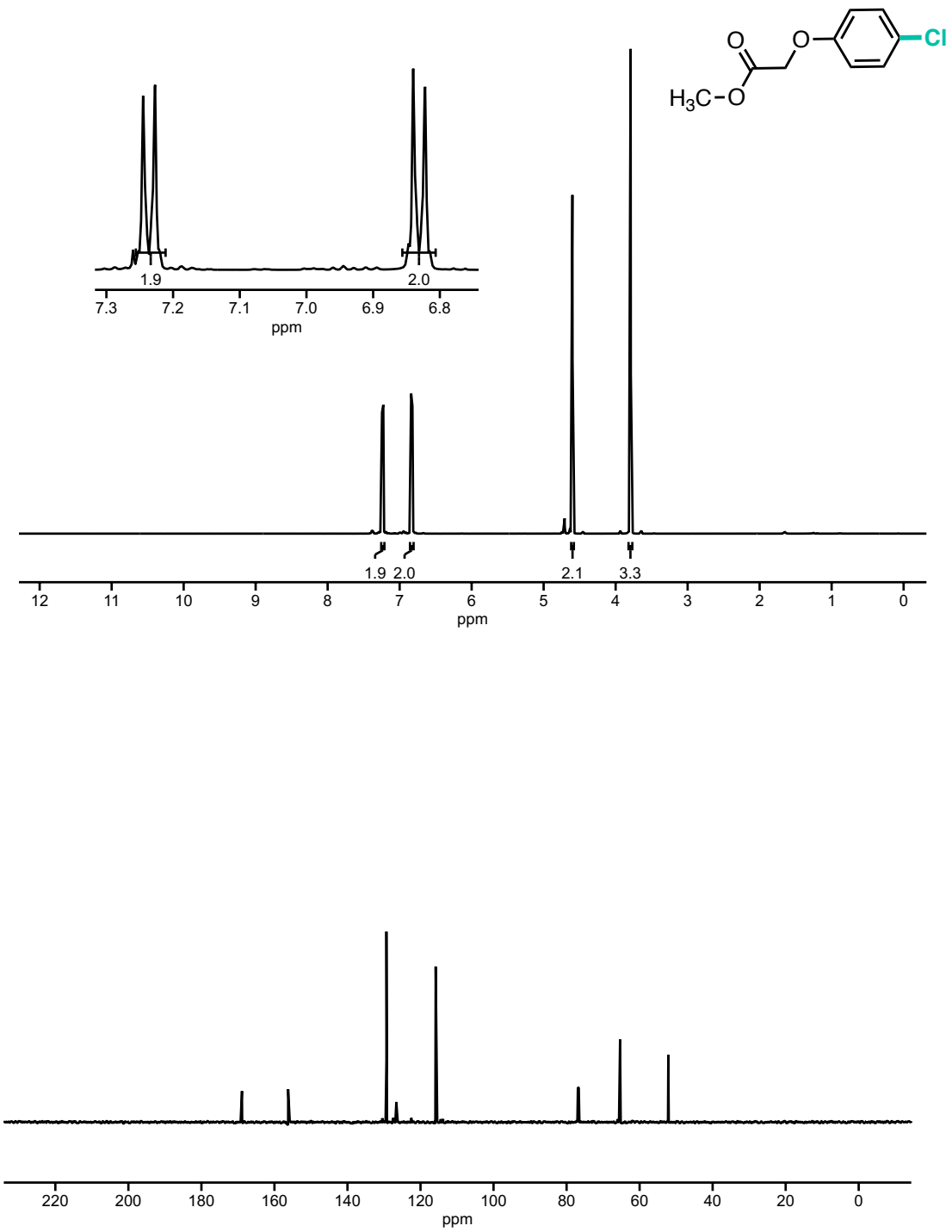

Figure A3.34 ^{1}H and ^{13}C NMR spectra of methyl 2-(4-chlorophenoxy)acetate (5). ^{1}H NMR (500 MHz, $CDCl_3$) δ 7.24 (d, J = 9.0 Hz, 2H), 6.83 (d, J = 8.8 Hz, 2H), 4.60 (s, 2H), 3.79 (s, 3H). ^{13}C NMR (126 MHz, $CDCl_3$) δ 169.15, 156.50, 129.59, 126.87, 116.10, 65.60, 52.40

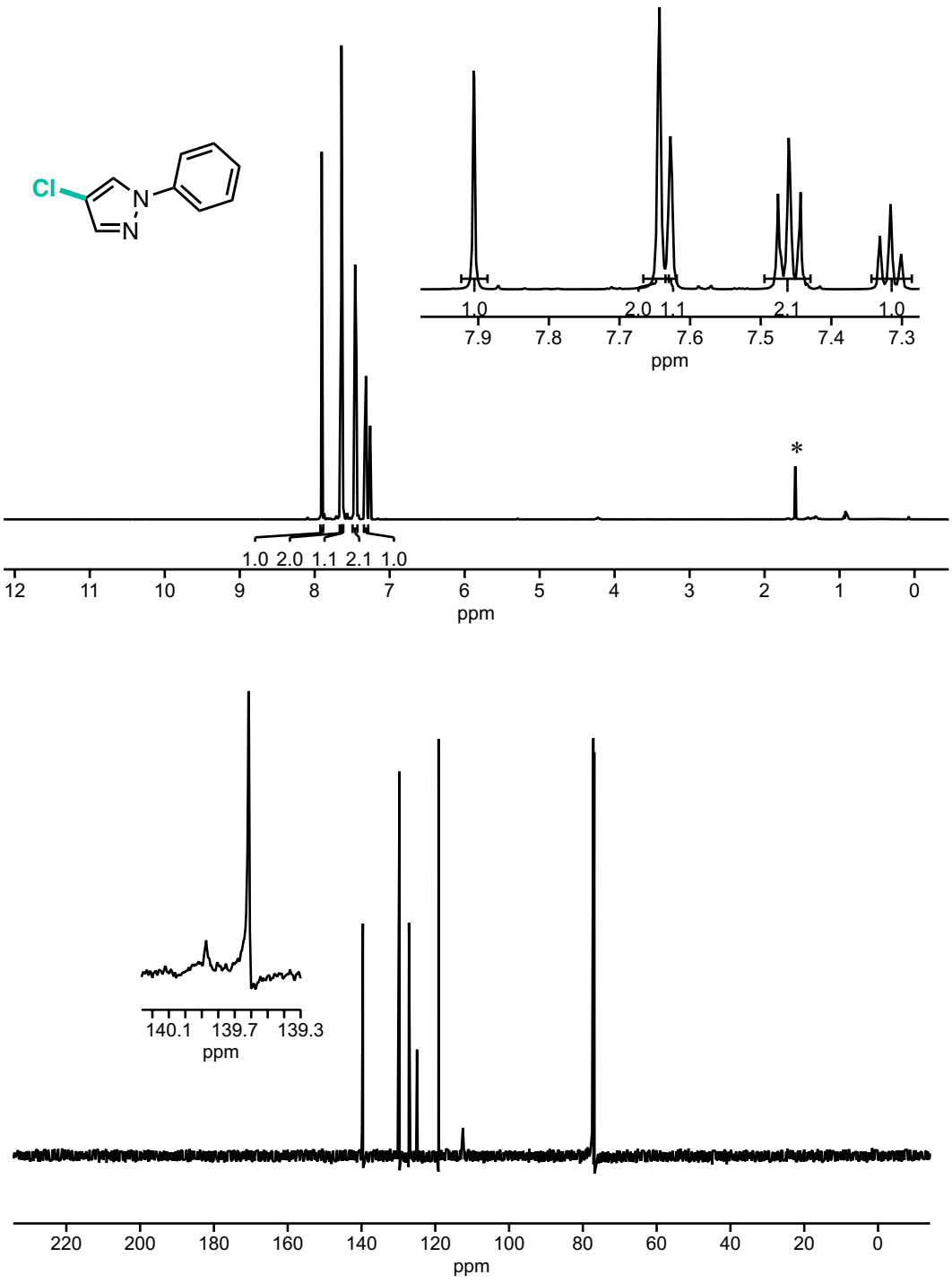

Figure A3.35 ^{1}H and ^{13}C NMR spectra of 4-chloro-1-phenyl-1H-pyrazole (6). ^{1}H NMR (500 MHz, $CDCl_3$) δ 7.91 (s, 1H), 7.64 (s, 2H), 7.63 (m, 1H), 7.46 (t, J = 8.0 Hz, 2H), 7.32 (t, J = 7.4 Hz, 1H). ^{13}C NMR (126 MHz, $CDCl_3$) δ 139.87, 139.62, 129.69, 127.14, 124.96, 119.12, 112.53. *water

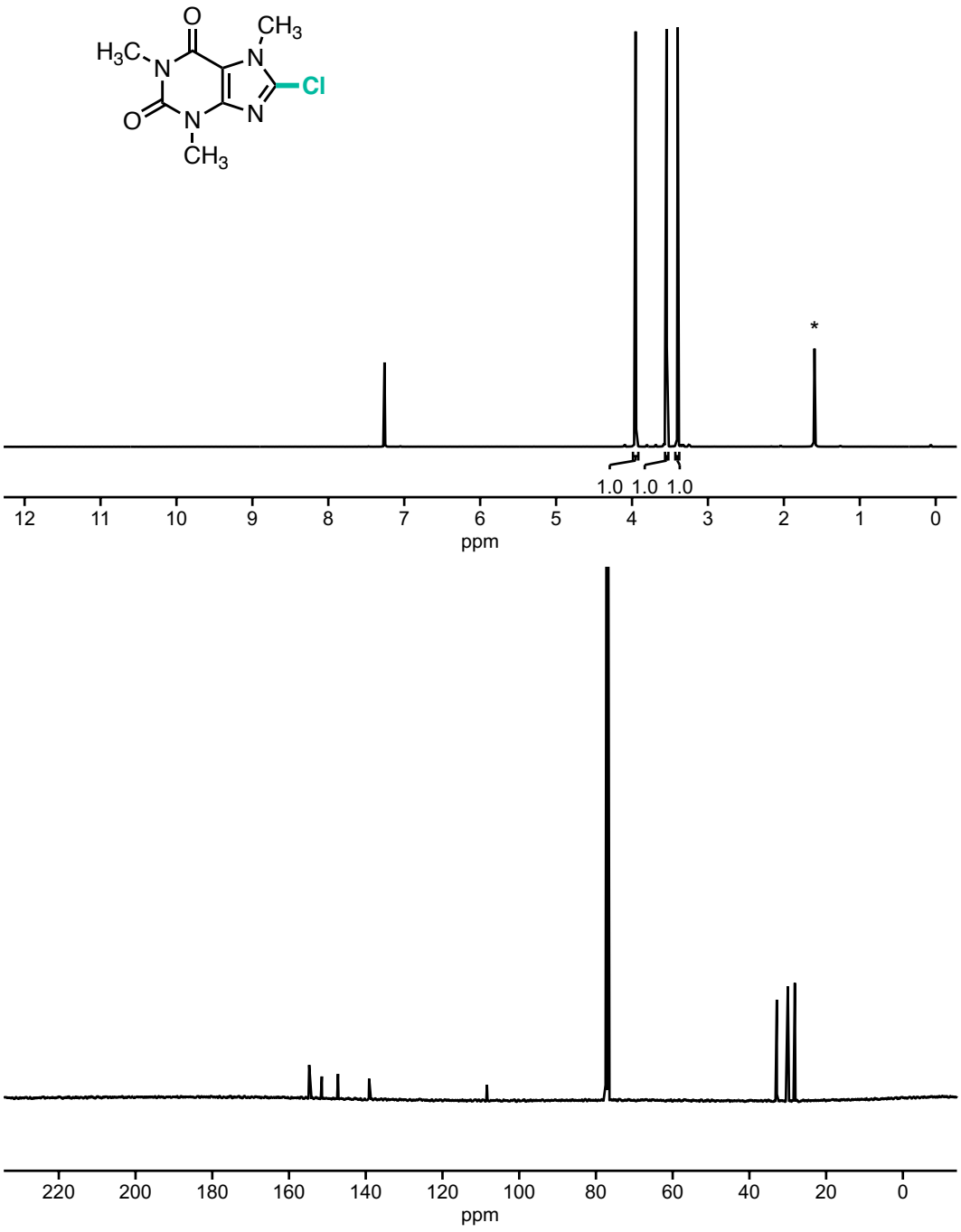

Figure A3.36 ^{1}H and ^{13}C NMR spectra of 8-chloro-1,3,7-trimethyl-3,7-dihydro-1H-purine-2,6-dione (7). ^{1}H NMR (500 MHz, $CDCl_3$) δ 3.95 (s, 1H), 3.55 (s, 1H), 3.40 (s, 1H). ^{13}C NMR (126 MHz, $CDCl_3$) δ 154.74, 151.45, 147.23, 139.12, 108.41, 32.85, 29.98, 28.16. *water

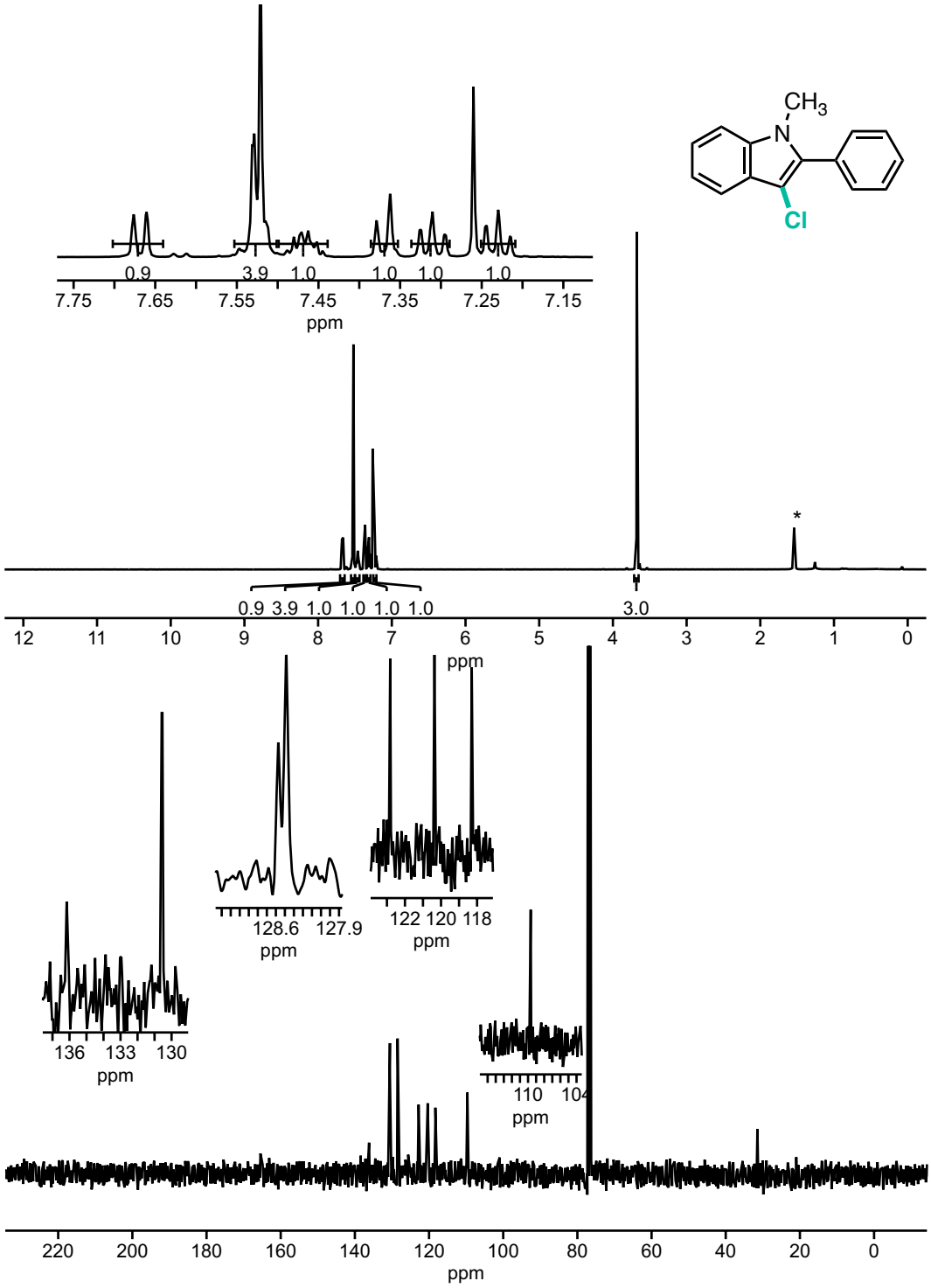

Figure A3.37 ^{1}H and ^{13}C NMR spectra of 3-chloro-1-methyl-2-phenyl-1*H*-indole (8). ^{1}H NMR (500 MHz, $CDCl_3$) δ 7.67 (d, *J* = 7.9 Hz, 1H), 7.52 (m, 4H), 7.46 (m, 1H), 7.37 (d, *J* = 8.2 Hz, 1H), 7.31 (t, *J* = 7.1 Hz, 1H), 7.23 (t, *J* = 7.4 Hz, 1H), 3.68 (s, 3H). ^{13}C NMR (126 MHz, $CDCl_3$) δ 136.17, 130.55, 128.58, 128.48, 125.62, 122.81, 120.36, 118.30, 109.67, 31.46. Note, some expected carbon peaks were not detected at the low concentration. *water

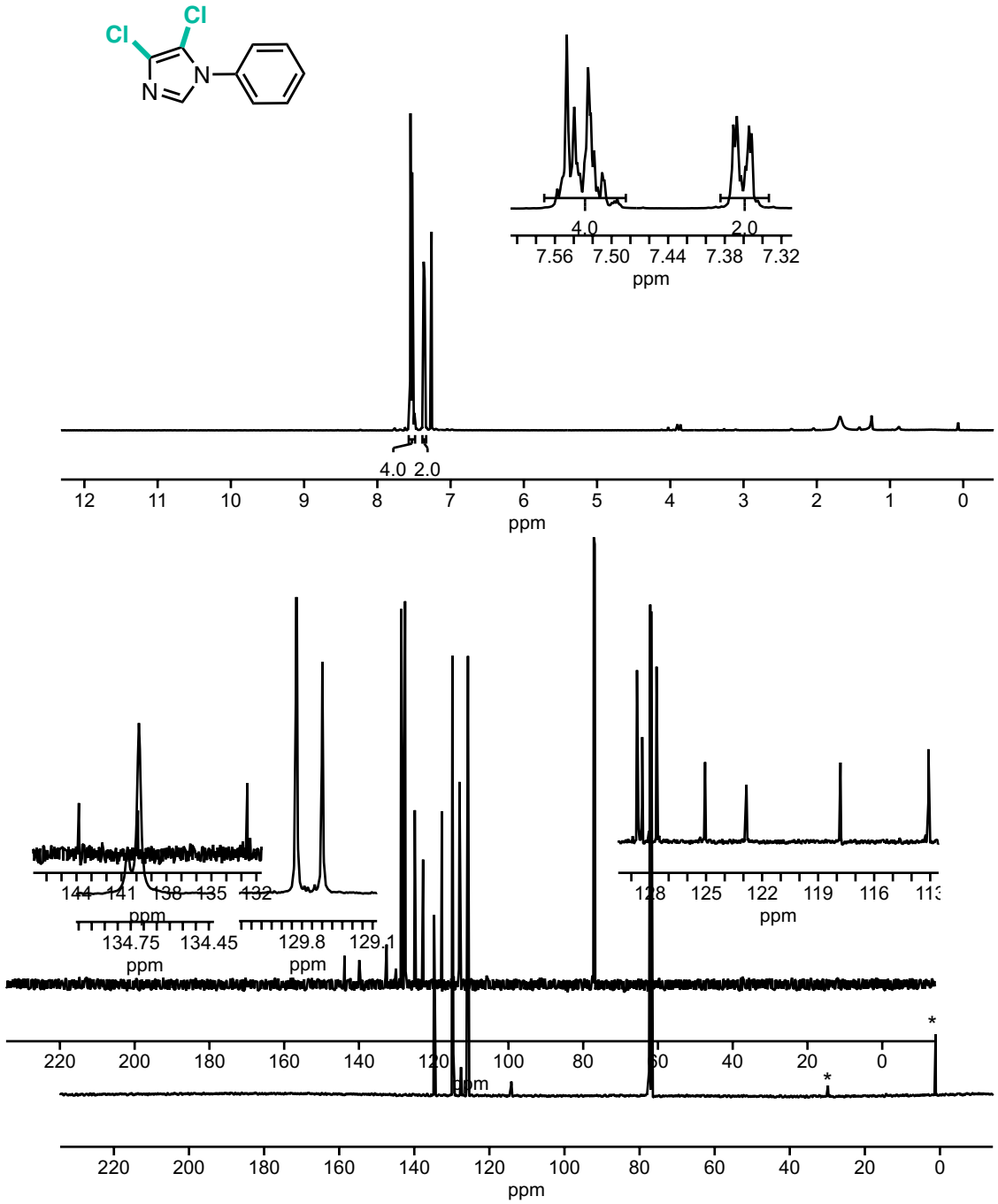

Figure A3.38 ^{1}H and ^{13}C NMR spectra of 4,5-dichloro-1-phenyl-1*H*-imidazole (9). ^{1}H NMR (500 MHz, $CDCl_3$) δ 7.57 – 7.48 (m, 4H), 7.38 – 7.33 (m, 2H). ^{13}C NMR (126 MHz, $CDCl_3$) δ 134.76, 134.72, 129.85, 129.60, 127.56, 125.71, 114.16, 29.84. *grease

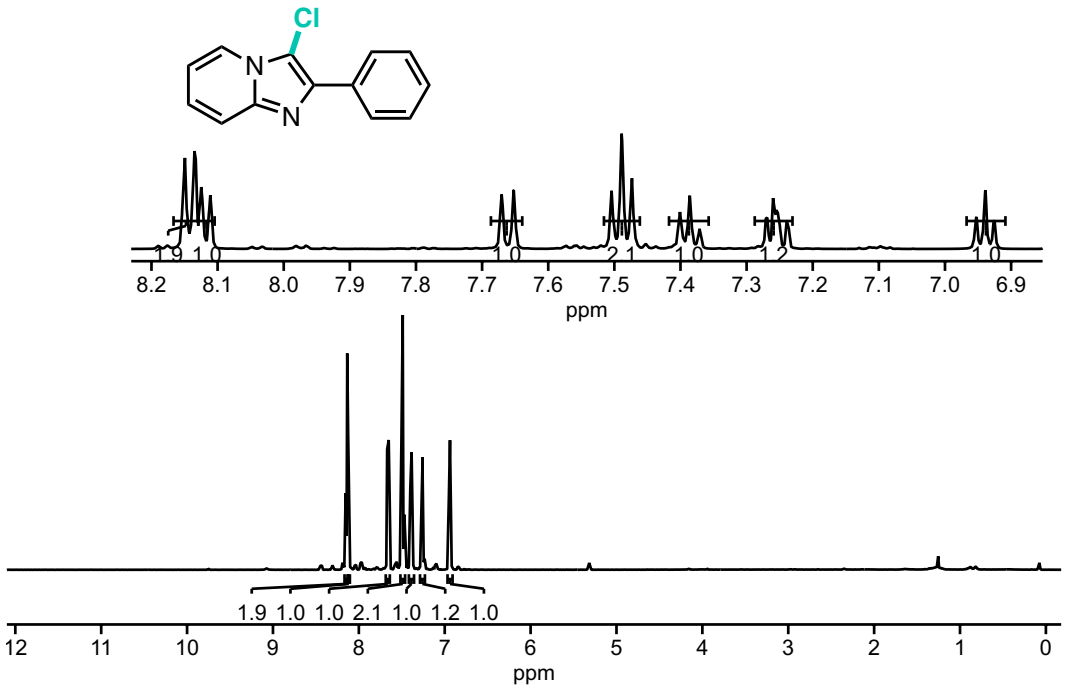

Figure A3.39 ^{1}H and ^{13}C NMR spectra of 3-chloro-2-phenylimidazo[1,2-*a*]pyridine (10). ^{1}H NMR (500 MHz, $CDCl_3$) δ 8.14 (d, *J* = 7.7 Hz, 2H), 8.12 (d, *J* = 6.9 Hz, 1H), 7.66 (d, *J* = 9.1 Hz, 1H), 7.49 (t, *J* = 7.7 Hz, 2H), 7.39 (t, *J* = 7.4 Hz, 1H), 7.25 (d, *J* = 16.9 Hz, 1H), 6.94 (t, *J* = 6.8 Hz, 1H). ^{13}C NMR (126 MHz, $CDCl_3$) δ 143.84, 139.90, 132.60, 128.70, 128.42, 127.65, 125.05, 122.84, 117.80, 113.10

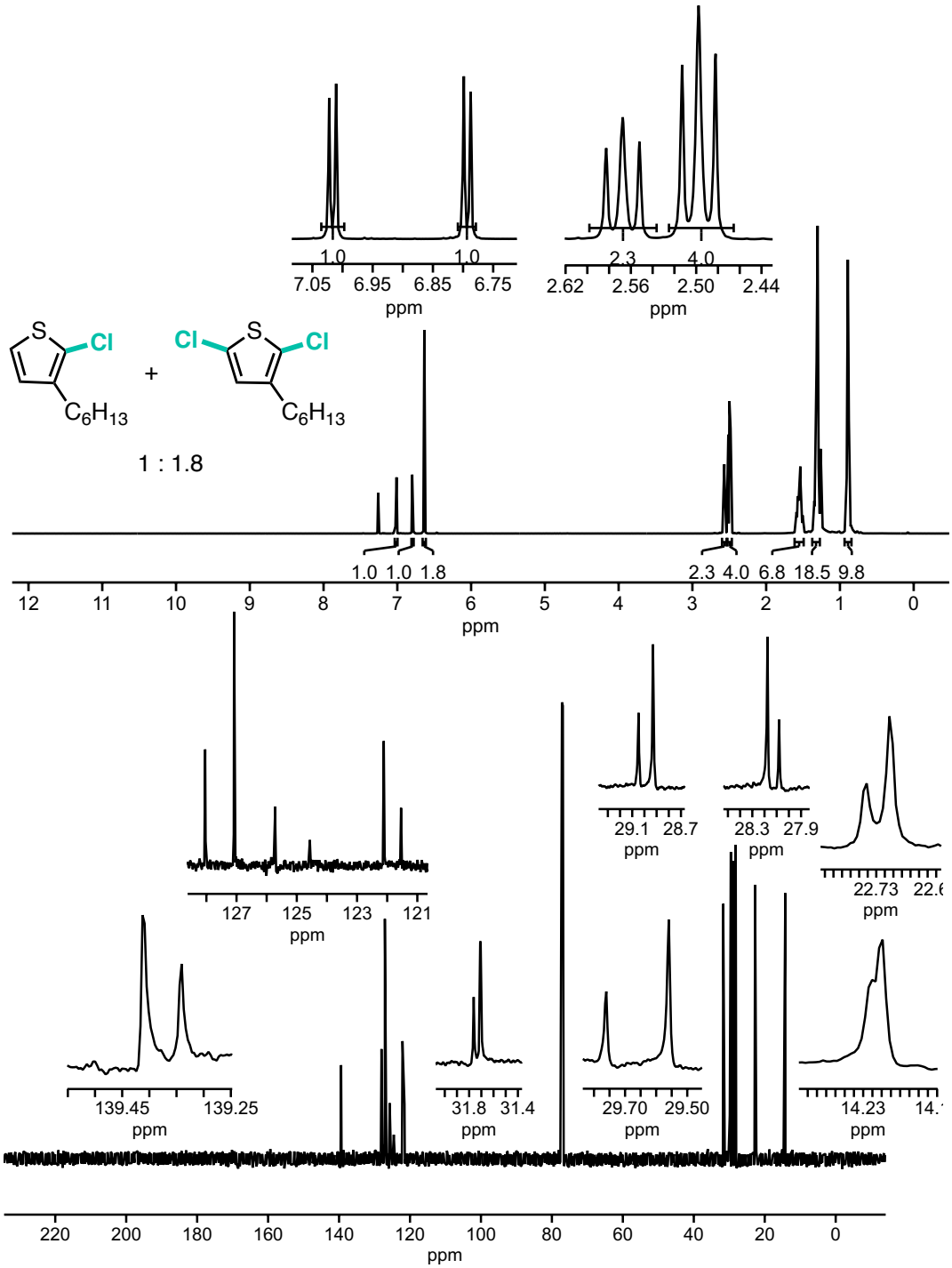

Figure A3.40 ^{1}H and ^{13}C NMR spectra of 1:1.8 mixture of 2-chloro-3-hexylthiophene: 2,5-dichloro-3-hexylthiophene (11). ^{1}H NMR (500 MHz, $CDCl_3$) δ 7.02 (d, J = 5.7 Hz, 1H), 6.79 (d, J = 5.7 Hz, 1H), 6.63 (s, 2H), 2.60 – 2.54 (m, 2H), 2.53 – 2.47 (m, 4H), 1.55 (ddt, J = 15.0, 12.7, 7.4 Hz, 7H), 1.37 – 1.27 (m, 19H), 0.94 – 0.84 (m, 10H).^{13}C NMR (126 MHz, $CDCl_3$) δ 139.41, 139.34, 128.04, 127.08, 125.72, 124.57, 122.11, 121.54, 31.76, 31.71, 29.76, 29.56, 29.05, 28.93, 28.18, 28.08, 22.74, 22.71, 14.21.

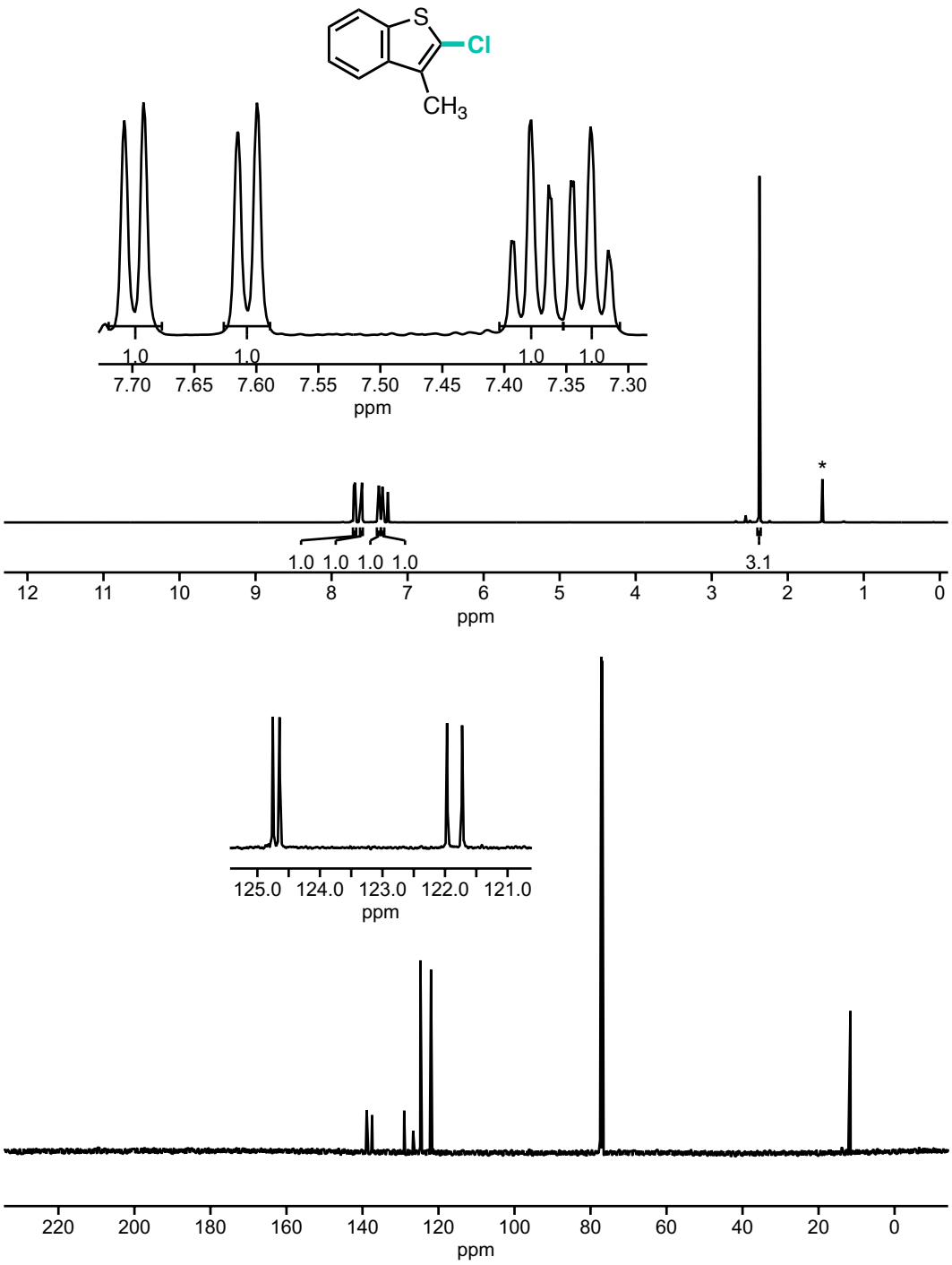

Figure A3.41 ^{1}H and ^{13}C NMR spectra of 2-chloro-3-methylbenzo[*b*]thiophene (12). ^{1}H NMR (500 MHz, $CDCl_3$) δ 7.70 (d, J = 7.8 Hz, 1H), 7.61 (d, J = 7.9 Hz, 1H), 7.38 (t, J = 7.5 Hz, 1H), 7.33 (t, J = 7.0 Hz, 1H), 2.37 (s, 3H). ^{13}C NMR (126 MHz, $CDCl_3$) δ 138.89, 137.46, 129.02, 126.67, 124.75, 124.65, 121.97, 121.73, 11.62

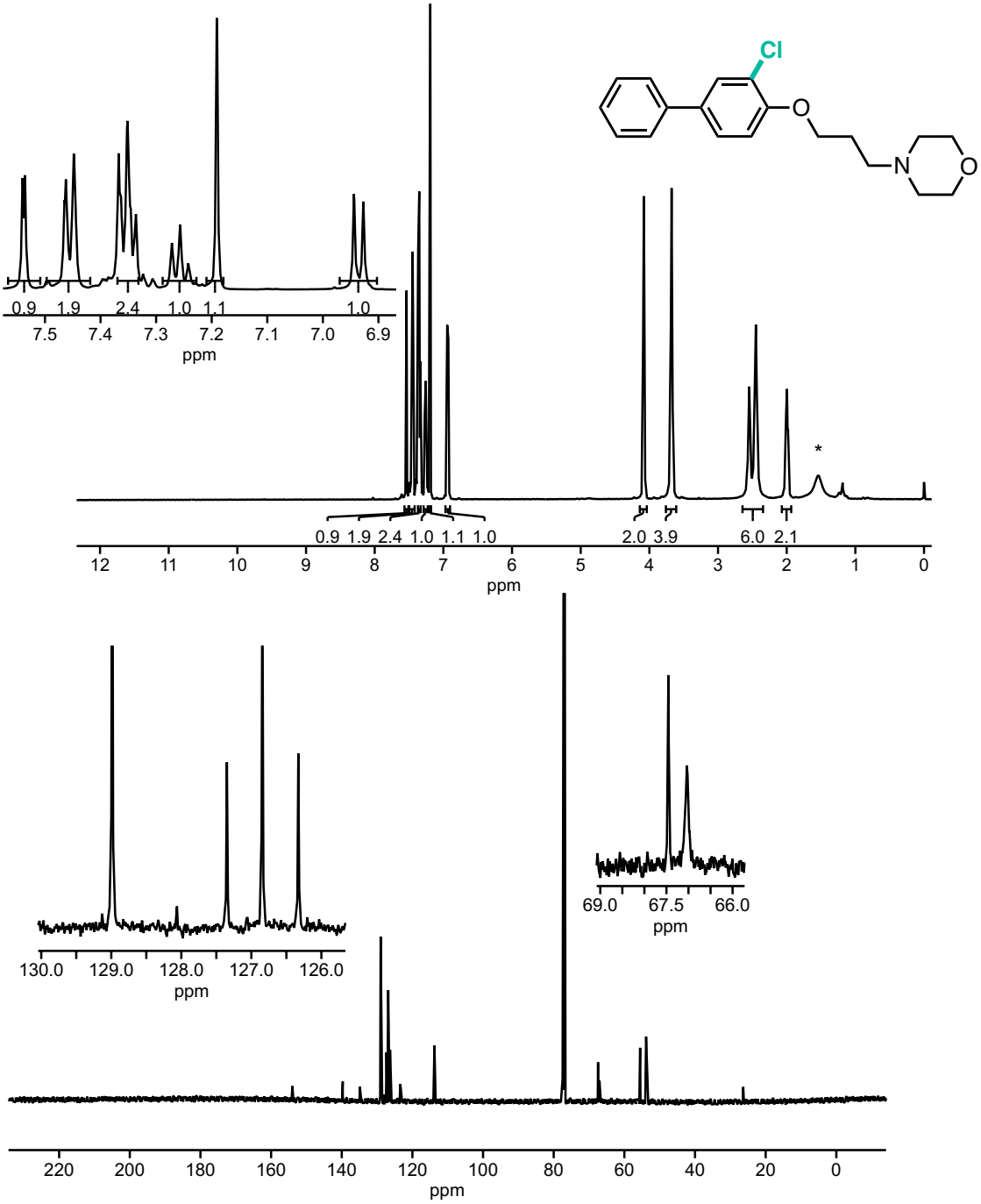

Figure A3.42 ^{1}H and ^{13}C NMR spectra of 4-(3-((3-chloro-[1,1'-biphenyl]-4-yl)oxy)propyl)morpholine (13). ^{1}H NMR (500 MHz, $CDCl_3$) δ 7.54 (d, J = 2.2 Hz, 1H), 7.45 (d, J = 7.7 Hz, 2H), 7.35 (t, J = 7.7 Hz, 2H), 7.26 (t, J = 7.4 Hz, 1H), 7.19 (s, 1H), 6.94 (d, J = 8.5 Hz, 1H), 4.08 (t, J = 6.2 Hz, 2H), 3.68 (s, 4H), 2.50 (m, 6H), 2.07 – 1.93 (m, 2H). ^{13}C NMR (126 MHz, $CDCl_3$) δ 153.96, 139.72, 134.86, 128.99, 128.06, 127.35, 126.84, 126.33, 123.41, 113.76, 67.46, 67.04, 55.54, 53.85, 26.40. *water

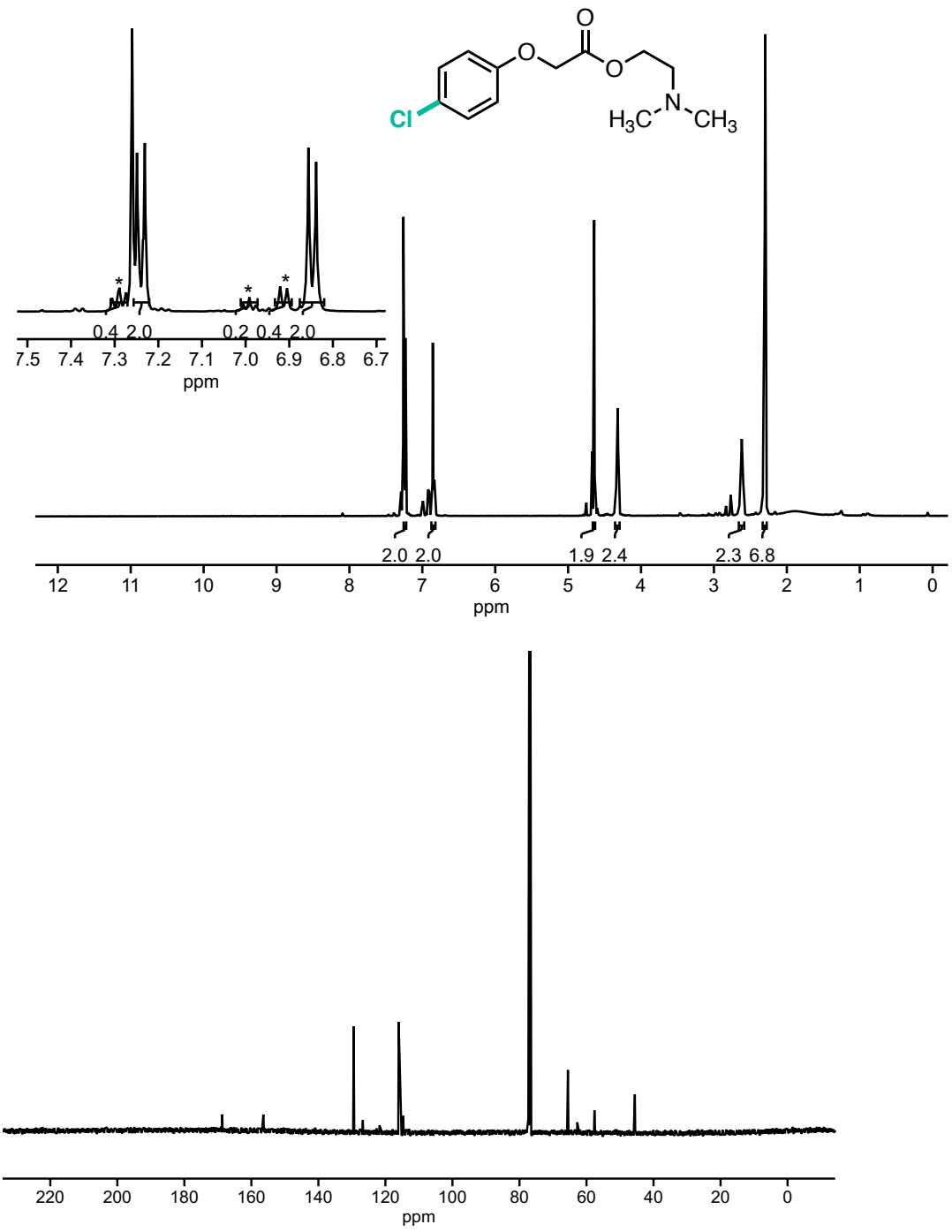

Figure A3.43 1H and 13C NMR spectra of 2-(dimethylamino)ethyl 2-(4-chlorophenoxy)acetate (14). 1H NMR (500 MHz, CDCl3) δ 7.24 (d, J = 9.0 Hz, 2H), 6.85 (d, J = 9.0 Hz, 2H), 4.64 (s, 2H), 4.32 (t, J = 5.3 Hz, 2H), 2.66 – 2.58 (m, 2H), 2.30 (s, 6H). 13C NMR (126 MHz, CDCl3) δ 168.68, 156.41, 129.47, 126.74, 116.04, 65.54, 62.74, 57.63, 45.57. *starting material

A3.14 References

(1) Density of 1-chloro-2-ethoxybenzene (25 °C): W. F. Anzilottie, B. Columba Curran, Electric moments of ortho-substituted phenols and anisoles. I. Halogen derivatives. *J. Am. Chem. Soc.* **1943,** 65, 607–611

Density of 1-chloro-4-ethoxybenzene (25 °C): R. R. Dreisbach, R. A. Martin, Physical data on some organic compounds. *Ind. Eng. Chem.* **1949,** *41,* 2875–2878

Density of ethoxybenzene (25 °C): R. R. Dreisbach, R. A. Martin, Physical data on some organic compounds. *Ind. Eng. Chem.* **1949,** *41,* 2875–2878

(2) http://www.tainstruments.com/pdf/literature/TS14.pdf (accessed: August 24, 2021)

(3) S. Cheng, K. H. Wong, C. P. Shen, X. L. Liu, C. Rudd, Shredding energy consumption of GRFP composite waste. *J. Phys.: Conf. Ser.* **2021,** *1765,* 0122015

(4) H. Jeswani, C. Krüger, M. Russ, M. Horlacher, F. Antony, S. Hann, A. Azapagic, Life cycle environmental impacts of chemical recycling via pyrolysis of mixed plastic waste in comparison with mechanical recycling and energy recovery. *Sci. Total Environ.* **2021,** *769,* 144483